Some Properties of Superplasticized and Retarding Concrete Under Effect of Accelerated Curing Methods

Asis.Lec. Dalia Shakir Atwan

College of Engineering / AL-Nahrain University/ Email:msc.dalia@yahoo.com`

ABSTRACT

In recent decades, tremendous success has been achieved in the advancement of chemical admixtures for Portland cement concrete. Most efforts have concentrated on improving the properties of concrete and studying the factors that influence on these properties. Since the compressive strength is considered a valuable property and is invariably a vital element of the structural design, especially high early strength development which can be provide more benefits in concrete production, such as reducing construction time and labor and saving the formwork and energy. As a matter of fact, it is influenced as a most properties of concrete by several factors including water-cement ratio, cement type and curing methods employed. Because of accelerated curing is deemed one of methods that achieved high early age strength of concrete and has been grown only gradually. So, the prime aim of this research work is to provide information about the some desired properties of superplasticized and retarding concrete succumbed to accelerated curing methods, such as compressive strength and water absorption and compared it with their corresponding normally curing concrete. Besides, the research discusses the influence of surface texture of aggregate and over-dosing for admixture on performance concrete in such as that conditions. The test results revealed that effect of admixture on properties of concrete are dependent upon it dosage, surface texture for aggregate and temperature used for curing.

Keywords: superplasticizer and retarding, accelerated curing, warm water, boiling water, setting time, slump, fresh density, compressive strength, water absorption

الخلاصة

في العقود الاخيرة تحققت الكثير من النجاحات فيما يخص تطوير المضافات الكيميائيـة لخرسـانة الـسمنت البورتلاندي. واغلب الجهود تركزت على تحسين خصائص الخرسانة وايضا دراسة العوامل المـؤثرة عليهـا. وبما ان مقاومة الانضغاط تعتبر الخاصية القيمة والعامل الاساس والثابت في التـصميم الانـشائي خـصوصا تطورها في الاعمار المبكرة حيث يمكن ان توفر العديد من الفوائد في انتاج الخرسانة مثل تقليـل مـدة وعمـل البناء و توفير القوالب. الا انها في واقع الامر كمعظم خصائص الخرسانة تتأثر بعدة عوامل بضمنها نسبة الماء الى السمنت،نوع السمنت وطرق الانضاج المتبعة. ولكون الانضاج المعجل يعتبر احد الطرق التي تحقق مقاومة عالية ومبكرة للخرسانة واصبحت تنمو بشكل تدريجي. لذا كان الهدف الرئيسي للبحث هو توفير معلومات عـن بعض الخصائص المرغوبة لخرسانة الملدن المتفوق والمبطيئ والخاضعة لتاثير الانضاج المعجل مثل مقاومـة الانضغاط وامتصاص الماء ومقارنتها مع خصائص الخرسانة في حالة الانضاج الاعتيادي. بجانب ذلك، ينـاقش البحث تاثير الملمس السطحي للركام الخشن والوزمات العالية للمضاف على اداء الخرسـانة فـي مثـل تلـك الظروف. وأظهرت نتائج البحث بأن تـأثير المـضاف علـى خـصائص الخرسـانة يعتمـد علـى وزمـة المضاف،الملمس السطحي للركام ودرجة الحرارة المستخدمة للانضاج.

INTRODUCTION

The practical use of concrete as a construction material depends upon the fact that it is plastic in the freshly mixed state and subsequently becomes hard, with considerable strength. This change in its physical properties is due to the chemical reaction between cement and water, a process known as hydration. Hydration involves chemical changes, not just a drying out of the material, hydration is irreversible. The reaction is gradual, first causing stiffening of the concrete, and then development of strength, which continues for a very long time. Under certain ideal conditions it is probable that concrete would continue to increase in strength indefinitely. Air temperature, ground temperature and weather conditions all play major roles in the rate with which cement hydrates (Corcoran, 2004). If the hydration process is speeded up it is possible to reduce the waiting period for test results from 28 days to only 1 or 2 days. This is done by using accelerated curing methods that either supply an external source of heat or retain the heat of hydration given off when cement and water react (ASTM C 684-99). As a results, many benefits can be achieved such as ;

- The fast trend of construction progress and its economic benefits attained from accelerating the construction schedules.
- Testing for quality control purposes.
- To check the suitability of concrete mixes much earlier than the 28-days test during the design stage (Torkey, 1980)

Accelerated curing is any method by which high early age strength is achieved in concrete. These techniques are especially useful in the prefabrication industry wherein high early age strength enables the removal of the formwork within 24 hours thereby reducing the cycle time resulting in cost saving benefits (Erdem, 2003).The criterion for concrete strength requirement is always based on the characteristic compressive strength obtained after 28-days curing. This delay in testing of concrete seriously limits the control of the matrix during production and hampers quality assurance at early ages (Lamond, 1983). The use of a reliable accelerated strength testing method would add in no small measure to a better control over the properties of concrete in the field by enabling the concrete engineer to make necessary adjustment during proportioning of concrete early enough to avoid the production of sub-standard concrete (Malhotra,1981).The current speedy construction due to improved and innovative construction methods also calls for the potential strength of concrete to be determined at the earliest possible time after concrete has been placed (Tokyay, 1999). In this study, three different curing regimes were applied, normally curing, warm water method (WWM) and boiling water method (BWM).

RESEARCH PROGRAM

The basic objective of this present research is to study the influence of accelerated curing methods on some properties of superplasticized and retarding concrete. In this work, warm water and boiling water curing techniques according to ASTM C684-99 were applied to accelerate the strength gain of concrete. Two concrete mixes in terms of surface texture for gravel, ordinary and crushed, were considered. Superplasticizer and retarding admixture type G were also applied. The effect of surface texture for gravel, curing methods and over doses for admixture were investigated.

ACCELERATED CURING METHODS

There are several ways to cure concrete in the field. One form of curing that has become popular at precast prestressed concrete plants is accelerated curing. This type of curing is advantageous where early strength concrete gain is important (Yazdani, 2005). First, concrete elements can be removed from their forms very early after placement; currently, a 24-hour turnover period for most precast elements is standard. Second, rapidly curing concrete means that manufactures require less space reserved for the explicit purpose of curing (Vollenweider, 2004). The rate of strength gain is well known to be a consecutive property from the hydration process of the cement. Since the degree of cement hydration depends on the surrounding temperature, so the strength gain could be accelerated at early ages by using various techniques of accelerated curing such as; heat water techniques, oven curing techniques, maturity methods, pressure and elevated temperature technique and expanded polystyrene molds technique (Torkey, 1980). The ASTM C684-99 recommends three different accelerated curing techniques:

– Warm water method (WWM), the specimens were cast in steel molds and were immediately placed in the curing tank for a periods of 23½hr±30min. The curing tank water temperature was 35˚C±3˚C.The top of the molds were covered to prevent loss of mortar to the water bath. After

that, the specimens were demoulded and tested at age of 24 hr±15 min.

– Boiling water method (BWM), the specimens were cast in steel molds and were cured initially for 23hr±15min in the laboratory environment (approximate temperature 21ºC). Then, the specimens were immersed in boiling water and remained there for a period of 3½hr±5 min, cooled for 1 hr and then tested at an age of 28½hr±15 min.

– Autogenous curing method, the specimens were cast in steel molds and were placed in an insulating container and held there for 48hr±15 min and then tested at an age of 49hr±15 min (ACI 517.2 R-87, 1992).

The focus of this paper is investigated the effectiveness of the warm water and boiling water methods for accelerating curing on concrete mixtures containing superplasticizer and retarding admixture.

EXPERIMENTAL INVESTIGATIONS AND SPECIFICATIONS

Properties of Materials

Cement; one type of Portland cement; ordinary portland cement (OPC) was applied. Total percentages for its oxides, compound composition and some properties were fulfilled to the requirement of Iraqi specification No.5/1984 as denoted in Table 1 .

Aggregate; the fine aggregate used was local sand, while the coarse aggregate used was two types; ordinary and crushed gravel with maximum size 19 mm. All their met the requirements of ASTM C33-03 with respect the sieve analysis and physical properties as denoted in Table 2,3,4,5,6 and 7.

Water; Normal tap water was used as mixing water.

Admixture; synthetic based superplasticizer with a retarding effect was used. Its commercial known as Eucobet super VZ and complied to ASTM C 494 type G. Its specific gravity was 1.1 and its chloride content was claimed nil. Table 8 shows the technical description for it.

Concrete Mixes Proportion and Its Fresh Tests

Throughout the laboratory experiment, the applied eight concrete mixes were selected to cover the effect of surface texture for gravel and the dosage of admixtures on the properties of produced concrete with normally water cured and accelerated cured. Control mixes (reference) designed for 28-days characteristic strength of 25MPa according to ACI 211.1-95. For both two types of gravel, four mixes were prepared with four dosages of admixture (0, 0.8,1.6 and 2.5)% by weight of cement. All mixes were designed to have fixed proportions of total cement content of 410 kg/m^3, 710 kg/m^3 sand, 1030 kg/m^3 gravel and 190 kg/m^3 free water content. After mixing the materials, the following fresh tests were determined for each concrete mix;

– Initial setting time according to ASTM C403-99
– Slump according to ASTM C143-2000
– Fresh density according to ASTM C138-01

Preparation of Specimens and Curing

The cubical molds of size 150 mm lightly oiled were filled with fresh concrete and compacted by using vibrating table. For each concrete mix, twenty four cubic specimens were used, twelve cubic specimens for accelerated curing according to specified procedure in ASTM C 684-99 (six for the warm water curing and another six for the boiling water curing). While the remaining twelve of cubic specimens were used for normally water curing, where the molds after casting were covered with polyethylene sheet and kept in the laboratory environment for a period of 24hr. After that, the specimens were demoulded and placed in the water curing tanks up to the wanted age for test.

Hardened Concrete Tests

Compressive Strength

Compressive strength tests involve the manufacture of test specimens which were square in shape measuring 150 mm according to B.S.I 1881: part 116: 1989. For normally water curing, the specimens were tested at age of 1,3 and 28-days strength of the concrete. While for accelerated cured specimens, accelerated strength were determined at ages of 24 hr±15 min and 28½hr±15 min for WWM and BWM respectively. In each test age, the average of three specimens was adopted.

Water Absorption

The water absorption test was performed according to ASTM C 642-06 and carried out on 150 mm cube specimens at age 28-days for normally curing specimens and at age 24 hr±15 and 28½hr±15 min for WWM and BWM respectively. The average of three specimens in each age was taken. In this test, the specimens

were weighed before and after immersion in water. Water absorption was then determined as the difference in the weight of specimen before and after immersion in water relative to the weight of specimen before immersion in water, expressed in percentage.

TEST RESULTS AND DISCUSSION

1. Table 9 summarizes the results of the tested fresh concrete. The measured properties were initial setting time, slump and fresh density. The results indicated that ordinary gravel mixes with and without admixture showed increase in an initial setting time and slump versus slight decrease in fresh density compared to their corresponding crushed gravel mixes as denoted in Fig.4,5 and 6. Where as the ratios of increasing in an initial setting time and slump for control mix (M1) compared to M5 were 7.81% and 8.64 % respectively, while the reduction in fresh density was 0.13%. This may be attributed to the fineness texture for gravel used which increase the workability of concrete mix consequently, decrease the internal friction between particles of mix.
2. The measured values for initial setting time, slump and fresh density indicate that the control mixes for both two types of gravel (M1and M5) have the lowest values when compared it with their corresponding mixes that containing of SPR as represented in Fig.7 and 8. This can be ascribed to the fact that the SPR used causes an increase in set retardation by slowing down the rate of early hydration of C_3S and increasing the fluidity concrete mix. Beside, the improvement which enhancement in the SPR mixes consistency and the better compactability of such mixes (Ramachandran, 1998). For example, the reduction in initial setting time, slump and fresh density for control mix (M1) compared to M2 mix were 28.86%, 36.70% and 0.38% respectively, versus 31.18%, 35.20% and 0.55% reduction in initial setting time, slump and fresh density respectively, for control mix (M5) compared to M6 mix.
3. The results also demonstrated that the retarding tendency of the SPR admixture increased with higher admixture content for both two types of gravel, where setting times were extended when admixture was incorporated into mixes compared with it corresponding control mixes as revealed in Fig.4. The retarding effects of a admixture when added to a mix continue until it is removed from the solution by reaction with C_3A from the cement or by some other way and incorporated into the hydrated material.
4. The results denoted that the concrete mixes (M4 and M8) demonstrated decrease in fresh density compared to M3 and M7 respectively. This is may be due to the overdosing for SPR used in these mixes which produce undesirable effects such as increase the fluid of concrete mix and setting time as a results induce the onset of segregation in particles the mix. That is why usually discouraging used higher contents for admixture because of adverse effectiveness. The reduction in fresh density for M4 and M8 mixes were 0.21% and 0.42% compared to M3 and M7 mixes respectively.
5. Table 10 summarizes the results of the compressive strength and water absorption tests for normally and accelerated curing specimens. From these results, it can be seen that crushed gravel mixes with different curing methods showed higher improvement in compressive strength and more reduction in water absorption compared to their corresponding ordinary gravel mixes. This is probably due to the fact that the rough particles tend to provide stronger bond than smooth particles. As a results, rough particles tend to produce higher strength (Kaplan, 1959). The results also showed that the effect of surface texture for gravel was more noticeable in accelerated curing (WWM and BWM) than that in normally curing. Besides, the difference due to the surface texture for gravel was less in the BWM than that in the WWM. The ratios of increasing in compressive strength of control mix (M5) relative to M1mix were 4.04%, 21.74% and 11.14% versus 6.77%, 2.98% and 3.40% reduction in water absorption at 28-days normally curing, warm water method (WWM) and boiling water method (BWM) respectively.
6. The results also showed that all the concrete mixes with presence SPR admixture and under effect various curing methods exhibited slight improvement in compressive strength and noticeable reduction in water absorption compared to their control mixes. The main reason is returned to the better dispersion of the cement particles (uniform distribution of products of hydration within the paste) which resulted in higher rate of cement hydration. Furthermore, because of its effectiveness in delay setting time lead to produce a denser gel. For example, the ratio increase in compressive

strength for M2 mix compared to M1mix were 4.08%, 1.30% and 2.17% versus 21.87%, 4.67% and 10.38% reduction in water absorption at 28-days normally curing, WWM and BWM curing respectively. While the ratio increase in compressive strength for M6 mix compared to M5mix were 7.10%, 2.30% and 3.55% versus 24.02%, 6.28% and 12.75% reduction in water absorption at 28-days normally curing, WWM and BWM curing respectively.

7. From Table 10, it can be seen that normally curing specimens at age 1-day have lower compressive strength than that corresponding accelerated curing specimens. This is may be strongly linked with raise the curing temperature from 21˚C for normally water curing to 35˚C and 100˚C for warm and boiling water curing respectively. On contrary, the results of normally curing specimens at age 3-days and 28-days showed higher values for compressive strength when compared it with corresponding accelerated curing specimens. This is may be associated with age of the specimens where the rate of gain of strength increase with age. On the other hand, when comparing the results of compressive strength for WWM and BWM, it can be observed that compressive strength of BWM curing specimens were higher compared to their corresponding of WWM curing specimens. This is attributed to increase the temperature for BWM than WWM, where an increasing in curing temperature has a more favorable effect on the strength gain due to the direct effect of the temperature on activating hydration (Dhir, 1988).
8. The results also demonstrate that M4 and M8 mixes in all curing methods showed slight decrease in compressive strength with slight increase in water absorption when compared it with their corresponding M3 and M7 mixes. This behavior is substantially ascribed to the discommendable influences on properties of concrete for overdosing admixture in these mixes. The reduction in compressive strength for M4 compared to M3 were 1.92%, 0.87% and 1.71% versus 6.25%, 1.28% and 2.44% increase in water absorption at 28-days normally curing, WWM and BWM curing respectively. While the reduction in compressive strength for M8 compared to M7 were 1.74%, 0.71% and 1.05% versus 4.08%, 0.91% and 1.16% increase in water absorption at 28-days normally curing, WWM and BWM curing respectively.

CONCLUSIONS

The following conclusions have been reached in this study;

1. The behavior of concrete mixes containing superplasticizer and retarding (SPR) admixture under condition of accelerated curing is effects by many factors such as dosage of admixture, surface texture of aggregate and temperature used on the rate of strength gain.
2. The surface texture for gravel was affects the properties of fresh concrete. Where, the concrete mixes was high workable and delay in setting time versus decrease in fresh density when smooth gravel used instead of rough gravel. The ratios of increasing in an initial setting time and slump for M1 mix compared to M5 were 7.81% and 8.64% respectively versus 0.13% reduction in fresh density.
3. The control mixes showed decrease in an initial setting time, slump and fresh density when compared it with their corresponding mixes containing SPR. The reduction in initial setting time, slump and fresh density for control mix (M1) compared to M2 mix were 28.86 %, 36.70% and 0.38 % respectively, versus 31.18%, 35.20 % and 0.55 % reduction in initial setting time, slump and fresh density respectively, for control mix (M5) compared to M6 mix. Furthermore, M4 and M8 mixes demonstrated decrease in fresh density compared to M3 and M7 respectively. The reduction in fresh density for M4 and M8 mixes were 0.21% and 0.42% compared to M3 and M7 mixes respectively.
4. The influence of surface texture for gravel on compressive strength and water absorption was greater demonstrated in the accelerated curing specimens than normally curing specimens. On the other hand, this influence was less in the BWM than that in the WWM. The ratios of increasing in compressive strength of control mix (M5) relative to M1mix were 4.04%, 21.74% and 11.14% versus 6.77%, 2.98% and 3.40% reduction in water absorption at 28-days normally curing, WWM and BWM respectively.
5. The values of accelerated strength with warm water method (WWM) and boiling water method (BWM) for all concrete testing specimens were greater than the strength of normally cured concrete specimens at corresponding age. While these values were less comparing to values

3-days and 28-days normally curing. Besides, BWM curing specimens were higher than that WWM curing specimens.

6. With presence superplasticizer and retarding (SPR) admixture and under effect various curing methods, the mixes were exhibited slight improvement in compressive strength and noticeable reduction in water absorption compared to their control mixes. The ratio increase in compressive strength for M2 mix compared to M1mix were 4.08%, 1.30% and 2.17% versus 21.87%, 4.67% and 10.38% reduction in water absorption at 28-days normally curing, WWM and BWM curing respectively. While the ratio increase in compressive strength for M6 mix compared to M5mix were 7.10%, 2.30% and 3.55% versus 24.02%, 6.28% and 12.75% reduction in water absorption at 28-days normally curing, WWM and BWM curing respectively
7. In all curing methods, the mixes incorporating higher content of SPR admixture (2.5% by weight of cement) showed slight decrease in compressive strength versus slight increase in absorption compared to their corresponding mixes that containing (1.6% by weight of cement). The reduction in compressive strength for M4 compared to M3 were 1.92%, 0.87% and 1.71% versus 6.25%, 1.28% and 2.44% increase in water absorption at 28-days normally curing, WWM and BWM curing respectively. While the reduction in compressive strength for M8 compared to M7 were 1.74%, 0.71% and 1.05% versus 4.08%, 0.91% and 1.16% increase in water absorption at 28-days normally curing, WWM and BWM curing respectively.

REFERENCES

ACI Committee 211.1-95, Standard Practice for Selection Proportions for Normal, Heavy Weight and Mass Concrete, ACI Manual of Concrete Practice, Part 1-1995.

ACI 517.2 R-87, Accelerated Curing of Concrete at Atmospheric Pressure-State of the Art, ACI Manual of Concrete 1992.

ASTM C33-03, Standard Specification for Concrete Aggregate, Philadelphia, PA: American Society for Testing and Materials.

ASTM C138–01,Test Method for Unit Weight, Yield and Air Content Gravimetric of Concrete, Annual Book of ASTM Standards, Vol. 04.02, Concrete and Mineral Aggregates.

ASTM C143-00, Standard Test Method for Slump of Hydraulic Cement Concrete, Annual Book of ASTM, Standards American Society for Testing and Materials, Vol.04.02.

ASTM C 403-99, Standard Test Method for Time of Setting of Concrete Mixtures by Penetration Resistance, Philadelphia, PA: American Society for Testing and Materials.

ASTM C494-92, Standard Specification for Chemical Admixtures for Concrete, Philadelphia, PA: American Society for Testing and Materials.

ASTM C 642-06, Standard Test Method of Specific Gravity, Absorption and Voids in Hardened Concrete, 2006.

ASTM C684-99,Standard Method of Making, Accelerated Curing and Testing of Concrete Compression Test Specimens, 2003.

British Standard Institution (B.S.I) 1881, Part 116, 1989, Method for Determination of Compressive Strength of Concrete Cubes, pp.3.

Corcoran, James, Concrete Technology Corporation, 1123 Port of Tacoma Road, Tacoma, WA 98421. Telephone interview on 2004.

Dhir, R., Development of Strength, Three day course-Modern Cements in Concrete Construction: Pulverized-Fuel Ash, Ground Granulated Blastfurnace Slag and Silica Fume, University, U.K, 28-30 June 1988.

Erdem, T., 2003, Setting time: an important criterion to determine the length of the delay period before steam curing of concrete. Cement and Concrete Research **33**: 741–050.

المواصفة القياسية العراقية رقم (5) لسنة 1984 "الاسمنت البورتلاندي" الجهاز المركزي للتقييس والسيطرة النوعية.

Kaplan, M.,F., Flextural and Compressive strength of Concrete as Affected by The Properties of Coarse Aggregate,proceedings of the American concrete institute, Vol.55, 1959, pp.1193-1208.

Lamond, J.F., Quality Assurance Using Accelerated Strength Testing, Concrete International : Design and Construction, 1983, pp. 47-51.

Malhotra,V.M., Accelerated Strength Testing: Is it a solution to a contractor's dilemma? Concrete International: Design and Construction, 1981,pp.17-21.

Ramachandran,V.S.,Malhotra,V.M.,Jolicoeur, C.and Spiratos,N.,Superplasticizers:Properties and Applicationsin Concrete, CANMET, 1998, pp. 397.

Torkey,A.A, Accelerated Strength for Quality Control of Mortar and Concrete, MSc thesis, Faculty of Engineering, Cairo University, 1980.

Tokyay, M., Strength Prediction of Fly Ash Concretes by Accelerated Testing, Cement and Concrete Research, 1999.

Vollenweider, B., Various Methods of Accelerated Curing for Precast Concrete Applications, and Their Impact on Short and Long Term Compressive Strength, Concrete Technology, CE 241, March 2004.

Yazdani, N., Accelerated Curing of Silica Fume Concrete, Summary of Final Report, BD-488, July 2005.

Table 1 Oxides, Compound composition and Physical properties of ordinary Portland cement

Oxides	%	I.S. No.5/1984	Property		Result	I.S. No.5/1984
SiO2	20.54	–	Fineness, m^2/Kg		341	≥230
Al2O3	5.88	–	Setting time, hrs:min	Initial set.	2:35	≥00:45
Fe2O3	3.28	–				
CaO	60.78	–				
MgO	1.93	≤ 5.0		Final set.	4:45	≤ 10:00
SO3	1.87	≤ 2.8	Compressive strength, MPa	3-day	18.8	≥15.00
L.O.I.	3.31	≤ 4.0				
I.R.	0.15	≤ 1.5				
L.S.F.	0.89	0.66-1.02				
C3S	41.74	–		7- day	23.3	≥23.00
C2S	27.48	–				
C3A	10.04	–				
C4AF	9.97	–	Expansion,%		0.03	≤ 0.8

Table 2 Sieve analysis of sand

Sieve size (mm)	9.5	4.75	2.36	1.18	0.30
Cumulative % passing	100	91.39	38.90	7.11	4.61
ASTM C33-03	100	85-100	10-40	0-10	0-5

Table 3 Physical properties of sand

Physical properties	Specific gravity	Sulfate content	Absorption
Test result	2.66	0.07	0.81%
I.S. No.45/1984	-	≤0.5%	-

Table 4 Sieve analysis of ordinary gravel

Sieve size (mm)	25	19	9.5	4.75	2.36
Cumulative % passing	100	97.29	46.03	8.88	2.9
ASTM C33-03	100	90-100	20-55	0-10	0-5

Table 5 Physical properties of ordinary gravel

Physical properties	Specific gravity	Sulfate content	Absorption
Test result	2.64	0.09	0.77%
I.S. No.45/1984	-	≤0.1%	-

Table 6 Sieve analysis of crushed gravel

Sieve size (mm)	25	19	9.5	4.75	2.36
Cumulative % passing	100	93.75	49.28	7.04	4.11
ASTM C33-03	100	90-100	20-55	0-10	0-5

Table 7 Physical properties of crushed gravel

Physical properties	Specific gravity	Sulfate content	Absorption
Test result	2.63	0.05	0.69%
I.S. No.45/1984	-	≤0.1%	-

Table 8 Technical description of Eucobet super VZ

Appearance	Liquid

Colour	Brown
Specific gravity	1.1
Chloride content	nil
Air entraining	Does not entrain air
Compatibility with cement	all types of Portland cement
Shelf life	Up to 2 years
Dosage	0.4-1.6% of the cement weight

Table 9 Results of fresh tests for concrete mixes

Type of gravel	No. of Mix	SPR %	Initial setting time hr:min	Slump mm	Fresh density Kg/m^3
Ordinary	M1	0	4:36	88	2329
	M2	0.8	6:28	139	2338
	M3	1.6	13:05	180	2344
	M4	2.5	22:01	225	2339
Crushed	M5	0	4:25	81	2332
	M6	0.8	6:12	125	2341
	M7	1.6	12:33	168	2354
	M8	2.5	21:23	211	2344

Accelerated curing	BWM	Absorption %	5.60	5.02	4.51	4.62	5.41	4.72	4.31	4.39

ng and accelerated curing specimens

Type of gravel	No. of Mix	SPR %	Normally curing				WWM		
			Compressive strength MPa			Absorption %	Compressive strength MPa	Absorption %	Compressive strength MPa
			1-day	3-days	28-days	28-days			
Ordinary	M1	0	5.29	12.15	25.96	1.92	5.38	7.71	10.14
	M2	0.8	5.40	13.81	27.02	1.50	5.45	7.35	10.36
	M3	1.6	5.62	15.90	29.14	1.12	5.70	7.01	11.11
	M4	2.5	5.54	14.14	28.58	1.19	5.65	7.10	10.92
Crushed	M5	0	6.47	13.42	27.01	1.79	6.55	7.48	11.27
	M6	0.8	6.64	15.06	28.93	1.36	6.70	7.01	11.67
	M7	1.6	7.00	17.31	31.54	0.98	7.03	6.62	12.39
	M8	2.5	6.88	16.31	30.99	1.02	6.98	6.68	12.26

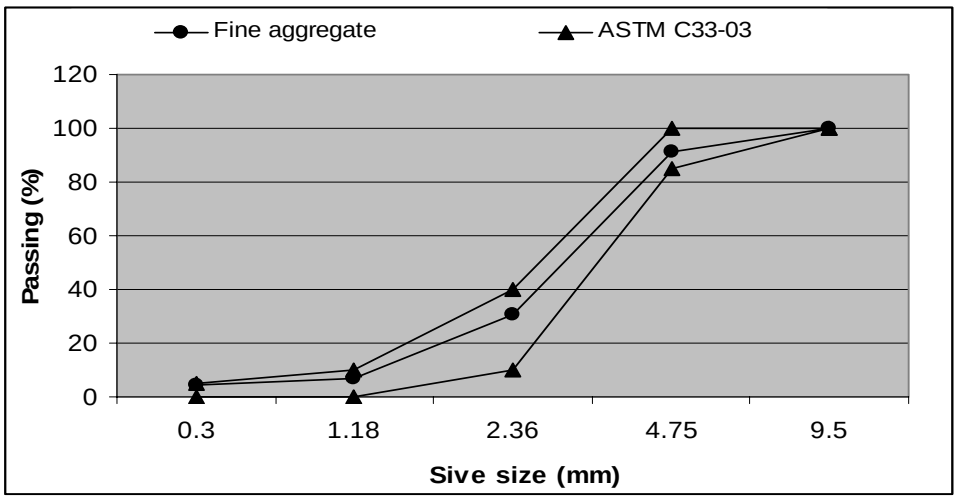

Fig.1 Grading curve for sand

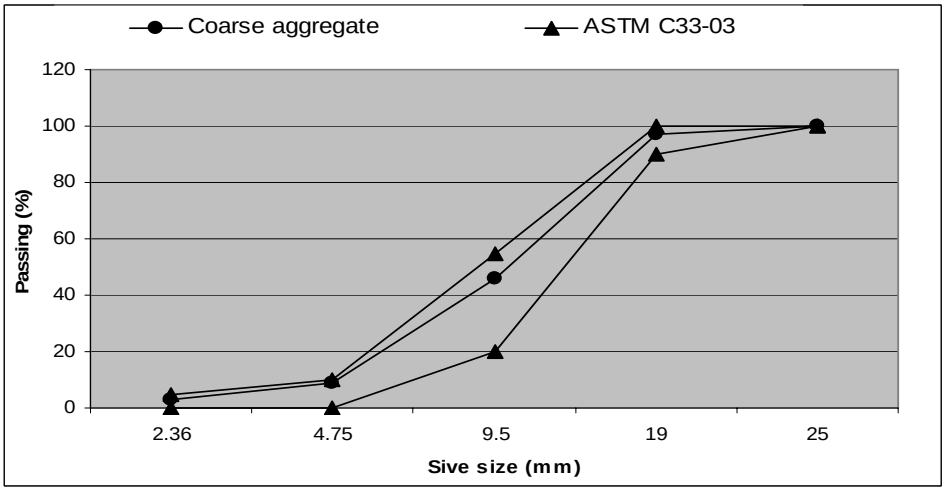

Fig.2 Grading curve for ordinary gravel

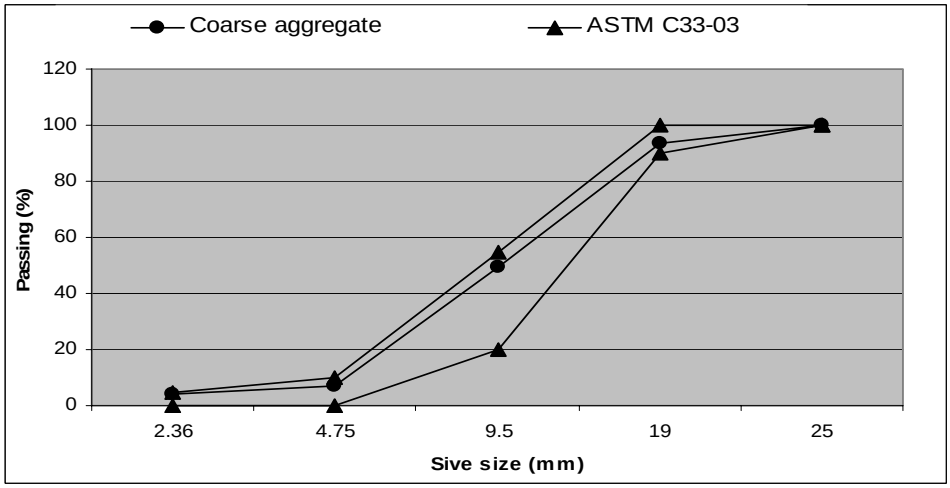

Fig.3 Grading curve for crushed gravel

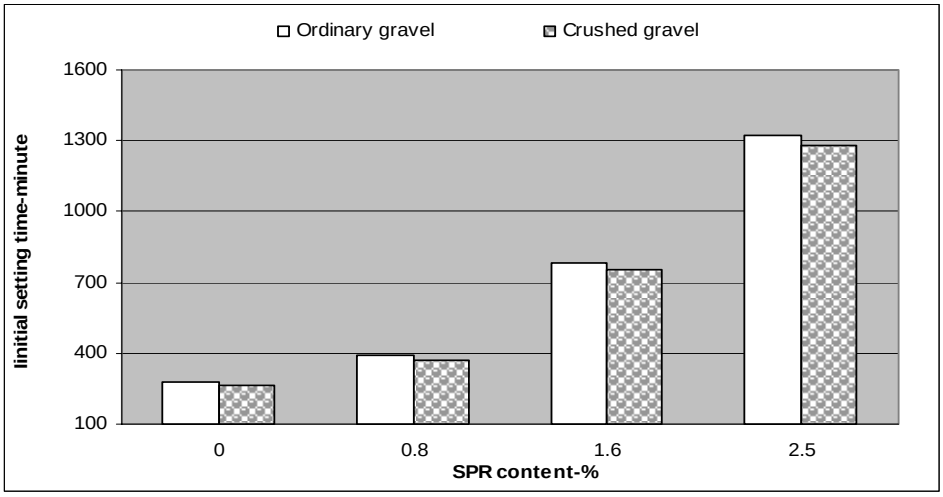

Fig.4 Initial setting time for mixes relative to type of gravel used at different SPR dosages

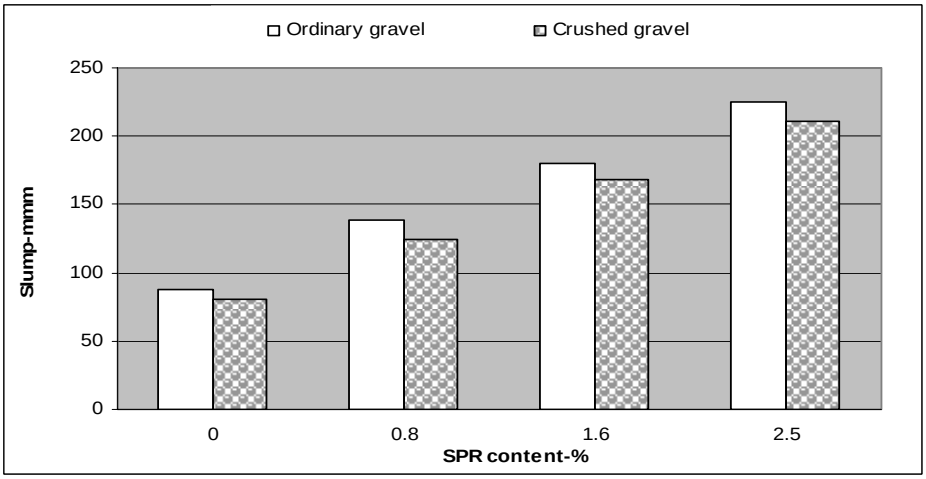

Fig.5 Slump of mixes relative to type of gravel used at different SPR dosages

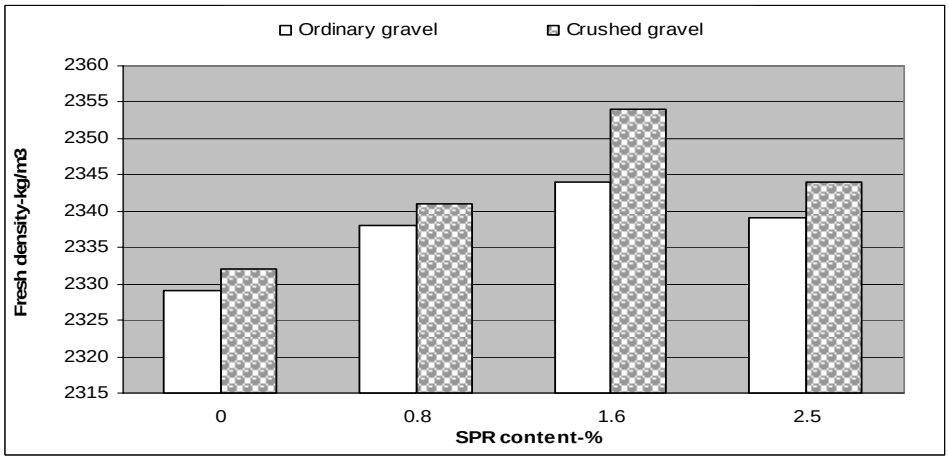

Fig.6 Fresh density for mixes relative to type of gravel used at different SPR dosages

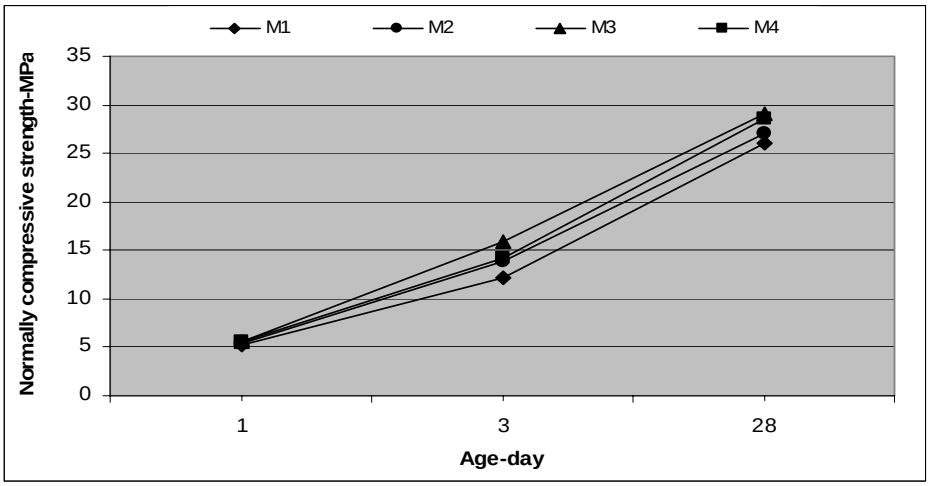

Fig.7 Normally compressive strength for ordinary gravel mixes at different SPR dosages

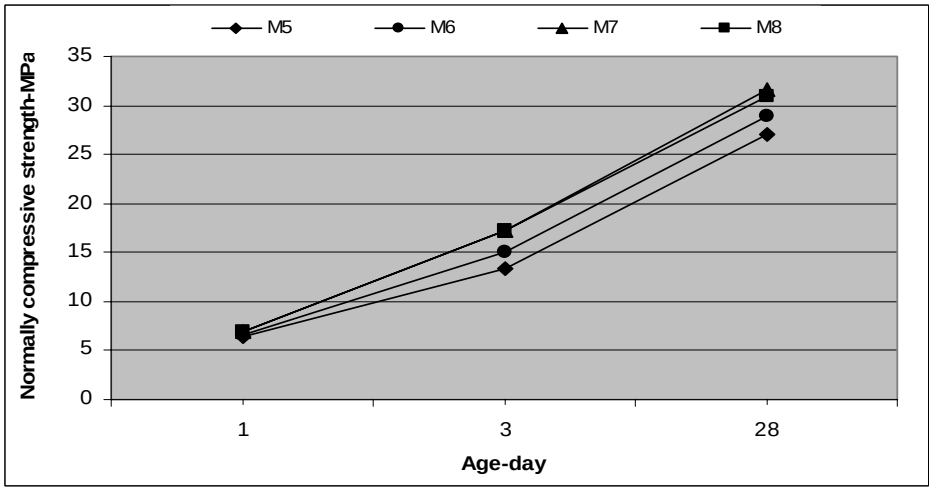

Fig.8 Normally compressive strength for crushed gravel mixes at different SPR dosages

MIXED CONVECTIVE AND RADIATIVE HEAT TRANSFER IN A HORIZONTAL CONCENTRIC AND ECCENTRIC CYLINDRICAL ANNULI

Ass. Prof. Manal Hadi Al-Hafidh
Mech. Engr. Dept.
College of Engineering
University of Baghdad

Lina S. Safwat
Mechanical Engineer
Ishtar_l21@yahoo.com

ABSTRACT

A numerical investigation has been performed to study the effect of eccentricity on unsteady state, laminar aiding mixed convection in a horizontal concentric and eccentric cylindrical annulus. The outer cylinder was kept at a constant temperature while the inner cylinder was heated with constant heat flux. The study involved numerical solution of transient momentum (Navier-Stokes) and energy equation using finite difference method (FDM), where the body fitted coordinate system (BFC) was used to generate the grid mesh for computational plane. The governing equations were transformed to the vorticity-stream function formula as for momentum equations and to the temperature and stream function for energy equation.

A computer program (Fortran 90) was built to calculate the bulk Nusselt number (Nu_b) after reaching steady state condition for fluid Prandtl number fixed at 0.7 (air) with radius ratio ($\bar{R}$=2.6), Rayleigh number (Ra=200), Reynolds number (Re=50) for both concentric and eccentric cylindrical annulus with different eccentricity ratios (ε=0, 0.25, 0.50, 0.75) and angular positions (φ_o=0°, 45°, 90°, 135°, 180°).

The results show a reasonable representation to the relation between Nusselt number and (ε, φ_o). Generally, $\boldsymbol{Nu_b}$ decreased with the increase in (ε and φ_o). Also, results show that the best thermal performance for the inner cylinder was at the angular position (φ_o=0°) for eccentricity ratio (ε=0.25), while the maximum reduction in the rate of heat transfer for the inner cylinder was at the angular position (φ_o=180°) for eccentricity ratio (ε=0.75).

Comparison of the result with the previous work shows a good agreement.

الخلاصة

تم إجراء بحث عددي لدراسة تأثير اللامركزية لجريان مختلط مساعد غير مستقر يقع بين اسطوانتين أفقيتين متحدة وغير متحدة المركز، تم حفظ الاسطوانة الخارجية بدرجة حرارة ثابتة بينما سخنت الاسطوانة الداخلية بفيض حراري ثابت . بينت الدراسة النظرية حل عددي لمعادلات الزخم والطاقة لمسألة البحـث باسـتخدام طريقة الفروقات المحددة وتم استخدام نظام الإحداثيات المطابقة للجسم (BFC) في توليد شـبكة العقـد بعـد تحويل هذه المعادلات إلى صيغة دالة الانسياب-الدوامية .

تم بناء برنامج (فورتران 90) لحساب رقم نسلت (Nu) بعد الوصول إلى حالة الاستقرار لقيمة رقم برانتل ثابتة 0.7 (هواء) ولنسبة نصف قطر ($\bar{R}$=2.6) ولخواص جريان ممثلة برقم رينولد (Re=50) ورقم رالـي (Ra=200) لحالتي الاسطوانتين المتحدة وغير متحدة المركز لنسب لامركزية (ε=0, 0.25, 0.50, 0.75) ولموقع زاوي للاسطوانة الداخلية ضمن التجويف (φ_o= 0°, 45°, 90°, 135°, 180°)

أعطت النتائج تمثيلاً معقولا لمعدل رقم نسلت بواسطة رسم مخططات تمثل تأثيركل من (φ_o, ε) على قيمة *Nu* . وبصورة عامة وجد إن رقم نسلت يقل مع زيادة (φ_o , ε). وبينت النتائج أيضا ان أفضل أداء حراري للاسطوانة الداخلية كان في الموقع الزاوي (φ_o=0°) ولنسبة لامركزية (ε=0.25) بينما كان أعظم انخفـاض في معدل انتقال الحرارة للاسطوانة الداخلية في الموقع الزاوي (φ_o=180°) ولنسبة لامركزية (ε=0.75). تم إجراء مقارنة مع البحوث السابقة وكانت جيدة.

KEY WORDS: Flow and Heat Transfer, Laminar, Mixed Convection, Concentric and Eccentric, Horizontal Annulus.

INTRODUCTION:

The process of heating and cooling of the flowing fluids inside channels was considered as one of the important subjects in heat transfer problems. Many researchers studied the heat transfer and fluid flow through the channels with different cross section areas to attain the best performance of the heat exchanger.

Mixed convection heat transfer in horizontal ducts of concentric and eccentric cylindrical annular form has received increased attention due to the interesting feature of specific heat transfer phenomenon and fundamental importance in practical applications.

An experimental and theoretical study has been conducted by [**Akeel Al−Sudani, 2005**] on mixed convection heat transfer of the flow through an inclined concentric annulus with uniformly heated inner cylinder and adiabatic outer cylinder with both fixed and rotating inner cylinder, little researches dealt with mixed convection in an eccentric annulus. [**William, 1963**], presented a solution for the temperature distribution in a fluid flowing in an eccentric annulus formed with circular cylinders under the assumption of slug flow. [**Shu and Wu, 2001**], presented an efficient numerical approach of using domain-free discretization method to solve partial differential equations on a doubly connected domain concentric and eccentric annulus. The consideration in the present study is given to laminar unsteady state mixed convection with radiation in concentric and eccentric horizontal annuls with the outer cylinder maintained isothermal while the inner cylinder was subjected to a uniform constant heat flux. **Fig. (1)** shows the annulus geometry and coordinate system of the problem under consideration

Important applications for mixed convection in an annulus may be summarized as follows: Double pipe heat exchangers, heating processes in nuclear reactors, the cooling of electrical equipments, the design of certain types of solar energy collectors and heating of process fluids [**Yasin et.al 2006**].

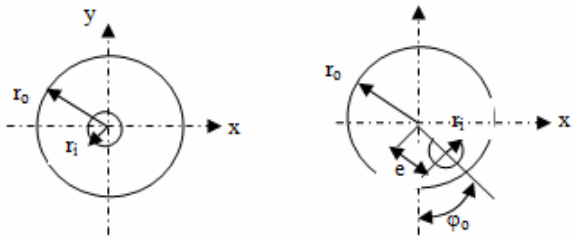

Figure (1) Schematic of the Present Study

GOVERNING EQUATIONS:

Unsteady steady state, quasi three-dimensional, incompressible, fully developed laminar aiding air flow was investigated.

Accordingly the governing, continuity, momentum and energy conservation equations were as follows:-

Continuity equation:

$$\frac{\partial u}{\partial x}+\frac{\partial v}{\partial y}=0 \qquad (1)$$

Momentum Equations:

$$\frac{\partial u}{\partial t}+u\frac{\partial u}{\partial x}+v\frac{\partial u}{\partial y}=-\frac{1}{\rho}\frac{dp}{dx}+\nu\left[\frac{\partial^2 u}{\partial x^2}+\frac{\partial^2 u}{\partial y^2}\right] \qquad (2)$$

$$\frac{\partial v}{\partial t}+u\frac{\partial v}{\partial x}+v\frac{\partial v}{\partial y}=-\frac{1}{\rho}\frac{dp}{dy}+\nu\left[\frac{\partial^2 v}{\partial x^2}+\frac{\partial^2 v}{\partial y^2}\right]+g\beta(T-T_w) \qquad (3)$$

$$\frac{\partial w}{\partial t}+u\frac{\partial w}{\partial x}+v\frac{\partial w}{\partial y}=-\frac{1}{\rho}\frac{dp}{dz}+\nu\left[\frac{\partial^2 w}{\partial x^2}+\frac{\partial^2 w}{\partial y^2}\right] \qquad (4)$$

Energy Equation:

$$\frac{\partial T}{\partial t}+u\frac{\partial T}{\partial x}+v\frac{\partial T}{\partial y}+w\frac{\partial T}{\partial z}=\alpha\left[\frac{\partial^2 T}{\partial x^2}+\frac{\partial^2 T}{\partial y^2}\right]+\frac{4\sigma k_r e T_w^4}{\rho c_p}(T_w-T) \quad (5)$$

The dimensionless parameters:

$\tau=\frac{\nu t}{De^2}$, $De = 2(r_o - r_i)$,

$X=\frac{x}{De}$, $Y=\frac{y}{De}$,

$Z=\frac{z}{De}$, $\varepsilon=\frac{e}{De}$, $U=\frac{uDe}{\nu}$,

$V=\frac{vDe}{\nu}$,

$W=\frac{wDe}{\nu}$, $\theta=\frac{(T_w-T)}{PrCDe}$,

$P=\frac{PDe^2}{\rho\nu^2}$, $Pr=\frac{\nu}{\alpha}$, $Ra=\frac{g\beta CDe^4}{\nu\alpha}$,

$C=\frac{\partial T}{\partial z}$, $A=-\frac{4\rho\nu^2\hat{R}e}{De^3}$,

$\hat{R}=\frac{r_o}{r_i}$, $N=\frac{4\sigma e T_w^3}{k k_r}$, $\hat{t}=k_r De$

By using these dimensionless forms, the above equations can be written as follows.

$$\frac{\partial U}{\partial X}+\frac{\partial V}{\partial Y}=0 \quad (6)$$

$$\frac{\partial U}{\partial \tau}+U\frac{\partial U}{\partial X}+V\frac{\partial U}{\partial Y}=-\frac{dP}{dX}+\left[\frac{\partial^2 U}{\partial X^2}+\frac{\partial^2 U}{\partial Y^2}\right] \quad (7)$$

$$\frac{\partial V}{\partial \tau}+U\frac{\partial V}{\partial X}+V\frac{\partial V}{\partial Y}=-\frac{dP}{dY}+\left[\frac{\partial^2 V}{\partial X^2}+\frac{\partial^2 V}{\partial Y^2}\right]-Ra\,\theta \quad (8)$$

$$\frac{\partial W}{\partial \tau}+U\frac{\partial W}{\partial X}+V\frac{\partial W}{\partial Y}=\left[\frac{\partial^2 W}{\partial X^2}+\frac{\partial^2 W}{\partial Y^2}\right]+4Re \quad (9)$$

$$\frac{\partial \theta}{\partial \tau}+U\frac{\partial \theta}{\partial X}+V\frac{\partial \theta}{\partial Y}=\frac{1}{Pr}\left[\frac{\partial^2 \theta}{\partial X^2}+\frac{\partial^2 \theta}{\partial Y^2}\right]+\frac{W}{Pr}+\frac{N\hat{t}^2\theta}{Pr} \quad (10)$$

The governing equations in dimensionless form above were written in terms of dependant variables (U, V, W, P, θ). The pressure term in the momentum equations will be eliminated in the resulting vorticity equation as can be shown below:

$$\frac{\partial \Omega}{\partial \tau}+U\frac{\partial \Omega}{\partial X}+V\frac{\partial \Omega}{\partial Y}=\left[\frac{\partial^2 \Omega}{\partial X^2}+\frac{\partial^2 \Omega}{\partial Y^2}\right]-Ra\frac{\partial \theta}{\partial X} \quad (11)$$

For this flow field, the only non-zero component of the vorticity is:

$$\Omega=\frac{\partial V}{\partial X}-\frac{\partial U}{\partial Y} \quad (12)$$

Also by making use of the vorticity definition of equation (12) and the definition of stream function (Ψ), which satisfy continuity equation, the horizontal and vertical velocities can be written as follows respectively:-

$$U=\frac{\partial \Psi}{\partial Y} \quad (13)$$

$$V=-\frac{\partial \Psi}{\partial X} \quad (14)$$

By substituting the velocity components of equations (13) and (14) in the vorticity definition equation (12) , stream function equation resulted as :-

$$-\Omega=\left[\frac{\partial^2 \Psi}{\partial X^2}+\frac{\partial^2 \Psi}{\partial Y^2}\right] \quad (15)$$

Boundary Nodes:

The positions of the inner and outer cylinders can be represented by the eccentricity (ε) and the angular position (φ_o), where ($0^o \le \varphi_o \le 360°$).

For an eccentric annulus, the origin was put at the center of the inner cylinder. So, $r_i(\varphi)$ was a constant, but $r_o(\varphi)$ was a function of **φ.** If the radius ratio is defined as $\tilde{R} = \frac{r_o}{r_i}$, then the non-dimensional radii of the inner and outer cylinders are $R_i=1/(\tilde{R}-1)$ and $R_o=\tilde{R}/(\tilde{R}-1)$. Therefore, $r_i(\varphi)$ and $r_o(\varphi)$ are given by [**Shu and Wu 2001**] :-

$$r_i(\varphi) = R_i = \frac{1}{(\tilde{R}-1)} \tag{16}$$

$$r_o(\varphi) = -\varepsilon\cos(\varphi-\varphi_o) + [R_o^2 - \varepsilon^2\sin^2(\varphi-\varphi_o)]^{1/2} \tag{17}$$

Initial Conditions:

Initial conditions may be chosen as zero:

At $\tau = 0$,

U = V = W = Ω = Ψ = 0 [No slip condition]

The boundary conditions which defined by [**Kotake and Hattori 1985**] and [**Kaviany 1986**], making use that the boundary conditions for a motionless rigid surface which required that both horizontal and vertical velocities components (U and V) to be vanished at surface.

This expressed in terms of stream function as follows:-

- Inner cylinder surface :

$$U = V = W = \Psi = 0 \quad , \quad \Omega = -\left.\frac{\partial^2\Psi}{\partial r^2}\right|_w \quad , \quad \theta_i = 0 \tag{18}$$

- Outer cylinder surface :

$$U = V = W = \Psi = 0 \quad , \quad \Omega = -\left.\frac{\partial^2\Psi}{\partial r^2}\right|_w \quad , \quad \frac{\partial\theta_o}{\partial n} = 0 \tag{19}$$

TRANSFORMATION OF GOVERNING EQUATIONS:-

Governing equations can be transformed from the Cartesian coordinates (X,Y) to generalized coordinates (ζ, η) as shown below:

1- Vorticity-Transport Equation:-

$$\frac{\partial\Omega}{\partial\tau} + \frac{(\Psi_\eta\Omega_\zeta - \Psi_\zeta\Omega_\eta)}{J} = \frac{(\varrho\Omega_\zeta + \varpi\Omega_\eta + \alpha\Omega_{\zeta\zeta} - 2\beta\Omega_{\zeta\eta} + \gamma\Omega_{\eta\eta})}{J^2} - Ra\frac{(\theta_\zeta Y_\eta - \theta_\eta Y_\zeta)}{J} \tag{20}$$

2- Axial Momentum Equation:-

$$\frac{\partial W}{\partial\tau} + \frac{(\Psi_\eta W_\zeta - \Psi_\zeta W_\eta)}{J} = \frac{(\varrho W_\zeta + \varpi W_\eta + \alpha W_{\zeta\zeta} - 2\beta W_{\zeta\eta} + \gamma W_{\eta\eta})}{J^2} + 4Re \tag{21}$$

3- Energy equation :-

$$\frac{\partial\theta}{\partial\tau} + \frac{(\Psi_\eta\theta_\zeta - \Psi_\zeta\theta_\eta)}{J} = \frac{1}{Pr}\left[\frac{(\varrho\theta_\zeta + \varpi\theta_\eta + \alpha\theta_{\zeta\zeta} - 2\beta\theta_{\zeta\eta} + \gamma\theta_{\eta\eta})}{J^2} + W + Nt^2\theta\right] \tag{22}$$

4- Stream Function Equation:-

$$-\Omega = \frac{(\varrho\Psi_\zeta + \varpi\Psi_\eta + \alpha\Psi_{\zeta\zeta} - 2\beta\Psi_{\zeta\eta} + \gamma\Psi_{\eta\eta})}{J^2} \tag{23}$$

5- Vertical Velocity:-

$$V = \frac{(\Psi_\eta Y_\zeta - \Psi_\zeta Y_\eta)}{J} \tag{24}$$

6- Horizontal Velocity:-

$$U = \frac{(\Psi_\eta X_\zeta - \Psi_\zeta X_\eta)}{J} \tag{25}$$

NUMERICAL SOLUTION:

Explicit finite difference technique was the numerical method used for solving the transient behavior of the fluid flow and heat transfer until the steady state was reached by marching out in time steps ($\Delta\tau$).

1- Discretization of Vorticity Equation:-

$$\Omega^{n+1}_{(i,j)} = A_1\Omega^n_{(i+1,j)} + A_2\Omega^n_{(i-1,j)} + A_3\Omega^n_{(i,j)} + A_4\Omega^n_{(i,j+1)} + A_5\Omega^n_{(i,j-1)} - A_6\left(\Omega^n_{(i+1,j+1)} - \Omega^n_{(i+1,j-1)} - \Omega^n_{(i-1,j+1)} + \Omega^n_{(i-1,j-1)}\right) - A_7 \quad (26)$$

Where:-

$$A_1 = \frac{\varphi_{(i,j)}\Delta\tau}{2J^2_{(i,j)}\Delta\zeta} + \frac{\alpha_{(i,j)}\Delta\tau}{J^2_{(i,j)}\Delta\zeta^2} - \frac{E\Delta\tau}{4\Delta\zeta\Delta\eta J_{(i,j)}} \quad (27\text{-a})$$

$$A_2 = -\frac{\varphi_{(i,j)}\Delta\tau}{2J^2_{(i,j)}\Delta\zeta} + \frac{\alpha_{(i,j)}\Delta\tau}{J^2_{(i,j)}\Delta\zeta^2} + \frac{E\Delta\tau}{4\Delta\zeta\Delta\eta J_{(i,j)}} \quad (27\text{-b})$$

$$A_3 = 1 - \frac{2\alpha_{(i,j)}\Delta\tau}{J^2_{(i,j)}\Delta\zeta^2} - \frac{2\gamma_{(i,j)}\Delta\tau}{J^2_{(i,j)}\Delta\eta^2} \quad (27\text{-c})$$

$$A_4 = \frac{\varpi_{(i,j)}\Delta\tau}{2J^2_{(i,j)}\Delta\eta} + \frac{\gamma_{(i,j)}\Delta\tau}{J^2_{(i,j)}\Delta\eta^2} + \frac{F\Delta\tau}{4\Delta\zeta\Delta\eta J_{(i,j)}} \quad (27\text{-d})$$

$$A_5 = -\frac{\varpi_{(i,j)}\Delta\tau}{2J^2_{(i,j)}\Delta\eta} + \frac{\gamma_{(i,j)}\Delta\tau}{J^2_{(i,j)}\Delta\eta^2} - \frac{F\Delta\tau}{4\Delta\zeta\Delta\eta J_{(i,j)}} \quad (27\text{-e})$$

$$A_6 = \frac{\beta_{(i,j)}\Delta\tau}{2J^2_{(i,j)}\Delta\zeta\Delta\eta} \quad (27\text{-f})$$

$$A_7 = \frac{Ra\Delta\tau}{J_{(i,j)}}\left[\left(\frac{\theta_{(i+1,j)}-\theta_{(i-1,j)}}{2\Delta\zeta} * \frac{Y_{(i,j+1)}-Y_{(i,j-1)}}{2\Delta\eta}\right) - \left(\frac{\theta_{(i,j+1)}-\theta_{(i,j-1)}}{2\Delta\eta} * \frac{Y_{(i+1,j)}-Y_{(i-1,j)}}{2\Delta\zeta}\right)\right] \quad (27\text{-g})$$

2- Discretization of Axial Momentum Equation :-

$$W^{n+1}_{(i,j)} = B_1W^n_{(i+1,j)} + B_2W^n_{(i-1,j)} + B_3W^n_{(i,j)} + B_4W^n_{(i,j+1)} + B_5W^n_{(i,j-1)} - B_6\left(W^n_{(i+1,j+1)} - W^n_{(i+1,j-1)} - W^n_{(i-1,j+1)} + W^n_{(i-1,j-1)}\right) + B_7 \quad (28)$$

Where:-

$$B_1 = \frac{\varphi_{(i,j)}\Delta\tau}{2J^2_{(i,j)}\Delta\zeta} + \frac{\alpha_{(i,j)}\Delta\tau}{J^2_{(i,j)}\Delta\zeta^2} - \frac{E\Delta\tau}{4\Delta\zeta\Delta\eta J_{(i,j)}} \quad (29\text{-a})$$

$$B_2 = -\frac{\varphi_{(i,j)}\Delta\tau}{2J^2_{(i,j)}\Delta\zeta} + \frac{\alpha_{(i,j)}\Delta\tau}{J^2_{(i,j)}\Delta\zeta^2} + \frac{E\Delta\tau}{4\Delta\zeta\Delta\eta J_{(i,j)}} \quad (29\text{-b})$$

$$B_3 = 1 - \frac{2\alpha_{(i,j)}\Delta\tau}{J^2_{(i,j)}\Delta\zeta^2} - \frac{2\gamma_{(i,j)}\Delta\tau}{J^2_{(i,j)}\Delta\eta^2} \quad (29\text{-c})$$

$$B_4 = \frac{\varpi_{(i,j)}\Delta\tau}{2J^2_{(i,j)}\Delta\eta} + \frac{\gamma_{(i,j)}\Delta\tau}{J^2_{(i,j)}\Delta\eta^2} + \frac{F\Delta\tau}{4\Delta\zeta\Delta\eta J_{(i,j)}} \quad (29\text{-d})$$

$$B_5 = -\frac{\varpi_{(i,j)}\Delta\tau}{2J^2_{(i,j)}\Delta\eta} + \frac{\gamma_{(i,j)}\Delta\tau}{J^2_{(i,j)}\Delta\eta^2} - \frac{F\Delta\tau}{4\Delta\zeta\Delta\eta J_{(i,j)}} \quad (29\text{-e})$$

$$B_6 = \frac{\beta_{(i,j)}\Delta\tau}{2J^2_{(i,j)}\Delta\zeta\Delta\eta} \quad (29\text{-f})$$

$$B_7 = \Delta\tau\left(4Re - Ra\theta_{(i,j)}\sin\delta\right) \quad (29\text{-g})$$

3- Discretization of Energy Equation :-

$$\theta^{n+1}_{(i,j)} = C_1\theta^n_{(i+1,j)} + C_2\theta^n_{(i-1,j)} + C_3\theta^n_{(i,j)} + C_4\theta^n_{(i,j+1)} + C_5\theta^n_{(i,j-1)} - C_6\left(\theta^n_{(i+1,j+1)} - \theta^n_{(i+1,j-1)} - \theta^n_{(i-1,j+1)} + \theta^n_{(i-1,j-1)}\right) + C_7 \quad (30)$$

Where:-

$$C_1 = \frac{\varrho_{(i,j)}\Delta\tau}{2Pr J^2_{(i,j)}\Delta\zeta} + \frac{\alpha_{(i,j)}\Delta\tau}{Pr J^2_{(i,j)}\Delta\zeta^2} - \frac{E\Delta\tau}{4\Delta\zeta\Delta\eta J_{(i,j)}} \quad (31\text{-a})$$

$$C_2 = -\frac{\varrho_{(i,j)}\Delta\tau}{2Pr J^2_{(i,j)}\Delta\zeta} + \frac{\alpha_{(i,j)}\Delta\tau}{Pr J^2_{(i,j)}\Delta\zeta^2} + \frac{E\Delta\tau}{4\Delta\zeta\Delta\eta J_{(i,j)}} \quad (31\text{-b})$$

$$C_3 = 1 - \frac{2\alpha_{(i,j)}\Delta\tau}{Pr J^2_{(i,j)}\Delta\zeta^2} - \frac{2\gamma_{(i,j)}\Delta\tau}{Pr J^2_{(i,j)}\Delta\eta^2} \quad (31\text{-c})$$

$$C_4 = \frac{\varpi_{(i,j)}\Delta\tau}{2Pr J^2_{(i,j)}\Delta\eta} + \frac{\gamma_{(i,j)}\Delta\tau}{Pr J^2_{(i,j)}\Delta\eta^2} + \frac{F\Delta\tau}{4\Delta\zeta\Delta\eta J_{(i,j)}} \quad (31\text{-d})$$

$$C_5 = -\frac{\varpi_{(i,j)}\Delta\tau}{2Pr J^2_{(i,j)}\Delta\eta} + \frac{\gamma_{(i,j)}\Delta\tau}{Pr J^2_{(i,j)}\Delta\eta^2} - \frac{F\Delta\tau}{4\Delta\zeta\Delta\eta J_{(i,j)}} \quad (31\text{-e})$$

$$C_6 = \frac{\beta_{(i,j)}\Delta\tau}{2Pr J^2_{(i,j)}\Delta\zeta\Delta\eta} \quad (31\text{-f})$$

$$C_7 = \left[\frac{\left(W_{(i,j)} + Q_{(i,j)} + N\hat{R}^2\theta_{(i,j)}\right)}{Pr}\right]\Delta\tau \quad (31\text{-g})$$

$$E = \Psi_{(i,j+1)} - \Psi_{(i,j-1)} \quad (31\text{-h})$$

$$F = \Psi_{(i+1,j)} - \Psi_{(i-1,j)} \quad (31\text{-i})$$

4- Stream Function Solving Method :-

$$\Psi^{n+1}_{(i,j)} = \Psi^n_{(i,j)} + \sigma\left(\Psi^{n+1}_{(i,j)} - \Psi^n_{(i,j)}\right) \quad (32)$$

5- Calculation of Average Axial Velocity :-

$$\overline{W} = \left(\sum_{i,j}^{Ni,Nj} W_{(i,j)}J_{(i,j)}\right)/J \quad (33)$$

6- Calculation of Bulk Temperature :-

$$\theta_b = \left(\sum_{i,j}^{Ni,Nj} \theta_{(i,j)}W_{(i,j)}J_{(i,j)}\right)/\overline{W}J \quad (34)$$

7- Calculation of Nusselt Number :-

$$Nu_b = \frac{\overline{W}_{(i,j)}(\hat{R}+1)}{4\theta_{b(i,j)}} \quad (35)$$

RESULTS AND DISCUSION:

Numerical investigations was conducted for different eccentricity ratios **ε** in different angular positions **φ₀** of the inner cylinder within the physical domain. The isotherms and streamlines for different **ε** and **φ₀** and the results for variation of eccentricity with Nusselt number were shown in figures [(2) to (8)], in which five angular positions of (φ_o=0°, 45°, 90°, 135°, 180°) and four eccentricities of (ε = 0, 0.25, 0.50, 0.75) where considered .

Isotherms & Streamlines:-

Figs. [(2) to (7)] illustrate the isotherms and streamlines for *Ra=200*, *Re=50*, *Pr=0.7*and $\hat{R}$*=2.6* with different values of **ε** and **φ₀**.

Pure conduction heat transfer is increased with eccentricity, which is revealed by the increasing in specific conductivity K_ε as a function of **ε**. Interpretation is as follows: because of

the narrowed gap in the large eccentricity annulus thermal convection by large recirculating vorticities become more and more difficult in contrast to the growing influence of the thermal conduction.

Fig. (2) shows the isotherms and streamlines for concentric annulus. The streamlines are symmetric with respect to the vertical line, there will be a stagnant region in the lower part of the gap, in this region the natural convection effect will be low and it is identical to the case of thermally steady state fluid flow between two horizontal plates, when the upper plate is much higher than the lower one.

Detailed isotherms and streamlines for eccentric annulus are presented in **Figs.[(2) to (7)]** respectively, the vortex strength current was un symmetric and the vortex strength will be increased in the wider part of the gap. Buoyancy plume will be deviated to the narrowed part of the gap and this deviation will be increased as ε increased due to the limitation in the fluid motion in the narrowed part and the buoyancy force will be unequal on each sides of the gap. As ε increased the buoyancy plume will be separated in the largest part of the gap due to the viscosity force.

In the narrowest part of the gap, the conduction dominancy is readily recognizable from the isotherm plots. Also, as seen from the streamline contours, more and more fluid is mobilized in the convection currents with decreasing φ_o to deliver thermal energy from the inner heated cylinder to the outer cold cylinder. It is noted that the positioned influence on the heat transfer is felt more strongly from the isotherm plots than from the streamlines, since the temperature inversion phenomenon becomes very distinguished as φ_o is decreased from (180° to 0°), this clearly indicates that the role of convection increases with lower φ_o. For high eccentricity the conduction dominating flow region at the narrowest gap of the annuli becomes locally stagnant which results in splitting of the core of the vortex in the constricted region into two sub vortices rotating in the same direction.

At first, the vortex core only is halvened, but as the gap is further narrowed local stagnant region grows large enough to bisect the whole vortex even much before the two cylinders come into contact. In the wider part of the eccentric annulus the vortex current is slowed down and location of its core is lowered as eccentricity increased. This clearly indicates that the relative role of convection is steadily decreased with higher eccentricity, whereas the overall heat transfer is changed to increasing pattern after a slight decrease near $\varepsilon=0.50$. This is again surely due to the contribution of conduction for increased eccentricities. It is noted that the decreased degree of plume development and temperature inversion with higher eccentricities and the slowed –down stream speed together with the vortex halvening and all consistently related with the magical interaction between the conduction and the convection discussed so far.

Also, the radiation effect plays a significant role with the position of the inner cylinder. Once the medium participates in the absorption and emission of radiation, the medium temperature tends to move uniform. Further more, as the participating medium alternates the radiation more, a direct interaction of the inner hotter cylinder with the cold outer cylinder, i.e., surface radiation, is decreased.

This is clearly evidenced by observing a downward shift of the isotherm closer to the outer cold cylinder for both cases of concentric and eccentric annulus as ***N*** increased. When the inner cylinder is displaced downward as shown in **Fig. (3)**, the location of the convective cell center barely changes. Moreover compared to the pervious case, ***N*** has an insignificant effect in the medium temperature variation; this is derived from the fact that the thermo-fluid dynamics characteristics become buoyancy dominant. In other wards, when the inner cylinder is located at the downward positions the internal buoyancy-induced flow becomes stronger, which in turn results in higher heat transfer rate.

The angular positions of $\varphi_o=0^o$ and $\varphi_o=180^o$ are two special cases in the eccentric annulus, for these two special cases, there is no global circulation. As a consequence, the flow and thermal fields are symmetric with respect to the vertical line connecting the centers of two cylinders. This can be clearly shown if **Figs.[(3) and (7)].** When the inner cylinder is moved near the bottom, the outer cylinder has a boundary layer every where, when the inner cylinder is moved near the top, there is no boundary layer on the bottom portion of the outer cylinder.

For $\varphi_o=0^o$ it is evident that the convective flows are both larger and stronger than the concentric annulus for low eccentricity ratio (ε=0.25, ε=0.5) but for large eccentricity for example (ε=0.75), the only effect which can be recognized is that the reduction in the rate of heat transfer and this is again due to the stagnant region in the narrowest gap.

Also, $\varphi_o=180^o$ provides least favored circumstance for the development of the heat transfer, both the size and strength of the fluid flow are markedly reduced.

On the other hand, it was found that the global circulation of the flow does exist around the hot inner cylinder for eccentricity cases of ($\varphi_o=45^o$, 90° and $\varphi_o=135^o$) as shown in **Figs. [(4), (5) and (6)]** . For these cases, the computed Ψ_{max} has a relatively large value. The magnitude of the circulation varies form zero for a concentric annulus to a maximum value for an intermediate eccentricity and back to zero for $\varepsilon\approx 1$. This is because for $\varepsilon = 0$ the flow field is symmetric, and no global circulation exists. When ε tends toward **1**, the two cylinder surfaces are very close at some point so that there is no sufficient space for fluid flow. Therefore, the global circulation for this case is very weak.

As can be shown from **Fig. (6)** that for $\varphi_o=135^o$ and ε = 0.50 and ε = 0.75, there will be a small vortex in the upper part of the gap. This small vortex will cause a deviation to the buoyancy plume to the largest part of the gap.

Effect of Eccentricity on Nu:

Fig.(8) illustrates the variation of ***Nu*** with angular location φ_o for different ε. For fixed eccentricity ε for example (ε=0.25), and the inner cylinder is moved circumferentially, by increasing φ_o , ***Nu*** will be decreased. This clearly indicates that the role of convection increases with lower φ_o .

For fixed angular position for example ($\varphi_o=90^o$) and different eccentricity, ***Nu*** will be decreased as ε increased from (0.25 to 0.75). That the relative role of convection is steadily decreased with higher eccentricity, this is again surely due to the contribution of conduction for increased eccentricity.

A correlation equation for the plotted curve of Nu for any eccentricity ratio and angular position had been written to show the eccentricity effect on the rate of heat transfer. Curve fitting method (Least square method) with two programs (Statistica and DGA) which were used to form this equation.

$$Nu = a_1 + b_1 . \varepsilon^{c_1} . \cos\varphi_o \qquad (36)$$

The above equation is valid for Re=50, Pr=0.7, Ra=200, $\hat{R}$=2.6 and $\varphi_o = 0°, 45°, 90°, 135°, 180°$. Where, a_1, b_1 and c_1 are constants and there values are as follows:-

Parameter	Estimate
a_1	6.80 for $\varepsilon = 0.25$
	6.03 for $\varepsilon = 0.50$
	5.94 for $\varepsilon = 0.75$
b_1	0.5
c_1	-0.64

Comparison of Results:

A comparison was made with the isotherms and streamlines resulted from the work of [**Ho, Lin and Chen 1989**] for natural convection heat transfer in an eccentric horizontal annulus with ($Ra=10^6$, ε=0.625 and $\varphi_o=180^o$) as shown in **Fig.(9),** the results show a good agreement .

CONCLUSIONS:

For fixed eccentricity ratio and radius ratio, the overall heat transfer increased due to the expanded convection as the angular position φ_o of the inner cylinder decreased. And for a fixed angular position, when the inner cylinder was moved outward from the concentric position along a horizontal line, convection heat transfer decreases contrary to the conduction heat transfer which grows with a faster rate. It was found that at ε=0.25 and $\varphi_o=0^o$, maximum heat transfer will be recognized.

REFERENCES:

Akeel A. M. Al−Sudani, 2005, "An Investigation Into Laminar Combined Convection Heat Transfer Through Concentric Annuli"، PhD. Thesis, University of Technology, Mechanical Engineering Department .

Ho C. J., Lin Y. H. and Chen T. C., 1989, "A Numerical Study of Natural Convection in Concentric and Eccentric Horizontal Cylindrical Annuli with Mixed Boundary Conditions", Int. J. Heat and Fluid Flow, Vol. 10, No. 1, PP. 40-47.

Kaviany M., 1986, " Laminar Combined Convection in a Horizontal Annulus Subjected to Constant Heat Flux Inner Wall and Adiabatic Outer Wall", J. Heat Transfer, ASME, Vol.108, PP.392-397.

Kotake S. and Hattori N., 1985, "Combined Forced and Free Convection Heat Transfer for Fully – Developed Laminar Flow in Horizontal Annuli", J. Heat and Mass Transfer, Vol.28, No.11, PP.2113-2120.

Shu C. and Wu Y. L., 2001, "Domain Free Discretization Method for Doubly Connected Domain and Its Applications to Simulate Natural Convection in Eccentric Annuli", Internet, Science Direct, Vol. 191, Issues 17-18, PP. 1827-1841 .

William T. Snyddi, 1963, "An Analysis of Slug Flow Heat Transfer in an Eccentric Annulus", A.I.Ch.E. Journal, Vol. 9, No. 4, PP. 503-506 .

Yasin K. Salman, Jalal M. Jalil and Ahmed F. Khudheyer, 2006, "Experimental Study of Mixed Convection Heat Transfer to Thermally Developing Air Flow in a Horizontal Rectangular Duct", convection heat transfer through concentric annuli"، University of Baghdad .

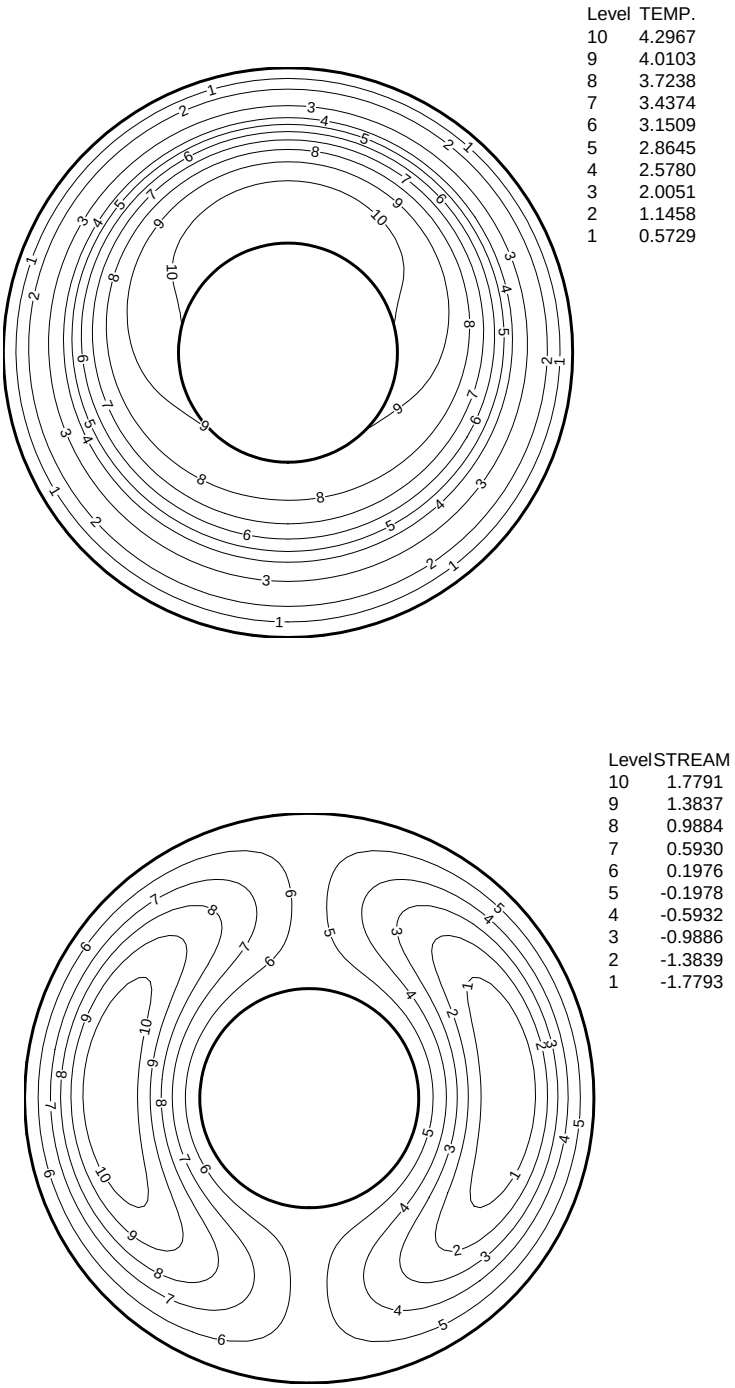

Figure (2)
Isotherms & Streamlines for Concentric Annulus ($\varphi_o=0^o,\varepsilon=0.0$)
Ra=200, Re=50, Pr=0.7, $\hat{R}$=2.6, N=3, $\hat{t}$=1

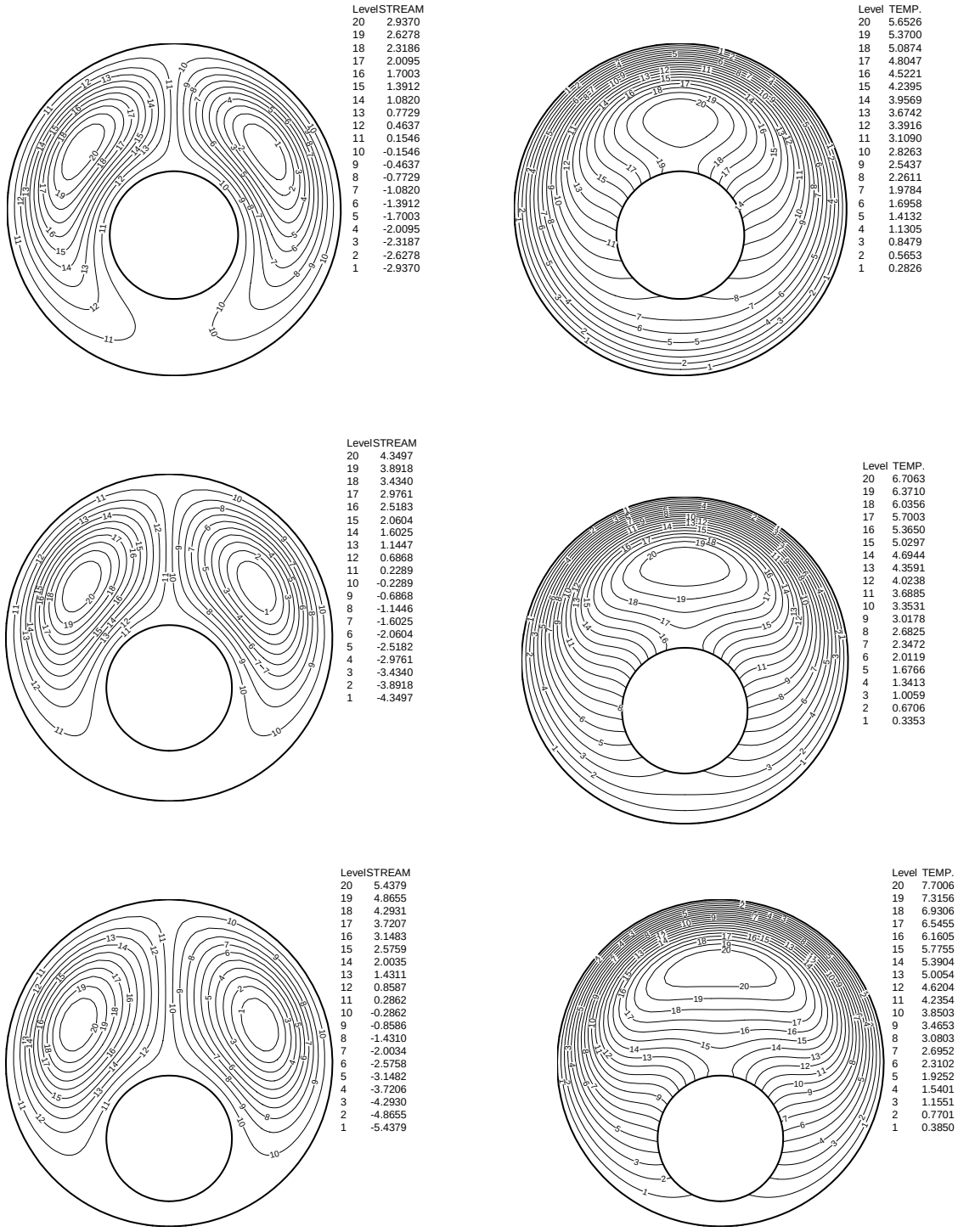

Figure (3)
Isotherms & Streamlines for Eccentric Annulus ($\varphi_o=0^o$)
Ra=200, Re=50, Pr=0.7, $\hat{R}$=2.6, N=3, $\hat{t}$=1

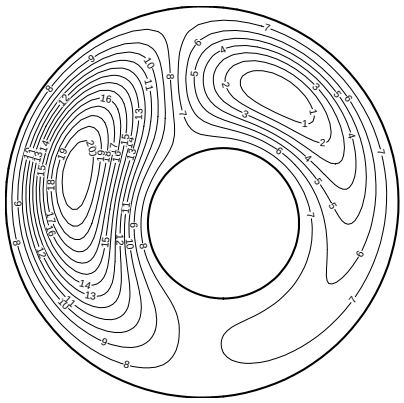

Level	STREAM
20	3.7173
19	3.4189
18	3.1206
17	2.8222
16	2.5239
15	2.2255
14	1.9271
13	1.6288
12	1.3304
11	1.0320
10	0.7337
9	0.4353
8	0.1370
7	-0.1614
6	-0.4598
5	-0.7581
4	-1.0565
3	-1.3549
2	-1.6532
1	-1.9516

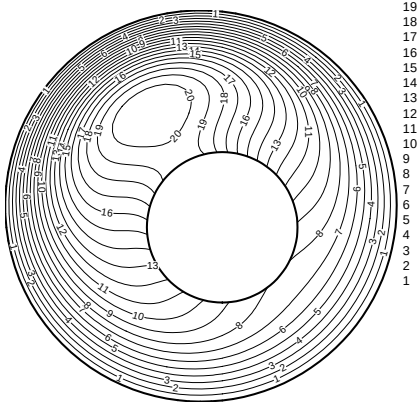

Level	TEMP.
20	5.7227
19	5.4365
18	5.1504
17	4.8643
16	4.5781
15	4.2920
14	4.0059
13	3.7197
12	3.4336
11	3.1475
10	2.8613
9	2.5752
8	2.2891
7	2.0029
6	1.7168
5	1.4307
4	1.1445
3	0.8584
2	0.5723
1	0.2861

Level	STREAM
20	4.8169
19	4.3771
18	3.9373
17	3.4975
16	3.0578
15	2.6180
14	2.1782
13	1.7385
12	1.2987
11	0.8589
10	0.4191
9	-0.0206
8	-0.4604
7	-0.9002
6	-1.3400
5	-1.7797
4	-2.2195
3	-2.6593
2	-3.0990
1	-3.5388

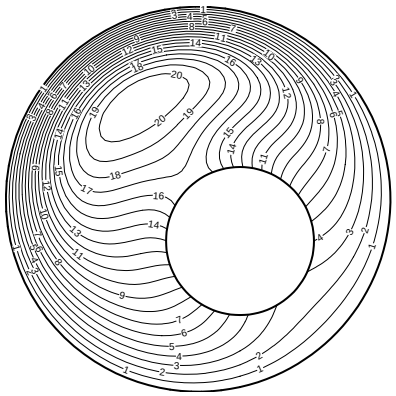

Level	TEMP.
20	6.8492
19	6.5067
18	6.1643
17	5.8218
16	5.4793
15	5.1369
14	4.7944
13	4.4520
12	4.1095
11	3.7670
10	3.4246
9	3.0821
8	2.7397
7	2.3972
6	2.0548
5	1.7123
4	1.3698
3	1.0274
2	0.6849
1	0.3425

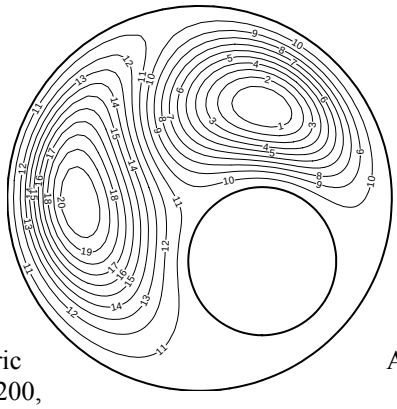

Level	STREAM
20	5.2179
19	4.6606
18	4.1033
17	3.5460
16	2.9886
15	2.4313
14	1.8740
13	1.3167
12	0.7594
11	0.2020
10	-0.3553
9	-0.9126
8	-1.4699
7	-2.0273
6	-2.5846
5	-3.1419
4	-3.6992
3	-4.2565
2	-4.8139
1	-5.3712

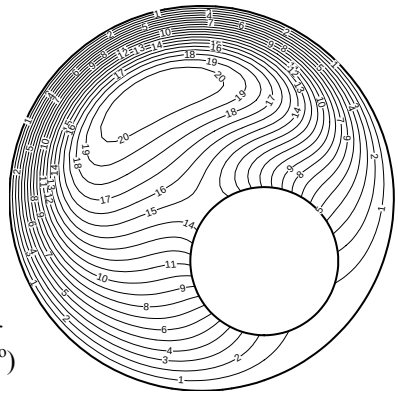

Level	TEMP.
20	7.8742
19	7.4805
18	7.0868
17	6.6930
16	6.2993
15	5.9056
14	5.5119
13	5.1182
12	4.7245
11	4.3308
10	3.9371
9	3.5434
8	3.1497
7	2.7560
6	2.3623
5	1.9685
4	1.5748
3	1.1811
2	0.7874
1	0.3937

Figure (4) Isotherms & Streamlines for Eccentric Annulus (φ_o=45°) Ra=200, Re=50, Pr=0.7, $\bar{R}$=2.6, N=3, $\bar{t}$=1

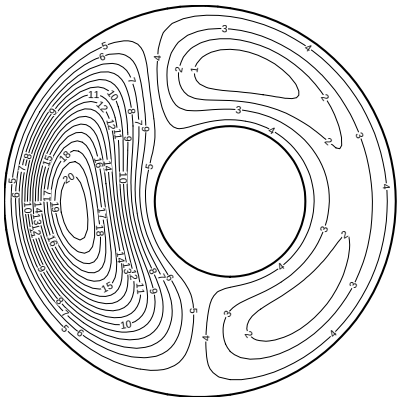

Level	STREAM
20	4.2525
19	3.9824
18	3.7124
17	3.4423
16	3.1723
15	2.9022
14	2.6322
13	2.3621
12	2.0920
11	1.8220
10	1.5519
9	1.2819
8	1.0118
7	0.7418
6	0.4717
5	0.2017
4	-0.0684
3	-0.3385
2	-0.6085
1	-0.8786

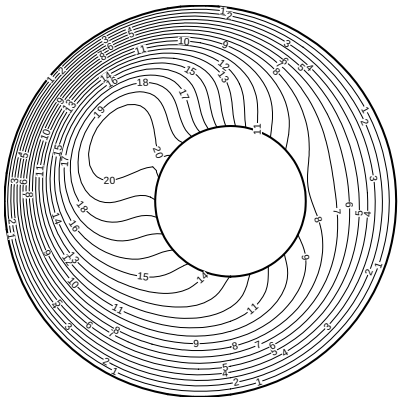

Level	TEMP.
20	5.8767
19	5.5829
18	5.2891
17	4.9952
16	4.7014
15	4.4076
14	4.1137
13	3.8199
12	3.5260
11	3.2322
10	2.9384
9	2.6445
8	2.3507
7	2.0569
6	1.7630
5	1.4692
4	1.1753
3	0.8815
2	0.5877
1	0.2938

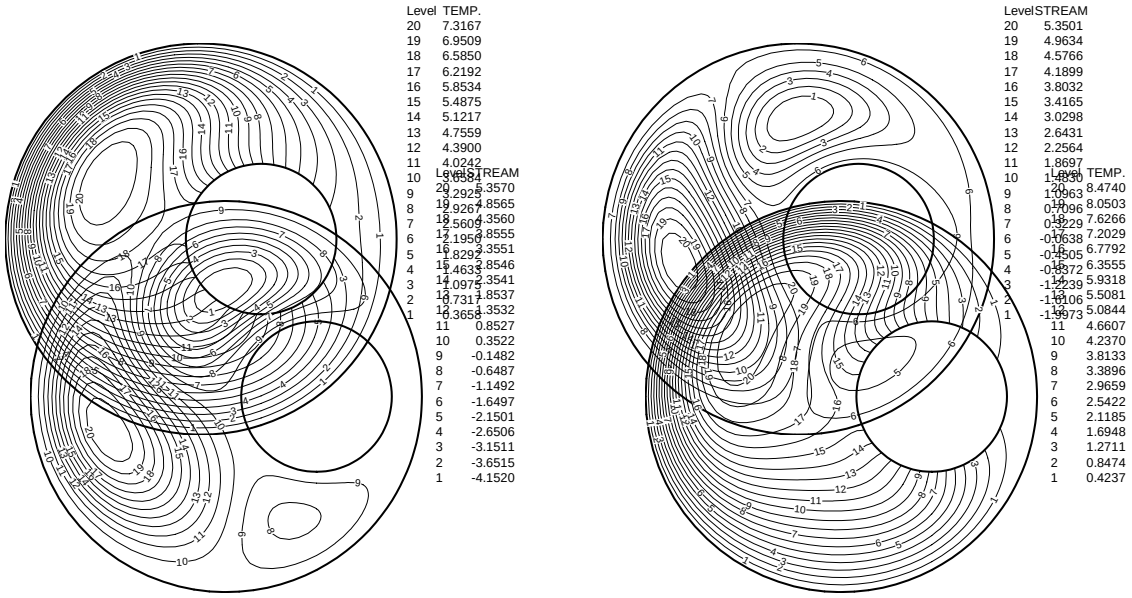

Figure (5)
Isotherms & Streamlines for Eccentric Annulus (φ_o=90°)
Ra=200, Re=50, Pr=0.7, $\hat{R}$=2.6, N=3, $\hat{t}$=1

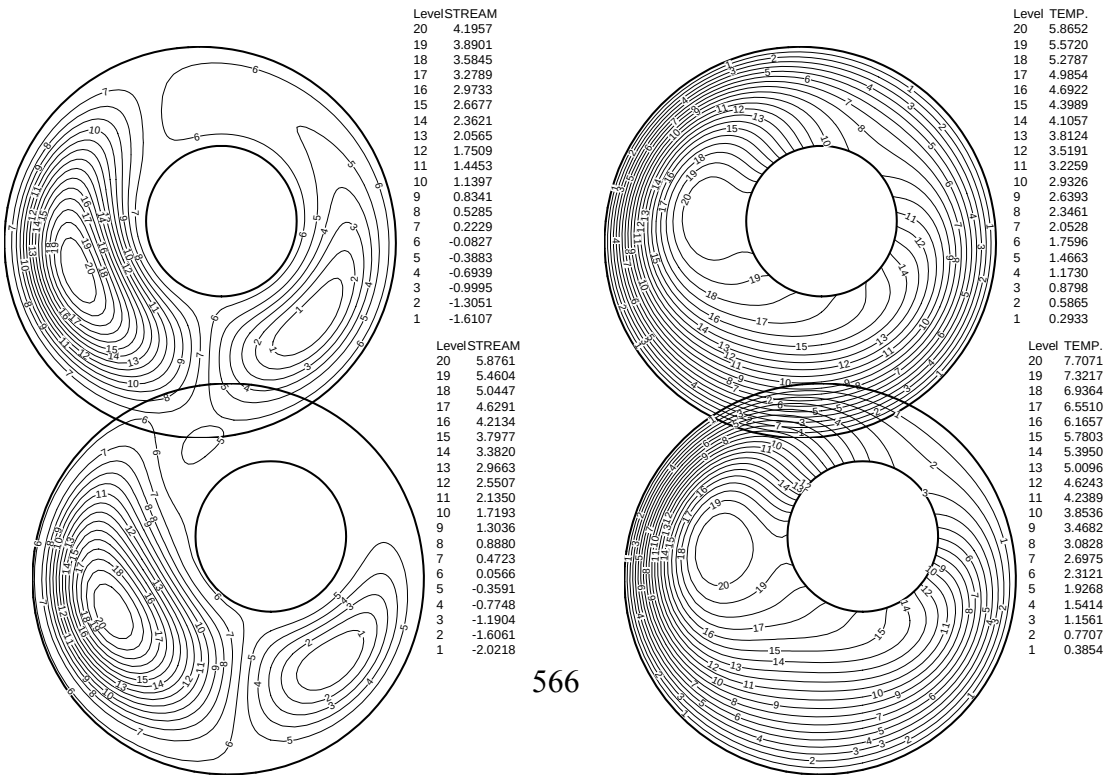

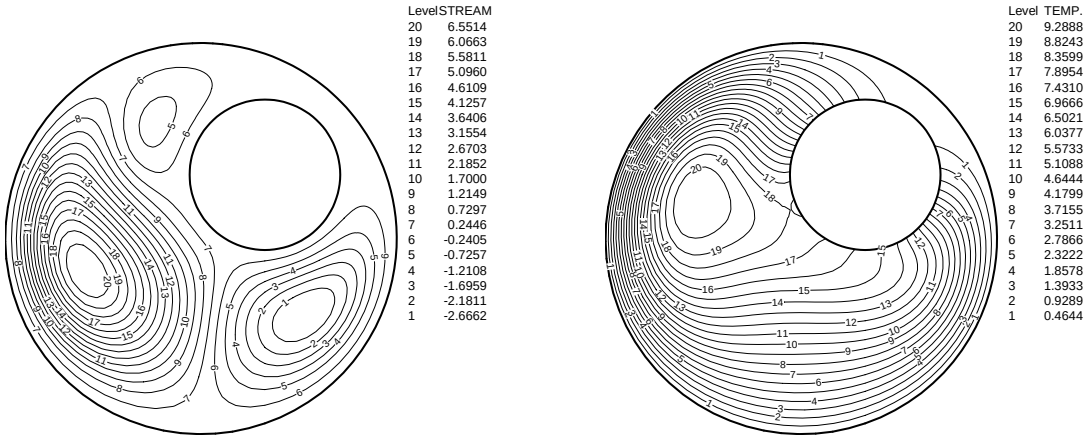

Figure (6)
Isotherms & Streamlines for Eccentric Annulus (φ_o=135°)
Ra=200, Re=50, Pr=0.7, $\bar{R}$=2.6, N=3, $\bar{t}$=1

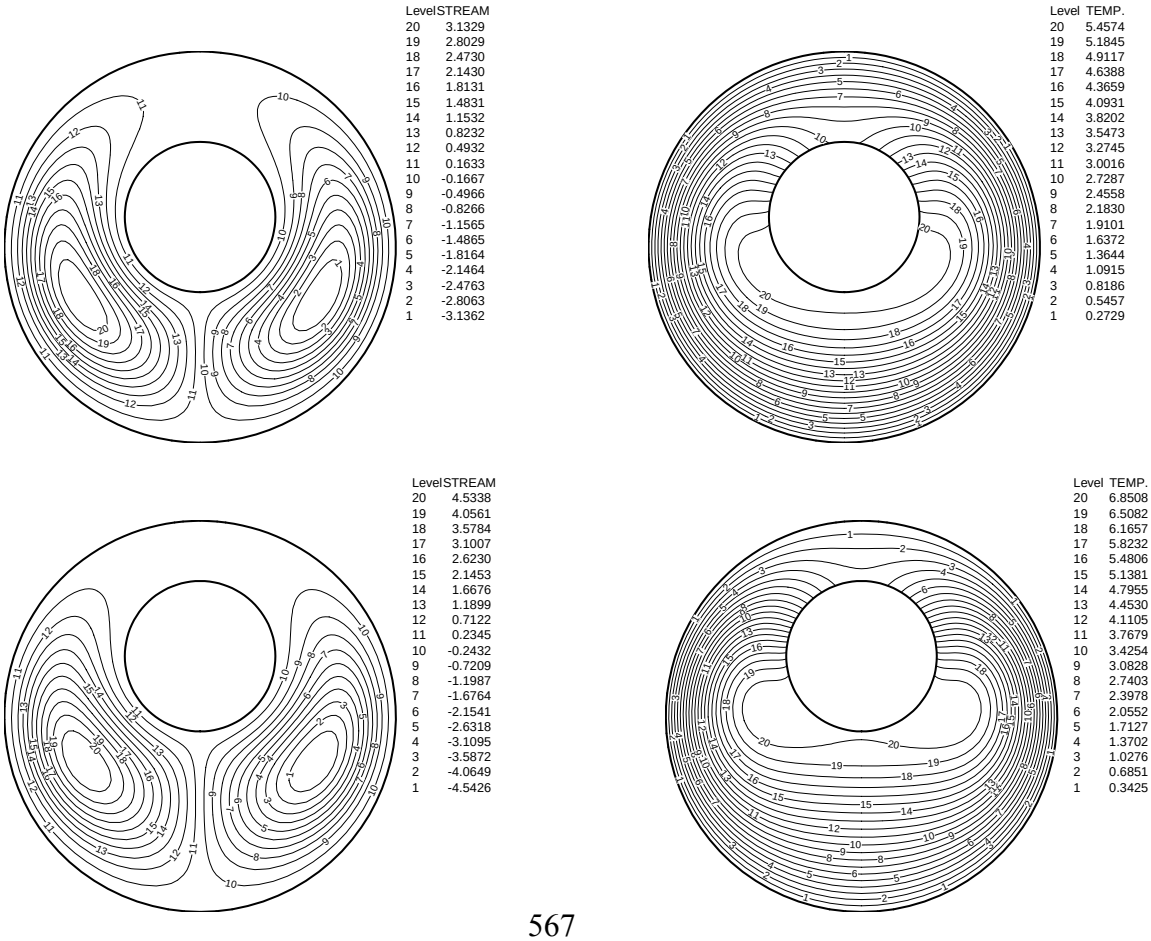

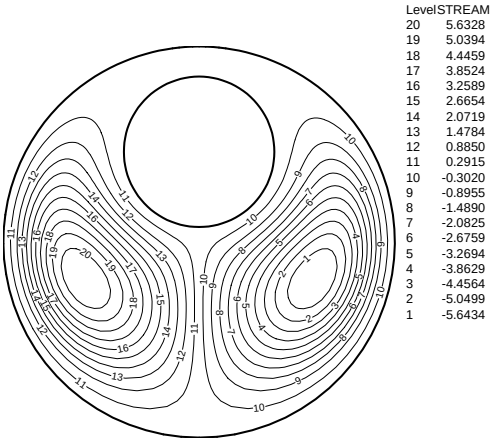

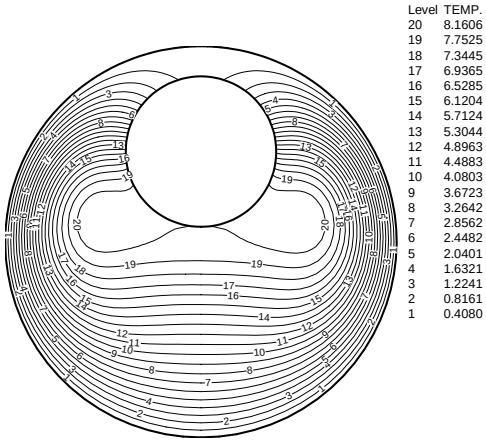

Figure (7)
Isotherms & Streamlines for Eccentric Annulus (φ_o=180°)
Ra=200, Re=50, Pr=0.7, $\bar{R}$=2.6, N=3, $\hat{t}$=1

Figure (8) Effect of ***Nu*** Eccentricity on Present Work

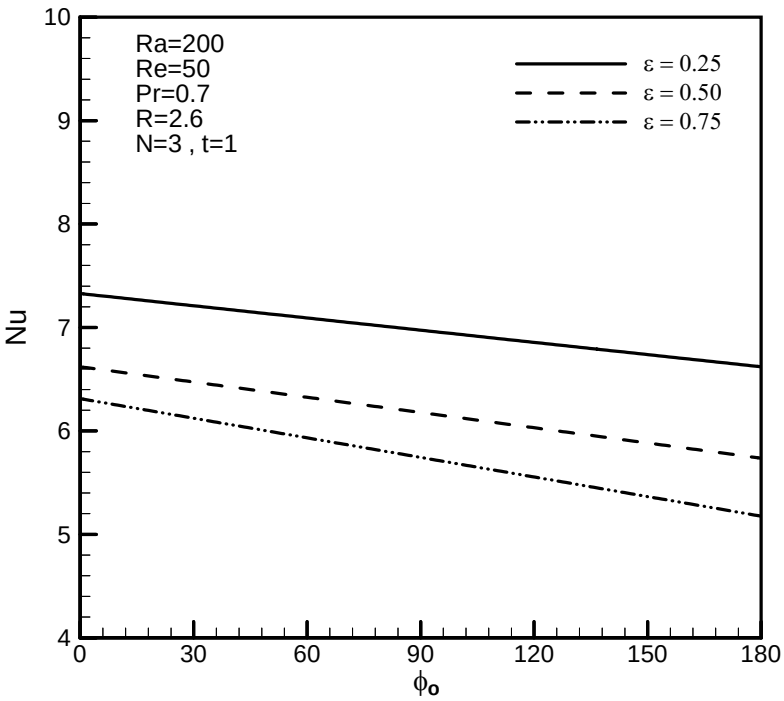

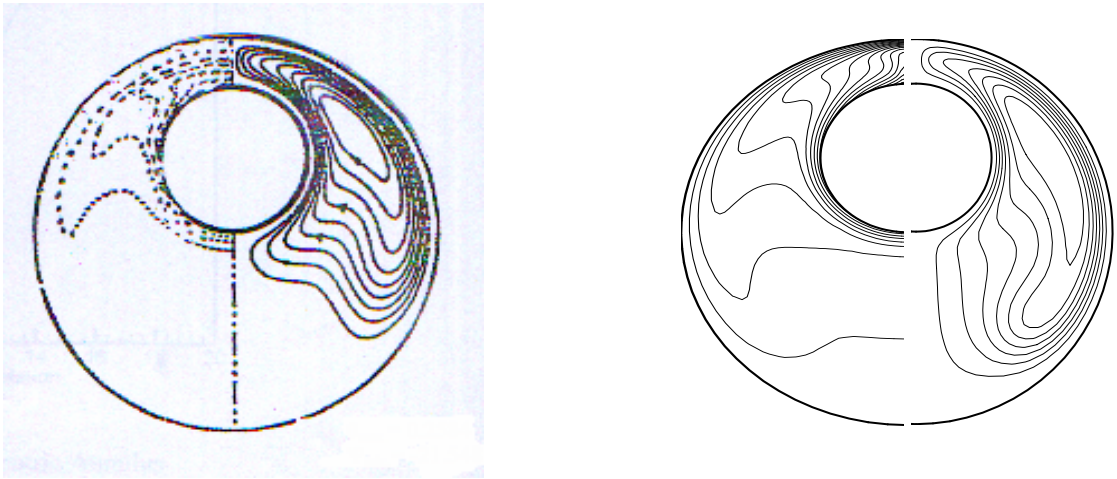

$\theta_{max.}$= 0.2942
$\Psi_{min.}$= -25.0405

$\theta_{max.}$= 0.2584
$\Psi_{min.}$= -21.548

Figure (9)
Comparison of Isotherms & Streamlines for Eccentric Annulus
(φ_o=180°,ε=0.625), Ra=10^6, Pr=0.7, $\hat{R}$=2.6, N=0, $\hat{t}$=0

NOMENCLATURE:
LATIN SYMBOLS:

Symbol	Description	Unit
$\hat{R}$	Radius Ratio ($\hat{R} = \frac{r_o}{r_i}$)	---
$\hat{t}$	Optical Thickness ($\hat{t} = k_r \mathrm{De}$)	---
A	Axial Pressure Gradient ($\mathrm{A} = -\frac{4\rho\nu^2 Re}{\mathrm{De}^3}$)	N/m^3
C	Axial Temperature Gradient ($\mathrm{C} = \frac{\partial T}{\partial z}$)	K/m
De	Hydraulic Diameter De = 2(r_o - r_i)	m
e	Space Between the Centers of the Inner and Outer Cylinders	m
g	Gravitational Acceleration	m/s^2
J	Jacobean of Direct Transformation	---
K	Thermal Conductivity of the Air	W/m.K
K_r	Volumetric Absorbtion Coefficient	m^{-1}
N	Radiation-Conduction Parameter ($N = \frac{4\sigma\epsilon T_W^3}{k k_r}$)	---
n	Dimensionless Outer Normal Direction	---
Ni	Number of Gridlines in the φ-direction	---
Nj	Number of Gridlines in the r-direction	---

Nu_b	Bulk Nusselt Number	---
P	Normalized Air Pressure	---
p	Air Pressure	N/m^2
Pr	Prandtl No. ($Pr = \frac{\nu}{\alpha}$)	---
Ra	Rayleigh Nnmber ($Ra = \frac{g\beta C De^4}{\nu\alpha}$)	---
Symbol	Description	Unit
Re	Reynolds Number ($Re = \frac{ADe^2}{4\rho\nu^2}$)	---
R_i	Dimensionless Inner Cylinder Radius	---
r_i	Inner Cylinder Radius	m
R_O	Dimensionless Outer Cylinder Radius	---
r_o	Outer Cylinder Radius	m
T	Air Temperature	K
t	Time	Second
u, v, w	Velocity Components in x, y and z Direction Respectively	m/s
U, V, W	Dimentionless Velocity Components in X, Y and Z Direction Respectively	---
x, y, z	The physical Coordinates of The Annulus	m
X, Y, Z	The Dimensionless Physical Coordinates of The Annulus	---

GREAK SYMBOLS:

Symbol	Description	Unit
φ	Angular coordinate around inner cylinder	Degree
ϱ, ϖ, γ	Coefficient of Transformation of BFC.	---
φ_o	Angular position for the inner cylinder	Degree
α	Thermal Diffusivity	m^2/s
	Coefficient of Transformation of BFC	---
β	Coefficient of Thermal Expansion	1/K
	Coefficient of Transformation of BFC	---
ε	Dimensionless Eccentricity ($\varepsilon = e / De$)	---
ζ , η	Coordinates in The Transformed Domain	m
θ	Dimensionless Air Temperature ($\theta = \frac{(T_w - T)}{PrCDe}$)	---
σ	Stefan Boltizman Constant	W/m^2K^4
	Relaxation Parameter	---
τ	Dimensionless Time ($\tau = \frac{\nu t}{De^2}$)	---
υ	Kinematic Air Viscosity	m^2/s
Ψ	Dimensionless Air Stream Function	---
Ω	Dimensionless Air Vorticity	---
ϵ	Emissivity	---

REVIEW THE ASSESSMENT OF EFFECTS OF LOST TIME INJURIES IN AN INDUSTRIAL SYSTEM BY USING AN EXPLANATORY PROGRAM

Ms. Iman Q. Alsaffar
Mech. Eng. Dep.
College of Eng. \ University of Baghdad
Baghdad – Iraq

ABSTRACT

Health and safety problem can be described by statistics it can only be understood by knowing and feeling the pain, suffering, and depression. Health and safety has a legal responsibility to protect it for everyone who can affect in the workplace. This includes manufacturers, suppliers, designers and controllers of work places and employees. Work injury is one of the major problems in manufacturing and production systems industries; it is reduced production efficiency and affects the cost. To gain flexibility from a traditional manufacturing system and production efficiency, this paper is about the application of estimating technology to preview and synthesis of *Lost Time of Work Injuries* in industry systems aims to provide a safe working environment for all employees to achieve safe workplaces, safe systems of work, and safety understanding within our workforce. Our industry often has a poor record in dealing with modern and development techniques. Thus, as one of the targets, this leads to perform a helpful program plane to provide guidelines of management, employees to eliminate hazards, given the enormous cost of occupational personal damage in industry and to develop safe work methods work site. This work proposed a general methodology for constructing an explanatory software system to review and analysis workers injuries in a work site. The program language used is Axes, which suitable to shows categories of incidences and estimates costs to workers, employers and society of workplace injuries and work-related ill health. Data of the system was collected in the State Company for Woolen Industries in Al-Kadhumiaa in Iraq. The resulting is to provide a simple obvious outline system to evaluate lost time injury and the net-costs on safety interfering at the company level to reduce occupational morbidity and generating a helpful system to estimate of the total costs to employers and workers of workplace accidents and work-related ill health.

الخلاصة

توصف الية الصحة والسلامة بالإحصائيات التي لا يمكن فهمها إلا من خلال المعرفة والشعور بالألم، والمعاناة والاكتئاب. تعد الصحة والسلامة المسؤولية القانونية لحماية كل شخص ومن هو مؤثر في موقع العمل، يتضمن ذلك كل من المصنعين، المجهزين، المصممين والمراقبين للعمل والموظفين. تعتبر اصابة العمل من المشاكل الرئيسية التي تقلل من كفاءة الانتاج وتؤثر في الكلف لعمليات التصنيع والانتاج في الانظمة الصناعية. يهدف البحث الى تطبيق تقنية للتقييم والعرض للوقت الضائع في اصابات العمل لنظام صناعي بغية الوصول الى توفير بيئة صحية سليمة لجميع المستخدمين ولتحقيق مواقع وانظمة عمل آمنة قادرة على التجديد والمرونة في الكفاءة الانتاجية لنظام تصنيع تقليدي. تعاني صناعاتنا في الغالب من مؤشرات ضعيفة في التعامل مع التقنيات الحديثة والمتطورة. لذلك، وكاحد اهداف هذا البحث هو ايجاد، خطة برنامج مساعد لتوفير تعليمات للادارة وللعاملين لإزالة المخاطر التي تؤدي الى الكلف الهائلةَ للضرر المهني في الصناعة. ولاجل تطوير والوصول الى طرق عمل آمنة لموقع العمل. مقترح البحث هو ايجاد الية عامة لبناء نظام برمجي توضيحي لاستعراض وتحليل إصابات العمل. لغة البرنامج المستخدمة (اكسس)، وهي ملائمة في العرض والتحليل لانواع الاصابات والكلف التخمينية للعاملين من عمال، وموظفين، وكذلك لمجتمع او بيئة الإصابات. بيانات النظام تم جمعها وتطبيقها في الشركة العامة للصناعات النسيجية- الكاظمية – العراق. النتائج المتحققة هو توفير مخطط واضح وبسيط لتقييم الوقت المفقود في الاصابة والكلف الكلية المؤثرة في السلامة لمستوى الشركةَ لتقليل الاصابات والامراض المهنية وتكوين نظام مساعد في تخمين التكاليف الكلية للحوادث والامراض المرتبطة بموقع العمل للعمال والعاملين.

Key words: Lost Time Injury, **Incidence Cost**, **Work Injury**, **(Key Performance Indicators) KPIs**

1. INTRODUCTION

1.1 Work Injury

Work injuries have been viewed as a major problem to affect the efficiency and cost of production. The work injuries are caused by the repetitive work operations during the production with a high frequency of the repetitive workload [li lin, 2008].

Every employer shall provide employment which shall be safe for the employee therein and shall furnish and use safety devices and safeguards, and shall adopt and use methods and processes reasonably adequate to render such an employment and place of employment safe, and shall do every other thing reasonably necessary to protect the life, health, safety and welfare of such employees; provided that, as used, the term "safe" or "safety" as applied to any employment or a place of employment shall include conditions and methods of sanitation and hygiene reasonably necessary for the protection of the life, health, safety and welfare of employees[Rock, L., 1997].

1.2 Industrial System and Work Injury

Work injury problem persist due to the tough competition in manufacturing industries today in terms of a desire to have a production system with low cost, quick lead-time and high quality of products, making the human in an ever-increasing stress situation. That state has both the right and the duty to make sure that those who are employed within its industries are provided with reasonably safe work places is well established [li lin, 2008].

The great majority of injuries, which, workers suffer in industrial employment, do not result from hazards. Instead, the great annual total of such injuries is, for the most part, built up injury-by-injury and day by day throughout the year from the almost endless variety of relative hazards that are involved in industrial operations [Rock, L., 1997].

1.3 Injuries Cost: Overview

Cost of work injuries includes the direct cost and indirect cost. The direct cost contains the expense on the resources of preventing, detecting and treatment. The indirect cost relates to the loss of production output in economics. The measurement of work injuries, which may occur in production, is the obstacle of cost analysis. The cost estimation of work injuries is limited by the uncertain measurement of them [Leigh, P., 2000].

The most observable form of ‘‘undesirable cost’’ is time away from work (recorded as a lost time injury). However, productive time will also be lost where workers are not able to equipment or work procedures causing (sore or tired muscles). Poor working conditions may contribute to people staying away from work or avoiding time in certain work areas. Poor quality job design and working conditions may also increase staff turnover and items that constitute the greatest proportion of additional costs are: overtime, over-employment, training, supervision, employee turnover, waste and rework, lost production time, and reduced productivity [Oxenburgh, M., and Marlow, P., 2005].

1.4 Industrial Costs of Injuries and Illnesses

“Safety Pays" helps estimate cost gains realized through the prevention of work injuries and illness claims. Industries can use this information to predict the direct and indirect costs of injuries and the sales needed to compensate for these losses [OSHA Home, 2010].

The Firms can provide information and assistance on developing and implementing an effective safety and health management systems that can help prevent injuries and / or illnesses to provide a safe working environment for the employees.

Compensation and medical costs (as direct costs) are obvious. It has however, taken careful studies by experienced cost accountants and industrial executives to show how large the other costs (as indirect costs) are. It is now clear that on the average the indirect costs of accidents in industry are not less than four times the direct costs. Figure (1-1) describes the different categories that make up the total costs for each of these items [Economic Advisers Unit June, 2004].

1.5 Objectives

a. Provide guidelines to promote among worker, making an increased under-standing of safety

through the efficient and accurate reporting and recording of accidents.

b. Design an illustrative program system for organized analysis of work injuries and for estimation the cost of work injuries in industry system.
c. Describes the concepts behind cost benefit analysis related safety and introduces a method by which an analysis may be performed relatively easily in a service or manufacturing workplace.

2. THE SAFETY STATE IN TEXTILE AND FABRIC INDUSTRIES

The injuries and illnesses among textile workers in a workplace as follow [Mahone, D, & NIOSH, 1997 & State Company for Woolen Industries 2010]:

- 70% of machine operators using foot controls report back pain.
- 35 % report persistent low back pain.
- 25 % have suffered a compensable Cumulative Trauma Disorder (CTD) where: 81 % of CTDs were to the wrist, 14% of CTDs to the elbow, and 5% of CTDs to the shoulder.
- 49% of workers experience pain in the neck.
- Absenteeism increases as working conditions worsen.
- Loss of workers due to Injuries or turnover is associated with working conditions.

2.1 Work Organization [Mahone, D, & NIOSH, 1997]

- As many as 100% of piecework operators in high manipulation jobs have symptoms of CTDs.
- Workers in piecework are 4 times as likely to develop severe disabilities as hourly workers.
- Workers in piecework are 9 times as likely to develop arthritic disorders as hourly workers.
- As duration of employment in piecework increases, so do severe disabilities.

2.2 Duration of Exposure [Mahone, D, & NIOSH, 1997]

- Machine operators experience cumulative damage to the neck and shoulders over time.
- Risk for persistent neck and shoulder pain increases with years of employment as a machine operator.
- Work for more than 8 years as machine operator increases risks for neck and shoulder pain.

2.3 State Company for Woolen Industries

State Company for Woolen Industries is the only publicly owned group of factories for woolen textile industries in Iraq. The company consists of seven production factories. The Headquarter of the company is the ninth location in Kadhumiaa**.**

The Company had suffered as many of the Iraqi industries, during the sanction time in the nineties and early years of this century. Only in year 2009, it started to recover from the consequences of the neglect and lack of resources during the last 2 decades. It has been working hard over the past years to promote health safety best practices to report that 2010 was another record-setting year in most of health safety aspects. This safety reports reflects the performance and demonstrates to the health and safety of the employees. Currently, a huge effort is taking place to make use of the available limited funds to bring the items of production lines into live again. The effect of such machines (old and not properly maintained) still running had affected the quality of the products and the safe of employee, so the requirement is to provide much better results in terms of quality, quantity, and safety can be achieved once some or part of the production lines can be replaced.

The financial results and costs are in no way a true reflection of the actual costs. At the moment, the salaries represent a huge junk of the cost (71%), this high cost is due to the production lines either not working or running at a very low efficiency and have poor workplace safety. The workforces are for 3- shift work while only one shift (hour shift of 8 hours per day).

The total hours worked by all employees in Al- Kadhumiaa plant during the period covered were (566 employees * 8 hours per day * 250 days) in one year.

Tables (2-1) and (2-2) shows the data and information that based on collection and the inquiring of employees from different members of the plant and the comments from the workshop participants.

3. METHODOLOGY \ STATISTICS OUTCOMES (KPIs)

The outcomes, such as work-related fatalities, injuries and illnesses, are a necessary component of reporting on an industrial system because they reflect the extent to which an organization system has been successful in preventing working injury and disease. Outcomes can be identified, as the most important (Key Performance Indicators) KPIs**.** The various categories of work injury and illness results are severity-based measures of work outcomes (O'Neill, S., 2009). KPIs can be detail as in Table (3-1), where:

- Number of work-related fatalities
- Number of permanent disabilities (medical discharge)
- Number and rate of permanent disability (return to work)
- Number and rate of long-term (more than 6 months) temporary disability
- Rate of the medium term temporary disability, (2 weeks to 6 months).

Rate of short-term temporary disability (up to 2 weeks).

System Outline: Most companies have some, if not all, of their data in creat or design programs, but most people don't know how to use these programs assessment, estimate to make graphs, charts, or diagrams of their improvement efforts. The program consists of *two subsystems*.These systems have the capability, flexibility,and easey in employment for changing, adding, and eliminating information. Figure (3-1) shows the daigram of the system,where:

Second: Entering through The *1st subsystem* (Rates calculation work incidents), another window will be activated with three enabled selections as clearly in figure (3-3), and each selection was described in (**Part A**) below.

Items: (Back) in each window will reverse to the previous window to do another option and (Quit) to be exit.

First: Main window which includes the two subsystems as shown in figure (3-2)

Third: Figure (3-4) represent the first selection of previous screen that lead to (KPI flow diagrams) mentioned in (**Part A\A1**) where the second selection to get the state in (**Part A\A2**).

Forth; With this window in figure (3-5), the selection between the two (Run Rate) will be demonstrate as stated in (**Part A\A3**).

Fifth: Recurring into the main window in figure

(3-2), *2nd subsystem* of (Cost estimation of work incidents) window will selected, these cost estimation activities will be implemented as described in (**Part B\B1**).

3.2 Process Performance Indicators (PPIs)

Occupational processes are those programs and activities used to identify and eliminate (or at least control) hazards. Process Performance Indicators PPIs are a number of safety performance indicators have become "standard" in many industry sectors. They are mostly expressed in terms of event frequency.

The number of hours worked being the common denominator representing the level of activity. Such parameters have the advantage of relying on a small number of simple inputs, which allows meaningful statistical analysis even when the data sets are incomplete. The performance indicators are: identified as most important to stakeholders related to: work injury audit non-conformances; monitoring of health exposures to risks; safety risk assessment and training; incident analysis and employee discussion (A. Burton, and, K.H. den Haan, 2008). Only when a company compares its injury experience with that of its entire industry, or with its own previous experience, can it obtain a meaningful evaluation of its safety accomplishments. To make such comparisons, a method of measurement is needed that will adjust for the effects of certain variables contributing to

differences in injury experience. Injury totals alone cannot be used for two reasons: **First**, a company with many employees may be expected to have more injuries than a company with few employees. **Second,** if the records of one company include all the injuries treated in the first aid room, while the records of a similar company include only injuries serious enough to cause lost time, obviously the first company's total will be larger than the second company's figure.

4. THE PRACTICAL IMPLEMENTING OF THE SYSTEM WORK

Part A: Incidences Rates

Return to Table (3-1) the system was applied with Information that was collected injuries or illness suffered by employees and workers with 11 or more employees (at any one time in the previous calendar year) must keep OSHA standards records when they are) [OSHA Home, 2010]:

- Engaged in activities involving the design, project engineering, production, handling, filling, sales, distribution and production units which, including associated administration and supporting services. The statistics include:
- Number of Recordable Injuries (RI) and Recordable Injuries Rate (RIR) per 200,000 employee-hours, as equivalent (100 employees working 40 hours per week for 50 weeks per year).
- Number of Lost Time Injuries (LTI) and Lost Time Injuries Rate (LTIR) per 200,000 employee-hours, as equivalent (100 employees working 40 hours per week for 50 weeks per year).
- Caused annual work injury costs (direct and indirect) which, impact of work injury on profit and sales. The calculations include:
- Work injury costs (estimated or actual).
- Work injury costs as a percent of profits.

$$\text{Incidence Rate of Recordable Cases} = \frac{\text{No. of injuries and illnesses} * 200{,}000}{\text{Total hours worked by all Employees during period covered}}$$

or

$$= \frac{\text{No. of lost work days} * 200{,}000}{\text{Total hours worked by all employees during period covered}}$$

Two other formulas can be used to measure the average severity of the recorded cases:

During that period, several safety reports were accomplished, to complete the requirements of the program as below, these tasks are:

A1: Designing flow diagrams to explain the current KPI, Figure (4-1).

A2: Evaluation data annually as worksheets that are classified according to each KPI and show their behavior diagrams, figure (4-2) explains data input to this window of the system. The data was collected in Al-Kadhumiaa plant which some of these information as mentioned in Table (2-2). The capability for changing, innovating, and coming first or next or last was clear in this window.

The information will be appearing as a worksheet window by (press to show data) with the behavior histogram that run out by using each key individually down the worksheet window as presented in figure (4-3) where the concepts of (LTIs, TRC & LWC) are denoted in Table (3-1) above.

A3: Reviewing the evaluation and diagrams behavior of the annual Incidence Rate IR and Lost Work Day Rate LWDR, for example, the related information for years 2009 & 2010 in figures (4-4) & (4-5) were linked with the above worksheet in figure (4-3), and then they run out to calculate and demonstrate histograms in figure (4-6) related information .

4.1 Procedure

Work injury rates are based on the exposure of 100 full-time workers using 200000 employee-hours as the equivalent (100 employees working 40 hours per week for 50 weeks per year).

- An injury rate can be computed for each category of cases or days lost depending on what number is put in the numerator of the formula.
- The denominator of the formula should be the total number of hours worked by all employees during the same time- period as that covered by the number of cases in the numerator.

I. Injury and /or Illness Incidence Rates: [OSHA Home, 2010]

$$\text{Average Lost Workdays} = \frac{\text{Total lost workdays}}{\text{Total lost workday cases}}$$

$$\text{Average day's away from work} = \frac{\text{Total days away from work}}{\text{Total days-away-from-work cases}}$$

- If these numbers are small, then it is known that the cases are relatively minor. If, however, the numbers are large, then the cases are of greater average severity and should receive serious attention.
- For example, to calculate the incidence rate for total recordable cases at the end of the year, one would simply multiply the number of recordable

cases by 200,000 and divide that by the number of hours worked by all employees for the whole year**.**

- The incidence rates may also be interpreted as the percentage of employees who will suffer the degree of injury for which the rate was calculated.
- That is, if the incidence rate of lost workday cases is 5.1 per 100 full-time workers, then about 5% of the establishment's employees incurred a lost-workday injury.

These rates are really a general terms. In addition to the total injury-illness incidence rate: (**1.** Injury rate, **2.** Illness rate, **3.** Fatality rate, **4.** Injury Severity Rate, **5.** Lost-workday-cases injury rate LWDI, **6.** Number-of-lost-workdays rate. The following as shown in the box below:

- Rate 5 counts cases in which one or more workdays were lost or in which the worker was transferred to another job.
- Rate 6 counts the total number of workdays lost or days in which the worker was transferred to another job.
- In counting the number of lost workdays, the date of the injury or start of illness should not be, even though the employee may leave work for most of that day.
- Thus, if the employee returns to his regular job and is able to perform all regular duties full time on the day after the injury or illness, no lost workdays are counted.
- The most widely recognized standard incidence rate is LWD incidence rate, which known as the
- A somewhat surprising characteristic of the LWDI is that it considers injuries only- not illnesses.
- Illnesses are more difficult to track than injuries because there are often time delays in their diagnosis. In addition, it is more difficult to prove work-relatedness for chronic exposures, which may have a variety of simultaneous causes.
- LWDI does not include fatalities, whether they are by illness or injury.
- Fatalities should always be considered a rare occurrence of serious importance and as such should not be averaged among the more common injury statistics on which the LWDI is based.
- Using National Safety Council average costs, 1998, includes both direct & indirect costs, excludes property damage

Part B: Cost Estimation

B1: Insert data from Table (4-1) with the window as illustrated in figure (4-7), noting that the activation of button (Injury Type Index) in this window lead to open a listed window includes data from (National Council on Compensation Insurance), data about average cost per workers compensation insurance claim by nature of injury as well as presented the cost multiplier and indirect cost ratio as shown in figure (4-8) [NCCI, 2010]. The behavior of cost estimation illustrated in figure (4-9).

This information can be obtained from the listed data of (NSCAC standards, 1998) shown in Table (4-2) which appears from the selection of (print preview). The analysis and histograms behavior will be appear in figures below:

II. Cost of Injury and Illness and Their Impact on Industry System

Direct Cost**:** To calculate the direct cost: The total value of compensation claim for an injury or illness (consist of medical costs and assurance payments).

These estimating compensation cost which ranging between (100000 & 150000) ID for (PPD & PTD) respectively per injury or case, paid to employers of damage to materials, machinery and property that caused by the same management failures that lead to injury accidents in the group of factories for woolen textile industries in Al-Kadhimyaa plant as present in Table (4-1), note that (1 $ ≈ 1190 ID) in 2010.

Indirect Cost: To calculate the indirect cost of the injury or illness, multiply by a cost multiplier shown in System Table (4-2), the cost multiplier that used will depend on the size of the direct cost.

Indi ct Cost:

Direct Cost * Cost Multiplier = Indirect Cost

Total Cost:

Direct Cost + Indirect Cost = Total Cost

5. CONCLUSIONS & RECOMMENDATIONS

5-1 Conclusion

During the period of coverage search, it is necessary to ensure that the workplace is safe and

without risk to health, everyone shall at all times undertaking to complete all work in a safe manner where people are not at risk due to an unsafe working environment. To achieve this, it is the responsibility of management, and employees to eliminate hazards and develop safe work methods.

The work provides a simple obvious outline system to estimate lost time injury and the net-costs on safety interfering at the company level to reduce occupational morbidity. It illustrates the structure with two explanatory subsystems. The particular formulation of the model was based on several other existing supports that are existing in the study and was adapted to the data that were readily made available by the company that had introduced such interventions over a number of years, note: the discussion about 2009\2010, during the application of the work and the outcomes in changing towards the best was clear in safety and reduction cost.

These results and conclusions have been drawn as follow:

1- There were 82 major injuries to employees reported in 2009/10, the distribution in figure (4-3) **(Part A\A2)** explain the difference that the reduction in injuries was possible comparing with what came in the recent three years this indicated by charts related to. There were 77 other injuries to employees causing absence from work of over three days were caused by handling, lifting or carrying, and nearly a quarter due to slipping or tripping.
2- This also corresponds with point in (1) that Lost Workday Incidence Rate (LTIR) and Incidence Rate (IR) are the lowest ever achieved and is significantly better than the industry situation.
3- This explanatory system provides estimations of the total costs of employers and workers for workplace accidents and work-related ill health.
   The financial results and costs in Al-kadihumiaa plant listed later in table (5-1) with the comparison between figures (5-1) for (*cost analysis in the plant)* and (4-7) for (*cost estimation of work incidence)* in this work, we find that the total estimated cost (7203000) given from the system formed 7% from the working expenses. That facilitates the process of analyzing the cost and how to find appropriate solutions to reduce.
4- It also discusses the efforts to reduce harm, to identify where the greatest burdens of health and safety failures fall. Although the estimates can never show how easy or successful attempts to reduce harm might be, unless provide a good starting point from which to analyze the problems.
5- Systems design features by high accuracy and effective efficiency guide to reduce lost time injury time and effort in cost. In addition, the proposed system has the capability to show information and dynamics in performance as well as proved to be flexible and easy to use

5.2 Suggestions for Future Work

- It is possible expansion the work system to include estimate to calculate the impact of injury or illness on profitability, using the profit margin to determine the sales of the company would need to generate to pay for this injury or illness where:

Total Profits ÷ Total Sales= profit margin

Keep the profit margin in dismal form

Total Cost of Injury or Illness ÷ Profit Margin = Sales Required to Pay for Injury or Illness

- The work could be extended in a variety fields of industry that it can be useful in future research.
- Finding methods to make the system more strong and generalized. This includes investigation of how the system needs to be modified to deal with other subjects in industrial engineering science.
- The system suitable for more functional items, such as time, cost, productivity…etc for example analysis the percentage of (LTI) according to accident activity, injury cause and body location.

REFERENCES

1. A. Burton and, K.H. den Haan, (2008)"*European downstream oil industry safety performance*", Statistical summary of reported incidents, CONCAWE Safety Management.

2. Economic Advisers Unit June, (2004)," *Interim update of the "Costs to Britain of Workplace Accidents and Work-Related Ill Health*".
3. Leigh, P., (2000), "*Costs of Occupational Injuries and Illnesses*," Retrieved from Frontline Web site: http://www.pbs.org/wgbh/pages/frontline/shows/workplace/etc/cost.html, Cited 08/03/06.
4. li lin, (2008). "*Computer Aided Design for Work Injury Elimination in Production Assembly System*", Thesis Canada.
5. Mahone, D., "*Ergonomics in the Textile and Apparel Industries*" CNA Insurance Companies, Chicago,IL www.toolboxtopics.com/Beyond%2520Safe
6. National Council on Compensation Insurance, Inc (NCCI), (2010), Worksheet.
7. National Institute for Occupational Safety and Health (NIOSH), (1997).
8. O'Neill, S., (2009). SIA Conference, Sydney.
9. Oxenburgh, M., and Marlow, P., (2005). "*The Productivity Assessment Tool: Computer-based cost benefit analysis model for the economic assessment of occupational health and safety interventions in the workplace"*. Journal of Safety Research - ECON proceedings 36 (2005) 209 – 214
10. Rock, L., (1997), "*Basic Safety Manual*", Arkansas Department of Labor.
11. , "*The voice of steel distribution*", Accident Survey Results, 2005.
12. State Company for Woolen Industries, (2010), Reports, Kadhimyaa, Iraq.
13. U.S. Department of Labor, Occupational Safety & Health Administration, OSHA Home, (2010), "*Estimated Costs of Occupational Injuries and Illnesses*" Constitution Ave., NW, Washington.

NOMENCLATURES

Symbol	Description
CTD	Cumulative Trauma Disorder
KPIs	Key Performance Indicators
LTI	Lost Time Injuries
LTIR	Lost Time Injuries Rate
LWC	Lost Workday Case
MTC	Medical Treatment Case
PPD	Permanent Partial Disability
PTD	Permanent Total Disability
PPIs	Process Performance Indicators
RI	Recordable Injuries
RIR	Recordable Injuries Rate
RWC	Restricted Work Case
TRC	Total Recordable Cases
WI	Work Injury

Table (2-1) Employees & Plants

Plant name	No. of Employees
Mechanical carpet	682
AL- Fateh	674
Al- Kadhumiaa	566
Al-Nassiriaa	1879
Al-Hurriaa	502
Al-Taji	126
Spinning & fitted carpet	384
Manuf. & spare part	65
General administration	341
Total	5219

Table (2-2) Occupational injuries
in Al- Kadhumiaa plant \2010

Types of Occupational injuries\ Illnesses	Lost Time Injuries \ Illness Cases LTI	Permanent Total & Partial Disability PTD & PPD
Back problems / Lower limb disorder	5	15
Neck / Upper limb disorder	5	8
Noise induced hearing	2	7
Respiratory disease (Asthma)	5	10
Skin disease	4	6
Burns-Related injuries	1	1
Cancer and malignant blood disease	0	0
Infections / preventable disease	0	0
Mental ill-health	0	0
Poisoning	0	3
Other Occupational illness	2	3
Total	24	53

Table (3-1) Statistics Definitions and Guiding Records

Name	Explanation	Evaluating the Extent of Recordable Cases
Incident	This is an uncontrolled or unplanned event, or sequence of events, that results in a fatality or injury to a o n company premises	• Criminal or terrorist activity; • A purposeful act on the part of another individual; • Incidents, which occur Off company premises but where the consequences appear onboard later.
Work Injury WI	This is any sign or of physical damage or impairment to any part of the body directly resulting from an incident, regardless of the length of time between the incident and the appearance of the injury	
Hours Worked	Includes hours actually worked by:	1. All permanent/regular employees - full time and part time. 2. All casual employees - full time and part time (include with full time permanents). 3. All engaged staff plus other permanent contractors.
Fatalities	A death directly resulting from a work injury regardless of the length of time between the injury and death.	Fatalities are included in the Lost Time Injury count
Lost Workday Case LWC	Lost workday cases occur when the injured or ill employee experiences days either away from work, or days of restricted work activity, or both.	1. Days must be taken off from the job for medical treatment or recovery, or 2. The employee is unable to perform his normal job duties over a normal work shift (which could be an extended hour shift of 8 to 12 hours)
Permanent Total Disability PTD	PTD is any work injury which harm an employee permanently and results in termination of employment on medical grounds(e.g. loss of limb(s) permanent brain damage, loss of sight) and precludes the individual from working	
Permanent Partial Disability PPD	PPD is any work injury which results in the complete loss, or permanent loss of use, of any member or part of the body, or any impairment of functions of parts of the body, regardless of any pre-existing disability of the injured member or impaired body function, that partially restricts or limits an employee's basis to work on a permanent basis	
Lost Time Injury LTI	The sum of: PTDs, PPDs and LWC.	***LTIs = Fatalities + LWC+ PTD + PPD***
Restricted Work Case RWC	This is an injury, which results in an individual being unable to perform all normally assigned work functions during a scheduled work shift or being assigned to another job on a temporary or permanent basis on the day following the injury.	**4.** The employee was temporarily assigned to another job, **5.** The employee worked at a permanent job less than full time, or **6.** The employee worked at his permanently assigned job but could not perform all the duties normally
Medical Treatment Case MTC	This is any work-related loss of consciousness (unless due to ill health), injury or illness requiring more than first aid treatment by a physician, dentist, surgeon or registered medical personnel, e.g. nurse or paramedic under the standing orders of a physician, or under the specific order of a physician.	MTCs include: injuries which result in loss of consciousness, even if the individual resumes work after regaining consciousness; sutures for non-cosmetic purposes; use of casts, splints or other means of immobilization; any general surgical treatment; removal of embedded objects from eye by surgical means; use of other than non-prescriptive drugs or medications; use of a series of compresses for treatments of bruises, sprains or strains
Total Recordable Cases TRC	The sum of (work-related fatalities), LTIs, RWCs, and MTCs.	***TRCs = LTIs + RWCs + MTCs.***

Table (4-1) Cost of Workers Compensation in Al – Kadhumiaa plant

Year	No. of Permanent Total Disability PTD*150000 ID	No. of Permanent Partial Disability PPD*100000 ID	Total Compen-sation
2006	1650000	3100000	7850000
2007	1650000	2300000	7850000
2008	750000	1700000	2450000
2009	1000000	3800000	4600000
2010	330000	3100000	3430000

Table 4.2 Cost multiplier (National Council on Compensation Insurance, NCCI, 2010)

Injury Type Index		
Injury Type	Average Direct Cost Multiplier	Indirect Cost Ratio
AIDS	$ 4,469	1.6
Amputation	$ 48,318	1.1
Angina Pectoris	$ 28,136	1.1
Asbestosis	$ 23,346	1.1
Asphyxiation	$ 88,126	1.1
Black Lung	$ 34,165	1.1
Burn	$ 27,380	1.1
Byssinosis	$ 13,523	1.1
Cancer	$ 52,785	1.1
Carpal Tunnel Syndrome	$ 24,695	1.1
Concussion	$ 68,456	1.1
Contagious Disease	$ 15,657	1.1
Contusion	$ 23,748	1.1
Crushing	$ 45,272	1.1
Dermatitis	$ 8,295	1.2
Dislocation	$ 59,207	1.1
Dust Disease, NOC (all other pneumoconiosis)	$ 27,682	1.1
Electric Shock	$ 86,448	1.1
Enucleation (to remove ex: tumor, eye, etc.)	$ 62,699	1.1
Foreign Body	$ 17,585	1.1
Fracture	$ 37,911	1.1
Freezing	$ 13,365	1.1
Hearing Loss or Impairment (traumatic only)	$ 15,304	1.1
Laceration	$ 15,398	1.1
Loss of Hearing	$ 13,145	1.1
Mental Disorder	$ 37,420	1.1
Mental Stress	$ 27,004	1.1
Multiple Injuries Including Both Physical and Psychological	$ 115,961	1.1
Multiple Physical Injuries Only	$ 58,607	1.1
Myocardial Infarction (Heart Attack)	$ 85,962	1.1
No Physical Injury	$ 22,093	1.1
Poisoning - Chemical (other than metals)	$ 43,690	1.1
Poisoning - General (not OD or cumulative injury)	$ 44,761	1.1
Poisoning - Metal	$ 25,054	1.1
Puncture	$ 15,381	1.1
Radiation	$ 36,124	1.1
Respiratory Disorders (gases, fumes, chemicals, etc.)	$ 35,266	1.1
Rupture	$ 61,506	1.1
Severance	$ 59,394	1.1
Silicosis	$ 31,393	1.1
Sprain	$ 23,098	1.1
Strain	$ 27,363	1.1
Syncope	$ 31,138	1.1
VDT-Related Diseases	$ 51,404	1.1
Vascular	$ 56,316	1.1
Vision Loss	$ 49,693	1.1
All Other Cumulative Injury, NOC	$ 30,647	1.1
All Other Occupational Disease Injury, NOC	$ 27,820	1.1
All Other Specific Injuries, NOC	$ 35,671	1.1

Table (5-1) Cost analysis in the plant

Expenses(million ID)	Million ID/year
Salary	3800
Working expenses	1385
Other expenses	103
Total Expenses	5288

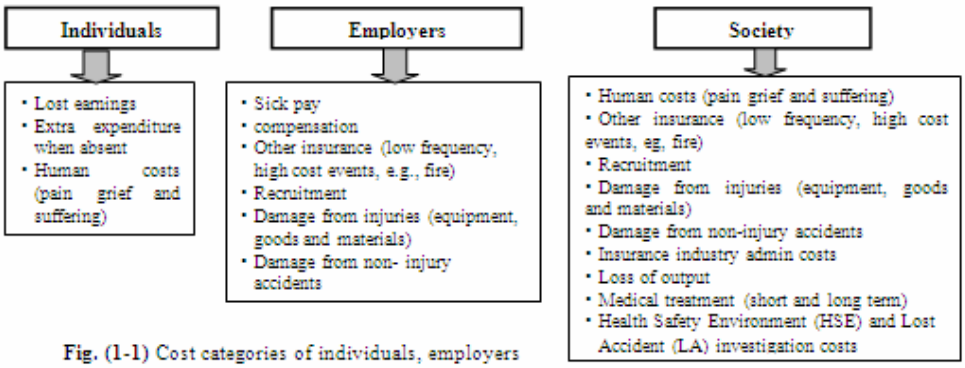

Fig. (1-1) Cost categories of individuals, employers and society of workplace
[Economic Advisers Unit June, 2004]

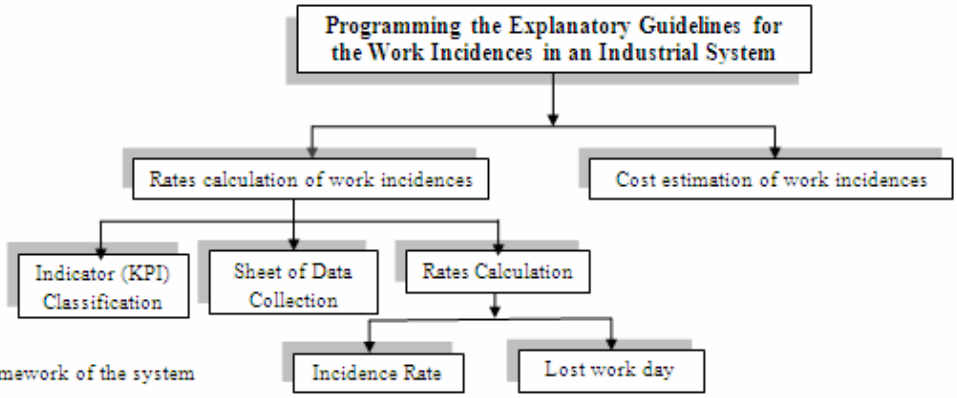

Fig. (3-1) Framework of the system

Fig. (3-2) Main window

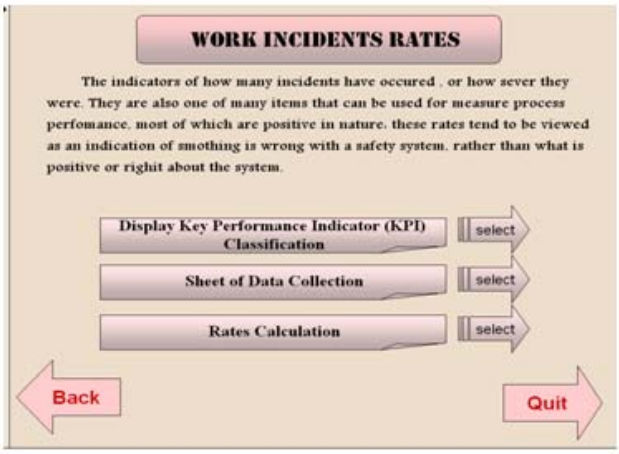

Fig. (3-3) First subsystem

Fig. (3-4) First selection of the subsystem

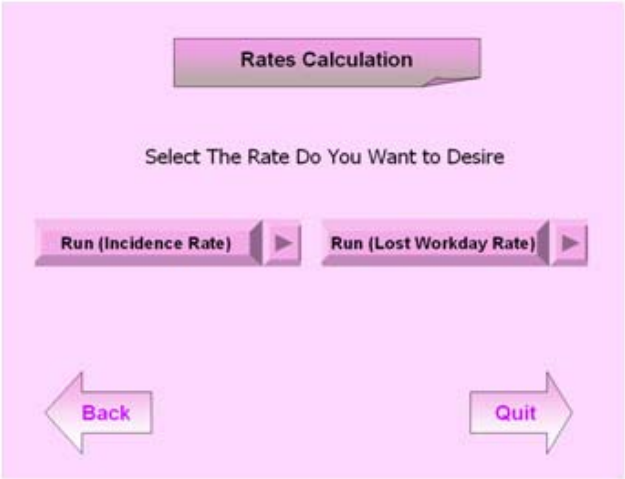

Fig. (3-5) Third selection of the subsystem

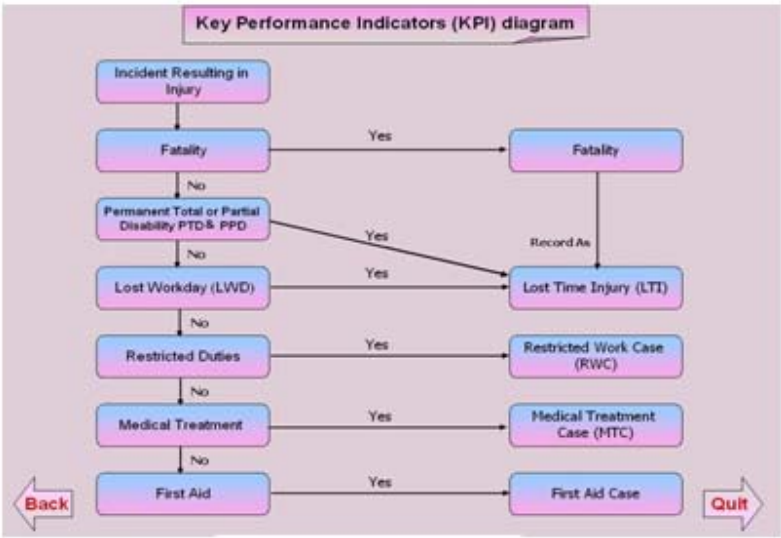

Fig. (4-1) KPI flow diagrams

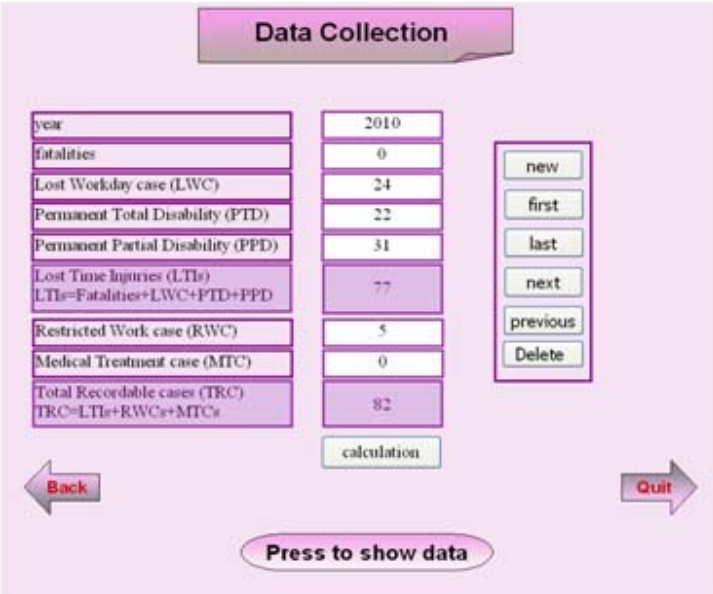

Fig. (4-2) Data input

Worksheet of Classification of Wasted Time Injuries

year	fatalities	Lost workday case (LWC)	Permanent Total Disability (PTD)	Permanent Partial Disability (PPD)	Lost Time Injuries (LTIs)	Restricted work case (RWC)	Medical Treatment case (MTC)	Total Recordable Cases (TRC)
2006	2	56	11	31	100	13	0	113
2007	0	43	11	23	77	9	0	86
2008	0	36	5	17	58	6	0	64
2009	0	53	6	36	95	9	0	104
2010	0	24	22	31	77	5	0	82
	0	0	0	0		0	0	

Total Recordable case (TRC) Chart

TRC=LTIs+RWCs+MTCs

year	Total Recordable case (TRC)
2006	113
2007	86
2008	64
2009	104
2010	82

Lost Time Injuries (LTIs) Chart

LTIs=fatalities+lwc+ptd+ppd

year	Lost Time Injuries (LTIs)
2006	100
2007	77
2008	58
2009	95
2010	77

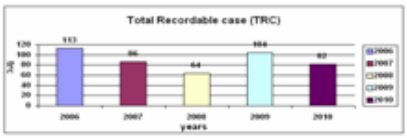

Lost Workday case (LWC) Chart

year	Lost Workday case (LWC)
2006	56
2007	43
2008	36
2009	53
2010	24

Fig. (4-3) Worksheet & distribution histogram

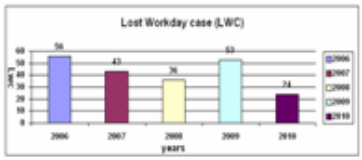

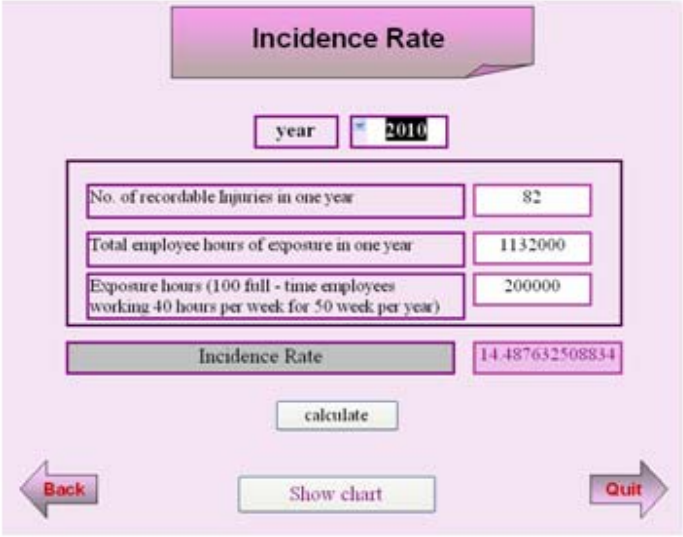

Fig. (4-4) Incidence Rate IR

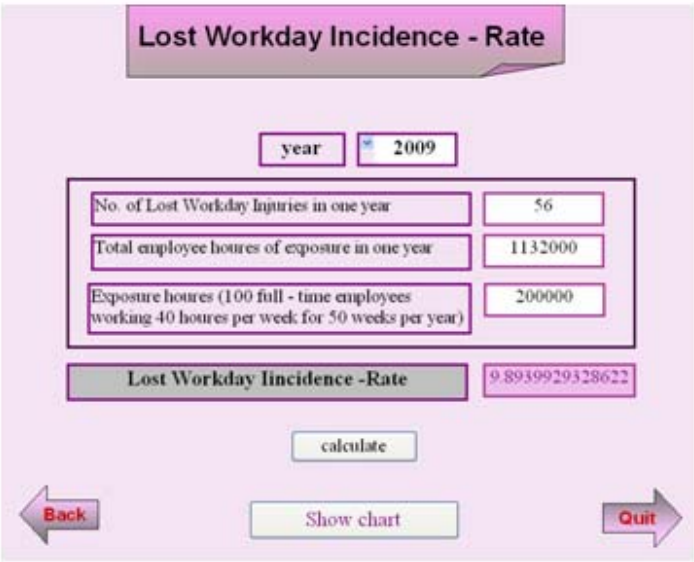

Fig. (4-5) lost Work Day Rate LWDR

Page 12 of 19

Incidence Rate chart

year	Incidence Rate
2006	20
2007	15
2008	11
2009	18
2010	14

Lost Workday Incidence Rate chart

year	Lost Workday Incidence Rate
2006	10
2007	8
2008	6
2009	9
2010	4

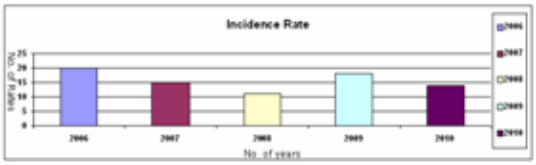

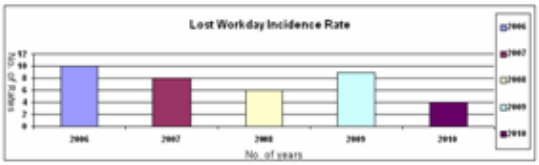

Fig. (4-6) Distribution histograms

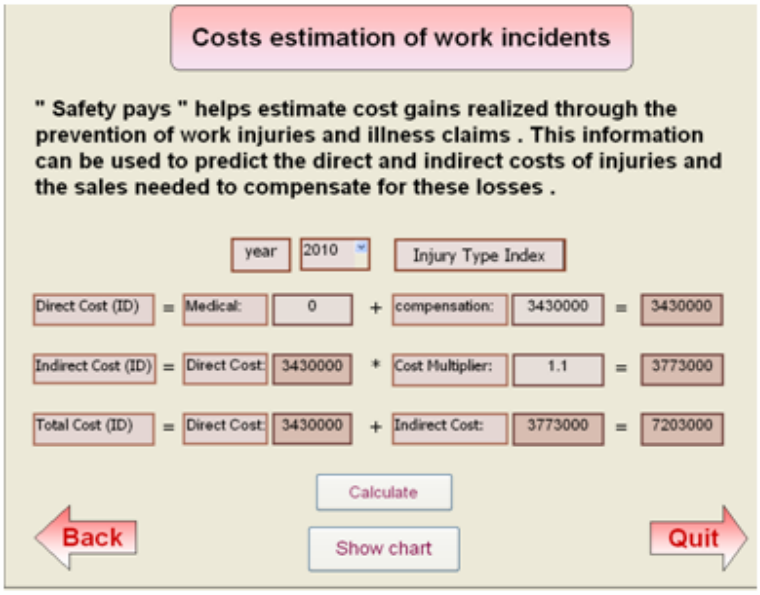

Fig. (4-7) Cost estimation of work incidence

Fig. (4-8) Injury type index

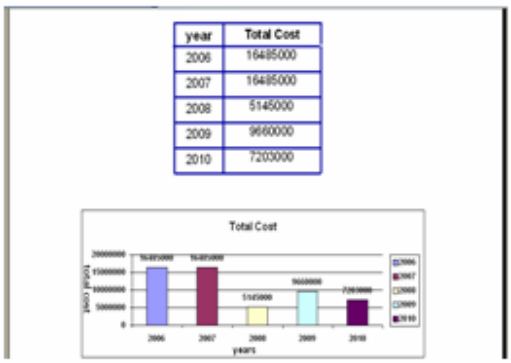

year	Total Cost
2006	16485000
2007	16485000
2008	5145000
2009	9660000
2010	7203000

Fig. (4-9) Distribution histogram of cost estimation

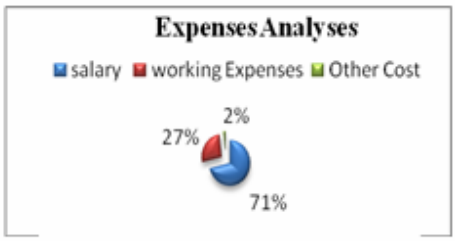

Fig. (5-1) Expenses Analyses in the Al- Kadhumiaa Plant

Compound Heat Transfer Enhancement in Dimpled and Sinusoidal Metal Solar Wall Ducts Fitted with Wired Inserts

Dr. Mohammed H. Mahmoud
Asst. Professor
Mech. Eng. Dept.
Al-Mustansiriyah Univ.

Dr. Fouad A. Saleh
Asst. Professor
Mech. Eng. Dept.
Al-Mustansiriyah Univ.

Abeer H. Faleh
Mech. Eng. Dept.
Al-Mustansiriyah Univ.
Baghdad - Iraq

ABSTRACT

An improved Metal Solar Wall (MSW) with integrated thermal energy storage is presented in this research. The proposed MSW makes use of two, combined, enhanced heat transfer methods. One of the methods is characterized by filling the tested ducts with a commercially available copper Wired Inserts (WI), while the other one uses dimpled or sinusoidal shaped duct walls instead of plane walls. Ducts having square or semi-circular cross sectional areas are tested in this work.

A developed numerical model for simulating the transported thermal energy in MSW is solved by finite difference method. The model is described by system of three governing energy equations. An experimental test rig has been built and six new duct configurations have been fabricated and tested. Air is passed through the six ducts with Reynolds numbers from 1825 to 7300.

Six, new, correlations for Nusselt number and friction factor are developed to assess the benefits that are gained from using the WI and the dimpled and sine-wave duct walls. It is found that higher heat transfer rates are achieved using the Dimpled, semi–circular duct with Wired Inserts (DCWI). Also, it is found that Nusselt number and the pressure drop in the DCWI are respectively (44.2% -100%) and (101.27% - 172.8%) greater than those of the flat duct with WI. The improvement in Nusselt number for flat duct with WI is found to be (1.4 – 2) times the values for flat duct with no WI. The results demonstrated that DCWI provides enhancements efficiency value that is higher than those obtained from other types of ducts. The developed MSW ducts have added to local knowledge a better understanding of the compound heat transfer enhancement.

Keywords :
compound heat transfer, wired inserts, dimpled duct, sinusoidal duct, Nusselt number.

الخلاصة

في هذا البحث تم تقديم جدار معدني شمسي (MSW) مطور ذو قابلية خزن حرارية ضمنية. ان الجدار المقترح يستخدم طريقتين لتحسين انتقال الحرارة. الطريقة الاولى تتضمن إملاء قنوات الجريان بحشوات نحاسية من الأسلاك (WI) المتوفرة تجاريا اما الطريقة الثانية فتستخدم مجاري الهواء ذات الجدران المتموجة جيبيا او المقعرة بدلا من المجاري ذات الجدران المستوية. لقد تم اجراء البحث على مجاري ذات مقاطع مربعة و نصف دائرية .

تم اجراء الحل للموديل العددي المطور الخاص بمحاكاة الطاقة الحرارية المنقولة باستخدام طريقة الفروقات المحددة. ان هذا الموديل العددي مكون من منظومه من ثلاثة معادلات حاكمه للطاقه. تم في هذا البحث بناء جهاز أختبار عملي وتم تصنيع وأختبار ستة مجاري هواء وإمرار الهواء خلال المجاري ضمن مدى لرقم رينولدز من 1825 الى 7300.

من النتائج المستحصلة من هذا البحث تم استحداث ستة معادلات جديدة خاصة برقم ناسلت و معامل الاحتكاك لتخمين الفوائد المكتسبة من الأستعمال المركب لكل من WI و مجاري الهواء ذات الجدران المتموجة جيبيا او المقعرة. لقد وجد ان اعلى معدل لانتقال الحرارة هو للمجرى المدمل ذو المقطع نصف الدائري المحشو (DCWI). النتائج بينت ان نسب رقم ناسلت ومقدار الانخفاض بالضغط للمجرى نوع DCWI هي على التوالي (44.2%-100%) و (101.27%-172.8%) اعلى من تلك العائدة الى المجرى المسطح مع WI . وجد ان التحسينات في رقم ناسلت قد بلغت (1.4 - 2) مرة بالنسبة للمجرى المزود ب WI بالمقارنة مع تلك غير المزودة ب WI. بينت النتائج الخاصة بالبحث الحالي ان الموديل المطور لمقترح DCWI يعطي كفاءة تحسين اعلى من الموديلات الاخرى. النتائج المستخلصة في هذا البحث أضافت للمعرفة المحلية فهم أفضل لتحسين انتقال الحرارة المركب.

1. Introduction

In Iraq, as well as in many countries in the Middle East, conventional massive external walls of building were designed without consideration to energy consumption. Therefore, research and development of techniques for improvement of thermal performances of existing external walls are of great interest. Metal Solar Wall (MSW) is a dark-colored, multi-duct metal cladding that mounted on the building external walls with a proper air gap between them. The metal ducts can be attached to the existing wall using metal fastening system. The Sun's radiation heats the metal panel, and the heated outside air is drawn through the metal wall ducts by fan mounted at the top of the wall.

The (MSW) system is almost maintenance-free, since there are no liquids or moving parts other than the fan system .So, the cost is minimal ,because the system doesn't require much mechanical equipment, and the metal wall doesn't require to be covered with glass (unlike glazed ,flat- plate solar collectors). The (MSW) can be designed as an integral part of a new building or it can be added in existing buildings. Actually, the (MSW) can enhance building's appearance even when added after the building is built by covering old, existing walls. Transformation of external walls into solar collectors will protect the building from unwanted summer heat gain, thus reducing the cooling demands and heat losses from building walls. Environmentally, the (MSW) is producing clean renewable energy, thus lowering the need for fossil fuel and reducing the pollution and green-house gases.

The (MSW) is most effective for many types of commercial and industrial buildings with high ceilings, such as; factories, schools, apartments, offices, supermarkets, sport halls, etc. The (MSW) could be used for a wide variety of industrial application such as crop drying, adsorbent beds regeneration in separation processes and meeting building heating load . In general , vertical walls subjected to a uniform heat flux are used in building components ,passive solar systems, solar collectors and electronic application (**Beilgen** [2009]).

Using air as a heat transfer media in these systems has some advantages compared with those requiring liquid. Freezing, boiling and corrosion problems are eliminated and the heated air can be used directly without the need for external fluid loop when using air as a working fluid. The major disadvantages of air systems when compared with liquid system arise from low heat transfer coefficient. There are three advantages of employing metal inserts inside ducts. First the porous metal material provides more contact area, so it conducts more heat. Second, the irregularly structure generates an irregular motion of the gas flow, thereby mixing the gas better. Third, as part of solar energy is transmitted through the metal inserts to increase the flowing air temperature, the rest excess energy is stored within the metal material.

Nowadays, a significant number of thermal engineering researchers are seeking for new enhancing heat transfer methods between surfaces and the surrounding gases .Forced convection heat transfer in porous media has many important applications, such as geothermal energy extraction, catalytic and chemical particle beds, petroleum processing, transpiration cooling, solid matrix heat exchangers and packed-bed regenerators.

An experimental investigation has been carried out by **Prasad et al.** [2009] on a packed bed solar air heater using wire mesh as packing material. Data pertaining to heat transfer and friction characteristics were collected for air flow rates ranging from 0.0159 to 0.0347 kg/s-m^2 for eight sets of matrices with varying geometrical parameters. It was found that an enhancement of the order of 76.9–89.5% can be obtained. **Aldabbagh et al.** [2011] investigated experimentally the thermal performances of single and double pass solar air heaters with steel wire mesh layers

are used instead of a flat absorber plate. The effects of mass flow rate of air on the outlet temperature and thermal efficiency were studied. The results indicate that the efficiency increases with increasing the mass flow rate. For the same flow rate, the efficiency of the double pass is found to be higher than the single pass by 34-45%.

The use of artificial roughness on a wall surface is an effective technique to enhance heat transfer to fluid flowing in ducts. The application of artificial roughness in the form of dimples on the heat transfer surface may be attractive roughness geometry as it does not require complicated manufacturing process, particularly if the dimple shape is a spherical indentation. Because of this characteristic, dimples do not add extra weight to the absorbing plate. **Hwang et al.**[2008] studied experimentally heat transfer characteristics on various dimple/protrusion patterned walls along with a straight and rectangular test channel. The dimple/protrusion arrays were positioned on top wall only (single-wall) or on both top and bottom walls (double-wall) in each test case. It was found that, for the dimple wall case, flow mixing was higher for the double-wall than the single-wall, which resulted in enhanced heat transfer. An experimental study was carried out by **Saini and Verma**[2008] to investigate the effect of roughness and operating parameters on heat transfer and friction factor in a roughened rectangular duct provided with dimple-shape roughness geometry. The results show that the maximum value of Nusselt number has been found corresponds to relative roughness height (e/D) of 0.0379. **Chang et al.**[2010] studied experimentally heat transfer and pressure drop in hexagonal ducts with smooth and dimpled surfaces .Nu and *f* correlations were individually obtained for each tested hexagonal duct using Re as the controlling parameter. **Durmus et al.** [2009] investigated experimentally the effects of surface geometries of three different type heat exchangers (flat plate, corrugated plate and Asterisk plate) on heat transfer and exergy loss. Results show that the heat gained from corrugated type is higher than that of the others.

The approach of utilizing simultaneously two different enhancement devices to gain better results compared to that by a single device is known as compound heat transfer enhancement (**Thianpong et al.**[2009]). **Pramanik and Saha** [2006] investigated the heat transfer and friction loss for flow of viscous oil through rectangular and square ducts with internal transverse rib turbulators on two opposite surfaces of the ducts and fitted with twisted tapes. The pressure drop and compound heat transfer characteristics of a converging–diverging tube with evenly spaced twisted tapes were considered by **Mengna et al.** [2007]. Their results showed that the heat transfer rates were 0.85 to 1.21 times of those in a plain tube. **Promvonge and Eiamsa** [2007] investigated the heat transfer characteristics in a tube with combined conical-ring turbulator and twisted tape. An experimental study of turbulent flow in a dimpled tube in conjunction with a twisted tape has been performed by **Thianpong et al.**[2009]. The experiments were performed using water as working fluid for Reynolds number in the range of 12000 to 44000.

The advantages of the compound heat transfer enhancement, shown in literature review, motivate us to investigate heat transfer enhancement inside MSW ducts. However, the survey of available published literature reveals a lack of information about the thermal-hydraulic behavior of dimpled or sinusoidal duct walls, together with the WI as compound enhancing device at the same time. Also, most of the previous investigations related to heat transfer enhancement have been done for flow of high Reynolds number. The range of Reynolds number investigated by them is not suitable for the airflow in solar air heater ducts **Saini and Verma**[2008].

To the best of the author's knowledge the heat transfer correlations for ducts of dimpled or sinusoidal walls that subjected to heat flux (in conjunction with the WI), has not been

investigated. Therefore, the main objectives of this work are to:

1. Investigate the combined effect of Wired Inserts (WI) together with different ducts surface profile (wavy, dimpled and flat) on heat transfer and flow friction .Both square and semi-circular ducts geometries shall be tested.
2. Develop a computational method to predict the thermal behavior of the (MSW) at any time. The method should be applicable for different duct geometries, inserts and surface profiles.
3. Investigate experimentally the developed laboratory scale ducts that are made locally. The duct is subjected to uniform heat flux to simulate the MSW using air as a working fluid.
4. Propose a developed method for evaluation of Nusselt number correlations for each new type of the MSW ducts.

2. Numerical Model

The numerical model proposed in this work consists of metal ducting that containing arbitrary shape wired inserts (WI), and is subjected to solar energy. The experimental results of **Dukhan and Chen** [2007] showed that the thermal boundary condition was neither uniform heat flux nor uniform wall temperature; a typical situation in solar collectors. So, the heated wall temperature was averaged and the heat transfer correlations were based on the uniform wall temperature boundary condition (**Dukhan and Chen** [2007]) .

The metal WI consists of irregularly-shaped flow passages. Convection and conduction heat transfer occurs between the metal ducting, solid WI and the flowing fluid. The geometric complexity and the random orientation of the solid material in the WI make exact solutions of the governing transport equations inside the pores virtually impossible (**Piao et al.** [1994]). Taking a volume element (dv) contained between (x) and (x + dx) over a time interval (dt) , three transient governing energy equations can be written for ducts with wire inserts (WI) , as shown in Figure (1).

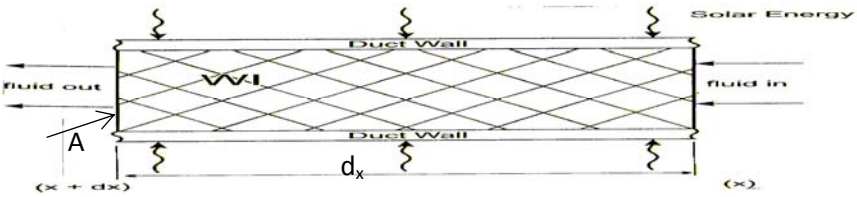

Figure (1): The control volume of the wired inserts duct.

The energy balance equation of the flowing fluid inside the control volume is;

Change of enthalpy of the flowing fluid with respect to time + Change of enthalpy of the flowing fluid with respect to axial position = net conduction heat transfer of the fluid inside the control volume + convection heat transfer between fluid and WI + convection heat transfer between fluid and duct walls

Therefore, the thermal equation describing the flowing fluid temperature is described by the following partial differential equation ;

$$\rho_a . A . dx . \varepsilon . C_a . \frac{\partial T_a}{\partial t} . dt + \rho_a . u_a A . C_a . \frac{\partial T_a}{\partial x} . dx . dt =$$

$$K_a . A . \frac{\partial^2 T_a}{\partial x^2} . dx . dt + h . dAc . (T_a - T_{WI}). dt + h_D . A_{SD} . (T_a - T_D). dt \quad .....(1)$$

For the wired inserts (WI) within the control volume, the energy balance is ;

Change of enthalpy of the WI with respect with time = convection heat transfer between fluid and WI

So, the following partial differential equation describes the transient thermal balance;

$$\rho_{WI} . A . dx .(1-\varepsilon). C_{WI} . \frac{\partial T_{WI}}{\partial t} . dt = h . dA_C .(T_{WI} - T_a). dt \quad \text{.....} \quad \text{.....}(2)$$

For the duct walls, the energy balance equation is ;

Change of enthalpy of the duct walls with respect with time = net conduction heat transfer of the duct walls + convection heat transfer between fluid and inside duct walls + convection heat transfer between ambient and outside duct walls

Therefore, the transient governing differential equation of the duct walls will be;

$$\rho_D . A_D . dx . C_D . \frac{\partial T_D}{\partial t} . dt = K_D . A_D . \frac{\partial^2 T_D}{\partial x^2} . dx . dt + h_D . A_{SD} .(T_D - T_a). dt + h_{SDo} . A_{SDo} .(T_{Do} - T_\infty). dt \text{.....}(3)$$

The coupled set of equations (1), (2), and (3) is approximated as a finite-difference equations to be ;

$$\rho_a . \varepsilon . C_a .[T_a(i,j,t+1) - T_a(i,j,t)/\Delta t] + \rho_a . u_a . C_a . \frac{Ta(i+1,j,t+1) - Ta(i-1,j,t+1)}{2(\Delta x)}$$

$$= K_a . \frac{Ta(i+1,j,t+1) - 2.Ta(i,j,t+1) + Ta(i-1,j,t+1)}{(\Delta x)^2} +$$

$$h . A_s .[T_a(i,j,t+1) - T_{WI}(i,j,t+1)] + h_D . A_{DV} .[T_a(i,j,t+1) - T_D(i,t+1)] \text{.....} \quad \text{..}(4)$$

$$\frac{T_{WI}(i,j,t+1) - T_{WI}(i,j,t)}{\Delta t} = [h . As / \rho_{WI} .(1-\varepsilon). C_{WI}].[T_{WI}(i,j,t+1) - T_a(i,j,t+1)] \text{.....} \quad \text{.....}(5)$$

$$\rho_D . C_D . \frac{T_D(i,t+1) - T_D(i,t)}{\Delta t} = K_D . \frac{T_D(i+1,t+1) - 2.T_D(i,t+1) + T_D(i-1,t+1)}{(\Delta x)^2}$$

$$+ h_D . A_{DD} .[T_D(i,m,t+1) - T_a(i,t+1)] + h_{Do} . A_{DD} .[T_{Do}(i,t+1) - T\infty(i,t+1)] \text{.....} \quad \text{.....}(6)$$

where; $A_{DV}=A_{SD} / A.d_x$, $A_S=dA_c / A.d_x$,
and $A_{DD}=A_{SD} / A_D.d_x$

The initial conditions involve assigning the initial temperatures of WI, air, and duct wall at each node. The formulation of the entrance plane boundary condition is done by assigning the inlet air temperatures. Since no further heat transfer after the air leaves the duct, the exit plane boundary condition is formulated by using backwards difference approximation for $\partial T/\partial x$.

The above equations are solved using a fully implicit scheme. The solution of the set of linear equations is accomplished with a decomposition and back-substitution algorithm for a banded matrix. The grid meshes and time steps sensitivity studies have been performed. The computational runs show that the algorithm was insensitive to spatial increment sizes. The coefficient matrix is updated after each iteration, with air properties and transport coefficients.

3. Experimental Setup

Figure (2) presents a schematic diagram of the experimental facility. Tests were carried out using a rig composed of three duct sections, joined together by flanges and screws. As shown in Fig. (2), a pair of ducting geometries were manufactured, one has a square cross-sectional dimensions of (6cm x 6cm) and the other of a semi-circular with diameter of (d=9.82 cm) .These ducts have been manufacturing from copper (CuZn37) (0.5 mm in thickness and 5.812 g/cm^3 in density) which have the following chemical

composition (tested at the engineering testing laboratories department in Specialized Institute for Eng. Industries):
37.76%Zn,0.008%Pb,0.026%Sn,0.006%P,0.0005 %Mn,0.037%Fe,0.004%Ni,0.001%Si,0.001%Cr, 0.01%Ag, 0.008%As, 0.01%Sb and Bal. cu%

For the purposes of comparison, three ducts have been constructed in the local workshops to have the same hydraulic diameter as shown in Figure (2).

For square duct; $d_h = 4(a.a)/ (4a)$ (7)

and for semi –circular duct ;

$d_h = 4(\pi d^2 / 8) / [(\pi d / 2) + d]$ (8)

A honeycomb rectifier installed at the entrance section, followed by three screens, 10 mm apart from one to another ,were employed in order to remove eddies and provide a more uniform velocity profile. However, the entrance duct has a length of 600mm, which is ten times the hydraulic diameter of all tunnels. Thus the first upstream duct removes any entrance effect before the flow reaches the heated test section.

Air drawn through the duct and exhausted by blower which operates by a single- phase, 0.8 kW electric motor. A photograph of the experimental apparatus is shown in Fig. (3).

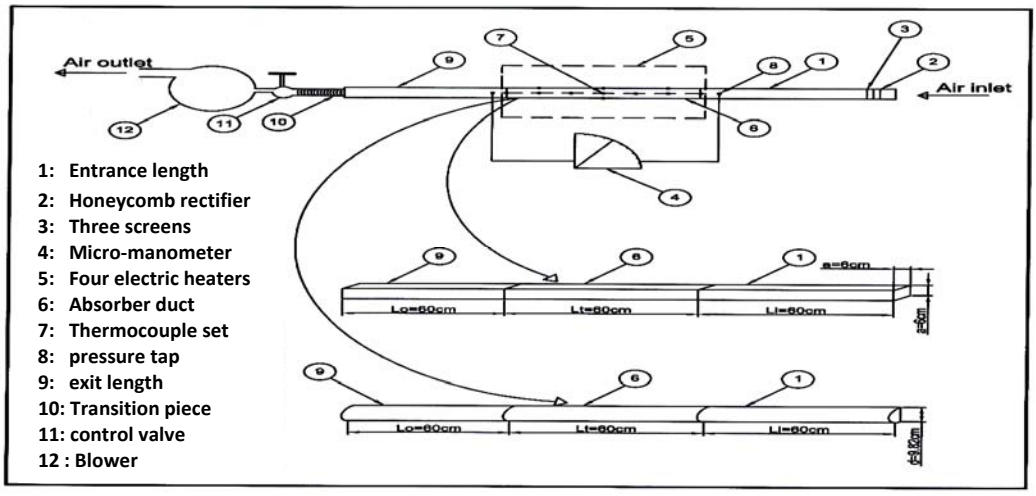

Figure (2) : The schematic layout of the experimental apparatus

Figure (3) : A photograph of the experimental apparatus.

For each shape of the cross-section geometry, three types of duct wall surface profile will be investigated. These types are; duct made from flat plate, duct made from sine-wave plate and duct made from dimpled plate. A schematic diagram of geometry of the duct walls is given in Figure (4) while the main dimensions of the ducts

are presented in Table (1). A total of six ducts sample will be tested as shown in Figure (5).

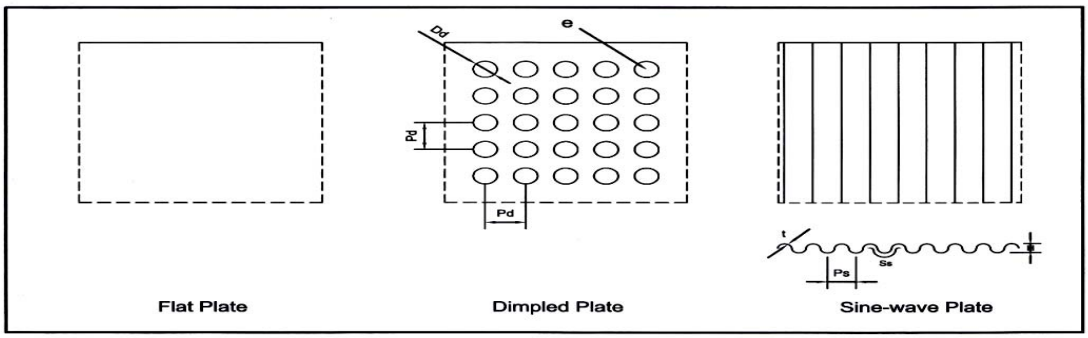

Figure (4): Surface profiles of the ducts wall

Table (1): Main dimensions of the ducts

Material of duct		(CuZn37)	
Duct thickness		0.5 mm	
Hydraulic diameter of ducts, (d_h)		6 cm	
Test section length, (Lt)		60 cm	
Semi-circular duct diameter, (d)		9.82 cm	
Side length of square duct,(a)		6 cm	
Dimpled duct		**Sine-wave duct**	
Dimpled pitch length, (Pd)	11 mm	pitch length, (Ps)	8.5 mm
Dimpled diameter, (Dd)	5.5 mm	Wave length, (Ss)	10 mm
Dimpled depth, (e)	2.3 mm	Amplitude, (H)	2.5 mm

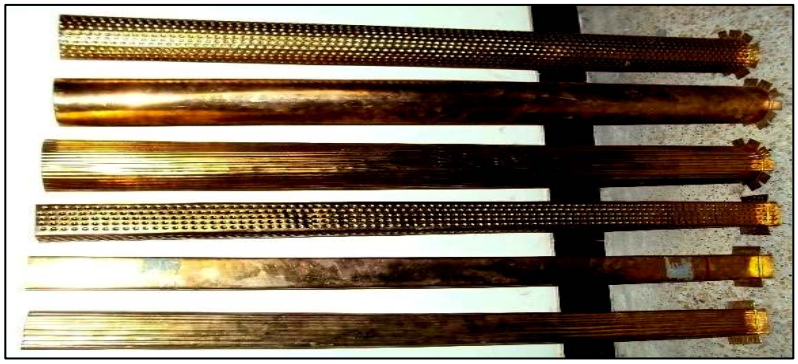

Figure (5): Types of ducts used in this work

The sinusoidally shaped duct walls were manufactured locally by bending. **Stasiek et al.** [1996] found that the most average value of pitch to amplitude ratio of wavy wall should be between (3) to (3.5) ,where this value gave a high heat transfer with lower pressure drop . Therefore, this ratio is kept constant at (3.4) throughout this work. The wire inserts (WI) are simple to manufacture and can be inserted inside these ducts to have a wide range of porosity. Also, it could be structured such that high thermal performance is maintained while fluid pressure drop is held at reasonable levels. Hence, the WI can be configured to have a wide ranging of porosity and a large specific surface area. Different voids and diameter of wires can be introduced, so that thermal properties can be tuned to a special application.

In this work, The wired inserts used for experiments were manufactured by cutting commercial copper wires that provided from the local market with a diameter (D_1=1.7mm) and a length(L_1=15m). These pieces were soldered

together to form the main frame for the WI as shown in Fig. (6-a). The spaces between the main frame were filled by using copper wire, with a diameter of (D_2=0.5 mm) and a length of (L_2=140 m) as shown in the Fig. (6-b).

- a - - b -

Figure (6): The square and semi-circular wired inserts

The WI samples fit hardly in the ducts test section to force the air to flow through the WI and allowing only a negligible flow between the WI and the duct walls. So, each wired inserts is inserted into the test section axially slowly, so the strip doesn't scratch the inner wall of the duct and get deformed .According to **ASTM C127** [2004], the porosity of the wired inserts have been found to be 0.92 for both square and semi-circular wired inserts.

For indoor testing, the collector duct is heated by a four flexible radiant electric heaters. These heaters produce uniform heat flux along the test section. Each heater provides 1000 watts maximum and placed in a semi-circular shield made of aluminum plate. The structures of heaters have been installed on the adjustable slots to allow freedom of movement of the heater and trends for the situation that gives the required temperature degrees for the duct surface as shown in Fig (7).

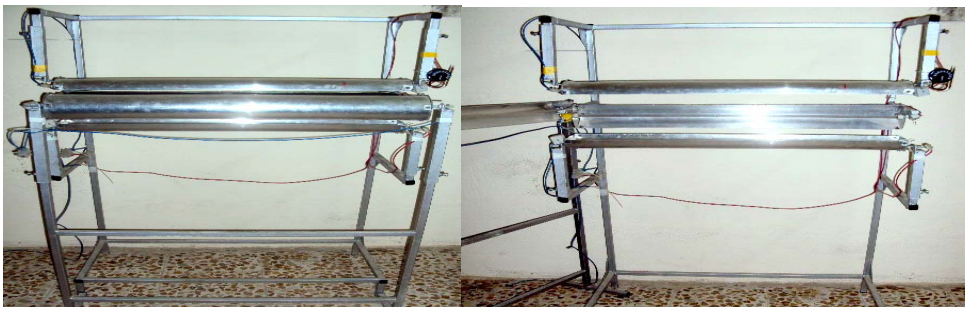

Figure (7): The Four heaters used in this work

Each one of the heaters was connected to a Solid State Relay (SSR) to adjust the magnitude of the heat flux. During the experiments, the angle and the distance between heaters and the heat transfer test section has been changed for imposing axially and circumferentially constant wall temperature boundary condition.

Thermocouples type K were used to measure the temperature. The thermocouples were calibrated within ±0.2°C deviation before being used .Four thermocouples were fixed on the sides of the duct surface to measure the temperature of the duct surface as shown in Fig.(8)

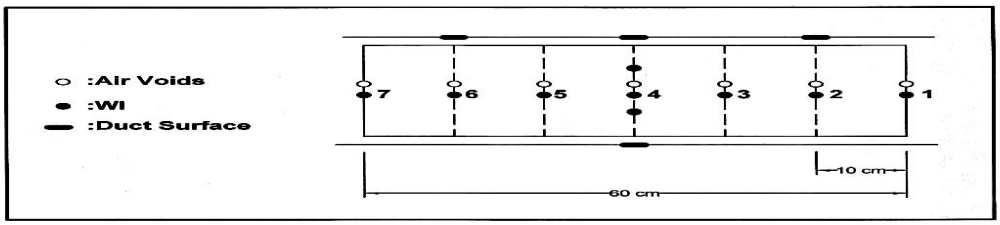

Figure (8): Positions of the thermocouples on the heated section.

The thermocouples were installed in an equally spaced distance to measure the temperatures at seven axial locations along the flow direction in the heater test section .Seven thermocouples instrumented in an equally spaced distance along the center line of the heated duct in the air voids between the WI; another seven thermocouple leads measured the WI temperatures. These thermocouples were glued directly on the WI surface. In addition, thermocouples are located in the WI surface at one-half the distance from the center line to the duct wall at x/L =0.5 .Another three thermocouples were used to measure the duct surface temperature profile at 1/6, 1/2 and 5/6of the test section length.

The pressure drop (Δp) across the wired inserts test section was measured by using adjustable slope micro-manometer. The friction factor was determined from pressure drop measurements in cold condition i.e. without heating the test section. This micro-manometer containing 0.784 specific gravity red fluid as a manometric liquid. This value of specific gravity ensures reasonable accurate measurement of the low pressure drop encountered at low Reynolds numbers.

The air velocities were measured by digital vane-type anemometer in different locations of the cross section .Five velocity reading were taken and the average of five reading was represented the velocity for each flow rate. A complete series of experiments consist of five Reynolds numbers ranging from the lowest possible flow at Reynolds number of 1825 to the largest possible flow at a Reynolds number of 7300 have been done.

All temperature measurements were taken at series of heated section types and Reynolds numbers. Before the measurements of each experimental run, the test rig was pressurized and any detected leak was carefully sealed .After the sources of leakage were treated from the ducting unit and heated test section, the test rig is ready for experimental runs. Tests were carried out for all the manufactured ducts with WI in the same rig. A constant heat input was supplied and the mass flow rate was adjusted so that the initial value of the Reynolds number was around 1825 .The temperatures of the air flow ,WI and duct surface along the heated section ,the mass flow rate of air as well as the pressure drop were continuously recorded .After collecting a set of data ,the mass flow rate of air was increased progressively until a maximum value of Re_{WI} ~7300 was reaches .This procedure was repeated for all six ducts under investigation.

For each duct type, all experiments were performed at least twice (on different days), to check the repeatability of the data, which was proved to be good. Because the data demonstrated repeatability, only results from one of the tests will be presented here. The uncertainties for important parameters and measurements made during the current research have been carried out on the basis of the method proposed by **Kline and McClintock** [1953]. The maximum uncertainties are ±2.27% for

Reynolds number, ±4.15% for Nusselt number and ±3.88% for friction factor.

4. Validity Test of Plain Duct

Prior to main experiments, the validity of the experimental set up was verified by conducting experiments for smooth duct. The convective heat transfer coefficient, h, was found by using the following equations;

$$Q^\circ = m^o .C.(Ta_{out} - Ta_{in}) \quad (9)$$

$$Q^\circ = h. A_C . (LMTD) \quad (10)$$

$$LMTD = [(T_D - Ta_{in}) - (T_D - Ta_{out})] / Ln [(T_D - Ta_{in}) / (T_D - Ta_{out})] \quad (11)$$

Hence, the values for Nusselt number were computed from; $Nu = h . d_h / k_a$ (12)

The experimental data were then compared with the results given by well known correlations under similar conditions. Figure(9,a and b) shows the comparison of the experimental values of Nusselt number and friction factor with those predicted by correlations proposed by **Gnielinski** [1976] for Nusselt number and by **Bhatti and Shah** [1987] for friction factor ;

$$Nu = 0.0214 (Re^{0.8} - 100)\{1 + (d_h/L)^{0.66} \} (T_b / T_D)^{0.45} Pr^{0.4} \quad \text{For } 2300 < Re < 10^6 \quad (13)$$

$$f = (1.0875 - 0.1125 H/W) fc \quad (14)$$, where fc =friction factor for the circular duct.

$$= 0.0054 + 2.3*10^{-8} Re^{1.5} \quad \text{for } 2300<Re<4000 \quad (15)$$

$$= 1.28*10^{-3} + 0.1143 Re^{-0.311} \quad \text{for } 4000<Re<10^7 \quad (16)$$

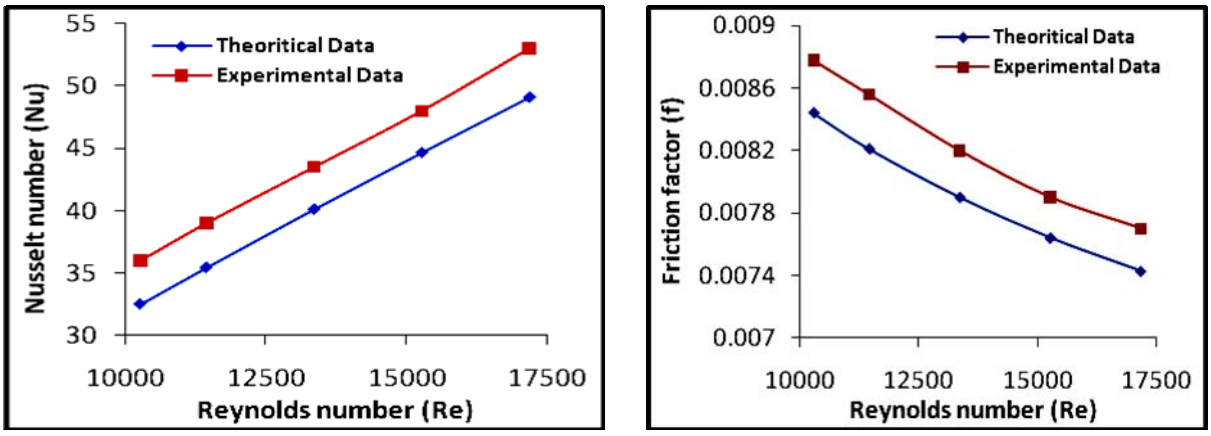

(a) (b)

Figure(9):Variation of Nusselt number and friction factor for square duct

The present plain duct data is found to be in good agreement with previous correlations from the open literature. The experimental values of Nusselt number have a maximum deviation of 9.86%, whereas the friction factor has a maximum deviation of 5.13%. This ensures the accuracy of the experimental data obtained from the present experimental setup.

5. Results

The results of the numerical computations were verified by the experimental tests. The exact conditions of the experiments performed were used in the numerical simulations, so that direct comparisons could be made. Typical results are shown in Figures (10) and (11) for the six different ducts under investigation.

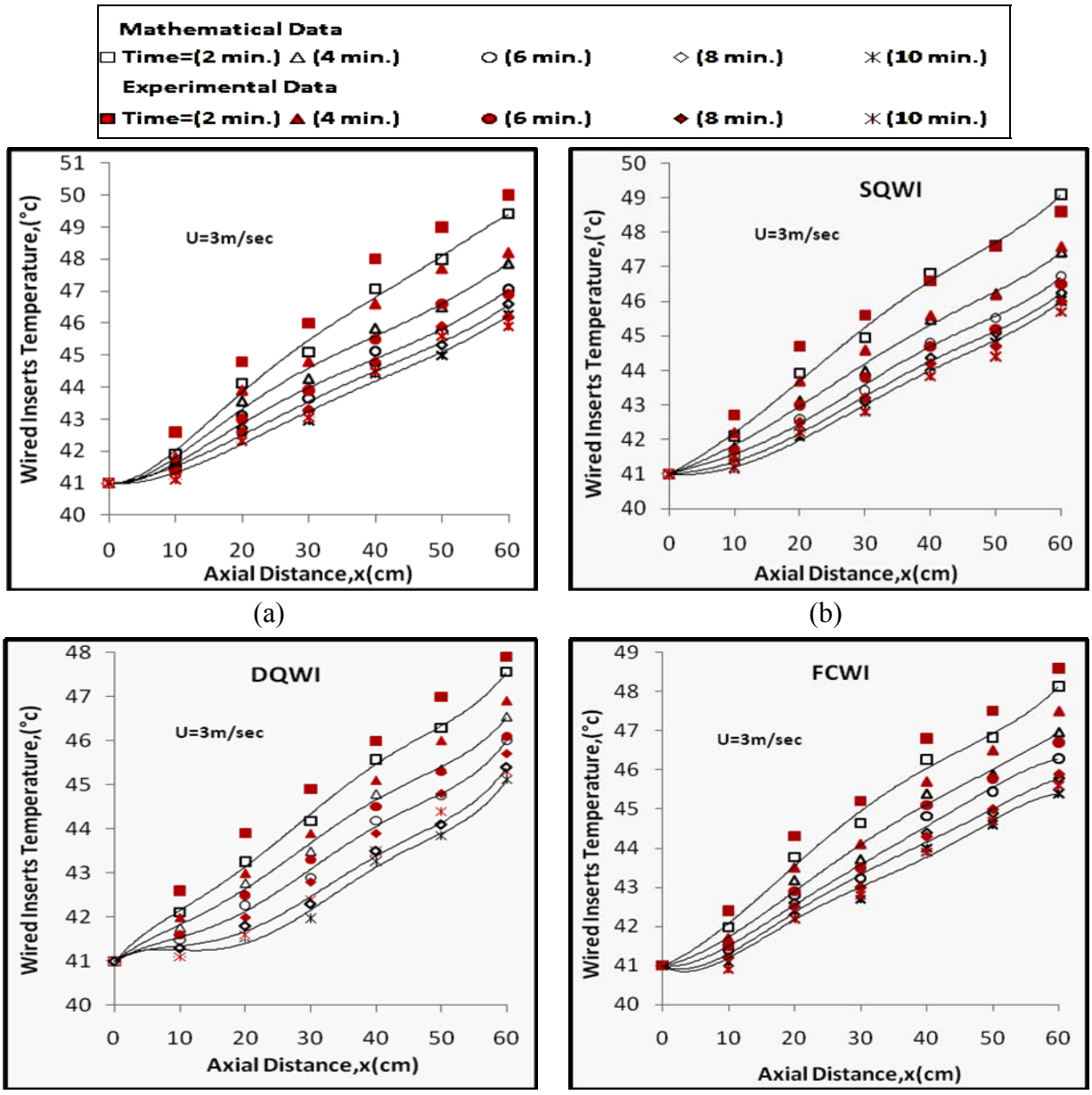

(a) (b) (c) (d)

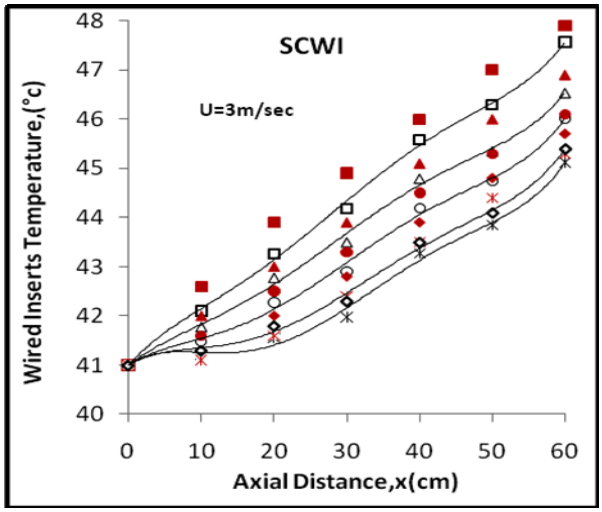

(e)

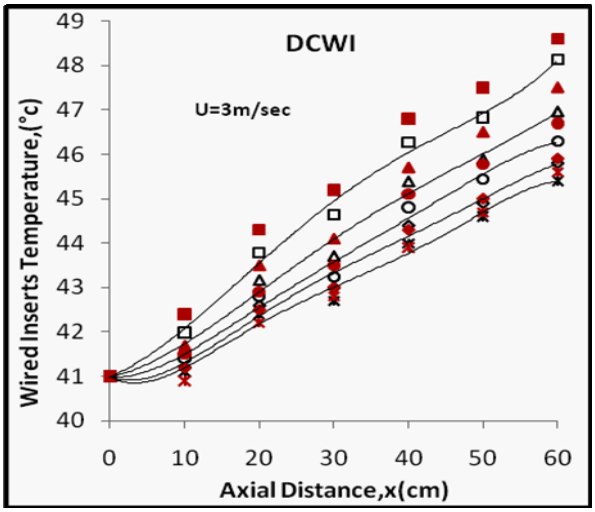

(f)

Figure (10): Comparison between experimental and numerical temperature distribution for WI at 3 m/sec air velocity.

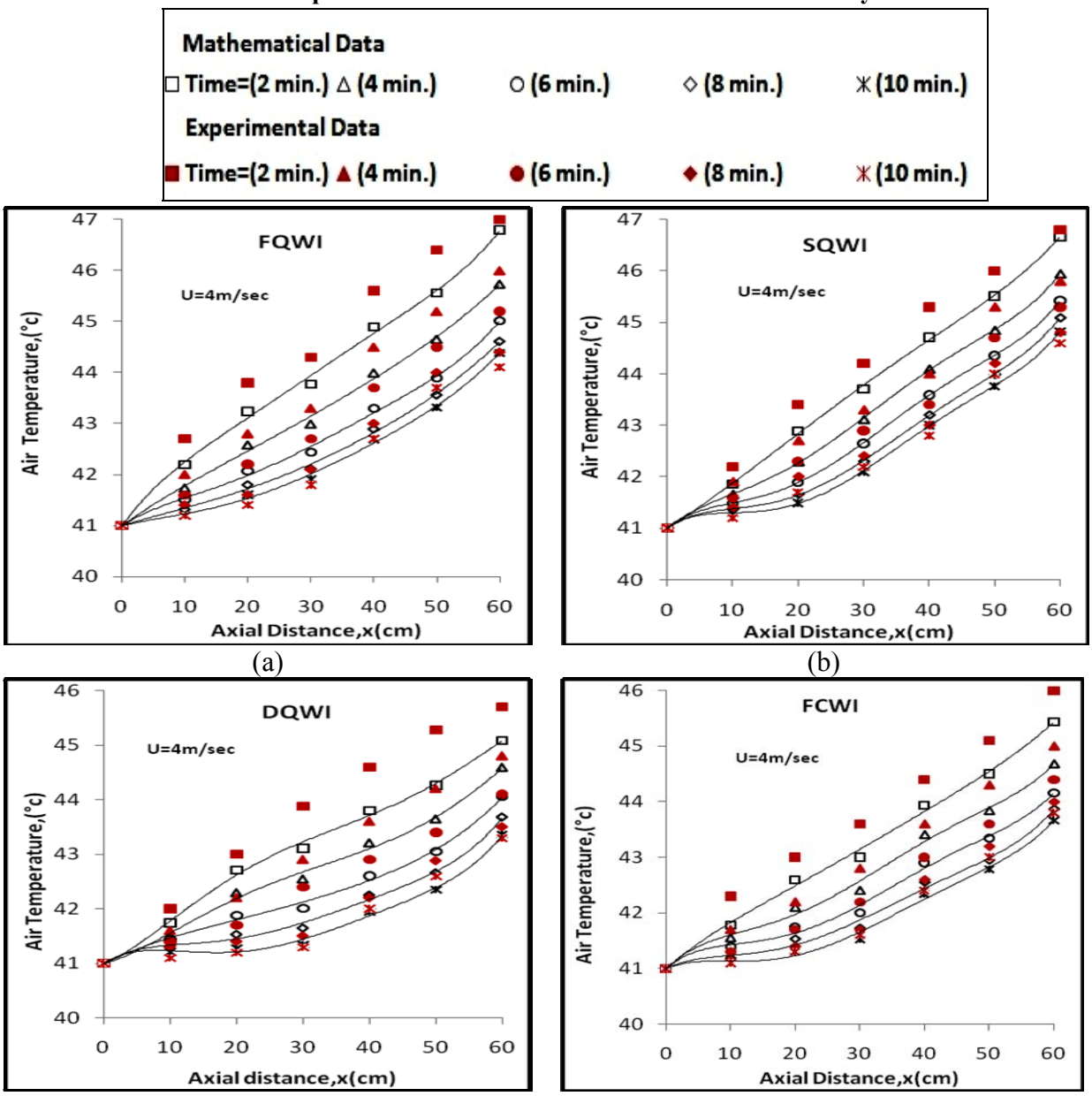

(a) (b)

(c) (d)

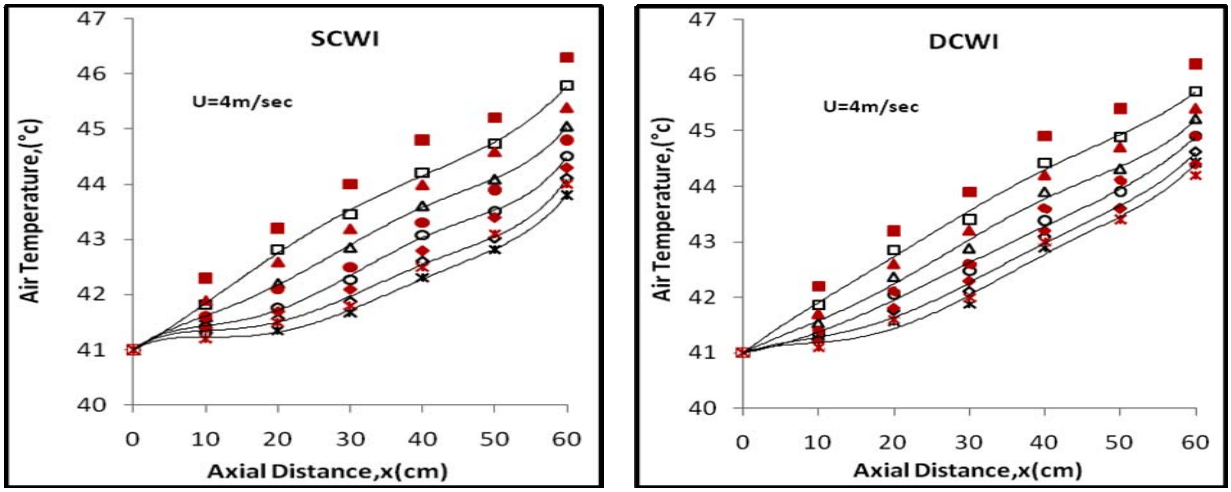

(e) (f)

Figure (11): Comparison between experimental and numerical temperature distribution for air at 4 m/sec air velocity.

The temperature profiles of both experiments and numerical simulations show that the results obtained from both these measurement techniques are in same general trends. In general, the agreements between mathematical and experimental results demonstrate that the computational scheme is adequately accurate to predict the transient thermal response of the MSW. It is clear from these figs. that both the air and WI (mathematical and experimental) temperature increases with the axial distance (x) of the test section but decreases with time of heating. Generally, the rate of increase in temperature is higher at the beginning than at the end of heating period because of the higher temperature difference existing at the beginning. The different response for each type of six ducts is clear in these Figures. The temperature fields of gases decrease in the direction of air flow through the heated section more rapidly for DQWI than FCWI and even FQWI.

Figure (12) shows the variation of the mathematical and experimental WI and air temperatures as a function of time at dimensionless distance (X/L=0.5) at the center point of the heated test section for various Re_{WI}. It is clear from these figs. that the temperature of air and WI (mathematical and experimental) decreases with time and decreases when the Reynolds number increase .This is an expected feature, as the air flow velocity is increased, the residence time is decreased, therefore, the exposure to heat transfer is decreased .With decreased exposure to the hot surface, the air will have a lower resulting temperature. The wired inserts temperature is higher than the air temperature at the same point because the WI specific heat capacity is higher than air .The theoretical result deviate from experimental data at the beginning of the heating period and then continuously decreased with progress of time.

Figure (13, a and b) shows the variation of outlet WI and air temperatures with Re_{WI} at time (t=10 min.). When the velocity is increased, an inefficient use of the unit for energy transfer has been determined, indicating the very important effect of the velocity. It is observed that modifying duct surface profile and duct cross-section geometry yields, appreciable temperature rise in the exit air. It's clear from these figures that the temperatures values for both the WI and air of flat, square duct with wired inserts are higher than the

other ducts. Therefore, by selecting the optimum type of ducting geometry and surface profile for the MSW, it is possible to increase the air outlet temperature with storing the excess energy in the WI at the same time.

The comparisons between experimental and numerical results in all above figures show that the predications produced by the present numerical model are reasonable for all ducts under investigation. However, it may be noted that there is a little difference between experimental and numerical data (the maximum difference is ± 5.72%) . This difference is believed to be mainly due to the effect of selected Nusselt number equations, as there is no such suitable equation available for each one of the ducts under investigation. Since the transient method can spend less time and money and give a more accurate measurement than the conventional steady-state method does, it is worth employing the transient method to measure the heat transfer coefficient in porous channels (**Jeng et al.** [2004]).

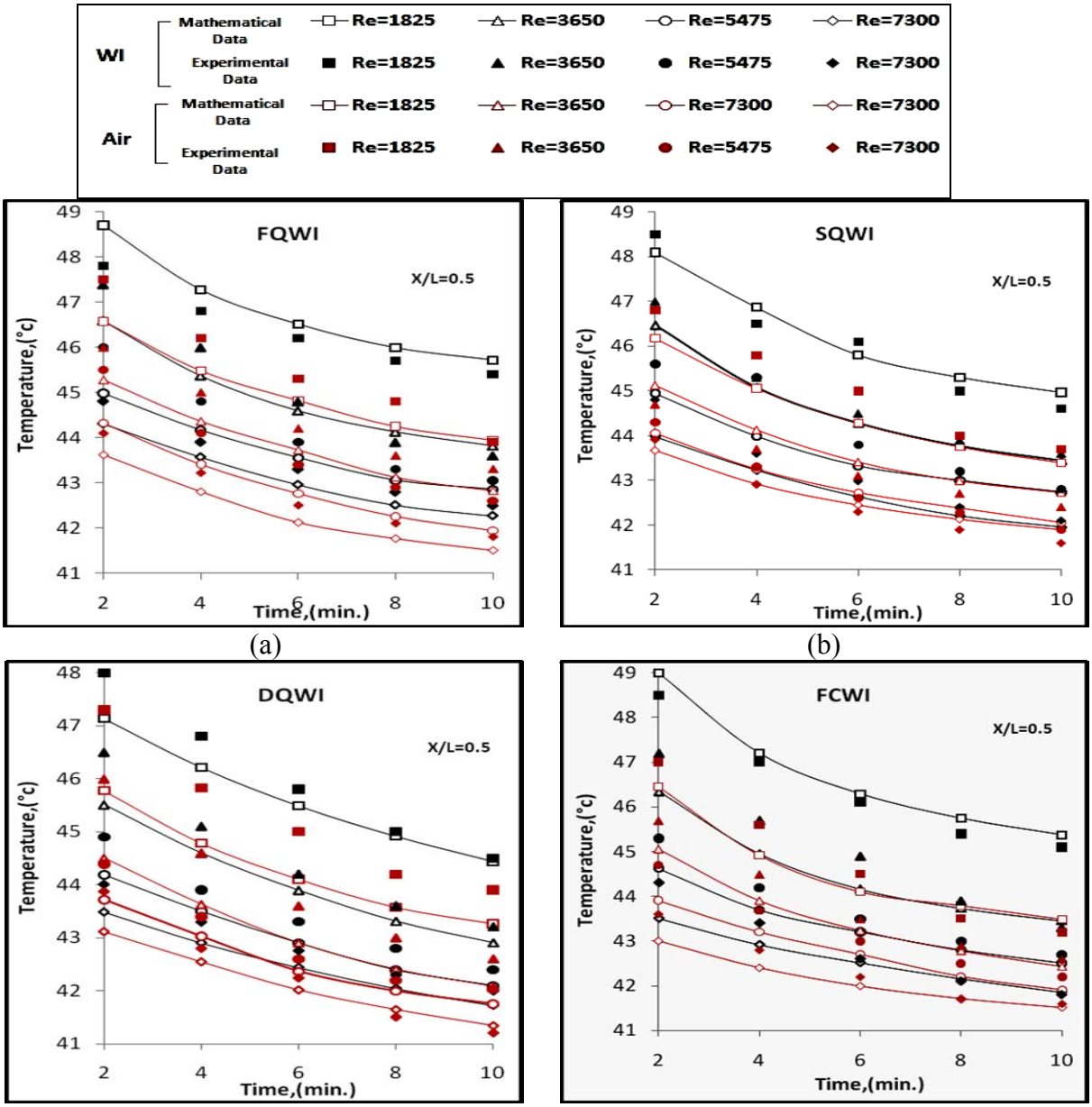

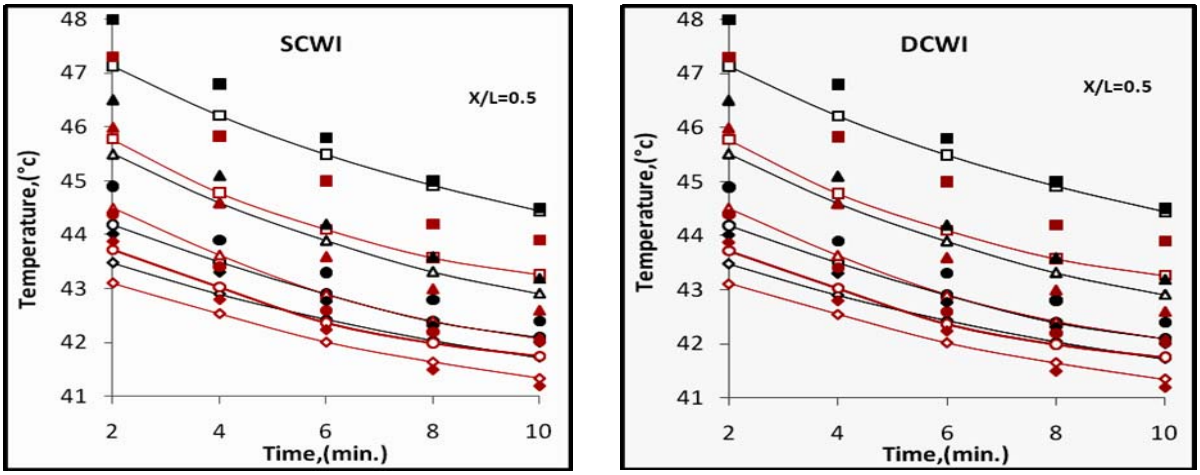

(e) (f)

Figure (12): Variation of WI and air temperature distribution with time at different Reynolds number.

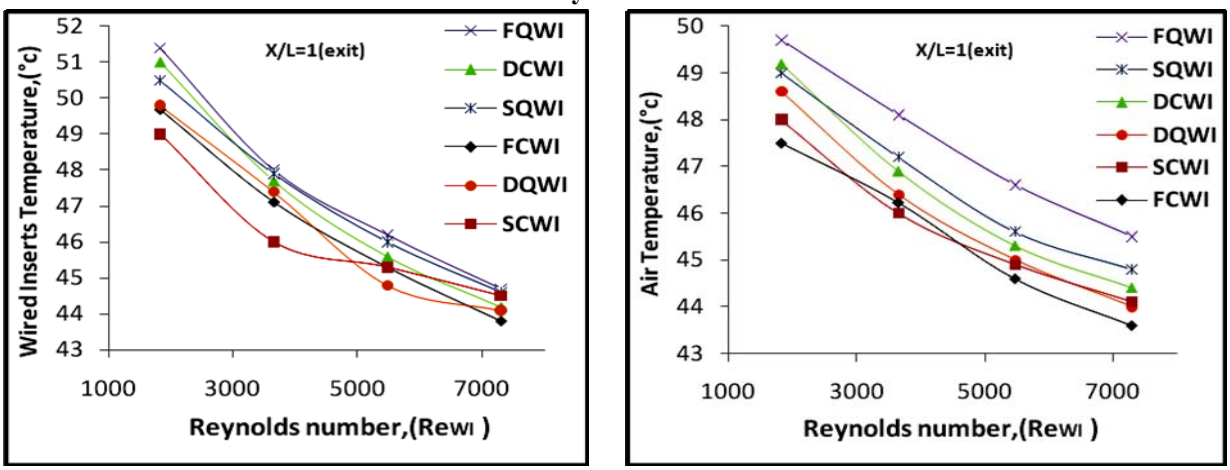

(a) (b)

Figure (13):Variation of outlet temperatures with Re_{WI} at time (t=10 min.).

Therefore, a Nusselt number correlation equation has been developed for each type of the ducts by selecting the value of the Nusselt number that causes the result of the numerical model to fit best the experimental data at each Reynolds number. All the data necessary to run the computer program are known, except for the expression of the Nusselt number. This method for the calculating the Nusselt number was used by **Coutier and Farber** [1981] to develop a new empirical equation for the volumetric heat transfer coefficient (= $h_* A_s$). Fig.(14) presents the Nusselt number for different types of ducts under investigation at various Reynolds numbers.

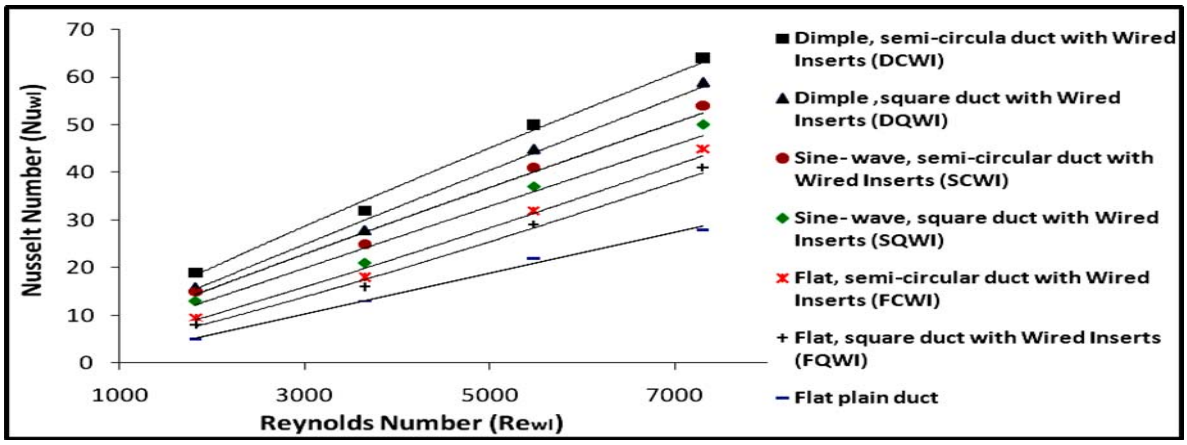

Figure (14): Effect of the duct geometry and WI on the Nusselt number

The results show that the Nusselt number (and therefore, the heat transfer coefficient) increases with increasing Reynolds number depending on the wired inserts Reynolds number (Re_{WI}). It's clear from Figure (14) that the Nusselt number of the dimpled ducts with a wired inserts are higher than all other ducts. It seems that the dimples generate strong vortices, which produce higher turbulence around the dimples and in the down stream area of the dimples, thus enhancing the heat transfer. From this Fig. it is noted that the Nusselt number for semi-circular dimpled duct is higher than square dimpled duct. Results reveal that the heat transfer rate from using both WI and dimpled or sinusoidal duct walls is higher than that from using WI alone. It is found that the Nusselt number in the DCWI is (44.2% -100%) greater than the values of the flat duct with WI. The results show that the improvement in Nusselt number for flat duct with WI is (1.4 - 2) times the values for flat duct with no WI.

The pressure drop importance is not only in selecting the fan but also in ensuring a uniform flow of air in the duct. Figures (15) and (16) show the influence of duct type on the friction factor and the pressure loss, respectively.

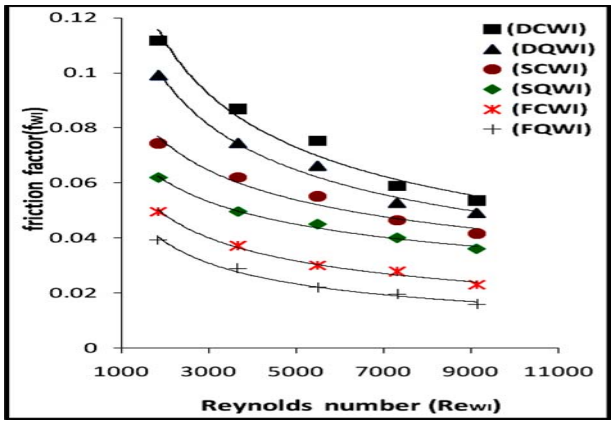

Figure (15): Variation of friction factor with Reynolds number.

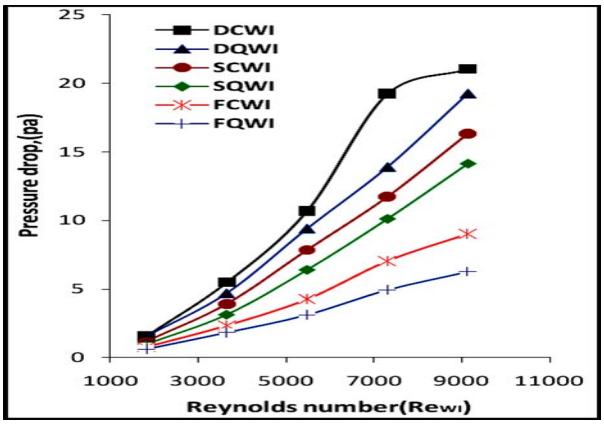

Figure (16): Variation of pressure drop with Reynolds number

The result show that the friction factor in the dimpled ducts combined with a WI are higher than other ducts because of the higher flow mixing effect for the dimpled duct that leading to greater turbulence intensity. It's shown from Figure (16) that the largest pressure drop occurs at duct yield the highest value of Nusselt number i.e. Dimpled, semi- circular duct with Wired Inserts DCWI. It is found that the pressure drop in the DCWI is (101.27% -127.8%) greater than the value of the duct with WI.

It would be useful for the practicing engineer if the results of Nusselt number and friction factor are presented as a function of the Reynolds number. By using the data predicted in Figures (14) and (15); six new correlations for Nusselt number and friction factor were developed to assess the real benefits in using the WI and the dimpled and sine – wave duct walls. The correlations are shown in Table (2).

Table (2): Predicted Nu_{WI} and f_{WI} correlations at 1825< Re_{WI}<7300.

Duct Geometry	Nu_{WI} correlation	R^2-value	f_{WI} correlation	R^2-value
DCWI	$Nu_{WI}=0.026\ Re_{WI}^{0.871}$	0.9934	$f_{WI}=3.659\ Re_{WI}^{-0.46}$	0.9711
DQWI	$Nu_{WI}=0.012\ Re_{WI}^{0.95}$	0.9935	$f_{WI}=2.766\ Re_{WI}^{-0.44}$	0.9816
SCWI	$Nu_{WI}=0.013\ Re_{WI}^{0.933}$	0.9875	$f_{WI}=1.112\ Re_{WI}^{-0.35}$	0.9651
SQWI	$Nu_{WI}=0.007\ Re_{WI}^{0.983}$	0.9755	$f_{WI}=0.729\ Re_{WI}^{-0.32}$	0.9901
FCWI	$Nu_{WI}=0.002\ Re_{WI}^{1.112}$	0.9905	$f_{WI}=1.586\ Re_{WI}^{-0.46}$	0.9863
FQWI	$Nu_{WI}=0.001\ Re_{WI}^{1.188}$	0.9929	$f_{WI}=2.464\ Re_{WI}^{-0.54}$	0.9868

As far as known, no study has determined the Nusselt number in duct filled across the entire cross-section with WI in conjunction with dimple-shape or sinusoidal-shape roughness geometry for the duct walls. Therefore, no comparison with other data can be provided.

One of the most important results for the purpose of this research is the compactness factor. The compactness factor is a ratio of the heat transfer to pressure drop. The definition of compactness factor is CF =j/f , where j is the Colburn factor and f is the friction factor. Figure (17) represents the thermo-hydraulic performance ratio as a function of the Reynolds number for all different ducts under investigation.

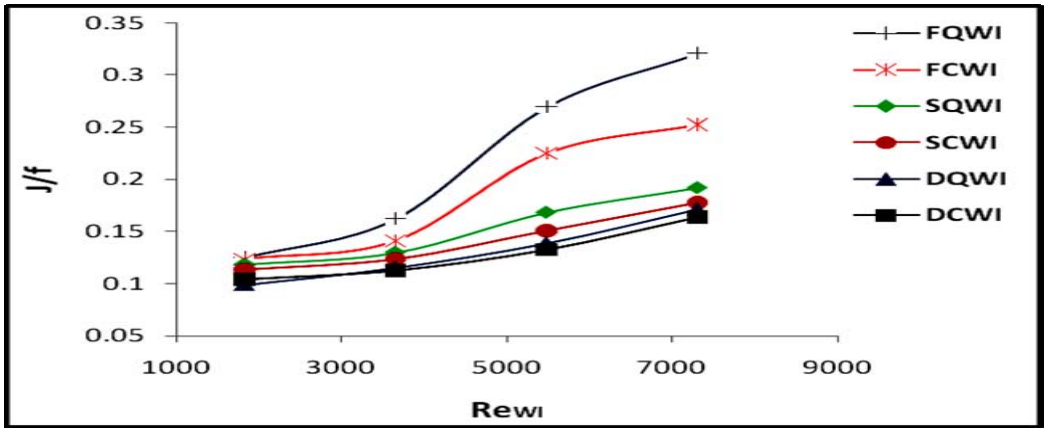

Figure (17): Variation of compactness factor with Reynolds number

It's clear from this figure that the [FQWI] shows the highest performance especially at high Reynolds numbers. Except for ducts with flat walls, all other types of ducts show very small dependence of compactness factor on the Reynolds number.

The enhancement efficiency of Roughened square and semi-circular duct walls (η_e) is defined as:

$$\eta e = \frac{Nu_R}{Nu_F} \qquad (17)$$

Figure (18) presents of η_e as a function of the Reynolds number for sine-wave and dimpled wired inserts ducts. It's clear from this figure that the enhancement efficiency tends to decrease with the rise of Reynolds number but variation is not the same for each type of the ducts roughness. The enhancement efficiency for sine-wave duct walls is nearly uniform at Reynolds number above 6000 and tends to reduce to unity .This indicates that the sinusoidal shaped duct walls is not feasible in terms of energy saving at higher Reynolds number. The results reveal that DCWI provides enhancement efficiency values higher than all other types of ducts.

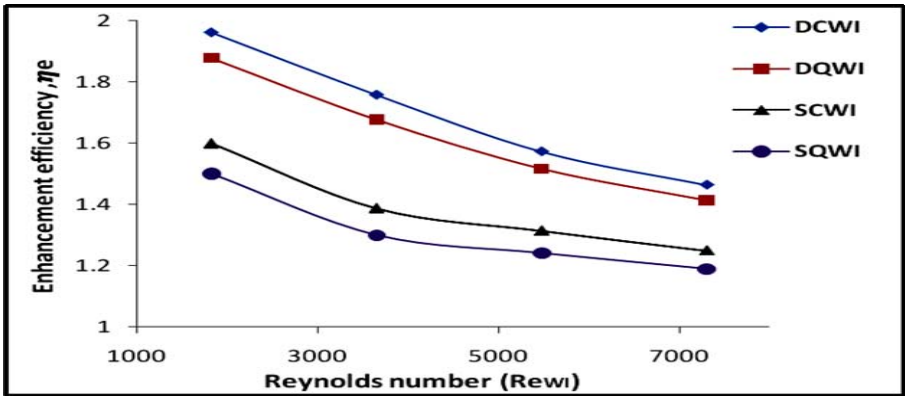

Figure (18): Variation of enhancement efficiency with Reynolds number

6. Conclusions:

Within the limitations of materials and experimental results obtained in this work, the main conclusions may be summarized as follows**:**

1- The two-dimensional numerical approach is generally found to be agreeing reasonably with the experimented results obtained in this work (the maximum deviation is found to be ± 5.72%). These agreements demonstrate that the computational scheme is adequately accurate to predict the transient behavior of the MSW ducts.

2- Six new correlation equations for the Nusselt number were devised for each type of ducts under investigation. The developed transient technique for determining the Nusselt number correlation was the best match between the measured experimental data and the one calculated by the numerical model. As far as known, no Nusselt number correlations in the open literatures for the same geometric design of the ducts under investigation.

3- It is found that the FQWI has the highest exit air temperature.

4- The results show that the Nusselt number for semi-circular duct is higher than that of square duct. The Nusselt number of DCWI was found to be (44.2% - 100%) greater than the values of flat duct with WI. The improvement in Nusselt number for flat duct with WI is found to be (1.4 – 2) times the value of flat duct with no WI.

5- The DCWI duct is found to be the most effective for heat transfer enhancement, but also to have the greatest pressure drop increase. The results show that the pressure drop in the DCWI is (101.27% - 172.8%) greater than the value of flat duct with WI.

6- Six design correlation equations for predicting the MSW ducts friction factors have been developed. It was found that the FQWI duct has the lowest friction factor.

7- The enhancement efficiency of the roughened walls tends to decrease with rise of Reynolds number, but the variation is not the same for each type of the ducts. It is found that the DCWI provides enhancement efficiency values higher than other types of ducts. Results indicate that the sinusoidal duct walls are not feasible in terms of energy saving at high Reynolds number.

8- The results of the compactness factor show different response. It is found that the FQWI has the highest performance especially at high Reynolds numbers. Except for ducts with flat walls, all other types of ducts show very small

dependence of compactness factor on the Reynolds number.

Although the present study was related to MSW ducts, the results were of more general interest for any investigation related to compound metallic inserts for enhancing heat transfer.

References :

* Aldabbagh a, L.B.Y. Egelioglu a,F. and Ilkan b,M., **"Single and Double Pass Solar Air Heaters with Wire Mesh as Packing Bed"** , Energy ,Vol.36, May 2011.

* Annual Book of ASTM Standards, Vol.04 02 , section E-11, 2004.

* Bhatti, M.S., R.K. Shah, **"Turbulent and Transitional Flow Convective Heat Transfer"**, Hand book of Single-phase Convection Heat Transfer, John Wiley, NY, 1987.

* Bilgen ,E., **"Conjugate Heat Transfer by Conduction and Natural Convection on a heated Vertical Walls"** ,Applied Thermal Engineering ,Vol.29, 2009.

* Chang,S.W., K.F. Chiang, T.C. Chou, **"Heat Transfer and Pressure Drop in Hexagonal Ducts with Surface Dimples"**, Exp. Thermal and Fluid Science, Vol. 34, 2010.

* Coutier, J.P. and E.A. Farber, **"Designing Rock Beds as Storage Units for Solar Air Systems Using an Optimized Method Based on Numerical Model"**, Proceeding of I.S.E.S. Congress, Brighton, England, Aug.1981.

* Dukhan, N. and Kuan-Chih Chen, **" Heat Transfer Measurements in Metal Foam Subjected to Constant Heat Flux"**, Exp. Thermal and Fluid Science, Vol. 32, 2007.

* Durmus ,A., H.Benli , I.Kurtbas and H.Gul , **"Investigation of Heat Transfer and Pressure Drop in plate Heat Exchangers Having Different Surface Profiles "** , Int. J. of Heat and Mass Transfer ,Vol.52, 2009.

* Gnielinski,**V., "New Equation for Heat and Mass Transfer in Turbulent Heat Channel Flow"**, Int. J. Chem. Eng., Vol.16(2), 1976.

* Jeng, T.M., M.P. Wang, G.J. Hwang and Y.H. Hung, **"A New Semi-empirical Model for Predicting Heat Transfer Characteristics in Porous Channels",** Experimental Thermal and Fluid Science, Vol.29, 2004.

* Kline, S. J. and F.A. McClintock, **"Describing uncertainties in single sample experiments",** Mech. Eng., Vol. 75, 1953.

* Mengna, H., D. Xianhe, H. Kuo and L. Zhiwu, **"Compound Heat Transfer Enhancement of a Converging–diverging Tube with Evenly Spaced Twisted-tapes"**, Chinese Journal of Chemical Eng., Vol.15, 2007.

* Piao,Y, E.G .Hauptmann, and M.Iqbal, **"Forced Convection Heat Transfer in cross-corrugated Solar Air Heaters"**, J. of Solar Energy Eng., Tr. of ASME , Vol. 116, 1994.

* Pramanik, D. and S. K. Saha, **"Thermo-hydraulics of Laminar Flow Through Rectangular and Square Ducts with Transverse Ribs and Twisted Tapes"**, J. of Heat Transfer, Tr. of ASME, Vol. 128, 2006.

* Prasad, S.B., J.S. Saini, Krishna M. Singh, "**Characteristics of Packed Bed Solar Air Heater Using Wire Mesh Investigation of Heat Transfer and Friction as Packing Material"**, Solar Energy, Vol. 83, 2009.

* Promvonge, P., and S. Eiamsa, **"Heat Transfer Behaviors in a Tube with**

Combined Conical-ring and Twisted-tape Insert", Int.Com. in Heat and Mass Tr.,Vol.34, 2007.

* Saini, R.P. and J. Verma, **"Heat Transfer and Friction Factor Correlations for a Duct Having Dimple-Shape Artificial Roughness for Solar Air Heaters**", Energy, Vol. 33, 2008.

* Sang Dong Hwang, Hyun Goo Kwon and Hyung Hee Cho, **"Heat Transfer with Dimple/Protrusion Arrays in a Rectangular Duct with a Low Reynolds number range"**, Int. J. of Heat and Fluid Flow, Vol. 29, 2008.

* Stasiek,J.,M.collins, M.Ciofalo,and P.Chew ,**"Investigation of Flow and Heat Transfer in Corrugated Passages"** , Int. J. Heat Mass Transfer, Vol.39, 1996.

* Thianpong, C., P. Eiamsa, K. Wongcharee and S. Eiamsa, **"Compound Heat Transfer Enhancement of a Dimpled Tube with a Twisted Tape Swirl Generator"**, Int. Com. in Heat and Mass Transfer, Vol. 36, 2009.

Nomenclatures:

A	: Cross–sectional area of the duct, (m^2)
As	: Surface area per unit volume, (1/m)
C	: Specific heat, (J/kg.K)
CF	: Compactness Factor
d_h	: Hydraulic diameter of ducts, (m)
D_h	: Hydraulic diameter of Wired Inserts, (m)
f	: Friction factor
h	: Area heat transfer coefficient, ($W/m^2.K$)
H/W	: Height to width ratio
J	: Colburn factor = $St.Pr^{2/3}$
K	: Thermal conductivity, (W/m. K)
L	: Length , (m)
$\overset{o}{m}$	:Mass flow rate , (kg/s)
Nu	:Nusselt number
p	: Pressure, (kPa)
Pr	: Prandtle number
$\dot{Q}$	: Rate of heat transfer , (W)
Re	: Reynolds number
t	: Time , (s)
T	: Temperature (^oC)
u	: Flow velocity, (m/s)
x	: Axial distance ,(m)

Subscripts:

a	: air
b	: bulk
c	: contact
D	:duct wall
F	: flat wall
o	: outside
R	: roughened
SD	: surface area

Abbreviations:

ASTM	: American Society for Testing and Materials
DCWI	:Dimpled, semi-circular duct with Wired Inserts
DQWI	: Dimpled, square duct with Wired Inserts
FCWI	: Flat, semi-circular duct with Wired Inserts
FQWI	: Flat, square duct with Wired Inserts
LMTD	: Log. Mean Temperature Difference
MSW	: Metal Solar Wall
SCWI	: Sine-wave, semi-circular duct with Wired Insert
SQWI	: Sine -wave, square duct with Wired Inserts

Greek Letters:

ε	:Void fraction
ρ	: Density
η_e	: efficiency

TOTAL AND MATRIC SUCTION MEASUREMENT OF UNSATURATED SOILS IN BAGHDAD REGION BY FILTER PAPER METHOD

Mohammed Y. Fattah[1] Asma Y. Yahya[2] Balqees A. Ahmed [2]

1) **Building and Construction Engineering Dept., University of Technoilogy, Baghdad, Iraq.**
2) **Civil Engineering Dept., College of Engineering, University of Baghdad, Iraq.**

ABSTACT

Soil suction is one of the most important parameters describing the moisture condition of unsaturated soils. The measurement of soil suction is crucial for applying the theories of the engineering behavior of unsaturated soils. The filter paper method is one of the soil suction measurement techniques

In this paper, five soil samples were collected from five sites within Baghdad city – al-Rasafa region. These soils have different properties and they were prepared at different degrees of saturation. For each sample, the total and matric suction were measured by the filter paper method at different degrees of saturation. Then correlations were made between the soil properties and the total and matric suction.

It was concluded that the suction increases with decrease of the degree of saturation. The relationships between the total and matric suction and the filter paper water content are approximately linear and indicate decrease of suction with increase of the filter paper water content. The total and matric suction increase with the decrease of the soil shear strength.

الخلاصة:

ان مص التربة هي واحدة من اهم المعاملات المستخدمة لوصف المحتوى المائي للترب الغير مشبعة. ان قياس المص للتربة مهم لتطبيق نظريات التصرف الهندسي للترب الغير مشبعة. ان طريقة ورق الترشيح هي تقنية لقياس المص للتربة.

في هذا البحث، تم جمع خمس نماذج لخمس مواقع في مدينة بغداد- في منطقة الرصافة. هذه الترب لها خواص مختلفة وقد تم تحضيرها بدرجات تشبع مختلفة . لكل نموذج تم قياس السحب الكلي (total suction) و (matric suction) بدرجات تشبع مختلفة. تم الحصول على علاقات تربط خواص التربة مع السحب للتربة (total and matric suction).

لقد تم استنتاج ان السحب يزداد بنقصان درجة التشبع. ان العلاقة بين السحب (total and matric suction) والمحتوى المائي لورق الترشيح تقريبا علاقة خطية وتشير الى نقصان السحب بزيادة المحتوى المائي لورق الترشيح. ان السحب يزداد عند نقصان مقاومة القص للتربة.

KEYWORDS: Total suction, matric suction, filter paper, unsaturated soil.

INTRODUCTION

The filter paper method is an inexpensive and relatively simple laboratory test method, at which both total and matric suction measurements are possible. With a reliable soil suction measurement technique, the initial and final soil suction profiles can be obtained from samples taken at convenient depth intervals. The change in suction with seasonal moisture movement is important information for many engineering applications.

This paper evaluates both the total and matric suctions for samples taken from five sites in Baghdad city within al-Rasafa region. These soils have different properties and they were prepared at different degrees of saturation. The aim of this paper is to determine relationships between the total and matric suctions and soil properties like, degree of saturation, liquid limit, plasticity index and unconfined compressive strength.

A BRIEF HISTORICAL BACKGROUND

There are many techniques and instruments to measure soil suction in the fields of soil science and engineering. Most limitations with regard to the range of measured suction, equilibration times, and cost. Therefore, there is a need for a method which can cover the practical suction range, and could be adopted as a basis for routine testing, and is inexpensive. One of those soil suction measurement techniques is the filter paper method, which was evolved in Europe in the 1920s and came to the United States in 1937 with Gardner (1937). Since then, the filter paper method has been used and investigated by numerous researchers (Fawcett and Collis-George 1967; McQueen and Miller 1968; Al-Khafaf and Hanks 1974; McKeen 1980; Hamblin 1981; Chandler and Guierrez 1986; Houston et al. 1994; Swarbrick 1995), who have tackled different aspects of the filter paper method.

SOIL SUCTION CONCEPT

Many engineering-related problems are associated with partially saturated soils where the void spaces between particles are partly filled with air and partly with water. This leads to negative pore water pressures (or suctions), which greatly influences the controlling stress regime. The accurate measurement and interpretation of soil suction is thus vital to understanding the behaviour of unsaturated soils. However, magnitudes of suction can vary enormously (between 0 and 1 GPa) and the instruments and measurement techniques are usable over only specific suction ranges. (Murray and Sivakumar, 2010).

In general, porous materials have a fundamental ability to attract and retain water. The existence of this fundamental property in soils is described in engineering terms as suction, negative stress in the pore water. In engineering practice, soil suction is composed of two components: matric and osmotic suction (Fredlund and Rahardjo 1993). The sum of matric and osmotic suction is called total suction. Matric suction comes from the capillarity, texture, and surface adsorptive forces of the soil. Osmotic suction arises from the dissolved salts contained in the soil water. This relationship can be formed in an equation as follows:

$$h_t + h_m + h_\pi \qquad (1)$$

where h_t = total suction (kPa),
h_m = matric suction (kPa), and
h_π = osmotic suction (kPa).

Total suction can be calculated using Kelvin's equation, which is derived from the ideal gas law using the principles of thermodynamics and is given as (Fredlund and Rahardjo,1993:

$$h_t = \frac{RT}{V} \ln\left(\frac{P}{P_o}\right) \qquad (2)$$

where h_t = total suction,
R = universal gas constant,
T = absolute temperature,
V = molecular volume of water,
P / P_o = relative humidity,
P = partial pressure of pore water vapor, and
P_o = saturation pressure of water vapor over a flat surface of pure water at the same temperature.

If Eq. (2) is evaluated at a reference temperature of 25°C, the following total suction and relative humidity relationship can be obtained.

$$h_t = 137182 . \ln(P / P_o) \qquad (3)$$

THE FILTER PAPER METHOD

The filter paper method has long been used in soil science and engineering practice and it has recently been accepted as an adaptable test method for soil suction measurements because of its advantages over other suction measurement devices. Basically, the filter paper comes to equilibrium with the soil either through vapor (total suction measurement) or liquid (matric suction measurement) flow. At equilibrium, the suction value of the filter paper and the soil will be equal. After equilibrium is established between the filter paper and the soil, the water content of
the filter paper disc is measured. Then, by using a filter paper water content versus suction calibration curve, the corresponding suction value is found from the curve.

This is the basic approach suggested by ASTM Standard Test Method for Measurement of Soil Potential (Suction) Using Filter Paper (ASTM D 5298). In other words, ASTM D 5298 employs a single calibration curve that has been used to infer both total and matric suction measurements. The ASTM D 5298 calibration curve is a combination of both wetting and drying curves.

SOIL TOTAL SUCTION MEASUREMENTS

Glass jars that are between 250 to 500 ml volume size are readily available and can be easily adopted for suction measurements. Glass jars, especially, with 3.5 to 4 inch (8.89 to 10.16 cm) diameter can easily contain the 3 inch (7.62 cm) diameter Shelby tube samples. A testing procedure for total suction measurements using filter papers can be outlined as will be described in the following sections.

EXPERIMENTAL PROGRAM

In this work, five soil samples were collected from five sites within Baghdad city – al-Rasafa region at depth equal to 3.5 m below the ground surface. The water table was 1.2 m below the ground surface. The samples were subjected to testing program which included the following tests:

1. Grain size distribution by sieve analysis and hydrometer.
2. Specific gravity.
3. Atterbegr limits; liquid and plastic limit.
4. Unconfined compression test.

All these tests were carried out according to the American Society for Testing and Materials standards. A summary of the index properties of these soils is shown in **Table 1**.

Table 1: Index properties of the soils.

Site	Liquid Limit LL (%)	Plastic Limit PL (%)	Plasticity Index PI (%)	Specific Gravity Gs	% Clay
Rasafa 1	34	19	15	2.74	66.5
Rasafa 2	45	27	18	2.76	68.3
Rasafa 3	54	27	27	2.78	80.3
Rasafa 4	64	25	39	2.79	82.3
Rasafa 5	73	29	44	2.80	85.3

The grain size distribution of the five samples is shown in **Fig. 1**. The figure shows that all these soils are classified as silty clays.

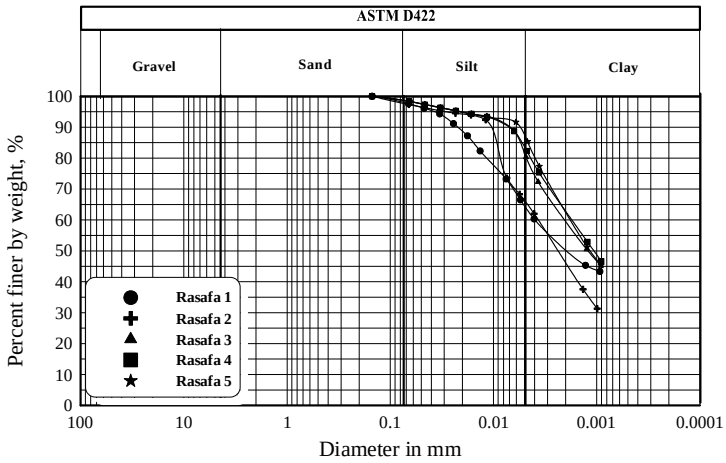

Fig. 1: Grain size distribution.

EXPERIMENTAL PROCEDURE

1. At least 75 percent by volume of a glass jar is filled up with the soil; the smaller the empty space remaining in the glass jar, the smaller the time period that the filter paper and the soil system requires to come to equilibrium.
2. A ring type support, which has a diameter smaller than filter paper diameter and about 1 to 2 cm in height, is put on top of the soil to provide a non-contact system between the filter paper and the

soil. Care must be taken when selecting the support material; materials that can corrode should be avoided, plastic or glass type materials are much better for this job.

3. Two filter papers one on top of the other are inserted on the ring using tweezers. The filter papers should not touch the soil, the inside wall of the jar, and underneath the lid in any way.
4. Then, the glass jar lid is sealed very tightly with plastic tape.
5. Steps 1, 2, 3, and 4 are repeated for every soil sample.
6. After that, the glass jars are put into the ice-chests in a controlled temperature room for equilibrium.

These steps are documented in photographs 1 to 9.

Researchers suggest a minimum equilibrating period of one week (ASTM D 5298, Houston et al. 1994, Lee 1991). After the equilibration time, the procedure for the filter paper water content measurements can be as follows (Bulut et al., 2001):

1. Before removing the glass jar containers from the temperature room, all aluminum cans that are used for moisture content measurements are weighed to the nearest 0.0001 g. accuracy and recorded.
2. After that, all measurements are carried out by two persons. For example, while one person is opening the sealed glass jar, the other is putting the filter paper into the aluminum can very quickly (i.e., in a few seconds) using tweezers.
3. Then, the weights of each can with wet filter paper inside are taken very quickly.
4. Steps 2 and 3 are followed for every glass jar. Then, all cans are put into the oven with the lids half-open to allow evaporation. All filter papers are kept at 105 $\pm 5^{o}$C temperature inside the oven for at least 10 hours.
5. Before taking measurements on the dried filter papers, the cans are closed with their lids and allowed to equilibrate for about 5 minutes. Then, a can is removed from the oven and put on an aluminum block (i.e., heat sinker) for about 20 seconds to cool down; the aluminum block functions as a heat sink and expedites the cooling of the can. After that, the can with the dry filter paper inside is weighed very quickly. The dry filter paper is taken from the can and the cooled can is weighed again in a few seconds.
6. Step 5 is repeated for every can.

SOIL MATRIC SUCTION MEASUREMENTS

Soil matric suction measurements are similar to the total suction measurements except instead of inserting filter papers in a non-contact manner with the soil for total suction testing, a good intimate contact should be provided between the filter paper and the soil for matric suction measurements. Both matric and total suction measurements can be performed on the same soil sample in a glass jar as shown in **Fig. 2**. A testing procedure for matric suction measurements using filter papers can be outlined as follows:

1. A filter paper is sandwiched between two larger size protective filter papers. The filter papers used in suction measurements are 5.5 cm in diameter, so either a filter paper is cut to a smaller diameter and sandwiched between two 5.5 cm papers or bigger diameter (bigger than 5.5 cm) filter papers are used as protectives.
2. Then, these sandwiched filter papers are inserted into the soil sample in a very good contact manner (i.e., as in Figure 2). An intimate contact between the filter paper and the soil is very important.
3. After that, the soil sample with embedded filter papers is put into the glass jar container. The glass container is sealed up very tightly with plastic tape.
4. Steps 1, 2, and 3 are repeated for every soil sample.
5. The prepared containers are put into ice-chests in a controlled temperature room for equilibrium.

Researchers suggest an equilibration period of 3 to 5 days for matric suction testing (ASTM D 5298, Houston et al. 1994, Lee 1991). However, if both matric and total suction measurements are performed on the same sample in the glass jar, then the final equilibrating time will be at least 7 days of total suction equilibrating period. The procedure for the filter paper water content measurements at the end of the equilibration is exactly same as the one outlined for the total suction water content measurements. After obtaining all the filter paper water contents the appropriate calibration curve may be employed to get the matric suction values of the soil samples.

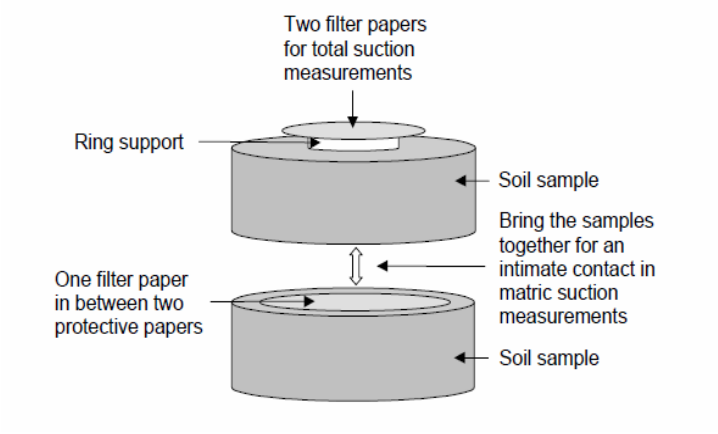

Fig. 2: Total and matric suction measurements (Bulut et al., 2001).

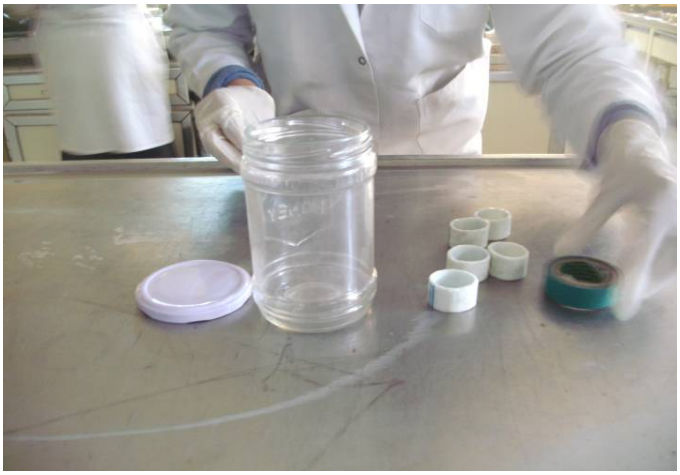

Photograph 1.

Photograph 2.

Photograph 3.

Photograph 4.

Photograph 5.

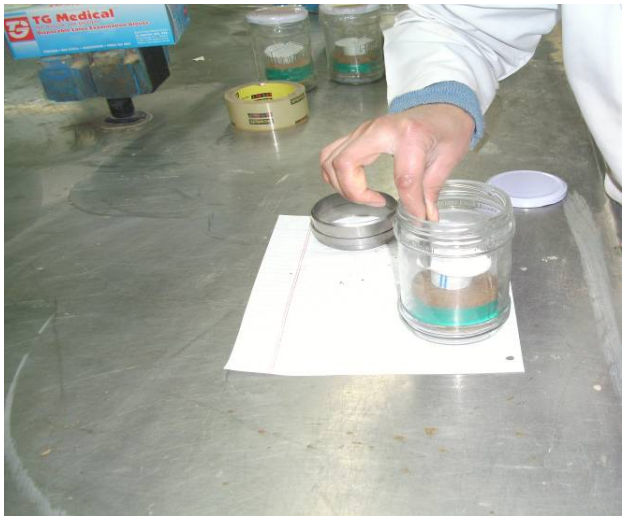

Photograph 6.

Photograph 7.

Photograph 8.

Photograph 9.

RESULTS AND DISCUSSION

The tests described in the previous section were carried out on five samples. A sample of the data measurement of soil suction by the filter paper method is shown in **Table 2**. The variation of the total and matric suction with the degree of saturation for the five soils is shown in **Figs. 3** and **4**, respectively. Both figures indicate that the suction increases with decrease of the degree of saturation.

Figs. 5 and **6** present the relationship between the total and matric suction and the filter paper water content. The relations are approximately linear and indicate decrease of suction with increase of the filter paper water content.

Figs. 7 and **8** show relationships between the soil consistency (liquid limit and plasticity index) and the total and matric suction, respectively at a degree of saturation equals to 70%. The figures indicate that the suction is measured for soils of low consistency (liquid limit < 40% or plasticity index < 20%). The measured suction becomes minimum at medium consistency (liquid limit ≈ 60% or plasticity index ≈ 40%).

Fig. 9 shows that the total and matric suction reveal decrease with the clay content and the suction decreases sharply when the clay content exceeds 80 %. The suction was measured for the soil having a clay content of about 70%.

The effect of the unconfined compressive strength on the suction is illustrated in **Fig. 10** which shows that the suction increases with the decrease of the soil shear strength. This may be attributed to the nature of flow through samples which becomes slower as the sample is stronger leading to generation of greater values of negative pore water pressure.

Table 2: Measurement of soil suction using filter paper – data sheet.

MEASUREMENT OF SOIL TOTAL SUCTION USING FILTER PAPER SAMPLE NAME: RASAFA 1 DATE TESTED: 23-1-2011 DATE SAMPLE: 16-1-2011					
Degree of Saturation %		70	80	90	100
Tin No.		1	2	3	4
Top Filter Paper (circle) (two filters)		Top	Top	Top	Top
Mass of Wet Filter Paper, g	M1	0.5482	0.5651	0.5651	0.5523
Mass of Dry Filter Paper, g	M2	0.4555	0.4607	0.4405	0.4193
Mass of Water in Filter Paper, g (M1-M2)	M_w	0.0927	0.1044	0.1596	0.1330
Water Content of Filter Paper % (M_w/M2)	Wf	20.3513	22.6612	28.2860	31.7195
Total Suction, (log kpa)	h_t	3.7416	3.5617	3.1258	2.8466
MEASUREMENT OF SOIL MATRIC SUCTION USING FILTER PAPER SAMPLE NAME: RASAFA 1 DATE TESTED: 23-1-2011 DATE SAMPLE: 16-1-2011					
Degree of Saturation %		70	80	90	100
Tin No.		5	6	7	8
Bottom Filter Paper (circle) (two filters)		Bottom	Bottom	Bottom	Bottom
Mass of Wet Filter Paper, g	M1	0.2929	0.3156	0.3303	0.3720
Mass of Dry Filter Paper, g	M2	0.2382	0.2371	0.2278	0.2294
Mass of Water in Filter Paper, g (M1-M2)	M_w	0.0547	0.0785	0.1025	0.1426
Water Content of Filter Paper % (M_w/M2)	Wf	22.9639	33.1084	44.9956	62.1622
Matric Suction, log kpa	h_m	3.5381	2.7478	1.8218	1.5728

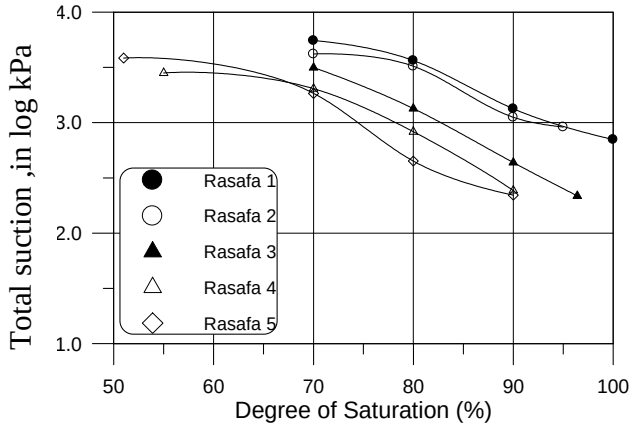

Fig. 3: Relationship between the total suction and degree of saturation.

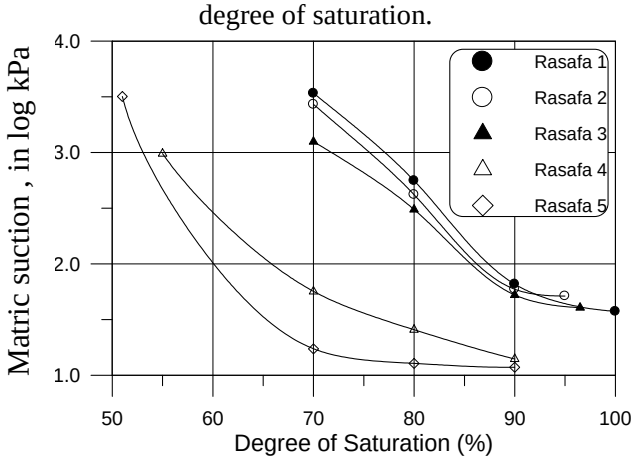

Fig. 4: Relationship between the matric suction and degree of saturation.

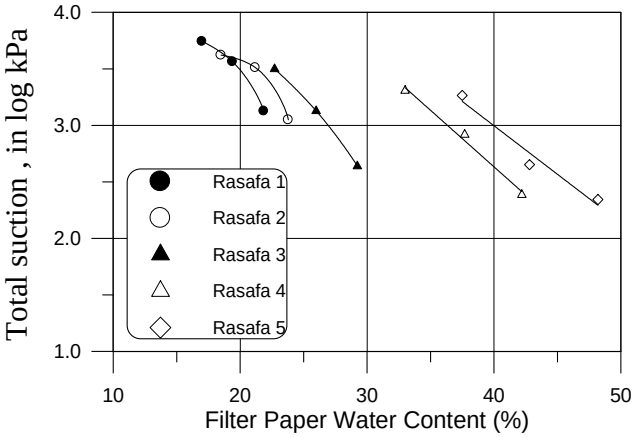

Fig. 5 Filter paper wetting curve (total suction).

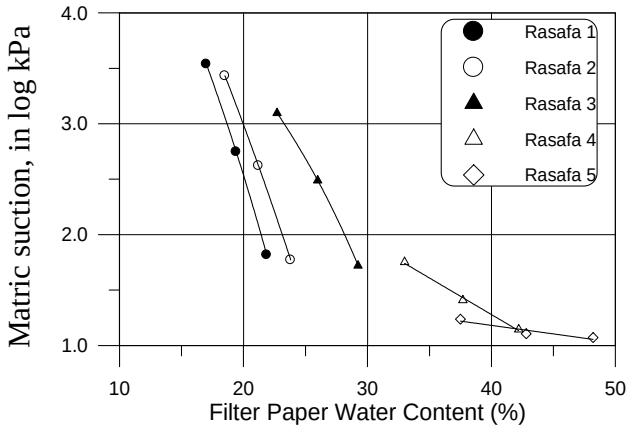

Fig. 6 Filter paper wetting curve (matric suction).

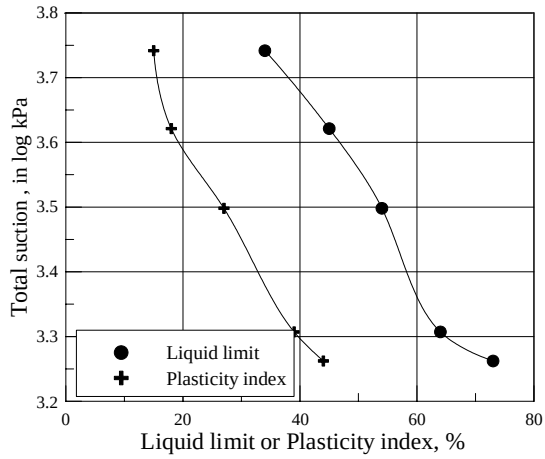

Fig. 7 Variation of the total suction with Atterberg limits at degree of saturation=70%.

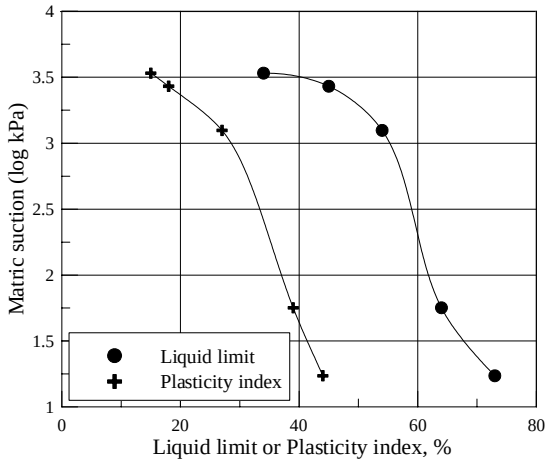

Fig. 8 Variation of the matric suction with Atterberg limits at degree of saturation=70%. .

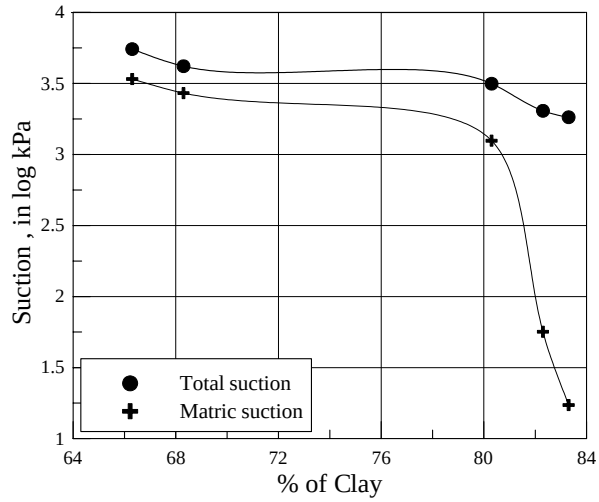

Fig. 9 Variation of the suction with the percentage of clay at degree of saturation=70%..

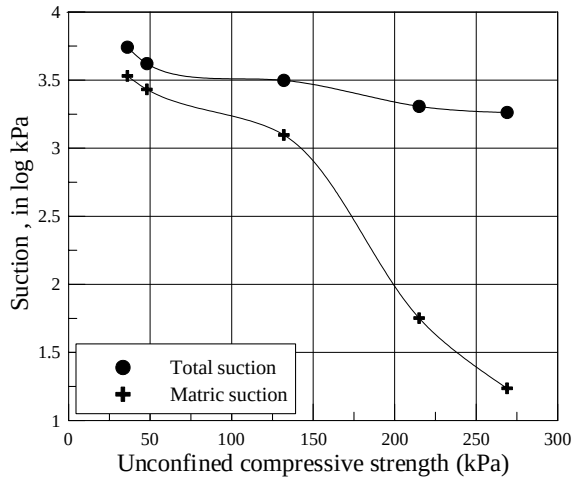

Fig. 10 Variation of the maximum suction with the unconfined compressive strength at degree of saturation=70%..

CONCLUSIONS

1. The suction increases with decrease of the degree of saturation. The relationships between the total and matric suction and the filter paper water content are approximately linear and indicate decrease of suction with increase of the filter paper water content.
2. The suction is measured for soils of low consistency (liquid limit < 40% or plasticity index < 20%). The suction was measured for the soil having a clay content of about 70%. The total and matric suction increase with the decrease of the Atterberg limit.

3. The total and matric suction increase with the decrease of the soil shear strength.

REFERENCES

- Al-Khafaf, S. and Hanks, R. J. (1974). "Evaluation of the Filter Paper Method for Estimating Soil Water Potential," Soil Science, Vol. 117, No. 4, pp. 194-199.
- ASTM Standard Test Method for Measurement of Soil Potential (Suction) Using Filter Paper (ASTM D 5298).
- Bulut, R., Lytton, R. L and Wray, W. K., (2001). "Soil Suction Measurements By Filter Paper**",** Geotechnical Special Publication Number 115, Proceedings of Geo-Institute Shallow Foundation and Soil Properties Committee Sessions at the ASCE 2001 Civil Engineering Conference, pp. 243-261.
- Chandler, R. J. and Gutierrz, C. I. (1986). "The Filter Paper Method of Suction Measurements," Geotechnique, Vol. 36, pp. 265-268.
- Fawcett, R. G. and Collis-George, N. (1967). "A Filter-Paper Method for Determining the Moisture Characteristics of Soil," Australian Journal of Experimental Agriculture and Animal Husbandry, Vol. 7, pp. 162-167.
- Fredlund, D. G. and Rahardjo, H. (1993). Soil Mechanics for Unsaturated Soils, New York: John Wiley & Sons, Inc.
- Gardner, R. (1937). "A Method of Measuring the Capillary Tension of Soil Moisture Over a Wide Moisture Range," Soil Science, Vol. 43, No. 4, pp. 277-283.
- Hamblin, A. P. (1981). "Filter Paper Method for Routine Measurement of Field Water Potential," Journal of Hydrology, Vol. 53, No. 3/4, pp.355-360.
- Hamer, W. J. and Wu, Y.-C. (1972). "Osmotic Coefficients and Mean Activity Coefficients of Uni-Univalent Electrolytes in Water at 25oC," Journal of Physics and Chemistry Reference Data, Vol. 1, No. 4, pp. 1047-1099.
- Houston, S. L., Houston, W. N., and Wagner, A. M. (1994). "Laboratory Filter Paper Measurements," Geotechnical Testing Journal, GTJODJ, Vol. 17, No. 2, pp. 185-194.
- Lee, H. C. (1991). "An Evaluation of Instruments to Measure Soil Moisture Condition," M.Sc. Thesis, Texas Tech University, Lubbock, Texas.
- McKeen, R. G. (1980). "Field Studies of Airport Pavement on Expansive Clay," Proceedings 4th International Conference on Expansive Soils, Vol. 1, pp.242-261, ASCE, Denver, Colorado.
- McQueen, I. S. and Miller, R. F. (1968). "Calibration and Evaluation of a Wide-Range Gravimetric Method for Measuring Moisture Stress," Soil Science, Vol. 106, No. 3, pp. 225-231.
- Murray, E. J., Sivakumar, V., (2010). "Unsaturated Soils A Fundamental Interpretation of Soil Behaviour", John Wiley & Sons, Ltd., Publication.
- Schofield, R. K. (1935). "The pF of the Water in Soil," Transactions, 3rd International Congress of Soil Science, Vol. 2, pp. 37-48.
- Swarbrick, G. E. (1995). "Measurement of Soil Suction Using the Filter Paper Method," First International Conference on Unsaturated Soils, Eds.: E. E. Alonso and P. Delage, Vol. 2, Paris, 6-8 September, ENDPC, pp. 701-708.

Numerical Simulation of flow in pipe with cross jet effects

Karema Assi Hamad

Assistant Lecturer

Department of Electromechanical Engineering

University of Technology – Baghdad

Abstract

A numerical method is developed to obtain two-dimensional velocity and pressure distribution through a cylindrical pipe with cross jet flows. The method is based on solving partial differential equations for the conservation of mass and momentum by finite difference method to convert them into algebraic equations. This well-known problem is used to introduce the basic concepts of CFD including: the finite- difference mesh, the discrete nature of the numerical solution, and the dependence of the result on the mesh refinement. Staggered grid implementation of the numerical model is used. The set of algebraic equations is solved simultaneously by "SIMPLE" algorithm to obtain velocity and pressure distribution within a pipe. In order to verify the validity for present code, the flow behavior predicted by this code is compared with these of another studies and there is a good agreement is obtained.

Keywords : numerical, CFD, laminar flow, cross flow, flow in pipe.

التمثيل العددي للجريان في انبوب بيتأثير نفث جانبي خلال الجريان المتقاطع

الخلاصة

تم تطوير طريقة حل عددية لمعرفة التوزيع الثنائي الأبعاد للسرعة والضغط خلال انبوب اسطواني المقطع مع جريان متقاطع . وقد اعتمدت الطريقة على حل المعادلات التفاضلية الجزئية لحفظ الكتلة والزخم (conservation of both mass and momentum) بواسطة استخدام طريقة الفرو قات المحددة (finite difference method) لتحويلها إلى معادلات جبرية. يستخدم هذا التطبيق المعروف جيداً لتطبيق مفاهيم الحل باستخدام ديناميك الموائع الحسابي (CFD) والمتضمنة كيفية توزيع عقد الفروقات المحددة وطبيعة واسلوب طريقة الحل العددية بتلك الطريقة وكذلك اعتمادية النتائج على اسلوب توزيع العقد ضمن الحيز من حيث تقليل المسافات البينية بين العقد. استخدم (Staggered grid) في نموذج الحل العددي. تم حل مجموعة المعادلات الجبرية في وقت واحد بطريقة ("SIMPLE" algorithm) لمعرفة توزيع السرعة والضغط خلال الانبوب . ولغرض التحقق من وثوقية الطريقة الحالية تمت مقارنة النتائج العددية الحالية مع نتائج الحل التحليلي للجريان احادي الابعاد خلال الانابيب ،وقد بينت المقارنة توافقية جيدة.

Introduction

The analysis of pipe flow is very important in engineering point of view. A lot of engineering problem dealt with it. Due to rigorous engineering application and implications the analysis is important. The flow of real fluid exhibits viscous effects in pipe flow. Here this effect is identified for laminar flow condition. The application of momentum equation is used to evaluate the velocity and pressure distribution in a pipe under laminar flow condition.

(**Baniasad et al.,2009).** Presented numerical prediction of two- dimensional laminar heat transfer to water flow at critical pressure. The set of governing equations containing continuity, momentum and energy are solved simultaneously using CFD technique. The discretized form of each equation is obtained by finite volume method and the SIMPLE algorithm is used for pressure-velocity calculations.

(Mahmud et al.,2009). Presented numerical study to predict hydrodynamic and thermal characteristics in a pipe with sinusoidal wavy surface for steady laminar flow . The integral forms of governing equations are discretized using control volume based Finite Volume method with collocated variable arrangement. SIMPLE algorithm is used and TDMA solver is applied for solution of system of equations.

(Shimomukai and Kanda 2008). Studies the computation of pipe flow in the entrance region. The pressure distribution and flow characteristics, particularly the effect of vorticity in the vicinity of the wall, are analyzed for Reynolds numbers ranging from 500 to 10000.

(Smith et al., 2008). Described the flow through circular orifice by using computational fluid dynamics (CFD) with various turbulence modeling. Effects of orifice diameter ratios (d/D = 0.5, 0.6, and 0.8) on flow field characteristics is extensively investigated. To study the influence of turbulence model on the predicted results, the standard k-ε turbulence model was employed to compare with the Reynolds Stress Model.

(Voronova and Nikitin 2006). Present complete Navier-Stokes equations for the turbulent flow in a pipe of elliptical cross-section with semiaxis ratio *b/a* = 0.5 is directly calculated for the Reynolds number Re = 6000 (determined from the mean-flow velocity and the hydraulic diameter). The distribution of the average and pulsatory flow characteristics over the pipe cross-section are obtained. In particular, the secondary flow in the cross-section plane, typical of turbulent flows in noncircular pipes, is calculated.

(Voronova and Nikitin 2006). Studied the turbulent flow in a pipe with an elliptical cross section is directly simulated at Re = 4000 (where Re is calculated in terms of the mean velocity and the hydraulic diameter). The incompressible Navier-Stokes equations are solved in curvilinear orthogonal coordinates by using a central-difference approximation in space and a third-order accurate semi-implicit Runge-Kutta method for time integration. The distributions of the mean and fluctuation characteristics of the turbulent motion over the pipe's cross section are computed.

(Akinlade 2005). reports the effects of surface roughness on the flow characteristics in a turbulent boundary layer. Both experimental and numerical investigations are used. A new wall function formulation based on a power law was proposed for smooth and fully rough wall turbulent pipe flow. The new formulation correctly predicted the friction factors for smooth and fully rough wall turbulent pipe flow.

(Gerald 2002). Presents a CFD mode based on Matlab implementation to predict fully-developed laminar flow in a pipe

(Surjosatyo and Ani 2001). Present a simulation study of a cold-flow in coaxial pipes with varying drive pipe diameter and entrance displacement. To predict these flow characteristics, a numerical method was employed by the differencing scheme for integrating the continuity equation and energy equation. A k-ε turbulent model was used to simulate the turbulent transport quantities. The 2-D flow pattern was created as the result of using fluent version 4.4 CFD modeling package

(Yakhot et al.,1999). Studied A pulsating laminar flow of a viscous, incompressible liquid in a rectangular duct. The motion is induced under an imposed pulsating pressure difference. The problem is solved numerically. Different flow regimes are characterized by a non-dimensional parameter based on the frequency (v) of the imposed pressure gradient oscillations and the width of the duct (*h*).

In the present study a two-dimensional numerical method is presented to obtain velocity and pressure distribution through a cylindrical pipe. The method is based on solving partial differential equations for the conservation of mass and momentum by finite difference method.

Numerical solution

The governing equations

The equations for conservation of mass and momentum for incompressible, steady and laminar flow in cylindrical coordinate system of the r and z directions are given below **(*Graebel*, 2007)**

(i) ***Mass Conservation*** **.**

$$\frac{1}{r}\frac{\partial}{\partial r}(\rho r v)+\frac{\partial}{\partial z}(\rho u)=0 \qquad (1)$$

(ii) ***Momentum Conservation*** **.**

(r) – direction

$$\rho\left(v\frac{\partial v}{\partial r}+u\frac{\partial v}{\partial z}\right)= -\frac{\partial P}{\partial r}+\mu\left(\nabla^2 v-\frac{v}{r^2}\right) \qquad (2)$$

(z) – direction

$$\rho\left(v\frac{\partial u}{\partial r}+u\frac{\partial u}{\partial z}\right)= -\frac{\partial P}{\partial z}+\mu\nabla^2 u \qquad (3)$$

Finite Difference Formulation of the Equations

The basic of the numerical method is the conversion of the differential equations (1, 2 and 3) into algebraic equations relating the value of the dependent variables at the considered grid point to the its values at the neighboring grid points. This was done by finite difference method.

After treating the governing equations by (FDM), the general form of the resultant equation can be termed as **(Patankar 1980)** :

$$A_P\Phi_P=\left(\sum_{E,W,N,S} A\Phi\right)+B \qquad (4)$$

Where Φ is the general form of the dependent variable **(Adisurjosatyo 2001).**

This equation is known as a two-dimensional discretization equation. Where (A_E, A_W, A_N, *and* A_S,) are the neighboring coefficient representing the convection and diffusion terms of the mass entering the cell at its boundary surfaces, which are equal to :

$$A_E=\rho\frac{1}{\Delta z}\frac{u_e}{2}-\mu\frac{1}{\Delta z^2} \qquad (5a)$$

$$A_W=-\rho\frac{1}{\Delta z}\frac{u_w}{2}-\mu\frac{1}{\Delta z^2} \qquad (5b)$$

$$A_N=\rho\frac{1}{\Delta r}\frac{v_n}{2}-\mu\frac{r_n}{r_j\Delta r^2} \qquad (5c)$$

$$A_S=-\rho\frac{1}{\Delta r}\frac{v_s}{2}-\mu\frac{r_s}{r_j\Delta r^2} \qquad (5d)$$

$$A_P=\left(\sum_{E,W,N,S} A\right)+B_1 \qquad (5e)$$

Where the subscript (*P*) denotes the corresponding grid point. The small letters subscript (*e, w, n and s*) denote the value of the variable at the faces of the control volume. Fig (1) shows the

corresponding grid point and its neighbor grid points, and the u velocity component.

Table (1) illustrates the value of (B) for Equation (4) and the value of (B_1) for Equation (5e) for the governing equations.

Method of Solution

The first step in the solution is dividing the flow field into grid points, then the partial differential equations would be transformed into an algebraic form by finite-difference method as illustrated in the previous section. The discretized procedure of the equation is based on the power law scheme **(Patankar 1980)** and the discretized equations are solved by (TDMA) (Try Diagonal Matrix Algorithm) with under-relaxation factor 0.75 for pressure and 0.45 for velocity. The pressure and velocity are linked by the SIMPLE algorithm **(Patankar 1980)**.

Computer Program Descriptions

A computer program in FORTRAN-90 is written to solve a set of the partial differential equations that govern the flow field. The field is divided into grid points, which are distributed in r and z coordinates. There are four sets of grid without clustering are tested, where (30*15) is chosen because this set ensure good results in addition is a time saving as shown in Figure (2) .

Boundary conditions

1. Steady state.
2. The velocity components at the wall are set equal to zero, because of the viscous nature of the flow.
3. At inlet the (u) velocity component is defined while the (v) component is set equal to zero.
4. At exit, the velocity are floating (smooth exit)

Staggered grid

Co-located storage of the pressure and velocity variables at the cell centers leads to the problem of checker boarding. This is because the cell centre values of pressure and velocity get cancelled out on expanding the face gradient terms. To overcome this problem staggered grid has been used for discretization of the momentum equations. The staggered grid for the u momentum equation is shown in Figure (1) along with the neighboring velocity vectors for calculation of velocity gradients. Staggered grid in vertical direction is used for v momentum equation. Pressure is stored on the original grid and the pressure difference terms are evaluated as a difference of cell centre pressure values.

Under-relaxation

The velocity corrections are approximated by dropping the velocity part of the corrected momentum equations which places the entire burden of the velocity correction on pressure correction. Large pressure corrections might lead to poor pressure iterates so the pressure correction is under-relaxed to correct p*.It is necessary to under-relax the momentum equations due to the nonlinear nature of the equations.

$$p = p^* + \alpha_p p' \qquad (6)$$

$$\Phi_P = (1-\alpha)\Phi_P + \alpha\left(\sum A_{nb}\Phi_{nb} + B\right)/A_P \qquad (7)$$

SIMPLE Solver Algorithm

Semi-Implicit Method for Pressure-Linked Equations was first proposed by Patankar and Spalding (1972). Here we start with the discrete continuity equation and substitute into this the discrete u and v momentum equations containing the pressure terms resulting in a equation for discrete pressures. SIMPLE actually solves for a relative quantity called pressure correction. We guess an initial flow field and pressure distribution in the domain. The set of momentum and continuity equations are coupled and are nonlinear so we solve the equations iteratively. The pressure field is assumed to be known from the previous iteration. Using this u and v momentum equations to solve for the velocities. At this stage the newly obtained velocities don't satisfy continuity since the pressure field assumed is only a guess. Corrections to velocities

and pressure are proposed to satisfy the discrete continuity equation.

$$u = u^* + u' \quad (8)$$

$$v = v^* + v' \quad (9)$$

$$p = p^* + p' \quad (10)$$

Where u* v* and p* are the guess values and u', v' and p' are the corrections. Figure (3) shows flow chart for SIMPLE algorithm .

Results

In order to validate the present code, the velocity profile is compared with that of **(Muppidi, and Mahesh 2006)** in figures (4) and (5) . These figures shown good agreement for velocity contours especially at the cross flow region and down stream up to the pipe end. This code was them used to simulate a laminar flow in pipe, where figure (6) shows the velocity vector and axial velocity contour along the pipe from inlet to exit. The velocity is reducing towards the pipe wall and becomes zero a the wall, while the maximum value of the velocity is at the center of the pipe. Figure (7) shows the pressure contour along the pipe. From this figure the pressure is reducing with the pipe length as a result of the friction losses inside the pipe thus the velocity increasing towards the exit of the pipe .

Figure (8) show the another case of cross flow which is found in a several engineering applications, where the velocity vector for this application for two cases are predicted , a) Cross flow from the upper wall of the pipe and b) Cross flow from both sides of the pipe. The effect of cross flow for both cases is seen by the separation and formation of vortex in the down stream regions. Therefore, cross flow can be used to eliminate the effect of boundary layer as seen in figure (6) of developing pipe flow which is unwanted in many engineering applications.

Conclusions

Two-dimensional numerical study of laminar flow in a pipe with cross flow is presented. Finite difference is used to solve two-dimensional Naviar Stokes equations; Staggered grid is used to avoid the difficulties that result from calculating the velocity and pressure at the grid point. The resultant algebraic equations are solved by "SIMPE algorithm" to define velocity and pressure distribution. The interaction of cross jet with the main pipe flow was predicted accurately .the vortices that formed at downstream region was seen to destroy the boundary layer originally generated in developing pipe flow.

References

Adisurjosatyo and Farid Nasir Ani, " A Numerical study of air flow in a coaxial pipe.", *Jurnal Teknologi*, 34(A) Jun 2001: 1–15, Universiti Teknologi Malaysia.

Baniasad Askari, S. A. Gandjalikhan Nassab and M. Peymanfard, "Nnmerical investigation of fluid flow and heat transfer for laminar water flow in a duct at critical pressure", Iranian Journal of Science & Technology, Transaction B, Engineering, Vol. 33, No. B3, pp 285-290, 2009.

Gerald Recktenwald " Fully-Developed Flow in a Pipe A CFD Solution" , 2002.

***Graebel*," Advanced Fluid Mechanics" , Academic Press is an imprint of Elsevier, 2007**

Muppidi, S. and Mahesh, K. " Passive scalar mixing in jets in cross flow" 4th AIAA Aerospace Sciences Meeting and Exhibit, Jan 9{12, Reno, Nevada, 2006.

Olajide Ganiyu Akinlade " Effects of surface roughness on the flow characteristics in a turbulent boundary layer", A Thesis Submitted to the College of Graduate Studies and Research in Partial Fulfillment of the

Requirements for the Degree of Doctor of Philosophy in the Department of Mechanical Engineering University of Saskatchewan Saskatoon December 2005

Patankar ,S. V. , "Numerical heat transfer and fluid flow ." McGraw–Hill Company, Now York, 1980.

Shohel Mahmud , A. K. M. Sadrul Islam and Prodip Kumar Das " Numerical prediction of fluid flow and heat transfer in a wavy pipe" , Journal of Thermal Science, Volume 10, Number 2, 2009.

Shimomukai and H. Kanda , " Numerical study of normal pressure distribution in entrance pipe flow", Electronic Transactions on Numerical Analysis.
Volume 30, pp. 10-25, 2008.

Smith Eiamsa-ard, Artit Ridluan, Prachya Somravysin, and Pongjet Promvonge , " Numerical investigation of turbulent flow through a circular orifice" KMITL Sci. J. Vol.8 No.1 January – June, 2008.

Voronova and N. V. Nikitin " Results of Direct Numerical Simulation of Turbulent Flow in a Pipe of Elliptical Cross-Section" 2006

Voronova and N. V. Nikitin " Direct numerical simulation of the turbulent flow in an elliptical pipe", Computational Mathematics and Mathematical Physics, Volume 46, Number 8,, 2006.

Yakhot , M. Arad and G. Ben-Dor " Numerical investigation of a laminar pulsating flow in a rectangular duct", *Int. J. Numer. Meth. Fluids* 29: 935–950 ,1999.

List of symbols

A	Combined convection-diffusion discretization coefficient ($kg/m^3.s$)
B,B1	Source term.
P	Pressure (N/m^2)
R	Radius of the pipe (m)
r	coordinate.
u	Axial velocity component (m/s).
v	Radial velocity component (m/s).
z	coordinate.
α	Under relaxation factor.
ϕ	General dependent variable.
μ	Laminar viscosity ($N.s/m^2$).
ρ	Density (kg/m^3).

Superscript

*	Previous iteration value.
'	correction quantities.

Subscript

E,W,N,S	Indicates to the neighbor nodes of node P.
e,w,n,s	Face of control volume.
P	Node P (control volume centre).
max	Maximum value.

Table (1) Value of B and B_1 for Equations (4and 5e) for governing equations.

r– direction momentum equation	
B_1	$-\mu \frac{v}{r^2}$
B	$\frac{P_N - P_P}{\Delta r}$
z– direction momentum equation	
B_1	0
B	$\frac{P_E - P_P}{\Delta r}$

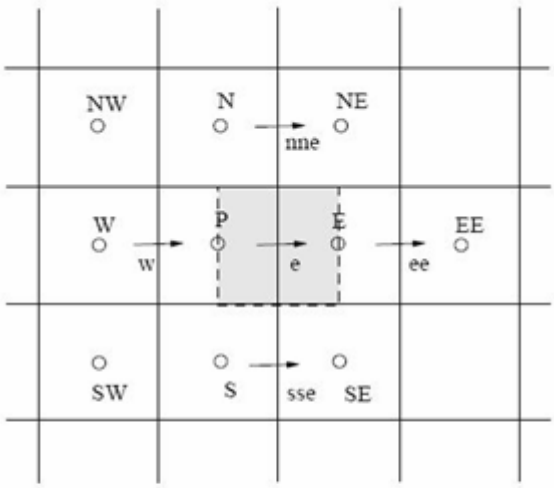

Figure(1). Neighbors for Ue momentum control volume

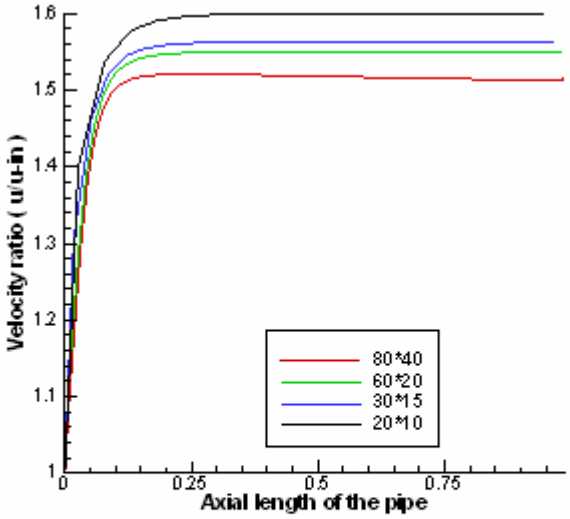

Figure(2) Grid independent Test

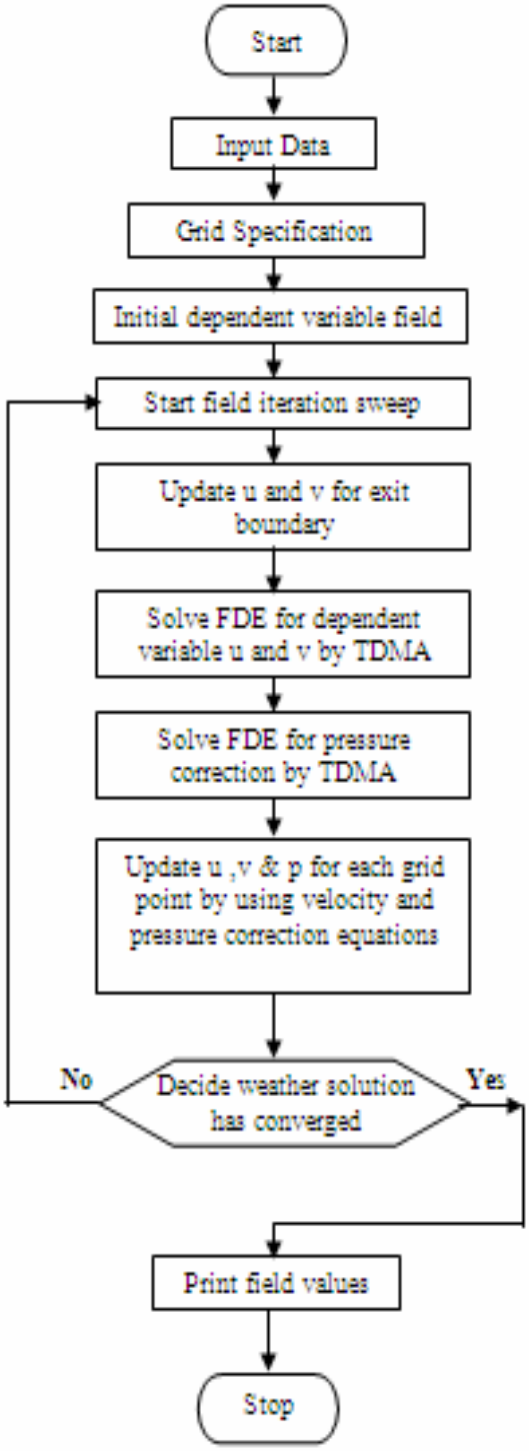

Figure (3). Flow chart showing the SIMPLE Algorithm

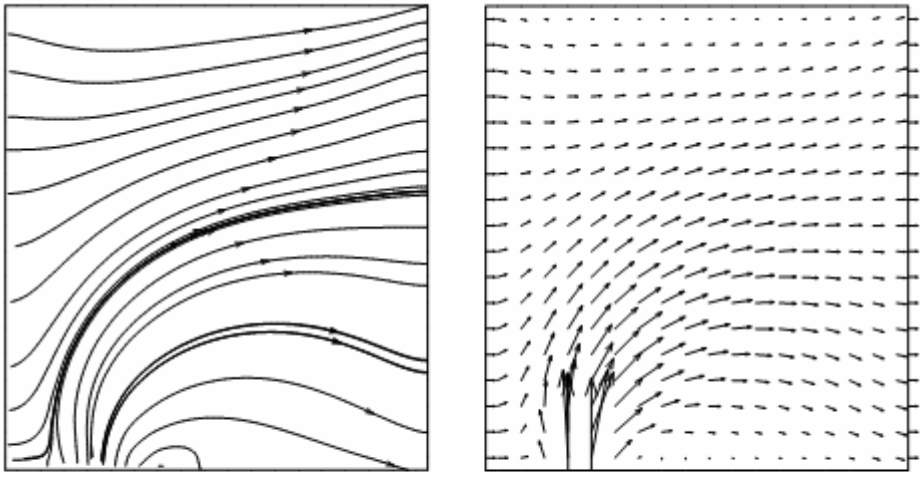

Figure (4): Velocity vector for laminar flow with turbulent jet cross flow.

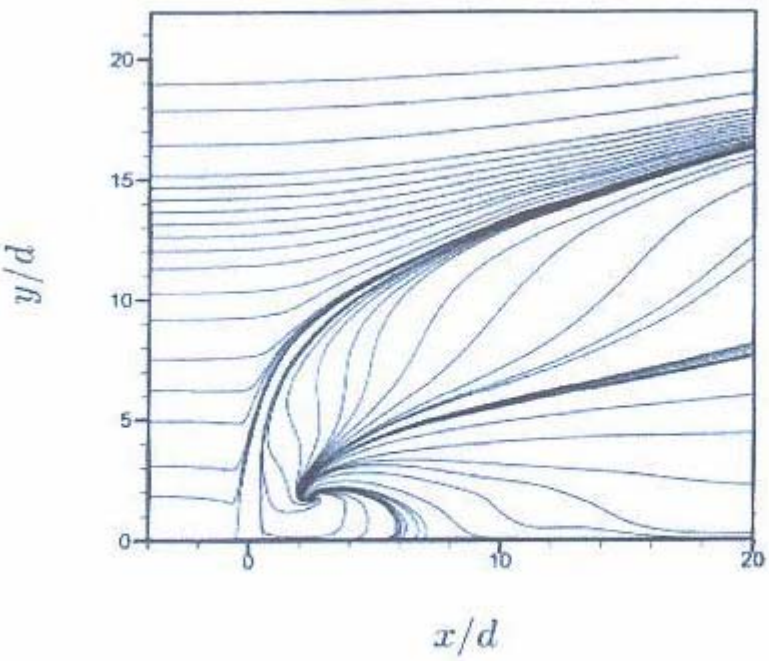

Figure (5): Velocity vector preducted by **(Muppidi and Mahesh, 2006)**
Where (d) is the jet diameter.

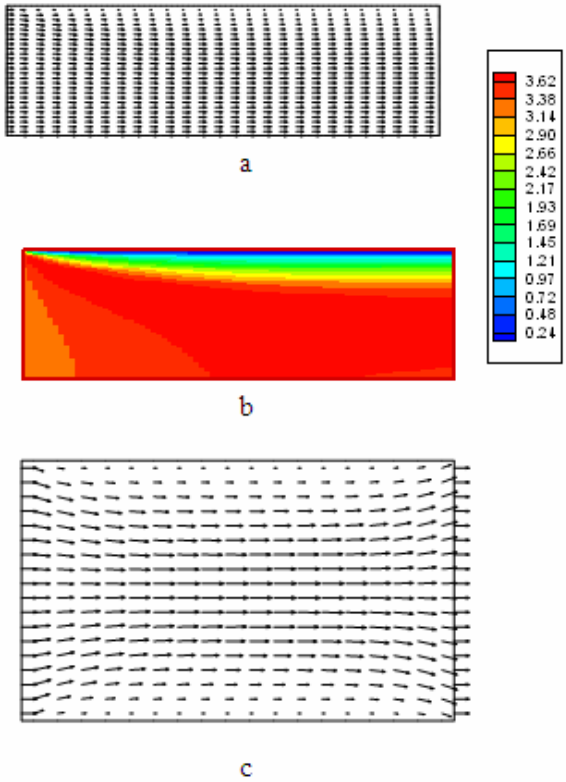

Figure (6): a) Velocity vector from centre to the wall of symmetry pipe , b) Axial velocity contour, c) Velocity vector for a pipe.

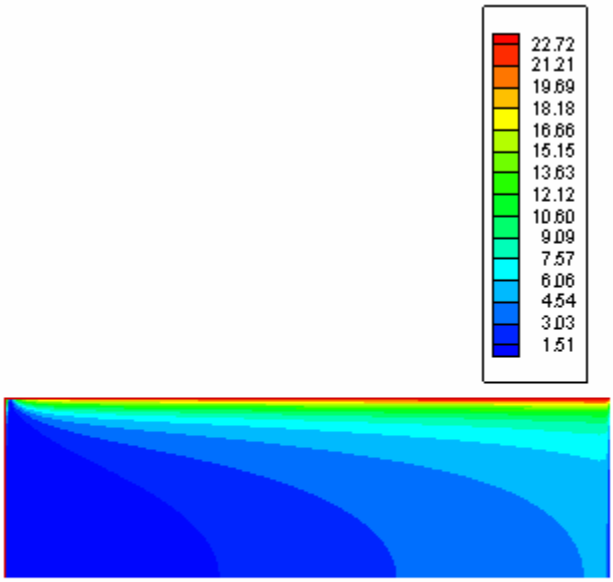

Figure (7): Pressure contour along the pipe from centre to the one wall .

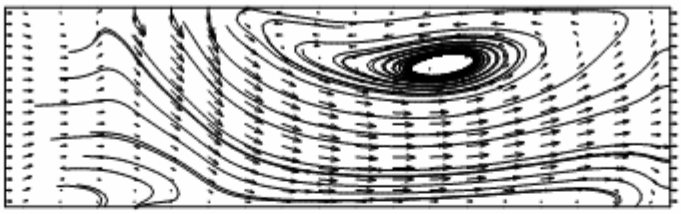

a

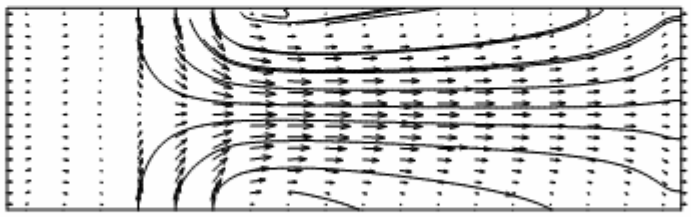

b

Figure (8): a) Velocity vector with cross flow from the north wall
b) Velocity vector with cross flow from both north and south walls.

A STUDY OF THE EFFECT OF SEMI-ANGLE OF CONE ON THE VIBRATION CHARACTERISTICS OF CYLINDRICAL-CONICAL COUPLED SHELL STRUCTURE

Dr. Muhsin J. Jweeg
Al-Nahrain University
College of Engineering.

Dr. Adnan D. Mohammed
University of Technology
Electromechanical Engineering Dept.

Dr.Mohsin A. Al-Shamari
University of Baghdad
College of Engineering.

ABSTRACT

In this work, the effect of variation of semi-angle of the conical part on the vibration characteristics of cylindrical-conical coupled structure is investigated. The shell is made of polyester resin reinforced by continuous E-glass fibers. The case is analyzed experimentally and numerically for orthotropic shell structures. The experimental program is conducted by exciting the fabricated structure by an impact hammer and monitoring the response using an attached accelerometer for different semi-angles of the conical part. Software named SIGVIEW is used to perform the signal processing on the acquired signal in order to measure the natural frequencies and the corresponding mode shapes. The numerical investigation is achieved using ANSYS (Finite Element software) which was verified by the experimental results. Good agreement is achieved when comparing the experimental and numerical results. The maximum deviation in results was found to be (5.9%). The maximum relative nodal rotational and translational amplitudes associated with the first normal mode of the orthotropic and isotropic shells are noted for the structure of semi-angle of cone of 45°.

الخلاصة

في هذا العمل أجريت دراسة تجريبية وعددية لتأثيرتغير نصف زاوية المخروط على الخواص الأهتزازية للهيكل القشري المخروطي – الأسطواني المرتبط المختلف والسوي. لقد تم تصنيع الهيكل القشري من مادة البولستر الرابطة المقواة بكمية من الألياف الزجاجية نوع E المستمرة. انجز الجانب العملي لحساب الترددات الطبيعية للهيكل باستخدام محلل FFT بمساعدة مقياس التعجيل ومطرقة مزودة بمتحسس قياس القوة. لقد تم انجاز الجانب العددي باستخدام طريقة العناصر المحددة (برنامج Ansys). لقد تم الحصول على تطابق جيد عند مقارنة النتائج العددية والعملية لقيم التردد الطبيعي الاول للهيكل.ان قيمة الأنحراف القصوى بالنتائج هي (5.9%). لقد تم التوصل الى ان القيم النسبية العظمى للعقد للسعات الانتقالية والدورانية الخاصة بشكل النسق الاول وللهياكل المصنعة من مواد مركبة مختلفة او سوية تحصل عند زاوية نصف زاوية مخروط مقدارها 45 درجة.

Key words: Coupled, Cylindrical-Conical, Orthotropic, Frequency

INTRODUCTION

The term "composite", nowadays, is referred to those engineering products exhibiting such diametrical opposite features to the familiar homogenous materials. Now, it is possible to earn a composite product relatively strong but light, flexible but tough and expensive but prosperous with similar products of a single constituent. Cone–cylinder intersections are commonly used in pressure vessels, aerospace structures and piping. Examples include conical end closures to cylindrical vessels and conical reducers between cylinders of different radii. The vibrational load is often an important loading condition for these intersections. The localized high stresses generally develop within a narrow region enclosing the joint and may significantly affect the response behavior. Although for the preliminary design purpose, the structural response of the individual components may be examined. However, for the prediction of global behavior and rigorous optimal design, it may be more appropriate to analyze the joined complete shell system experimentally and numerically. The experimental work was done in ERDA company (Electrical Research Development Association), Gujarat, India, the experimental models were made in MARUTI Fibers, Maharashtra, India, and the tensile test was achieved in KEMROCK company , Gujarat, India.

Liang and **Chen** [1] investigated in details the natural frequencies and mode shapes for a conical shell with an annular end plate or a round end plate by combining the vibration theory with the transfer matrix method. The feasibility of using the transfer matrix method to analyze a composite laminated conical-plate shell was explored theoretically by **Liang** et. al. [2]. The conclusions illustrated that this investigation will provide an important foundation for the advanced development of the laminated composite combination shells, it showed that the transfer matrix method can reveal the dynamic characteristics of the composite laminated conical-plate structures. Parametric instability study of a conical-cylindrical shell subjected to a periodic in-plane load was examined by **Kamat** et. al. [3] by considering a two-nodded axisymmetric shell element based on the shear flexible theory. Numerical results have been obtained for isotropic, orthotropic, and laminated shells with different conical sections joined with circular cylindrical shells. Segmented shells are shells that are built of several pieces form together an axisymmetric shell with a joint axis. These can be cylindrical, conical or plate segments, which are connected to form a complete shell. **Efraim** and **Eisenberger** [4], derive the exact dynamic stiffness matrix for each segment which was then used in the assembly of the complete structure dynamic stiffness matrix. The natural frequencies of the vibrations were found as the frequencies that cause this matrix to become singular. Examples were given for the frequencies and modes of segmented shells made of conical, cylindrical, and plate segments. The truncated conical shape having a superimposed top cylindrical cap is widely used as a containment vessel for elevated water tanks. The evaluation of the wind and seismic responses of these tanks requires the knowledge of the dynamic characteristics of the vessels. A study done by **El Damatty** et. al. [5] who reported the results of the first experimental and numerical investigation conducted to assess the dynamic behavior of the combined conical vessels. **Irie** et. al. [6] presented an analysis for the free vibration of the joined conical-cylindrical shell. The flügge equations of the free vibration of the conical and cylindrical shells have been expressed in a matrix equation by using the transfer matrix of the shell.

FABRICATION OF EXPERIMENTAL MODELS

The Cylindrical-Conical shell models used in this study are manually fabricated. The first set of molds is made at a carpentry workshop using a wood lathe machine. Four molds are prepared with four different semi-cone angles; 15°, 30°, 45° and 60° as shown in **Fig.1**. The next step is to fabricate the second set of molds that would be used to make the test final molds. Each one of these molds are made with two parts of fiber reinforced resin, which are then welded together to obtain the molds that are used to fabricate the test models in the last step, as shown in **Fig.2**. The molder applies a pigmented "release" material to the mold as the first step in making any open mold product. Without such material, the part permanently bound the mold to the mold surface.

Many different release systems are available. The choice depends upon the type of inner surface to be molded, the degree of luster desired on the finished product and whether or not painting is required. The second step in this open mold process is the application of a specially formulated resin layer called a "gel coat". The polyester layer is first applied to the mold which becomes the inner surface of the laminate when completed. A moderately skill worker can maintain this activity by spreading the polyester fine layer with a fine brush homogeneously. This produces a decorative, high protective, glossy, colored surface which requires little or no subsequent finishing. After properly preparing the mold and gel coating, the next step in the molding process is the preparation of E-glass fibers. A fiberglass strands is used in the fabrication process, as shown in **Fig.3**. In order to align the fiber strands on the semi-soldered film of polyester layer previously mentioned, a sufficient number of pins are fixed on the two sides of the mold, and then the mold is held suitably between centers of the easily constructed winding machine shown in **Fig.4**. After a while, an additional film of polyester layer is gently spread on the mold surface to perform the single ply of the shell. The fiber orientation, in the style of composition, is referred to (0°) scheme of layer configuration, i.e., the direction of fibers is horizontally made with the open mold centerline. To fabricate a (90°) scheme of a single fiber-polyester layer of a cylindrical shell, the fibers orientation must now made normal to the open mold centerline. This trend of construction does not differ very much from the previous (0°) ply construction in processing of the matrix (polyester) films within the complete shell wall. However, the difference here is related to the opposite alignment of the fiber strands on the first polyester surface. The general procedure, explained above, is repeated for each design angle to produce the overall schemes of the design composite cylindrical-conical shell structure. The final product is then simply ejected from the mold by hammering on the conical edge of the product. The ends are then cut to final precise dimension. Four different composite shells are manufactured in the light of procedure explained above described as shown in **Table 1**

VIBRATION TESTS

Before commencing any vibration test on the fabricated test models, the mechanical properties of the coupled structure are obtained by performing tensile tests on specimens made of the same material as that of the Cylindrical-Conical coupled composite shell structure. The results are shown in **Table 2**. Each manufactured test model, described above, is attached to the test rig (an isolated earthquake table) as shown in **Fig. 5**. The foundation of the rig is very stiff, so the fundamental natural frequency of the fixture was considered to be infinite. The test model is fixed to the test rig at the end of the cylindrical part while the end of the conical part is left free to simulate a cantilever configuration. Each test model is supplied with small stud of a mass of 1 gm. This stud is glued on the top face of the shell at the intersection circle of the Cylindrical-Conical coupled structure. This stud is used to fix the 4 grams KISTLER type accelerometer. The accelerometer and impact hammer cables are connected to the data acquisition system (DAS). The output signal from DAS is fed to the FFT analyzer as shown in schematic diagram of **Fig.6**. The complete experimental setup is shown in **Fig.7**.

RESULTS AND DISCUSSION

The effect of the semi-angle of cone on the vibrational characteristics of the orthotropic Cylindrical-Conical shell structure is experimentally and numerically investigated. The coupled shell structure made of composite material, described above, has a thickness of 1.825 mm, L/D=2 and 0,90,0 fiber orientation. The numerical and experimental results of the fundamental natural frequency of the coupled structure for different semi-cone angles are shown in **Fig.8**. This figure shows that the value of fundamental natural frequency increases as the value of semi-angle of cone increases. The frequency behaves in such manner because the structure becomes stiffer. Also, this figure shows that the fundamental natural frequency exhibits an asymptotically constant value for structures with a semi-angle of cone of more than 45°. The reason is that the modal mass of the structure increases proportionally as the modal stiffness of the structure does. The comparison shows a good agreement between the experimental and

numerical results. A maximum deviation of 5.9% is noted. **Fig.9** displays the response spectrum obtained from the vibration test of the coupled shell structure for a value of semi-angle of cone of 60°. The curve shown in this figure is inferred from the Fourier transform of the time history of the transient response of the excited structure. It displays clearly the first resonance peak response that indicates the position of the fundamental natural frequency of the coupled Cylinder-Conical structure on the frequency axis. **Fig.10** shows the variation of the fundamental natural frequency of an isotropic shell structures for different semi-angle of cone. Similar behavior for the natural frequency is noted as that for the orthotropic shell. It can be seen from **Table 3** displays the effect of variation of the semi-angle of cone of orthotropic shell structures on the instantaneous maximum nodal configurations (translation and rotation) associated with the fundamental normal mode. The variation of angle, in general, has very little effect on the relative displacement amplitudes at x, y and z coordinates. The large values of the instantaneous relative nodal displacement amplitudes (translation and rotation), are noted for the shell structure of 45° angle. For isotropic shell structures, it can be seen from **Table 4** that the effect of variation of the semi-angle of cone on the maximum, relative nodal displacement amplitudes is the same as that of the orthotropic shell structures. Also, it can be seen that the y-translational amplitudes for all angles are of large values compared with the other values. This table shows also that the values of the rotational amplitudes about the y-axis and those of the z-translational relative amplitudes are the largest for the angle of 45°. The y-translational amplitudes and rotational amplitude about the z-axis are the lowest among the others for the same semi-angle of cone.

CONCLUSIONS

From the experimental and numerical investigations of the effect of variation of semi-angle of conical part on the vibration characteristics of a coupled Cylindrical-Conical composite shell structure, the following conclusions may be drawn;

I. The value of the fundamental natural frequency increases as the semi-angle of cone increases. The frequency exhibits an asymptotically constant value for structures having a semi-angle of cone of more than 45°. This behavior is noted for both orthotropic and isotropic shell structures. Very good agreement is reported during the comparison between experimental and numerical results.

II. The maximum relative nodal rotational and translational amplitudes associated with the first normal mode of the orthotropic and isotropic shells are noted for the structure of semi-angle of cone of 45°.

REFERENCES

1. S. Liang, and H.L. Chen, “The natural vibration of a conical shell with an annular end plate”. Journal of Sound and Vibration, 294, pp. 927–943, 2006.
2. S. Liang, H.L. Chen, T. Chen, and M. Y. Wang, “The natural vibration of a symmetric cross-ply laminated composite conical-plate shell”. Composite Structures, 80, pp. 265–278, 2007.
3. S. Kamat, M. Ganapathi, and B.P. Patel, “Analysis of parametrically excited laminated composite joined conical-cylindrical shells”. Computers and Structures, 79, pp. 65-76, 2001.
4. E. Efraim and M. Eisenberger, “Exact vibration frequencies of segmented axisymmetric shells”. Thin-Walled Structures, 44, pp. 281–289, 2006.
5. A. El Damattya, M. S. Saafana, and A. M. I. Sweedan, “Dynamic characteristics of combined conical-cylindrical shells”. Thin-Walled Structures, 43, pp. 1380–1397, 2005.
6. T. Irie, G. Yamada and Y. Muramoto, “Free vibration of joined conical-cylindrical shells, journal of sound and vibration, 95(1), pp. 31-39, 1984.
7. FE package (ANSYS).

Table 1: Geometrical data of test Specimens

Sample No.	Semi Cone-angle	Orientation	Thickness (mm)	Mass (gm)
1	15°	0-90-0	1.73	499
2	30°	0-90-0	1.746	461.5
3	45°	0-90-0	1.93	500.5
4	60°	0-90-0	1.825	439.5

Table 2: Results of Tensile tests of orthotropic specimens.

Specifications	Orthotropic specimens
E_1	9.27 GPa
E_2	1.8278 GPa
E_3	1.8278 GPa
G_{12}	1.1755 GPa
G_{13}	1.1755 GPa
G_{23}	0.9607 GPa
ν_{12}	0.43
ν_{13}	0.43
ν_{23}	0.66
Density	1452 (kg/m^3)
Volume fraction	0.11

Table 3: Values of the maximum nodal amplitudes (translation and rotation) of the first normal mode of the coupled cone-cylinder shell structure made of orthotropic material.

Semi - cone angle	**Translation**			**Rotation**		
	x	y	z	x	y	z
15°	0.39	2.74	2.74	2.7	7.72	4.34
30°	0.466	0.248	2.7	2.39	8.7	3.92
45°	0.5	2.73	2.7	11.45	9.0	8.0
60°	0.48	0.17	2.6	2	9.04	4.8

Table 4: Values of the maximum nodal amplitudes (translation and rotation) of the first normal mode of the coupled cone-cylinder shell structure made of orthotropic material

Semi - cone angle	**Translation**			**Rotation**		
	x	**y**	**z**	**x**	**y**	**z**
30°	0.54	2.46	1.5	1.646	7.75	10.3
45°	0.57	0.26	2.8	1.726	12.96	5.76
60°	0.58	1.42	2.348	1.883	12.43	9.32

Fig.1: The wooden molds (up) and the female mold (down)

Fig. 2: The final molds

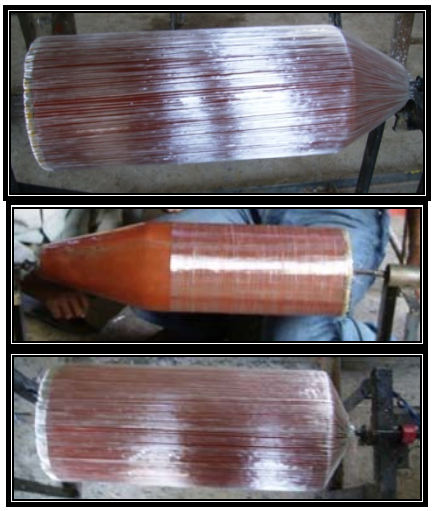

Fig. 3: Applying the E-glass to the mold

Fig. 4: A basic winding machine

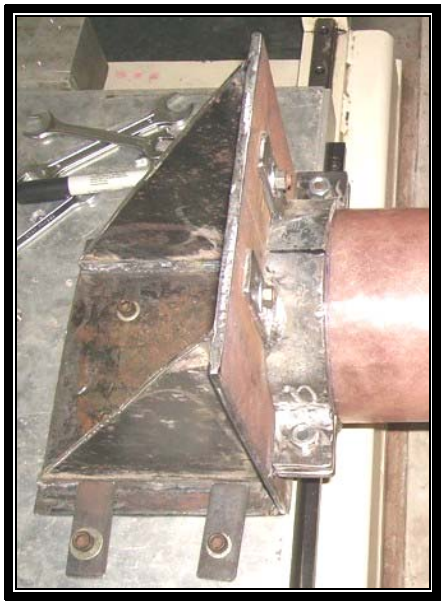

Fig. 5: The fixed end of the structure

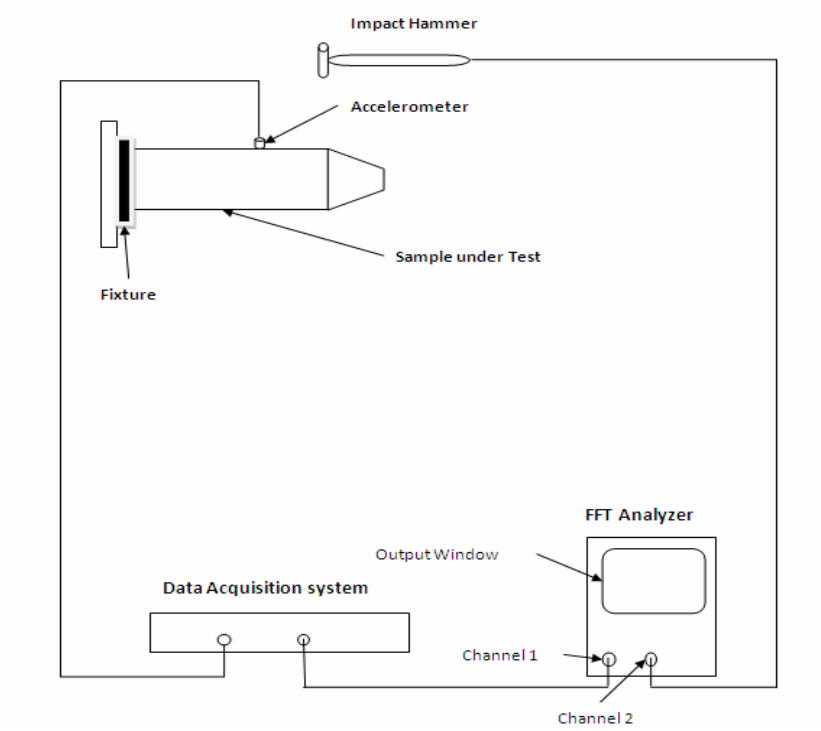

Fig. 6: A schematic diagram for the experimental set-up

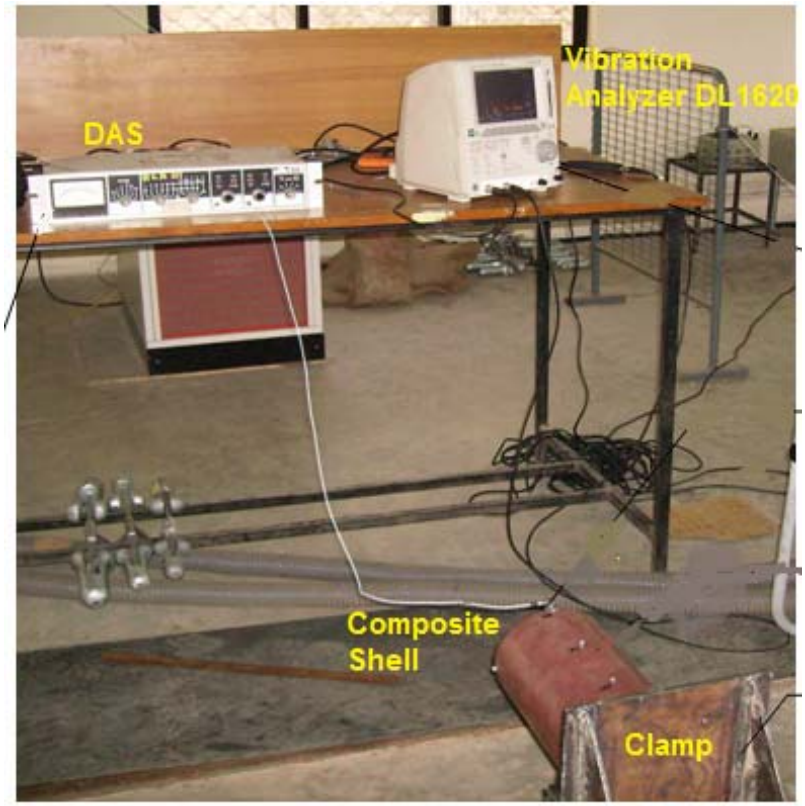

Fig. 7: The test rig

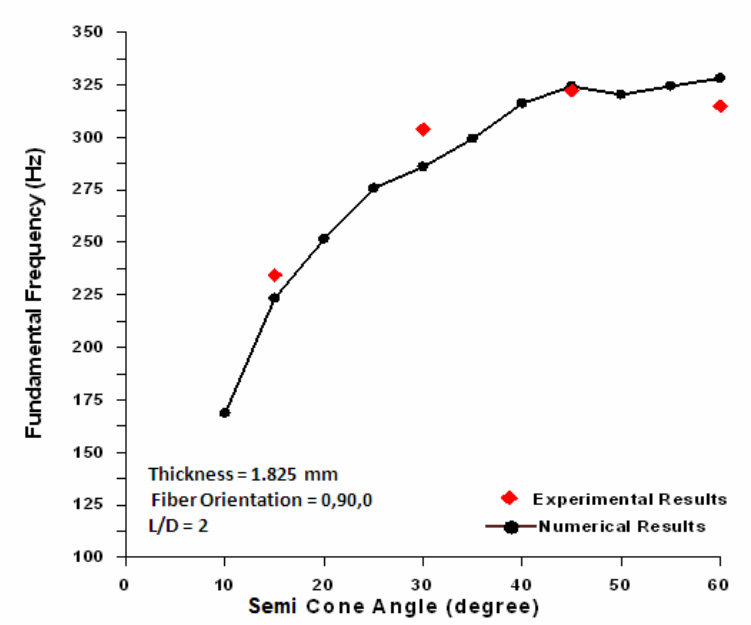

Fig.8: Fundamental frequencies of the coupled shell structures, made of orthotropic material, having different semi-angle of cone.

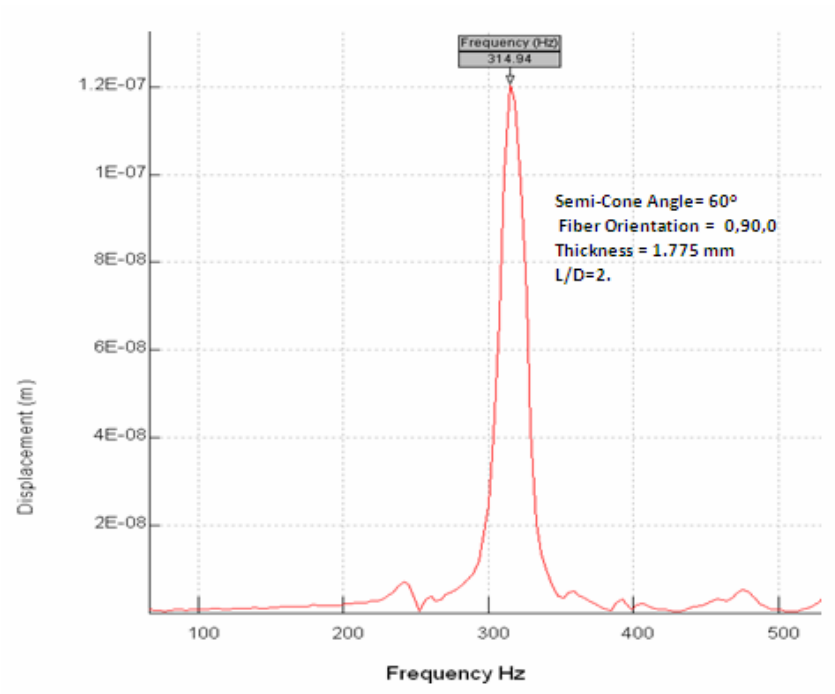

Fig. 9: Experimental results of the displacement response spectrum of the coupled Cylindrical-Conical shell structure.

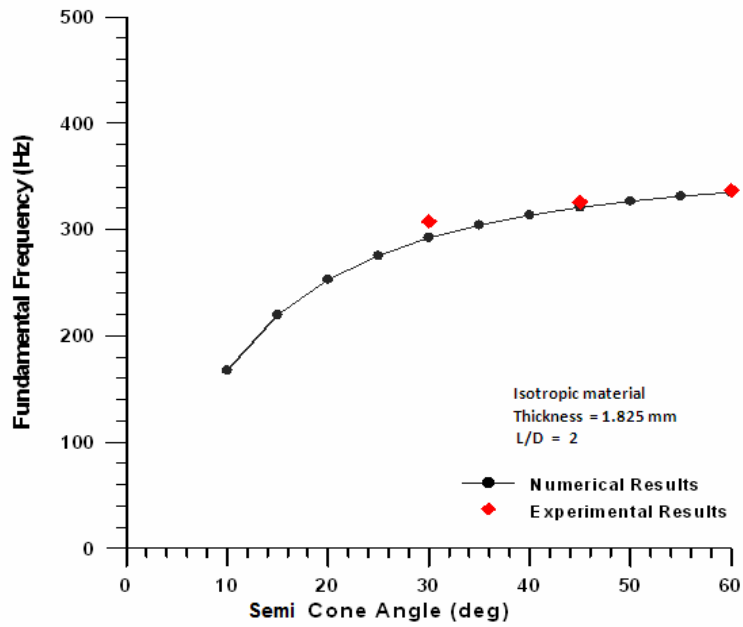

Fig. 10: Fundamental frequencies of the coupled shell structures, made of isotropic material, having different semi-angle of cone.

PARAMETRIC STUDY OF LAMINAR FREE CONVECTION IN INCLINED POROUS ANNULUS WITH FINS ON THE INNER CYLINDER

Dr. Saad M. AL-Mashaat
Ass. Prof. /University of Baghdad

Manal H. AL-Hafidh
Ass. Prof. /University of Baghdad

ABSTRACT

An experimental and numerical study has been carried out to investigate the heat transfer by natural convection in a three dimensional annulus enclosure filled with porous media (silica sand) between two inclined concentric cylinders with (and without) annular fins attached to the inner cylinder under steady state condition; The experiments were carried out for a range of modified Rayleigh number ($0.2 \leq Ra^* \leq 11$) and extended to $Ra^*=500$ for numerical study, annulus inclination angle of ($\delta = 0^\circ, 30^\circ, 60^\circ$ and 90°). The numerical study was to write the governing equation under an assumptions used Darcy law and Boussinesq's approximation and then solved numerically using finite difference approximation. It was found that the average Nusselt number depends on (Ra^*, Hf, δ and Rr) and the maximum value of the local Nusselt number for vertical cylinder is about two times as large as that of the horizontal case. The results showed that, increasing of fin length increases the heat transfer rate for any fins pitch unless the area of the inner cylinder exceeds that of the outer one, then the heat will be stored in the porous media. A correlation for Nu in terms of Ra, Rr and δ, has been developed for inner cylinder. A comparison was made between the results of the present work and with other researches for the case without fins and excellent agreement was obtained and reveals deviation less than 5 % for average Nusselt number.

دراسة إستدلالية للحمل الحر الطباقي في فجوة حلقية مملوءة بوسط مسامي مع زعانف على الأسطوانة الداخلية

الخلاصة:

أجريت في هذا البحث دراسة عملية ونظرية لإنتقال الطاقة الحرارية بالحمل الحر في فجوة حلقية ثلاثية الأبعاد مملوءة بوسط مسامي(رمل) بين أسطوانتين مائلتين متحدتي المركز بوجود (وعدم وجود) زعانف متصلة بالإسطوانة الداخلية تحت شروط حالة الإستقرار. أجريت التجارب العملية لمدى عدد رالي المعدل ($0.2 \leq Ra^* \leq 11$) ولمدى $Ra^*=500$ في الجزء النظري ولزاوية ميل ($\delta = 0^\circ, 30^\circ, 60^\circ$ and 90°). تم كتابة المعادلات الحاكمة في الدراسة النظرية تحت فرضيات قانون دارسي وتقريب بوسنسك وتحويلها الى معادلة بدلالة الجهد المتجه والتي بدورها حلت عدديا باستخدام طريقة الفروق المحددة. تتضمن إمكانية الحل العددي حساب الجهد المتجه ودرجة الحرارة وعدد نسلت الموقعي والمتوسط. بينت النتائج أن عدد نسلت المتوسط يعتمد على عدد رالي المعدل وطول الزعنفة وزاوية ميل الأسطوانة ونسبة الأقطار، وأن أقصى عدد نسلت الموقعي للأسطوانة العمودية حوالي الضعف لتلك في حالة الأسطوانة الأفقية. بينت النتائج أن زيادة طول الزعنفة لأي خطوة زعنفة يسبب زيادة في أنتقال الطاقة الحرارية إلا في حالة زيادة المساحة السطحية للأسطوانة الداخلية على تلك التي للأسطوانة الخارجية فإن ذلك يتسبب في خزن الطاقة الحرارية في الوسط المسامي. مثلت النتائج العملية والنظرية بمعادلات تجريبية للأسطوانة الداخلية تربط عدد نسلت الموقعي بعدد رالي المعدل ونسبة الأقطاروزاوية الميل. قورنت النتائج للبحث الحالي مع نتائج بحوث أخرى في حالة عدم وجود زعانف وأعطت توافق جيد بنسبة إنحراف 5% لعدد نسلت المتوسط.

KEY WORDS: natural convection, three dimensional, inclined annulus, porous media and annular fins

INTRODUCTION:

Recent advances in heat transfer and fluid mechanics, together with the development of large digital computers has made feasible the study of many natural phenomena of great practical importance. A case in point is the analysis of enclosure problem (free convection of a fluid in an annular container)

Also natural convection in porous annuli has a wide variety of technological applications such as the insulation of an aircraft cabin and thermal insulation of buildings or horizontal pipes, reactors, the storage of thermal energy, and underground cable systems, ground water flows oil recovery processes and geological of high – level nuclear waste, food processing, design of regenerative heat exchangers and solar energy collectors etc. representative reviews of these applications and other convective heat transfer applications in porous media may be found in the resent books and researches by **(Prasad et.al., 1985), (Prasad 1986), (Nield and Bejan, 1999) and (Taha et. al., 2004).**

A genetic algorithm was used by **(Giampietro, 2005)** to find the optimum profile of longitudinal convective heat dissipating fins located in a tube where a viscous fluid passes through in laminar flow. To this aim, velocity and temperature distributions in the finned tube were determined with the help of a finite element model, which took the effect of viscous dissipation into account. A global heat transfer coefficient was consequently calculated. After having assigned a polynomial lateral profile to the fins of the tube, the geometry was then optimized in order to maximize the heat transferred per unit of tube length respecting constraints on the tube weight or the pressure drop along the duct.

(Irfan et. al., 2006) investigated the steady state heat transfer in a porous medium fixed in a vertical annular cylinder. The Darcy model of flow is employed. The inner surface of the vertical annulus was maintained at constant wall temperature and the outer surface remains at ambient temperature and the heat transfer was assumed to take place by convection and radiation for Ra range (50 -200). The equations governing the flow behavior are solved using finite element method. The results show that when the radius ratio increased the isotherm of the fluid as well as solid phase move toward the hot surface and away from cold surface. It's found that the Nusselt number of the solid phase does not vary much with respect to aspect ratio ($0 < A < 10$) of the annulus when the inter phase heat transfer coefficient and the modified conductivity ratio is small. The Nusselt number of the fluid phase decrease with increase of the inter phase heat transfer coefficient whereas the Nusselt number of the solid increase with the increase of the inter phase heat transfer coefficient.

Natural convection heat transfer between two horizontal concentric cylinders with two fins attached to the inner cylinder was numerically investigated by **(Alshahrani and Zeitoun, 2007)** using finite element technique together with SIMPLER algorithm. Laminar conditions up to Rayleigh number Ra of 5×10^4 were investigated as well as effects of annulus diameter ratio, fin length and fin inclination angle on this type of flow. A conduction thermal resistance of finned annulus was obtained by means of conduction heat transfer analysis. The thermal

resistance decreases as fin length increases or as annulus diameter ratio decreases. Results of natural convection in finned annuli were presented in the forms of streamlines and isothermal plots. Data of heat transfer in annuli were presented in terms of Nusselt number and effective thermal conductivity ratio ke/k versus Rayleigh number.

To extend the existing studies, the parametric of the three dimensional laminar free convection in an inclined annulus with porous media and with (and without) fins attached to the inner cylinder will be addressed.

EXPERIMENTAL STUDY

Three outer cylinders of different diameters was manufactured to vary the radius ratio and to vary fin length, ten inner cylinders was manufactured one without fins and others with different fin length(Hf =3mm, 7mm and 11mm), radius ratios of ($Rr=(r_1/r_2)$ = 0.293, 0.364 and 0.435), number of fins (n=12, 23 and 45) and pitch length of (s = 19.2mm, 8.4mm and 3mm) to investigate the effect of these parameters and the effect of modified Rayleigh number by the variation of the temperature difference between the two concentric cylinders by means of a variable electric input power. Aluminum was chosen due to its high thermal conductivity and easy machinability. The test section consists of a three Aluminum outer cylinders of (100 mm), (82 mm) and (70 mm) outside diameters, (4 mm) thick and (260mm) long to which ten Aluminum inner cylinders of (27mm) outside diameter, (260 mm) long and (5 mm) thick. The inner cylinder was heated by passing an alternating current to a heater inside the inner cylinder and the outer cylinder was subjected to the surrounding temperature (freezer) where the minimum temperature was 270 K. The inner cylinder surface temperatures were measured at six locations using thermocouples type K.

MATHEMATICAL MODEL

The schematic drawing of the geometry and the Cartesian coordinate system employed in solving the problem is shown in **Fig.1.**

In order to model the incompressible flow in the porous medium, the steady-state equations of the Darcy flow model, namely, the mass, the momentum (Darcy), the energy conservation laws and the Boussinesq's approximation are employed. These equations in vectorial notation are given by **(Nield and Bejan 1999)** and fin equation by **(Ramón and Sergio, 2007).**

Governing Equations

The conservation equations of mass, momentum and energy in steady state and the supplementary equation are:

$$\rho = \rho_2 \{1 - \beta(T - T_2)\} \tag{1}$$

Where:

$$\beta = \frac{1}{\rho}\frac{\partial \rho}{\partial T} \tag{2}$$

β Is the thermal coefficient of the volume expansion, this constant is evaluated at T_2 which is the temperature at the inner surface of the outer cylinder, ρ_2 is the density at T_2 and ρ is the density at T, **(Fukuda et. al.1980)**. This technique is called Boussinesq's approximation.

Mass Conservation

$$\frac{\partial u_r}{\partial r} + \frac{u_r}{r} + \frac{1}{r}\frac{\partial u_\phi}{\partial \phi} + \frac{\partial u_z}{\partial z} = 0 \tag{3}$$

Momentum Equations

The most common model used for flow in the porous media is the Darcy flow model. Darcy's law states that the volume average velocity through the porous material is proportional with the pressure gradient. In three dimensional flows, the Darcy's model **(Wang and Zhang 1990)** is:

Momentum Equation In Radial Direction

$$u_r = \frac{K}{\mu_f}\left[-\frac{\partial p}{\partial r} - \rho\, g\, \cos\phi\, \cos\delta\right] \tag{4}$$

Momentum Equation In Angular Direction

$$u_\phi = \frac{K}{\mu_f}\left[-\frac{1}{r}\frac{\partial p}{\partial \phi} + \rho\, g\, \sin\phi\, \cos\delta\right] \tag{5}$$

Momentum Equation In Axial Direction

$$u_z = \frac{K}{\mu_f}\left[-\frac{\partial p}{\partial z} - \rho\, g\, \sin\delta\right] \tag{6}$$

Energy Equation

$$\frac{\partial(\rho\, C_p T)}{\partial t} + u_r \frac{\partial}{\partial r}(\rho\, C_p T) + \frac{u_\phi}{r}\frac{\partial}{\partial \phi}(\rho\, C_p T) + u_z \frac{\partial}{\partial z}(\rho\, C_p T) = \frac{1}{r}\frac{\partial}{\partial r}\left\{r\frac{\partial(k\, T)}{\partial r}\right\} + \frac{1}{r^2}\frac{\partial^2(k\, T)}{\partial \phi^2} + \frac{\partial^2(k\, T)}{\partial z^2} + \mu\, \Phi \tag{7}$$

Where Φ is viscous dissipation function.

Fin Equation

Within the fin itself, the energy equation is **(Ramón and Sergio, 2007):**

$$\frac{\partial T}{\partial r} + \frac{T}{r} + \frac{1}{r}\frac{\partial T}{\partial \theta} + \frac{\partial T}{\partial z} = 0 \tag{8}$$

Following **(Aziz and Hellums 1967)** a vorticity vector Ω and a vector potential Ψ with its components:

$$\Psi = (\psi_r,\ \psi_\phi,\ \psi_z))$$

Defined by:

$$U = \alpha_{eff.}\ \nabla\ \mathrm{X}\ \Psi \tag{9}$$

$$\nabla^2\psi_r = \frac{1}{R}\frac{\partial U_z}{\partial \phi} - \frac{\partial U_\phi}{\partial Z} \tag{10}$$

$$\nabla^2\psi_\phi = \frac{\partial U_r}{\partial Z} - \frac{\partial U_z}{\partial R} \tag{11}$$

$$\nabla^2\psi_Z = \frac{1}{R}\frac{\partial(RU_\phi)}{\partial R} - \frac{1}{R}\frac{\partial U_r}{\partial \phi} \tag{12}$$

Non Dimensional Variables

The characteristic length for the present study is r_2 **(Fukuda et. al.1980)** to convert the governing equations to the dimensionless form, the dimensionless magnitudes must be defined as follow:

$$R = \frac{r}{r_2},\quad Z = \frac{z}{r_2},\quad U_r = \frac{u_r\, l}{\alpha_m},$$

$$U_\phi = \frac{u_\phi\, l}{\alpha_{eff}}, U_z = \frac{u_z\, l}{\alpha_{eff.}},$$

$$\theta = (T - T_2)/(T_1 - T_2),\quad P = \frac{p\, K\, l}{\alpha_{eff}\ \mu_f\ r_2},$$

,

$$Ra^* = g\ \beta\ K\ (T_1 - T_2)\ (r_2 - r_1)/\alpha_{eff.}\ \upsilon$$

$$S_1 = \frac{s}{2\ r_2},\ S_2 = \frac{\frac{s}{2}+t}{r_2} \quad H_1 = \frac{H_f}{r_2}$$

Substitute these dimensionless magnitudes in the governing equations. Alternative expressions of eq. (3) may be written in terms of $\psi_r,\ \psi_\phi\ and\ \psi_z\ as:$

$$U_r = \left(\frac{1}{R}\frac{\partial\psi_z}{\partial\phi} - \frac{\partial\psi_\phi}{\partial Z}\right) \tag{13}$$

$$U_\phi = \left(\frac{\partial\psi_r}{\partial Z} - \frac{\partial\psi_z}{\partial R}\right) \tag{14}$$

$$U_z = \frac{1}{R}\left\{\frac{\partial}{\partial R}\left(R\ \psi_\phi\right) - \frac{\partial\psi_r}{\partial\phi}\right\} \tag{15}$$

Taking curl of momentum equations to eliminate pressure terms, the momentum equations will be:

$$Ra^*\ \frac{l}{(r_2 - r_1)}\left(\frac{1}{R}\sin\delta\frac{\partial\theta}{\partial\phi} + \sin\phi\ \cos\delta\frac{\partial\theta}{\partial Z}\right) =$$
$$-\frac{\partial^2\psi_r}{\partial R^2} - \frac{1}{R^2}\frac{\partial(R\psi_r)}{\partial R} - \frac{2}{R}\frac{\partial\psi_r}{\partial R} - \frac{1}{R^2}\frac{\partial^2\psi_r}{\partial\phi^2}$$
$$-\frac{\partial^2\psi_r}{\partial Z^2} - \frac{2}{R}\frac{\partial\psi_z}{\partial Z} \tag{16}$$

$$Ra^*\ \frac{l}{(r_2 - r_1)}\left(\cos\phi\ \cos\delta\frac{\partial\theta}{\partial Z} - \sin\delta\frac{\partial\theta}{\partial R}\right) =$$
$$-\frac{\partial^2\psi_\phi}{\partial Z^2} - \frac{\partial^2\psi_\phi}{\partial R^2} - \frac{1}{R^2}\frac{\partial^2\psi_\phi}{\partial\phi^2}$$
$$-\frac{2}{R^2}\frac{\partial\psi_r}{\partial\phi} + \frac{\psi_\phi}{R^2} - \frac{1}{R}\frac{\partial\psi_\phi}{\partial R} \tag{17}$$

$$-Ra^*\ \frac{l}{(r_2 - r_1)}\ \cos\delta\left(\frac{1}{R}\cos\phi\frac{\partial\theta}{\partial\phi} + \sin\phi\frac{\partial\theta}{\partial R}\right) =$$
$$-\frac{\partial^2\psi_z}{\partial R^2} - \frac{1}{R}\frac{\partial\psi_z}{\partial R}$$
$$-\frac{1}{R^2}\frac{\partial^2\psi_z}{\partial\phi^2} - \frac{\partial^2\psi_z}{\partial Z^2} \tag{18}$$

The vector potential equation was obtained in the dimensionless form as

$$\nabla^2\psi_r = \frac{\partial^2\psi_r}{\partial R^2} - \frac{1}{R^2}\frac{\partial(R\ \psi_r)}{\partial R}$$
$$-\frac{2}{R}\frac{\partial\psi_r}{\partial R} - \frac{1}{R^2}\frac{\partial^2\psi_r}{\partial\phi^2}$$
$$-\frac{\partial^2\psi_r}{\partial Z^2} - \frac{2}{R}\frac{\partial\psi_z}{\partial Z} \tag{19}$$

$$\nabla^2\psi_\phi = -\frac{\partial^2\psi_\phi}{\partial Z^2} - \frac{\partial^2\psi_\phi}{\partial R^2} - \frac{1}{R^2}\frac{\partial^2\psi_\phi}{\partial\phi^2}$$
$$-\frac{2}{R^2}\frac{\partial\psi_r}{\partial\phi} + \frac{\psi_\phi}{R^2} - \frac{1}{R}\frac{\partial\psi_\phi}{\partial R} \tag{20}$$

$$\nabla^2\psi_z = -\frac{\partial^2\psi_z}{\partial R^2} - \frac{1}{R}\frac{\partial\psi_z}{\partial R}$$
$$-\frac{1}{R^2}\frac{\partial^2\psi_z}{\partial\phi^2} - \frac{\partial^2\psi_z}{\partial Z^2} \tag{21}$$

And the energy equation will be:

$$\left(\frac{1}{R}\frac{\partial\psi_z}{\partial\phi} - \frac{\partial\psi_\phi}{\partial Z}\right)\frac{\partial\theta}{\partial R} + \frac{1}{R}\left(\frac{\partial\psi_r}{\partial Z} - \frac{\partial\psi_z}{\partial R}\right)\frac{\partial\theta}{\partial\phi}$$
$$+\left(\frac{\psi_\phi}{R} + \frac{\partial\psi_\phi}{\partial R} - \frac{1}{R}\frac{\partial\psi_r}{\partial\phi}\right)\frac{\partial\theta}{\partial Z}$$
$$= \frac{l}{r_1}\left[\frac{\partial^2\theta}{\partial R^2} + \frac{1}{R}\frac{\partial\theta}{\partial R} + \frac{1}{R^2}\frac{\partial^2\theta}{\partial\phi^2} + \frac{\partial^2\theta}{\partial Z^2}\right] \tag{22}$$

And fin equation will be:

$$\frac{\partial\theta}{\partial R}+\frac{\theta}{R}+\frac{1}{R}\frac{\partial\theta}{\partial\phi}+\frac{\partial\theta}{\partial Z}=0 \qquad (23)$$

Dimensionless Hydraulic Boundary Conditions

For the vector potential field, the boundary conditions are given as:

$$\frac{1}{R}\frac{\partial}{\partial R}\left(R\psi_r\right)=\psi_\phi=\psi_z=0 \qquad at\, R=R_1,1$$

$$\psi_r=\frac{\partial\psi_\phi}{\partial\phi}=\psi_z=0 \qquad at\,\phi=0,\ \pi$$

$$\psi_r=\psi_\phi=\frac{\partial\psi_z}{\partial Z}=0 \qquad at\, Z=0,\ L$$

And for the fin, the boundary conditions are given as:

$$\frac{1}{R}\frac{\partial}{\partial R}\left(R\,\psi_r\right)=\frac{\partial\psi_\phi}{\partial\phi}=\frac{\partial\psi_Z}{\partial Z}=0$$

On the fin faces which were located on the following planes

(fin base)

At R = R_1 *for* $\phi = 0, \pi$
See **Fig.2**

(fin tip)

At $r = r_1+H_f$ *for* $\phi = 0, \pi$

At S_1 *and* S_2 *for any r and* ϕ

Dimensionless Thermal Boundary Conditions

For the temperature field, the dimensionless thermal boundary conditions are:

$$\theta=1 \qquad at\ R=R_1=r_1/r_2$$

$$\theta=0 \qquad at\ R=R_2=1$$

$$\frac{\partial\theta}{\partial\phi}=0 \qquad at\ \phi=0,\ \pi$$

$$\frac{\partial\theta}{\partial Z}=0 \qquad at\ Z=0,\ L$$

$at\ R=H_1$

$$-k_{fin}\frac{\partial\theta}{\partial R}\Big|_{fin}=-k_{eff.}\frac{\partial\theta}{\partial R}\Big|_{medium}$$

$at\ S_1$ $at\ any\ R\ and\ \phi$

$at\ S_2$ $at\ any\ R\ and\ \phi$

$$-k_{fin}\frac{\partial\theta}{\partial Z}\Big|_{fin}=-k_{eff.}\frac{\partial\theta}{\partial Z}\Big|_{medium}$$

$at\ \phi = 0,\ \pi$ $and\ any\ R$

$$-k_{fin}\frac{\partial\theta}{\partial\phi}\Big|_{fin}=-k_{eff.}\frac{\partial\theta}{\partial\phi}\Big|_{medium}$$

Where

$$k_{ef}=\left(1-\varepsilon\right)k_s+\varepsilon\,k_f \qquad (24)$$

COMPUTATIONAL TECHNIQUE

Eq. (16, 17, 18, 22 and 23) were transformed into the finite difference equations, where the upwind differential method in the left hand side of the energy eq.(22) and the centered – space differential method for the other terms were used, and solved by using (SOR) method **(Wang and Zhang 1990).** A computer program was built using Fortran 90 language to meet the requirements of the problem.

The value of the vector potential ψ will be calculated at each node, in which the value of vector potential is unknown, the other node

will appear in the right hand side of each equation. As an initial value of iteration, zero is chosen for the vector potential field, while a conduction solution is adopted for temperature field. The index (n) was used to represent the nth – approximation of temperature denoted by θ^n and substituted into the approximated equations, which were solved to obtain the nth approximation of vector potential ψ, then ψ was substituted into eq. (22) to obtain θ^{n+1}. A similar procedure is repeated until the prescribed convergence criterion given by inequality:

$$Max \left| \frac{\theta^{n+1} - \theta^n}{\theta^n} \right| \leq 10^{-8}$$

was established **(Fukuda et. al. 1980).**

It is clear that as the grid becomes finer, the convergence of the results becomes better. The number of grid points used was 21 grid points in the R – direction, 31 in the ϕ – direction and 301 in the Z – direction which seems reasonable and will be used in the present study.

Calculation of Local and Average Nusselt Number

Local Nusselt number is the dimensionless parameter indicative of the rate of energy convection from a surface and can be obtained as follows **(Fukuda et.al. 1980]:**

$$Nu = \frac{q(r_2 - r_1)}{k(T_1 - T_2)} \qquad (25)$$

The local Nusselt number Nu_1 and Nu_2 on the inner and the outer cylinders are written in the form **(Fukuda et.al. 1980):**

$$Nu_1 = -(1 - R_1) \left(\frac{\partial \theta}{\partial R} \right)_{R=R_1} \qquad (26)$$

$$Nu_2 = -(1 - R_1) \left(\frac{\partial \theta}{\partial R} \right)_{R=1_1} \qquad (27)$$

The average Nusselt number Nu_{in} and Nu_{out} on the inner and the outer cylinders are defined as:

$$Nu_{in} = -(1 - R_1) \frac{1}{\pi L} \int_0^L \int_0^\pi \left(\frac{\partial \theta}{\partial R} \right)_{R=R} d\phi \, dZ \qquad (28)$$

$$Nu_{out} = -(1 - R_1) \frac{1}{\pi L} \int_0^L \int_0^\pi \left(\frac{\partial \theta}{\partial R} \right)_{R=1} d\phi \, dZ \qquad (29)$$

RESULTS AND DISCUSSION

Temperature Field

The dimensionless temperature distribution within the enclosure is presented in a contour map form. One section was selected in the (Z-R) plane along the length of the annulus, and two others in the (R-□) plane in the top and bottom of the annulus, in a manner allowed studying the temperature distribution within each plane.

Fig.3 shows the symmetry of the temperature distribution for horizontal annulus and it was observed that as Rr decrease, isotherms shift towards the outer (cold) cylinder and the waviness will be clear due to the existence of the fins as shown in **Fig.4.** Increase Ra^* and/or decrease in radius ratio results in a thicker cold layer near the bottom wall and a high temperature field near the top wall. More heat is transported upward, and a large difference of temperature is observed between the upper and lower parts of the annulus as shown in **Fig. 5-6**. A reduction in the isotherms observed at the ends of the annulus which was due to the losses of heat transfer by

conduction through the sides (Teflon pieces) and increase as the radius ratio decrease (in other word as the outer radius increase). As Ra^* increase and/or H_f increase, the temperature distribution on the upper boundary gets closer to the temperature distribution predicted for perfectly insulated boundary conditions. Hence the effects of conduction loss through the sides diminish. A swell of the isothermal lines can observed when Ra^* increase which implies a low Nu on the inner cylinder and a high Nu on the outer cylinder. For the same fin length, decreasing fin pitch (in other word increasing the number of fins) cause more shift of the isotherms to the outer cylinder. For vertical annulus the warm region was adjacent to the insulated top wall (see **Fig. 6)** and a decrease of Rr introduce increase in temperature much faster near the hot wall and much slower near the cold wall. This further indicates that the sink temperature for the boundary layer on the hot wall reduces as the curvature effects increase. Also, for low radius ratios, the conduction in the core is very small for any given Ra^*. Previous figures show that for the same H_f and n, increasing the annulus inclination angle from $\delta=0^\circ$ to 60° cause the symmetry of temperature distribution to vanish and an increase in the region of temperature distribution clarify. Since this research was achieved for a steady state laminar region, thus the warm region at the top end when $\delta=90^\circ$ come to be as a concentric circles located at the center of the annulus and distributed between the hot and cold cylinders **Fig. 6.**

When the surface area of the inner cylinder is less than that for outer cylinder and referring to the equation of heat transfer

$$Q = h_i \; A_{in}\left(T_1 - T_2\right) = h_o \; A_{out}\left(T_1 - T_2\right),$$

h_i will be greater than h_o and owing to this Nu_{in} will be greater than Nu_{out} because the thermal resistance on the inner surface is less than that on the outer one, thus the heat will be transferred to the outer cylinder and the isotherms shift outward. Increasing H_f and decreasing the pitch (i.e. increasing the number of fins) to the limit cause A_{in} to be greater than A_{out}, cause the thermal resistance on the inner surface to be increased causing the heat to be stored in the porous media.

Velocity Fields, Vector Potential and Effect of Inclination

For a horizontal annulus without fins, U_z has constant value along the length of the cylinder for all values of Rr and increasing δ to 30 □ and 60 □ cause the existence of unicellular and bicellular flow which cause the velocity to increase and fluid flow toward the top of the annulus. **Fig.7** illustrates a high values of the velocity on the two faces of the fins and on the tip causing the fluid to rise up toward the outer cylinder and decreasing Rr (increasing the outer radius) cause the fluid to cooled before reaching the outer cylinder and its velocity will be reduced. The existence of fins cause the flow to be wavy which in turn enhance the heat transfer toward the outer cylinder but increasing the number of fins or decreasing Rr cause this wavy flow to diminish. The growths of the boundary layers on the vertical wall are also observed to be affected by variation of Rr. The decrease in Rr is seen to reduce the rate of boundary layer growth on the hot wall as shown in **Fig. 8-9.** This behavior is reversed on the cold wall. The net result is a shift of the core toward the top edge of the cooled

wall. This shift is further strengthening if there is an increase in Ra^*. Generally higher convective velocities in the top right – hand corner are produced as a result of the shift. The change in the temperature field brings a noticeable change in the flow patterns as compared to those in vertical annulus as in **Fig.10** for δ = 90 □.

In the (R-□) plane, the radial velocity was not uniform and there exist two cellular; one for negative or low velocity near the outer cylinder and the other for the positive or high velocity near the inner cylinder which move away to the outer cylinder with the decreasing of Rr.

The gravity acceleration vector which aligned with the flow and the density imbalance helps the circulation of the fluid inside the enclosure. When the angle of inclination is zero, the gravity acceleration component aligned with the vertical stream flows is in maximum value, whereas at the horizontal stream flow, the gravity acceleration component is equal zero because it is in the right angle to the flow. As the enclosure inclined in an intermediate angle the gravity acceleration component which is aligned with the stream flow is not zero in all the directions. Therefore, the mass density differences due to the temperature differences of the fluid in all directions can increase the driving force. It is clear that, the influences of increasing the angle of inclination become an increase in the length and/or turn the direction of the streams in a manner of increasing the convection flow.

Fig.11 illustrates for δ =90 □, the regions of high and low velocities in the two sides of each fin which are an indication to the enhancing of heat transfer due to the existence of these fins; as δ increase these regions vanish.

Increasing the number of fins and/ or the length of fins for constant Rr, cause U_r to increase in the region away from the inner cylinder because these fins considered to be a hinder for the movement of the fluid.

Figs. 3-6 show the R – component of the vector potential ψ_r. **Fig.3** illustrates the contour as unicellular of negative value at the center and positive at the boundaries, as the number of fins increase the negative streams abate and the cellular calm down. The same behavior was observed as H_f increased and so was observed as Rr decrease as shown in **Figs. 4-6** and/or as Ra^* decrease as shown in **Fig. 3.**

Figs.12 shows the existence of two regions one of negative stream and another of positive one which extended to the outer cylinder taking larger area as Rr decrease. As δ increase, the stream appear at the bottom of the annulus upper the inner cylinder and another one at the top lower the surface of the inner cylinder extended along the length of the cylinder, its strength increase far away from the surface of the cylinders and its value become zero or negative at the boundaries of the inner and outer cylinders. These Figures show that increasing fin length cause to decrease the strength of the stream.

Effect of Modified Rayleigh number and Other Parameteres

Fig. 13 shows the variation of the average Nusselt number on the hot cylinders with Ra^* for different radius ratios, without and with fins respectively. These figures show that for any radius ratio, the average *Nu* generally constant for low values of Ra^*, this indicate that *Nu* hardly affected by δ for low Ra^*, then as Ra^* reached nearly 100, *Nu* increased with increasing Ra^*. These values increased

as *Rr* decrease due to the enlarge of the distance between the two cylinders. For low values of Ra^*(with or without fins), the maximum values of *Nu* was for maximum *Rr* until Ra^* reached nearly 100, then the situation will inverse and the maximum values of *Nu* would be for minimum *Rr* which improve that for low values of Ra^* the heat transferred by conduction and as Ra^* increased the convection heat transfer would be the dominant. The results show as Ra^* exceed 100, the value of *Nu* increase and as H_f increase *Nu* decrease and decreasing the pitch (by increasing fin numbers) cause *Nu* to decrease. In order to reveal the effect of inclination angle and fin number (which is an indication to fin pitch) on the average Nusselt number, a comparison between the curves in **Fig.14** indicates that there is a reduction in the average Nusselt number with increasing the number of fins and δ, and the maximum heat achieved was for horizontal annulus.

Fig.15 indicates that there is a reduction in the average Nusselt number with increasing H_f from 3mm to 11mm. For the same value of Ra^*, reduction in the average Nusselt number may be ranged between (18% to 38 %).

Local and Average Nusselt Number

Distribution of local Nusselt number along the circumstance of hot and cold cylinders is illustrated in **Fig. 16** at three locations; located at the top of the cylinder, at the center of the cylinder and the third at the bottom of the cylinder. These curves illustrate all the cases with and without fins and for different values of parameters. The local Nusselt number on the cold wall had an increasing trend from ($\phi = 0^\circ$) to ($\phi = 180^\circ$), where the highest values were reached. There were three regions which could be distinguished. Most of the experimental values were lower than that of the numerical; one of the reasons may be the conduction losses through the top and bottom and hence the absence of perfectly insulated ends boundaries and this is true even by this research or by **(Prasad and Kulacki 1985) and (Havstad and Burns 1982)**

Fig.16 illustrate For horizontal annulus (δ = 0°), attaching fins to the inner cylinder cause the local Nu to be wavy and this wavy phenomenon increased with the increasing of Ra^* and decreased with decreasing the radius ratio and vanish with the increase of the angle of inclination and/or the number of fins, while increasing the fin length cause a disturb of the flow and an increase in the wavy local Nu would be observed.

To the best of the investigator knowledge there is no previous work was found in the literature that studied the effect of annular fins on heat transfer and fluid flow characteristics of buoyancy driven flow in a three dimensional inclined annulus filled with porous media. Therefore, comparison of the present work (case with fins) with that of the literature cannot be achieved. However, the present work of case without fins can be compared with previous works. A comparison for the variation of the average Nusselt number on the inner and outer cylinders with Ra^* was made with that of **(Fukuda et. al. 1980)** in **Fig. 17** and its clear that Nu is constant for low values of Ra^*, until Ra^* equal nearly 100, then Nu will increase with the increasing of Ra^* as presented in this work.

The comparison was made for streamlines and isotherms for the case of natural convection in a horizontal cylindrical annulus filled with porous layer by**(Charrier and Mojtabi 1991)** as shown in **Fig. 18.**

CONCLUSIONS

The following major conclusions can be drawn from the experimental and numerical study:

1- Average Nu number increases with increasing fin length at the same Ra^* and fin number unless the surface area of the inner cylinder exceeds that of the outer cylinder, then the heat will be stored in the porous media.

2- Maximum value of local Nu number increasing with the increase of inclination angle and it may be reached twice the value of that for horizontal cylinder.

3- For all parameters, results showed that the average Nu number increases with an increase in modified Rayleigh number and hardly affected by δ for low values of Ra^*.

4- Increasing Rr cause a clearly increase in average Nusselt number for Ra^* 100.

5- The peak of the local Nu on the outer cylinder wall generally appeared at a position of Z=L (at the top) and with some deviation from π. while for the inner cylinder the peak appeared at a position of Z=0 (bottom of the cylinder).

REFERENCES

Al-Shahrani D. and Zeitoun O., "Natural Convection in Horizontal Annulus with Attached to Inner Cylinder", Submitted for Publication in Alexandria Engineering Journal, Alexandria, Egept, 2007.

Aziz K. and Hellums J. D., "Numerical Solution of the Three Dimensional Equations of Motion for Laminar Natural Convection", The Physics of Fluids, V0l. 10, No. 2, pp. 314 – 324, 1967

Fukuda K., Takata Y., Hasegawa S., Shimomura H. and Sanokawa K., "Three – Dimensional Natural Convection in a Porous Medium Between Concentric Inclined Cylinders", Proc. 19th Natl Heat Transfer Conf., Vol. HTD – 8, pp. 97 – 103, 1980.

Giampietro Fabbri, "Optimum Cross-Section Design of Internally Finned Tubes Cooled By a Various Fluid", Control Engineering Practice, Vol. 13, pp. 929-938, 2005. www.elsevier.com.

Irfan Anjum Badruddin, Zainal Z. A., Aswatha P. A. and Seetharamu K. N., "Thermal Non-Equilibrium Modeling of Heat Transfer Through Vertical Annulus with Porous Medium", Int. J. Heat and Mass Transfer, Vol. 49, pp. 4955-4965, 2006. www.sciencedirect.com.

Nield D. A. and Bejan A., "Convection in Porous Media", Springer-Verlag, New York, 1999.

Prasad, V. and Kulacki, F. A., "Natural Convection in Porous Media Bounded by Short Concentric Vertical Cylinders", Transaction of ASME, J. of Heat Transfer , Vol. 107, pp. 147-154, February, 1985.

Prasad, V., "Numerical study of Natural Convection in a vertical, Porous Annulus with constant heat flux on the inner wall", Int. J. Heat and Mass Transfer. Vol. 29 No. 6, pp. 841-853, 1986.

Ramón L. F. and Sergio G. M., "Three Dimensional Natural Convection in Finned Cubical Enclosure", Int. J. of Heat and Fluid Flow. Vol. 28, pp. 289-298, 2007.

Taha K Alddoss, Mohammad Alkam and Mohammad Shatrah, "Natural Convection from Horizontal Annulus Partially Filled with a Porous Medium", Int. comm. Heat and Mass Transfer, Vol. 31, No. 3, pp. 441-452, 2004. www.sciencedirect.com.

Wang Bu – Xuan and Zhang Xing, "Natural Convection in Liquid Saturated Porous Media Between Concentric Inclined Cylinders" Int. J. Heat and Mass Transfer Vol. 33. No 5, pp. 827-833, 1990.

NOMENCLATURE

Latin Symbols

Unit	Description	Symbol
kJ/kg □ C	Specific heat at constant pressure	C_p
m/s^2	Acceleration due to gravity	g
m	Fin length	H_f
W/m K	Thermal conductivity of the fluid	k_f
W/m K	Thermal conductivity of the solid	k_s
W/m K	Effective thermal conductivity of the porous media	$K_{eff.}$
m^2	Permeability	K
m	Cylinder length	l
-	Dimensionless cylinder length	L
-	Local Nusselt number on the inner cylinder	Nu_1
-	Local Nusselt number on the outer cylinder	Nu_2
-	Average Nusselt number on the inner cylinder	Nu_{in}
-	Average Nusselt number on the outer cylinder	Nu_{out}
N/m^2	Pressure	p
W	Local heat flux	q
m	Radial coordinate	r
m	Dimensionless radial coordinate	R
-	Modified Rayleigh number	Ra^*
-	Radius ratio	Rr
m	Fin pitch	S
K	Temperature	T
m/s	velocity component in r,□ and z - direction	$u_r, u_{\square}, u_z$
-	Dimensionless velocity component in R, □ and Z direction	U_r, $U_{\square}$, U_z
m	Cartesian coordinate system	x, y, z
-	Dimensionless axial coordinate	Z
	FAI in Fig. 16 means □ (angular direction)	FAI

Greek Symbols

Unit	Description	Symbol
m^2/s	Effective thermal diffusivity	α_{eff}
m^2/s	Medium thermal diffusivity	α_m
1/K	Volumetric thermal expansion coefficient	β
degree	Angle of inclination	δ
-	Dimensionless temperature	θ
-	Vector potential component in R, □ and Z – direction	ψ_r, $\psi_{\square}$, ψ_z

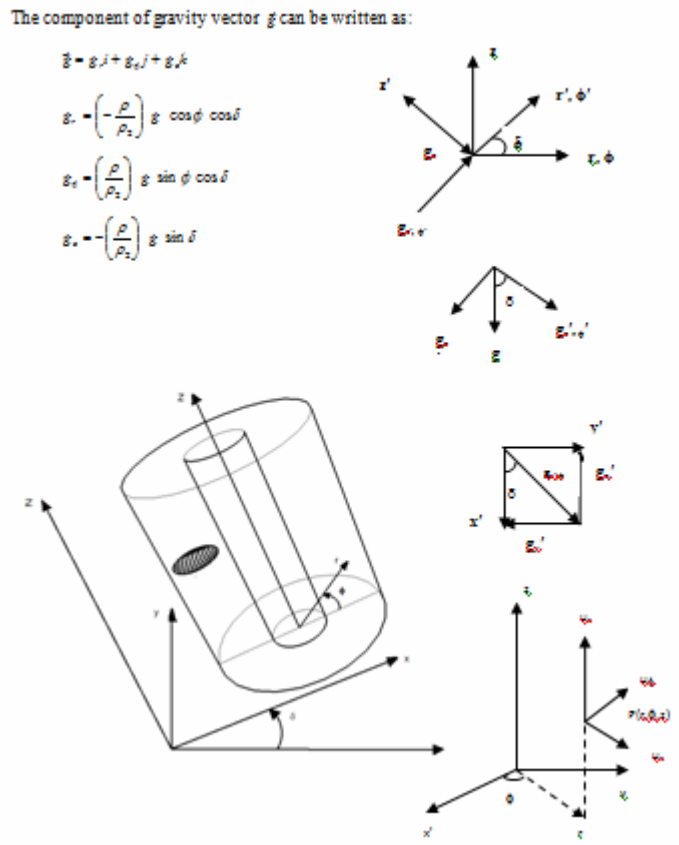

Fig.1 geometry and coordinates system

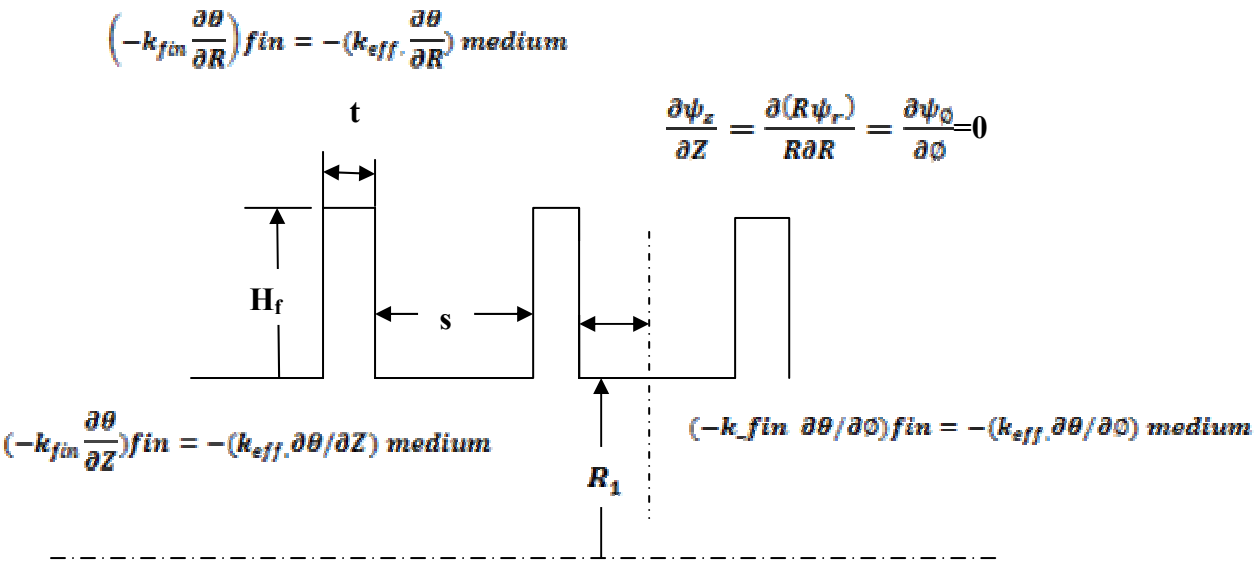

Fig. 2 fin boundary conditions

Top

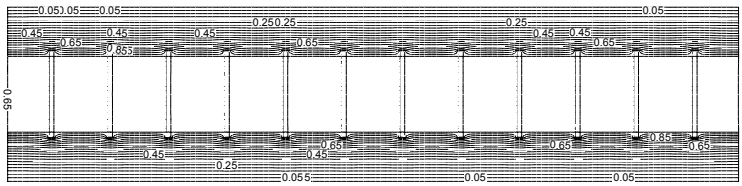

Bottom

a

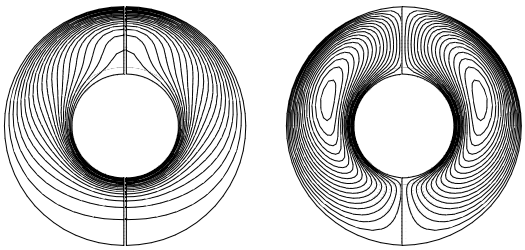

b c

Fig.3 (a) isotherms along the cylinder length (b&c) isotherms and streamlines at the top and bottom sections for Ra^*=500,n=12, Rr=0.435, H_f=3mm

a

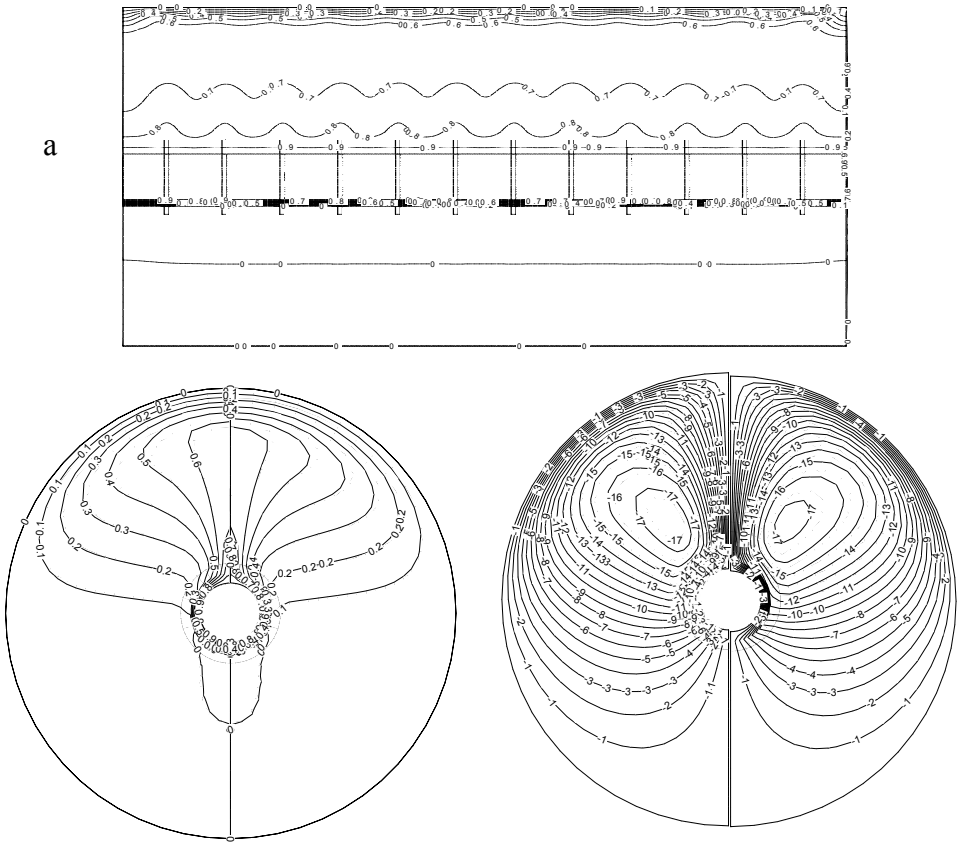

b c

Fig.4 (a) isotherms along the cylinder length (b&c) isotherms and streamlines

at the top and bottom sections for Ra^*=500,n=12, Rr=0.135, H_f=3mm

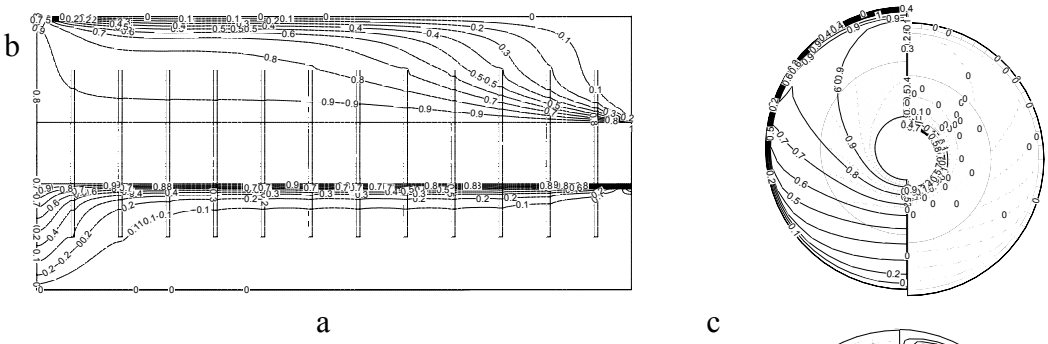

Fig.5 (a) isotherms along the cylinder length (b&c) isotherms and streamlines at the top and bottom sections for Ra^*=500,n=12, Rr=0.225, H_f=11mm,δ=60

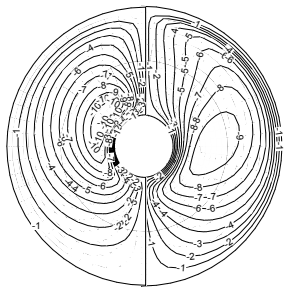

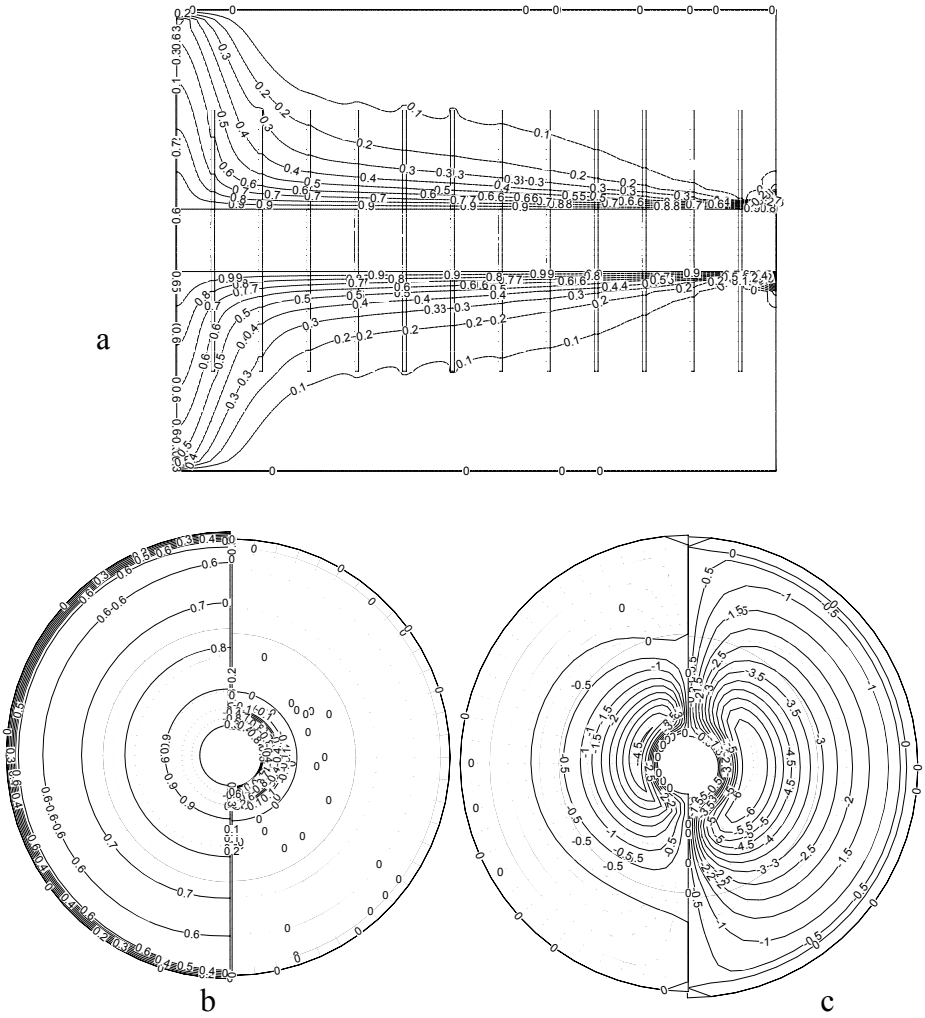

Fig.6 (a) isotherms along the cylinder length (b&c) isotherms and streamlines

at the top and bottom sections for Ra^*=500,n=12, Rr=0.135, H_f=11mm,δ=90□

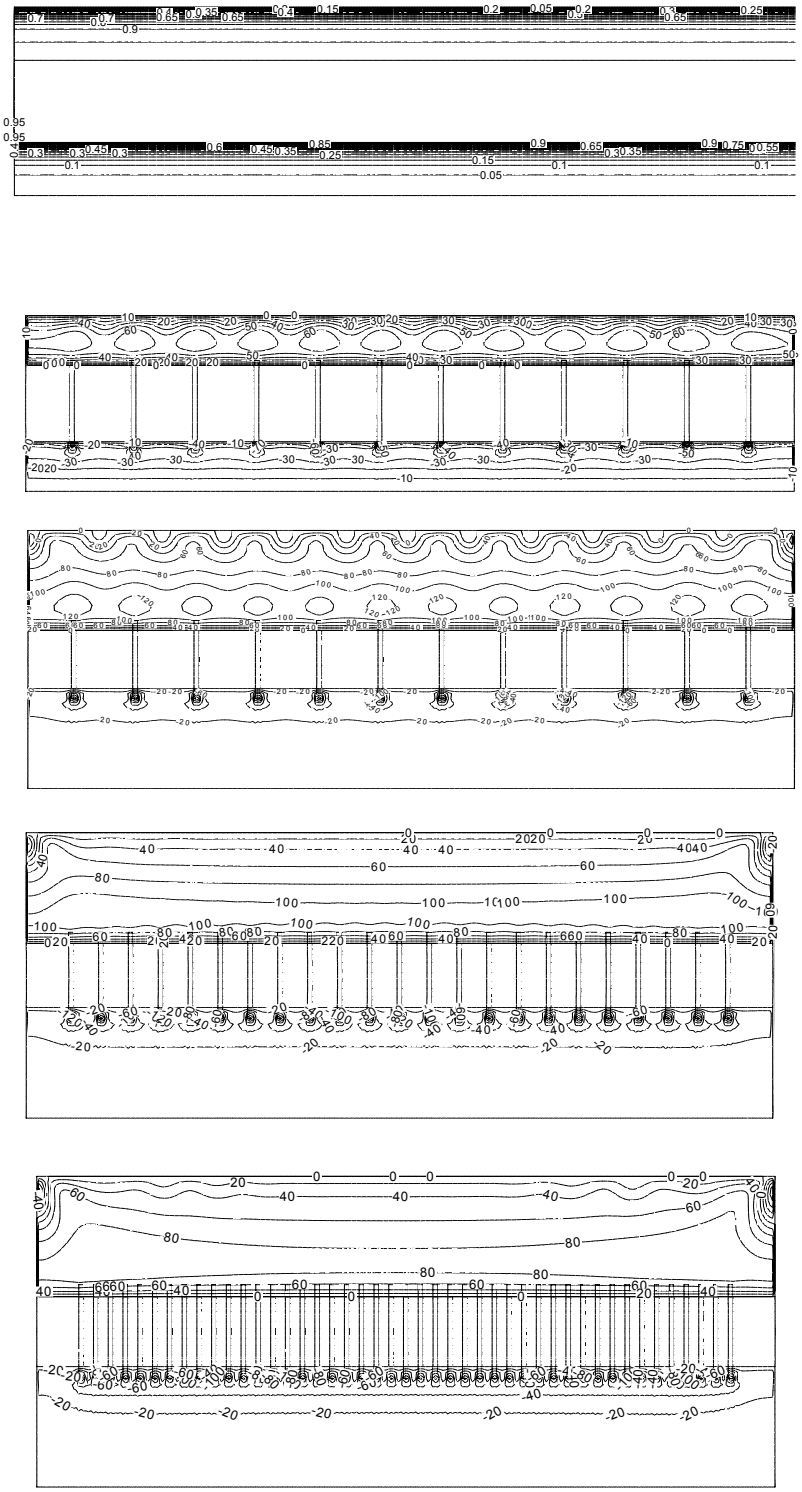

Fig.7 the axial velocity U_z for Ra^*=500,n=0 Rr=0.225, n=12, 23 and 45

H_f=3mm,δ=0□, Rr=0.225 & 0.169 respectively

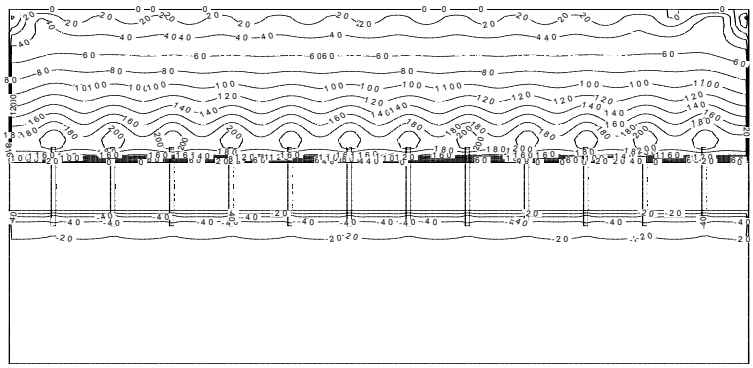

Fig.8 the axial velocity U_z for Ra^*=100,n=12,H_f=3mm,δ=30□, Rr=0.225

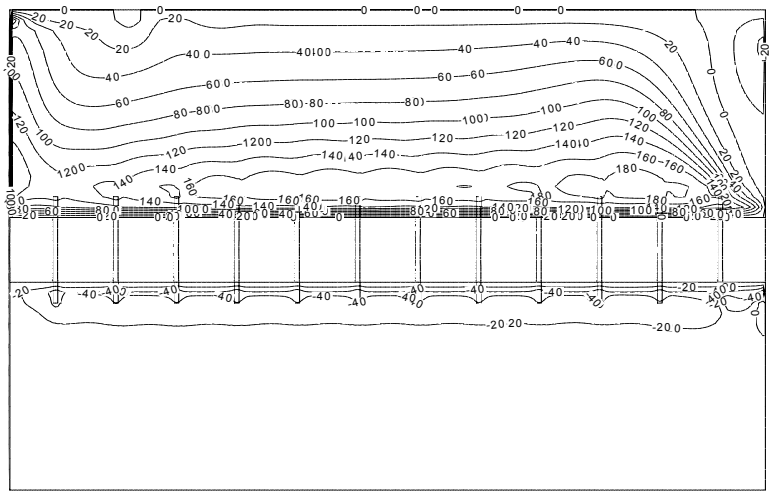

Fig.9 the axial velocity U_z for Ra^*=500,n=12,H_f=3mm,δ=60□, Rr=0.225

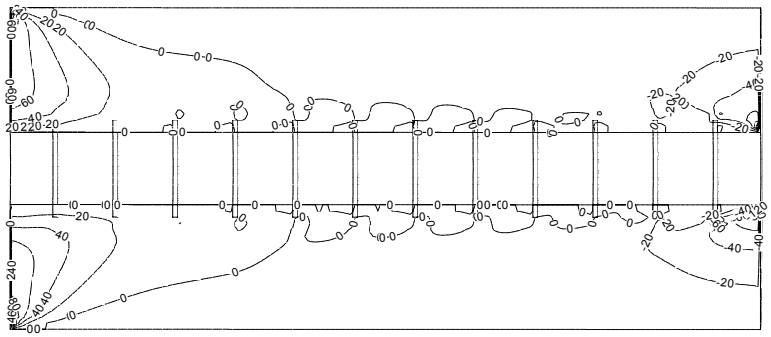

Fig.10 the Axial Velocity U_z for Ra^*=500,n=12,H_f=3mm,δ=90□, Rr=0.225

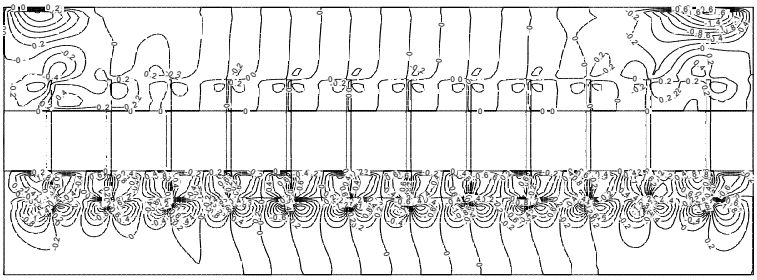

Fig.11 the radial velocity U_r for Ra^*=100,n=12,H_f=7mm,δ=90□,Rr=0.225

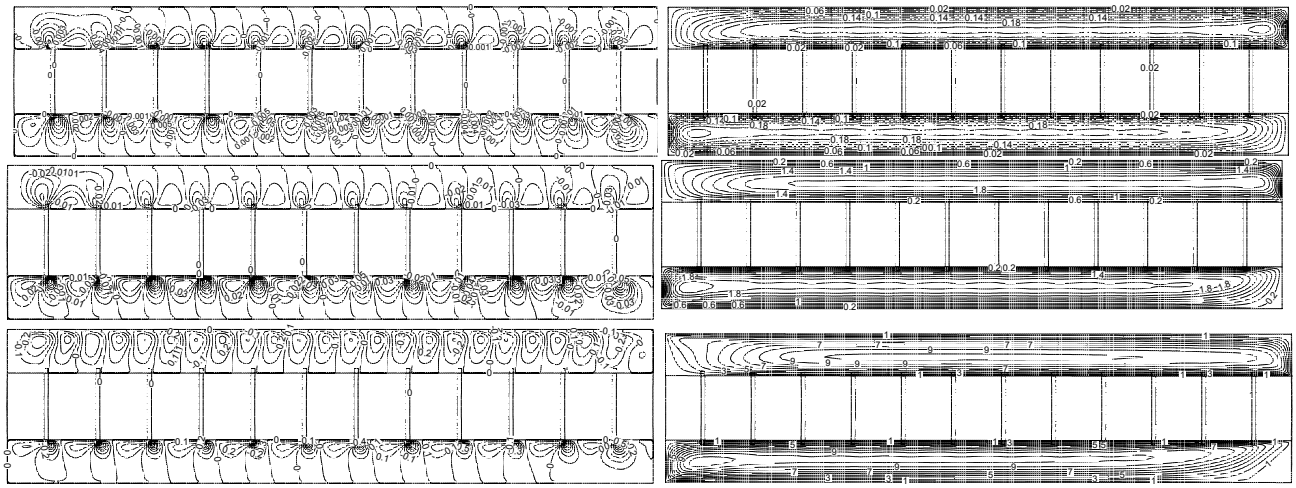

δ=0□ **δ=90□**

Fig. 12 vector potential Ψ_z for n=12, Ra=10,100 and 500 respectively Rr=0.435,Hf=3mm

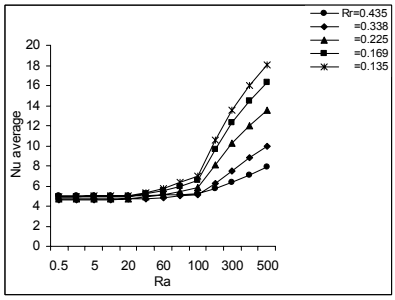

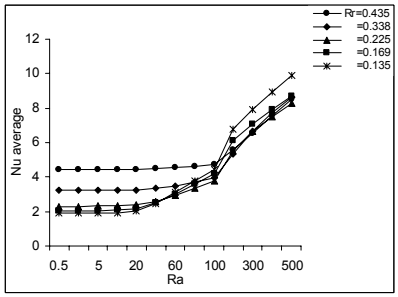

n=0 n=45

Fig.13 the variation of average Nusselt number with Ra^* for different values of Rr

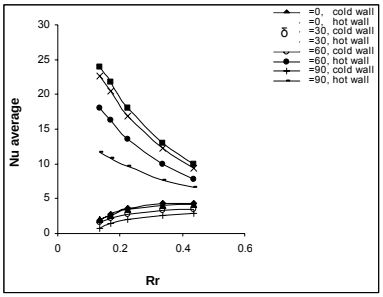

n=0

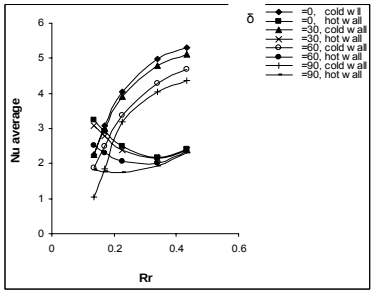

n=45

Fig.14 the variation of average Nusselt number with radius ratio for different values of inclination angle and number of fins

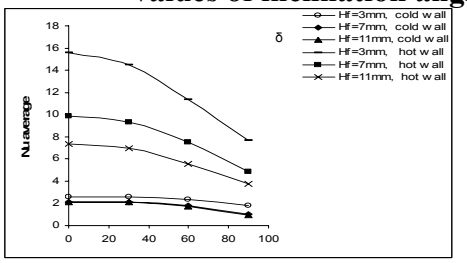

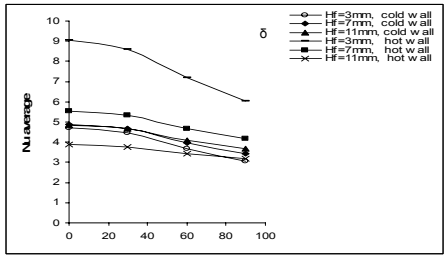

Rr=0.135, Ra=500 n=23 Rr=0.435, Ra=500

Fig.15 variation of average Nu with δ for different H_f, Ra, Rr

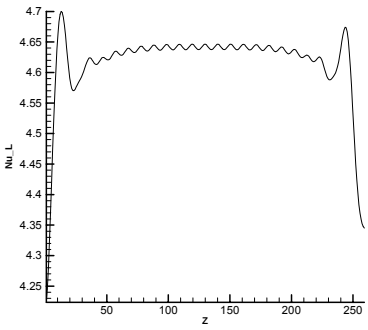

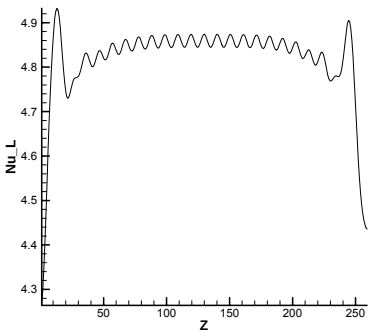

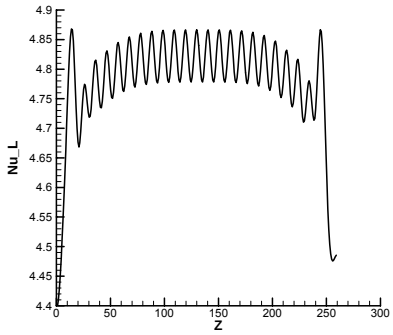

H_f=3mm H_f=7mm H_f=11mm

Fig.16 local Nusselt number along the length of the hot cylinder for n=23,Ra^*=500,Rr=0.435

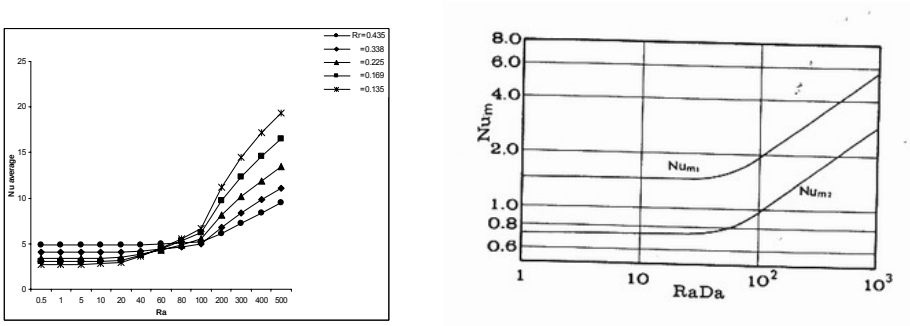

Fig.17 a comparison for the variation of the average Nusselt with Ra^* for the present work with that of [Fukuda and et. al., 1981] respectively

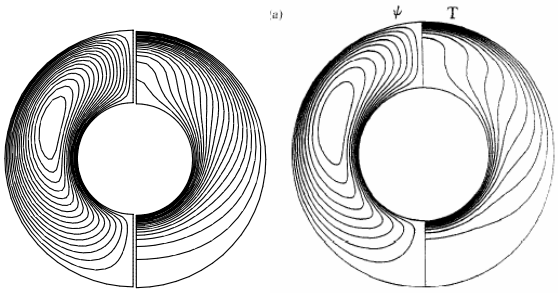

Fig.18 comparison for streamlines and isotherms for the case of convection in a horizontal cylindrical annulus filled with porous media for the present work and by [Charrier and Mojtabi 1991] respectively

OPTIMUM WATER ALLOCATION FOR ABO-ZIRIQ MARSH ECOLOGICAL RESTORATION

Dr.Rafa h.Al-Suhili, Civil Eng.Dept
Dr.Shahlaa E.Ebrahim Environmental Eng.Dept
Hussein J.Al-Khazaali Water Resource Eng. Dept

ABSTRACT

Optimum allocation of water for restoration of Iraqi marshes is essential for different related authorities. Abo-Ziriq marsh area about 120 km^2 is situated 40 km east of Al-Nassryia city. After comparing the measured annual water qualities with the Iraqi standards for surface water quality evaluation, Abo-Ziriq marsh water quality was in acceptable limit. Hydro balance computation were done for each month by using interface among the HEC-RAS, HEC-GeoRAS and ArcView GIS software and built a number of eco-hydro relationships to simulate the marsh ecosystem by using HEC-EFM program to estimate water allocation adequate for ecosystem requirement and constructs a GIS hydraulic reference map to show inundation area, depth grid and velocity distribution, the optimal flow result consists of three different scenarios (24, 30.3 and 33.6 m^3/s) for marsh operation during the year. A computer program in MATLAB 7 was developed to simulate the optimization model to determine the optimum flow value entry to lower zone. The priority of each parameter is represented by a weight associated with each of them (penalty factor). The model was used for different scheme of penalty factor value and examines three cases of flow (wet, moderate and dry years). The results obtained from the program run show that the optimum flow values are not affected significantly with changing the scheme of the penalty factors. Hence, any set of solutions can be use for operation the control structure of two inlets in the lower zone that best fits the objective of the system and increase flow release from Abo Jiry inlet to minimum deviation in water quality during the most time of the year

Keywords: Water quality, Ecosystem requirements, Water allocation.

الخلاصة

ان توفير الحصص المائية المثلى بالكميات والنوعيات اللازمة لاعادة الحياه الطبيعية الى سابق عهدها في مناطق الاهوار في جنوب العراق يمثل احدى اهم الاولويات بالنسبة للمهتمين بهذا الموضوع. يتناول هذا البحث دراسة الحصص المائية المثلى لاعادة الانعاش الاحيائي لهور ابوزرك حيث تبلغ مساحته مايقارب 120 كم^2 ويقع في محافظة ذي قار على مسافة 40 كم شرق مدينة الناصرية. بعد مقارنة نوعية المياه المقاسة مع المحددات القياسية العراقية تبين ان مياه هور ابو زرك مازالت في حالة مقبولة وكذلك تم عمل موازنة مائية لكل شهر من خلال الاستتباع الهيدرولوجي بأستخدام التداخل بين البرامج التالية HEC-RAS،ArcView GIS، HEC-GeoRAS حيث تضمن إعداد منحنيات المساحة-المنسوب والحجم-المنسوب وتمثيل المساحة السطحية المغمورة لكل شهر وتخمين التبخر والاستهلاك والحصص المائية في الجزء الجنوبي والشمالي من الهور. لتحقيق متطلبات الانعاش الاحيائي لهور ابوزرك توجب بناء عدة علاقات لتمثيل النظام الاحيائي ووصف علاقة النظام الاحيائي بطبيعة نظام الجريان في الهورمن خلال تطبيق برنامج HEC- EFM حيث اختيرت ثلاثة سيناريوهات للتشغيل على طول السنة المائية وهي (24، 30.3 ، 33.6) م^3\ثا وتم تمثيل تلك القيم والحصول على خرائط لاعماق المياه وسرعة الجريان والمساحة المغمورة. تم تطوير برنامج (MATLAB 7) يهدف لتقليل المجموع الكلي لانحرافات التصريف ومعاملات نوعية المياه عن القيم المسموح بها وحسب برنامج EFM والمواصفات العراقية لتقييم نوعية المياه السطحية. استخدم النموذج عدة حالات مختلفة من قيم معاملات الجزاء ولثلاث حالات من الجريان (رطب وطبيعي وجاف) لكل فرع يدخل الى الجزء الجنوبي، وبعد ملاحظة النتائج تبين ان تغير معاملات قيم الجزاء لاتؤثر بصورة مباشرة على النتائج لكل حالة من حالات الجريان وامكانية اجراء مناقلة بكميات المياه الداخلة الى فرع (ابو الجري) وزيادتها بحيث تحقق افضل نوعية للمياه داخل الجزء الجنوبي للهور من خلال التحكم بمنشاة السيطرة للجزء الجنوبي على مداخل فرعي (ابو الجري و ابو سميسم).

1. Introduction

The Mesopotamian Marshlands of South Iraq represents one of the largest wetland ecosystems in all of Asia and covered more than 15,000 Km^2 (UNEP, 2002), The Mesopotamian marshland has wide ecological and environmental importance. It represents habitats for biodiversity, wildlife, and cultural richness; a 5000 year old culture, heir to the ancient Sumerians and Babylonians (Ochsenschlager, 2004). These marshes are considered by many to be the "cradle of western civilization" and are often referred to as the Garden of Eden (Nicholson et al., 2002).

Around 85% of the Mesopotamian Marshlands have been lost mainly as a result of drainage and damming, (UNEP, 2002). Most of the damage was done between 1991 and 1995; the vegetation cover was reduced by 79 % (Munro and Touron, 1997). The scale and speed of land cover changes in the marshes has resulted in effectively destroying over 90 percent of the ecosystem of one of the most important wetlands in the world in less than 10 years (UNEP, 2002).

In May 2003, water began to return to the marshlands through the actions of local marsh dwellers and Iraq's Ministry of Water Resources. As of May 2004, up to 40% of the former marshlands have been refolded. On the ground, some of the reflooded areas have experienced rapid regrowth of marshland vegetation; other areas are slowly recovering; while some reflooding areas remain barren. The recovery of the ecosystem has yet to be fully assessed.
The main problem that faces the enhancement of the ecosystem in Iraqi marshland is the lack of management and efficient operation systems for controlling the water inputs and outputs.

In such a way to make these enhancements to ensure restoration of the ecosystem in the marshes, most of the previous studies concerning the optimum allocation and operation of the Iraqi marshes deal with water quantity parameter only. Few models had been considered before, to adopt criteria in the optimum operation model that covers both quality and ecosystem requirements, in this research an attempt to reach this goal.

The main objectives of the present work are Assessment of the improvements in water quality using comparison before drying and after flooding (after April 2003) and building a hydrological routing model for the marsh by using topographical survey and hydrological data to implement hydro-balance inside the marsh

Computing the required water quantities that should be recharge to the marsh and adequate for ecosystem requirements by using the Ecosystem Functions Model EFM software. EFM analyses involve statistical analyses of relationships between hydrology, hydraulics, and ecology, and implement hydraulic model, and also GIS programs to display results and other relevant spatial data to visual form to show the different operation scenario's by using interface between HEC-RAS, ArcView GIS and HEC-GeoRAS programs.

Building an optimization model for the lower part of the marsh to minimize the penalty sum of the water quality parameters and ecological factors deviation from its allowable values as mentioned in the Iraqi standards for surface water quality evaluation.

2. Abo-Ziriq Marsh Description

Abo-Ziriq marsh is situated about 40 km east of Al-Nassryia city.

The main source of water supply to the marsh is through Shatt Abo-Lihia and the channel of this river runs through the marsh until it dissipates at the tail end into the central marsh.

The two main towns around the marsh are Al-Islah in the north and Al-Fuhod in the south of Thi-qar governorates shows in Fig. 1. Scattered villages of fishermen are located all along the embankments that surround the marsh (IMET and IF, 2005). The area of the marsh is about 120 km^2 which is 3% of the total marshes area in Iraq, the monitoring of Abo-Ziriq marsh started since late of 2003.

The marsh divided into two sectors namely Upper zone between Islah village and Islah-Fuhod (Said Yousha'a) road embankment and lower zone between the road and Al Fuhod village

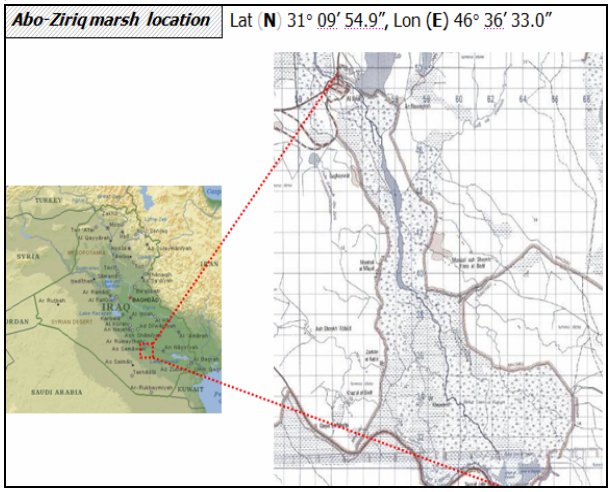

Figure 1: General location of Abo-Ziriq marsh (IMET and IF, 2005).

3. Field Work Monitoring Stations

The number of monitoring stations adopted for the field work is 6 represent upstream of the marsh (feeding point), entrance to lower zone and outflow from of the marsh, Fig. 2 shows the names and locations of the stations. The monitoring of the marsh required to extend more than one season, therefore, the period of data collected extends one year started on October 2009 to September 2010 with one monthly test for each station, Table 1 represent The parameters measured with a method and location.

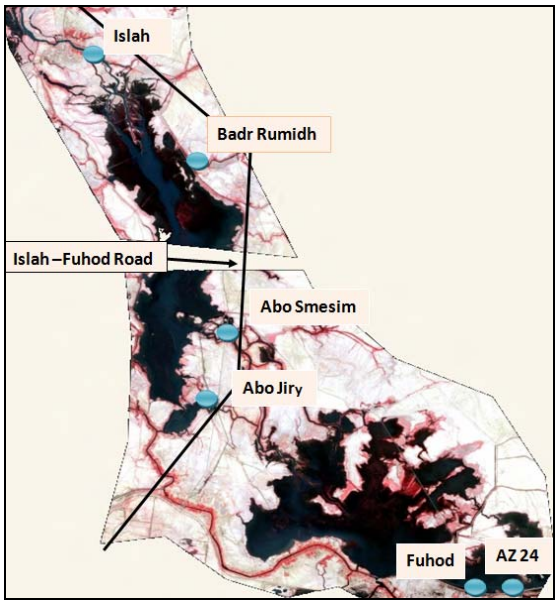

Figure 2: Monitoring station in Abo-Ziriq marsh

Table 1: Parameters measured with a method and location.

Parameters No.	Data measurement	Units	Location measurement	Instruments used
1	pH	-	On site	Multi-Meter
2	D.O	mg/l	On site	Multi-Meter
3	Water temp.	°C	On site	Multi-Meter
4	E.C	µS/cm	On site	Multi-Meter
5	T.D.S	mg/l	On site	Multi-Meter
6	NO_3	mg/l	Lab.	UV- Visible spectrophotometer
7	PO_4	mg/l	Lab.	UV- Visible spectrophotometer
8	Turbidity	NTU	On site	Turbidity meter
9	Discharge	m^3/s	On site	Flow Meter

4. HEC-EFM Relationship

The Ecosystem Function Model (HEC-EFM) is a planning tool that aids in analyzing ecosystem response to change in flow regime. Through using HEC-EFM program the amount of water required to recharge into Abo-Ziriq marsh can be estimated according to ecosystem requirements. In this study, historical flow data for the period from water year (2003-2004) to water year (2009-2010). HEC-EFM relationships are statistical representations of links between hydrology and ecology, and these relationships were selected to demonstrate how the channel restoration would affect ecosystem habitat in the marsh. Each scenario described below represents' information about an aspect of the ecosystem of the marsh. The statistical and geographical queries used to define each as an HEC-EFM relationship, and the logic used to craft those criteria (HEC, 2009).

4.1 Wetland Health

Water exchange between river and marsh areas has also been noted as a key component of wetland health. With frequent exchange, water quality in the wetlands remains good, but with isolation, dissolved oxygen levels drop, wetland areas become anoxic and aquatic species die. This is only an issue in the warm summer months, mid-May to mid-September. The healthy conditions are created when active exchange between the river and wetlands occurs 30% of the time (HEC, 2009).

HEC-EFM Relationship:

Season: 5/15 to 9/15, Duration: 1 day, Percent

exceedance: 30% (of time), Flow duration

4.2 Benthic Macro Invertebrate Biodiversity

Reservoirs tend to reduce high flows and increase low flows, which creates a more stable flow regime. In these regulated systems, communities of benthic macro invertebrates often have reduced biodiversity because the few species that thrive in the more stable flow conditions out compete all of the others. Flooding initiates a return to more natural conditions which encourages the community to rebound to its original biodiversity, the timing is not important, but the high flows should occur once every two years, on average (HEC, 2009).

HEC-EFM Relationship:

Season: 10/1 to 9/30, Duration: 1 day, Means and then Maximum, Percent exceedance: 50% (2 year), Flow frequency

4.3 Riparian Shrub Recruitment and Inundation

Reservoir influence and transition of floodplain lands to agriculture has proved a destructive combination for riparian tree and shrub. Through scientific study, riparian shrub establishment has been tied to high flows that occur and recede during germination periods. After germination, survival is a function of water level. If inundated, seedlings are prone to drowning and, conversely, if water levels recede too rapidly, roots desiccate and seedlings are lost germination periods that occurs between mid-Junes through July, after germination, if water levels drop by more than 0.176 m per week then riparian shrub seedlings will have a lower chance of survival. A high stage needs to occur at least once every 5 years to keep sustainable riparian shrub establishment (HEC, 2009).

HEC-EFM Relationship:

Season: 06/15 to 07/31, Duration: 1 day, Rate of change: 0.176 m per weeks - falling (stage), Percent exceedance: 20% (5 year) - Flow frequency

4.4 Fish Spawning Habitat

Fish is important economic source for the Mesopotamian dweller, they are 12 type of fish recorded in the marsh belong to 6 families, the most common family are *Cyprinidae*, the main type is *Cyprinus carpio* (carp), *Barbus luteus* (himmry) and *Barbus sharpeyi* (benny) (MOE, 2008). Most of little fish spawn in shallow, vegetated floodplain areas between February and May. Eggs require sustained high flows for approximately 21 to 28 days before hatching; the successful spawning depends on having a sustained inundation long enough for the eggs to incubate. The fish reach sexual maturity in their first or second year and have a lifespan of approximately 4years, the good spawning conditions do not need to occur every year - it would be sufficient if there were good conditions in 25% of years, so that, on average, each little fish would have a chance to spawn in their lifespan (HEC, 2009).

HEC-EFM Relationship:

Season: 02/01 to 05/31, Duration: 24 days, Minimums (sustained highs) and then Maximum Percent exceedance: 25% (4 year) - Flow frequency

4.5 Macrophytes Habitat

Macrophytes divided according water level to 3 types; emergent plant, submerged plant and floating plant, consider *Phragmites australis* (reed) and *Typha domengns* (barrdi) are often macrophytes found in Iraqi marsh specially Abo-Ziriq marsh, it have high ability afford against salinity and make self-purification of water inside marsh. Macrophytes have economic important for marsh dwellers, there widely used in many workmanship industry of them such as homes, mats, furniture and using as livestock feeding specially buffalo (MOE, 2008).

HEC-EFM Relationship:

Season: 01/01 to 04/31, Duration: 1 day, Percent exceedance: 15% (time) - Flow duration.

5. Optimization Analysis

A MATLAB program was used to find the optimum flow values for lower part of Abo-Ziriq marsh using direct search method. Search methods consist of iteratively determining improved values for the decision variables as measured by an objective function. Most nonlinear problems following the manner; choose some point to start with; find the function value there; take a tentative short step in some direction; find the function value at new

point; if the values is less than the previous value, discard the first point in favor of the second, otherwise stay at the first; go on doing this till you find a point where the value is least within some prescribed tolerable limits.

The proposed optimization model in this study represented by the following function:

$$Min(f) = \sum_{k=1}^{nk} \left[\frac{\sum_{i=1}^{2} Q_{i,j} C_{i,j,k}}{\sum_{i=1}^{2} Q} - C_k \right] * P_k + \sum_{i=1}^{2} (Q_{i,j} - Qe_{i,j}) \ldots (1)$$

Subject to the following constraints:

$$Q_{i,j} \le Q_{i,j\max} \cdots (2)$$ During wet years

$$Q_{i,j} \ge Q_{i,j\min} \cdots (3)$$ During dry years

$$Q_{i,j\max} \ge Q_{i,j} \ge Q_{i,j\min} \ldots (4)$$ During normal years

$$Q_{i,j\max} \ge Qe_{i,j} \ge Q_{i,j\min} \cdots (5)$$

Where: - C_k = Acceptable limit for water quality parameter (k), P_k = Different Relative penalty weight for each quality parameter (k), J = 1, 2 .12, represent the month starting from October and ending on September, respectively, as the water year, n = No. of water quality parameters, i =1, represent Abo Smesim inlet, i =2 Abo Jiry inlet, $Q_{i,j}$: Optimum water release from the inlet i, at month j, $Q_{i,j\max}$: Maximum flow from inlet i at month j, $Q_{i,j\min}$.: Minimum flow from inlet i at month j, $Q_{i,j\,avr}$: Average flow from inlet i at month j, $C_{i,j,k}$: Average parameter concentration of the inlet i, at month j of the water quality parameter k, $Qe_{i,j}$: Flow result from ecosystem relationship of the inlet i, at month j.

For the upper limit acceptable of the water quality parameter P_k will be:

$$P_k = \begin{bmatrix} greater\ \ than\ \ 0, less\ or\ equal\ \ 1 \\ o \end{bmatrix} \begin{matrix} C^*_{k,j} < 0 \\ C^*_{k,j} \ge 0 \end{matrix}$$

For the lower limit acceptable water quality parameter P_k will be:

$$P_k = \begin{bmatrix} greater\ \ than\ \ 0, less\ or\ equal\ \ 1 \\ o \end{bmatrix} \begin{matrix} C^*_{k,j} > 0 \\ C^*_{k,j} \le 0 \end{matrix}$$

$$C^*_{k,j} = \frac{\sum_{i=1}^{2} Q_{i,j} C_{i,j,k}}{\sum_{i=1}^{2} Q} - C_k$$

The objective function was adopted by assuming complete mixing of water at the lower part of the marsh, The above formulated optimization model requires the monthly flow values of the two inlet in the lower zone of the marsh, monthly flow result from EFM and the average value of EC, TDS, NO3,PO4,TUR, DO and pH for each inlets.

6. Results and Discussions

6.1 Water Quantity Data Analysis

The water quantity analysis during the onsite monitoring in the study area of Abo-Ziriq marsh during the water year 2009-2010 consist of three stages represents the discharge of upstream of the marsh, flow entrance to lower zone and outflow from of Abo-Ziriq marsh as show in Fig. 3, where the maximum flow entering the marsh is 17.75 m³/s in May, and the minimum value of flow in January was 3 m³/s .The average inflow entrance to the marsh was 8.19 m³/s. The inlet flow to the lower zone of the marsh represents the outflow passes from the upper zone via the road embankment opening; it mainly consists of flow from Abo Smesim and Abo Jiry control structure stations. The average flow rate passing to the lower zone was 6.14m³/s. The outlet flow from lower zone of the marsh represents the total outflow from the marsh; this flow is computed as the summation of all flows measured along the southern zone including AZ 24 and Fuhod stations, the average flow passing from the marsh was 2.27m³/s.

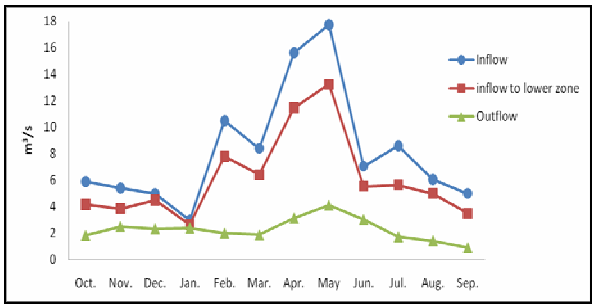

Figure 3: Flow measured in Abo-Ziriq marsh.

6.2 Water Quality Result

It presents the results gathered during the onsite and laboratory monitoring; water quality monitoring activities are divided into two types.

- Physical properties
- Chemical properties

The results present in Fig. 4 below for each parameter were compared with the allowable limits according to the law No.25/1967 (Protection of Rivers and Water from Pollution, Standards of lakes and pools and any collection of water, Ministry of Environment) for each monitoring station in Abo-Ziriq marsh shows more acceptable limits especially in TDS, EC and nutrients measurements along the water year 2009-2010 with respect of allowable value.

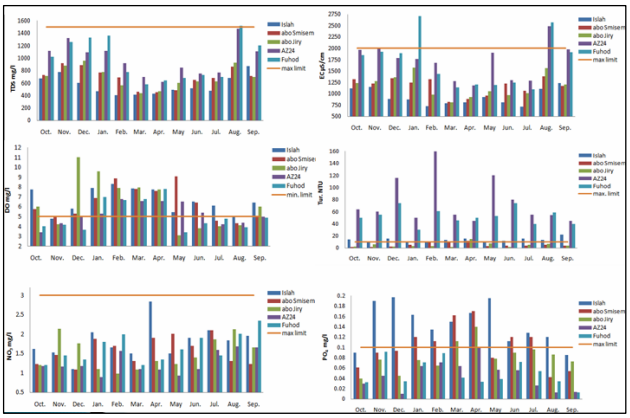

Figure 4: Water quality measurements

6.3 Hydro Balance Result

The overall hydro-balance modeling approach is depended on the following steps:

1. Available Digital Elevation Models (DEM) was used to create the updated digital elevation model concerning the marsh. The different existing obstructions such as: agricultural areas, small towns, hydraulic structures, etc… were considered in the construction of the DEM.

The updated DEM provided a powerful background for the analysis, particularly the stage-volume curve of the marsh area within any scenario of inundation.

2. Applying HEC-RAS and GIS programs to satisfy hydraulic routing in the marsh

3. Construct the Area-Elevation and Volume-Elevation curves to estimation Evapotranspiration (ET) from the surface area of the marsh.

4. Specifying the inflow and outflow from the marsh.

The achieved DEM according to the collected topographical data, surveyed data, cross sections of the Abo Lihia feeder and the marsh area are the major tool in the construction of the required geometric data in HEC-RAS Software. The constructed cross sections are obtained from the DEM through the Arc-View GIS with HEC-GeoRAS extension. The total numbers of cross sections were 22 sections; manning N (roughness coefficient) was taken equals 0.04. The hydrologic data of the recent years have been used in the implementation of the hydraulic model. This model was used to account area and storage curve and find the best solution for marsh restoration during the drought season with the results of hydrologic routing and GIS program.

Management of the hydro-balance model requires construction of Area and Volume-Elevations curves to estimation (ET) from marsh surface area. The interface between hydraulic models in HEC-RAS and graphical user interface with Arc-View GIS through HEC-GeoRAS software were used with the help of DEM to account the area inundation and the volume of water in the marsh at any elevation. The Area-Elevation and Volume-Elevation curves were show in Fig. 5.

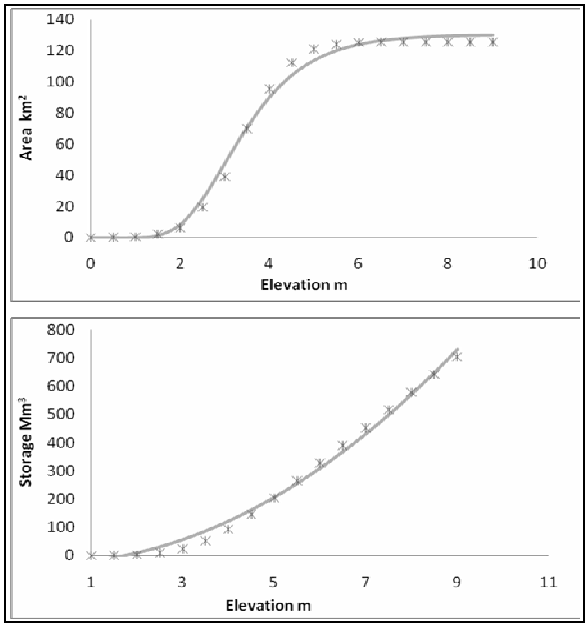

Figure 5: Volume and area elevation Curves.

The result of hydro-balance for Abo-Ziriq marsh can expressed as percentage of inlet flow (Islah station) for each month as shown in the equations below:

Inflow = Outflow

Inflow (100%) = % ET + % Water allocation in Upper and lower zone + % Outflow

Where:

Inflow (100%): Represents the total monthly flow entrance to the marsh for each month in (Islah) station as 100% percentage.

% ET: Represents the amount of water loss from the marsh as percentage from the total inflow to the marsh. % (ET) was calculated by substituted the inlet flow as volume per month in Storage-Elevation curve, then computed the elevation produced through this flow and substituting in Area-Elevation, through the surface area and mean value of ETo, the ET can be computed as apercentage of the total inflow in the marsh for each month during water year.

% Water allocation in Upper and lower zone: Represents the amount of water remaining and using in the upper and lower zone, it was computed by subtraction losses of evapo-transpiration and outflow, from total inflow entrance to the marsh.

%Outflow: Represents the percentage of total monthly flow outlet from the marsh for each month in (Fuhod and AZ24) stations.

The final results of hydro-balance distribution percentage of flow entrance in the marsh for each month are shown in Table 2. Fig. 6 shows the schematic diagram of the total hydro-balance distribution along water year 2009-2010. The percentage of allocation flow in upper zone always less than the lower zone for all the study time because of the large area of the lower zone compared with the upper zone, and there are more chanals provided water for irrigation, drinking and other requirment. Fig. 7 shows the storage and surface area produced from the inlet inflow.

Table 2: Percentage distribution of water entrance in the marsh

Hydro-balance percentage												
	Oct.	Nov.	Dec.	Jan.	Feb.	Mar.	Apr.	May.	Jun.	Jul.	Aug.	Sep.
Inlet (Islah)	100	100	100	100	100	100	100	100	100	100	100	100
Total Evapo-transpiration	21.9	9.5	5.5	2.5	6.5	10.7	19.2	31	40	37.5	34.3	31.6
Sharing upper zone	20.1	23.5	9.2	10.9	23.7	20.3	20.1	15.2	6.5	18.2	9.6	18.5
Sharing lower zone	27	20.7	38.7	7.0	50.7	46.6	40.6	30.7	10.8	24.2	32.4	31.7
Outlet (Fuhod+AZ24)	31	46.3	46.6	79.5	19	22.3	19.9	23.1	42.8	20.1	23.6	18.3

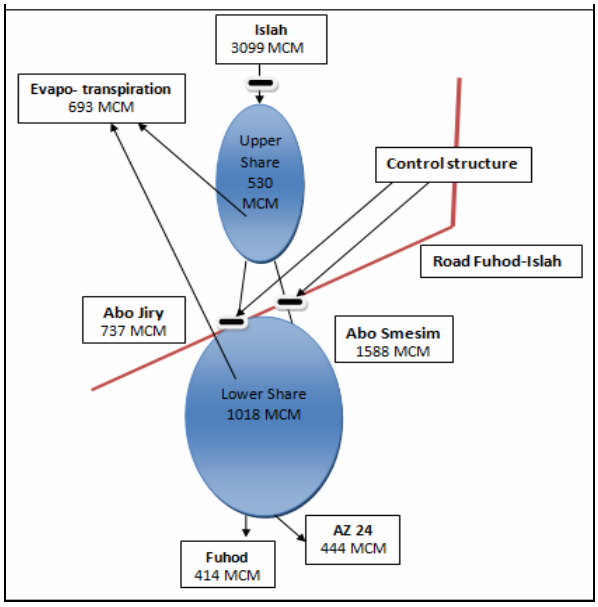

Figure 6: Schematic of the total hydro-balance distribution

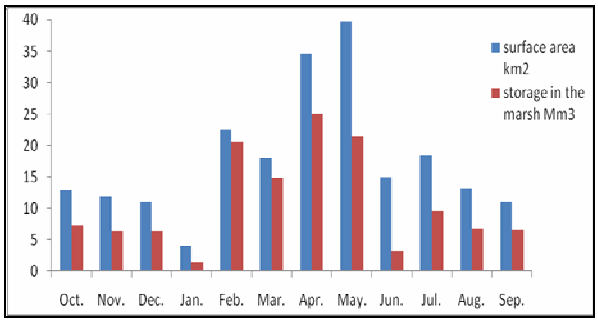

Figure 7: Storage and surface area in the marsh

6.4 HEC-EFM Results

The HEC-EFM output depended upon relationship demonstrate the eco-hydro relationships in the marsh restoration ecosystem, there are many scenarios allow to operate and monitor the ecological restoration inside the marsh, these scenarios depend on the time along the water year and relationship at that time, Table 3 shows each relationship during water year

Table 3: HEC-EFM optimum flow result for each relationship (m^3/s)

Relation	Oct.	Nov.	Dec.	Jan.	Feb.	Mar.	Apr.	May.	Jun.	Jul.	Aug.	Sep.
Average. flow	18.5	19.5	20.7	20.4	20.2	25.3	26	21.4	21.7	22	16	19
Marsh health								23	23	23	23	23
Fish					33.6	33.6	33.6	33.6				
Benthic biodiversity	24	24	24	24	24	24	24	24	24	24	24	24
Macrophytes				30.3	30.3	30.3	30.3					
Riparian shrub									19.6	19.6	19.6	19.6
Max. Optimum	24	24	24	30.3	33.6	33.6	33.6	33.6	24	24	24	24

In order to graphically display the inundation area, velocity distribution and depth grid; the computed water surface elevations and flow velocities from the HEC-RAS model were exported into HEC-GeoRAS to construct water surface and velocity distribution. The water surface and velocity data were then compared with terrain data by HEC-GeoRAS to delineate floodplains and flow velocity distributions. The floodplains generated by the various flows from the hydrologic analysis were overlain with substrate characteristics to predict zones that would be suitable for different ecosystem functions. The net required inflow to satisfy ecological restoration in the marsh contains three suggested scenarios was depended on the HEC-EFM results, these scenarios were divided according to time along the water year:

A) First Scenario: Represent flow on January 30.3 m^3/s. Fig. 8, show inundation area, water depth and velocity distribution respectively. In addition to satisfy ecosystem requirement in January, this scenario make sure that the inundation area about 67 km^2 with velocity range 0-0.64 m/s.

Figure 8: First scenario

B) Second Scenario: Represent high flow in the marsh 33.6 m^3/s, extent from February to May. Fig. 9, shows inundation area, water depth and velocity distribution respectively. In addition to satisfy ecosystem requirement during spring season, this scenario make sure inundation area about 72 km^2 with velocity range 0-0.85 m/s.

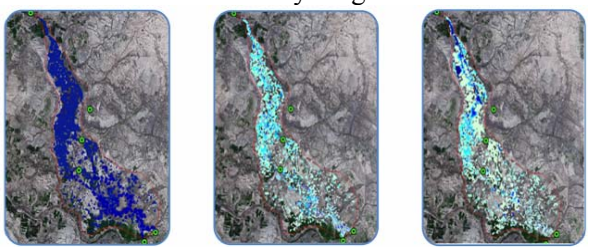

Figure 9: Second scenario

C) Third Scenario: Represent low flow duration, extent from June to December, it was 24 m^3/s. Fig. 10, shows inundation area, water depth and velocity distribution respectively. In addition to satisfy ecosystem requirement during the summer season, this scenario make sure that the inundation area about 52 km^2 with velocity range 0-0.4 m/s

Figure 10: Third scenario

6.5 Optimization Result

The optimum monthly flows of the lower zone system for Abo-Ziriq marsh were calculated by a MATLAB 7.0 program using the monthly data for both quantity and quality to formulate an optimization model. The program used the following data for obtaining the optimum flow entrance to the lower zone:

1. Monthly historical flow data for many years of the two inlets for wet, normal and dry cases.
2. Monthly flow data for EFM and hydro-balance results of each inlet to the mixing zone.
3. Water quality measurements data.

MATLAB 7.0 program used in the present study to minimize the objective function by using the allowable values (pH between 6.5-8.5, EC < 2000 µS/cm, TDS < 1500 mg/l, DO > 5 mg/l, TUR < 10 NTU, NO3 < 3 mg/l, and PO4 < 0.1 mg/l) in equation (1) and applying a penalty factor on the values of $C^*_{K,J}$ as follow:

a. For the upper limits (EC, TDS, TUR, PO4, NO3 and pH=8.5):

$$If \quad C^*_{K,J} \geq 0 \Rightarrow p_k = 0$$
$$If \quad C^*_{K,J} < 0 \Rightarrow 0 < p_k \leq 1$$

b. for the lower limits (DO and pH=6.5):

$$If \quad C^*_{K,J} \leq 0 \Rightarrow p_k = 0$$
$$If \quad C^*_{K,J} > 0 \Rightarrow 0 < p_k \leq 1$$

The Different schemes of the penalty factors assignment were used in order to evaluate its effect on the results of the optimum flow. These schemes depend on the ecological effect of each parameter on aquatic system in the marsh:

a. scheme 1 (salinity effect):

$$p_k Ec = 1$$
$$p_k TDS = 1$$
$$p_k NO_3 = 0.5$$
$$p_k PO_4 = 0.5$$
$$p_k DO = 0.6$$
$$p_k pH = 0.6$$
$$p_k TUR = 0.8$$

b. scheme 2 (nutrient effect):

$$p_k Ec = 0.7$$
$$p_k TDS = 0.7$$
$$p_k NO_3 = 1$$
$$p_k PO_4 = 1$$
$$p_k DO = 0.8$$
$$p_k pH = 0.8$$
$$p_k TUR = 0.6$$

c. scheme 3 (DO effect):

$$p_k Ec = 0.6$$
$$p_k TDS = 0.6$$
$$p_k NO_3 = 0.7$$
$$p_k PO_4 = 0.7$$
$$p_k DO = 1$$
$$p_k pH = 0.7$$
$$p_k TUR = 0.7$$

The optimum flow calculated for 3 schemes and 3 cases of flow wet, normal and dry years.

6.5.1 Optimum Wet Flow

For the wet years the optimum flow values for Abo Smesim and Abo Jiry inlet showed low flow variations comparing to the values of each scheme effect as shown in Fig. 11. The most optimum flow for Abo Smesim inlet more than Abo Jiry obvious to reduce flow values with respect to values of the wet flow case because the water quality in these months more acceptable from Abo Jiry inlet, it occurs at the range 6-18 m^3/s for Abo Smesim inlet and 3-10.5 m^3/s for Abo Jiry inlet, while wet flow ranges 9.5-22 m^3/s and 4.5-10.5 m^3/s for Abo Smesim and Abo Jiry inlets respectively.

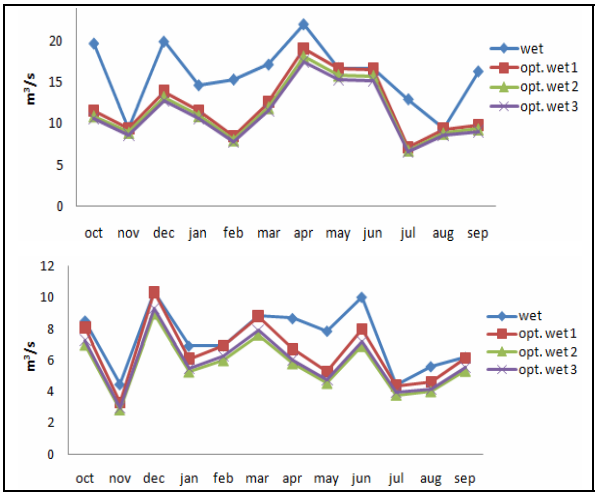

Figure 11: Optimum wet flow for different schemes.

6.5.2 Optimum Normal Flow

The optimum flow for the normal case represent the more flow values and it can be depend for controlling of the water passes through control structure in each inlet. The most probable flow for Abo Smesim inlet occurs in the range 7-17 m^3/s and 3.27-8 m^3/s for Abo Jiry inlet, comparing optimum flow values of the two inlets with those values, shows that the most optimum flow values fall in the same range, for Abo Smesim inlet flow occurs in the range 4.5-20.5 m^3/s and 2-9.5 m^3/s for Abo Jiry inlet. The optimum normal flow values show low flow variations comparing to the values of each scheme effect as shown in Fig. 12.

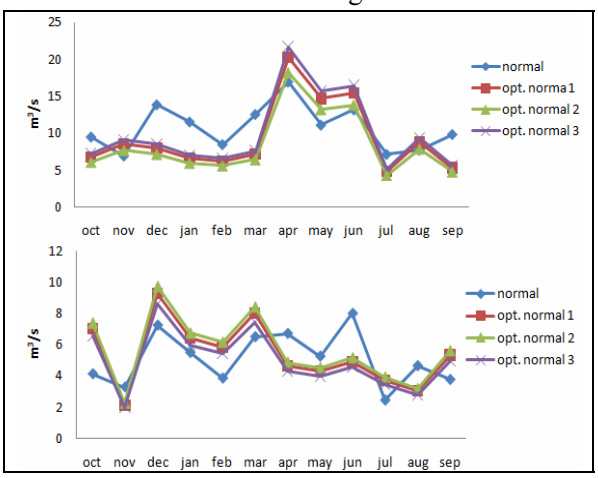

Figure 12: Optimum normal flow for different schemes.

6.5.3 Optimum Dry Flow

For the dry years the optimum flow for Abo Smesim and Abo Jiry inlet showed various flow variations comparing with the values of the dry flow in each inlet, especially in Abo Jiry inlet as shown in Fig. 13, optimum dry result appears most optimum flow for Abo Smesim inlet than Abo Jiry obvious to reduce flow values with respect to values of the dry flow case except April and August because the water quality in these months more acceptable from Abo Jiry inlet which have high optimum dry flow extend from December to May and September to October, the optimum dry flow occurs at the range 3-15 m^3/s and 1.6-8 m^3/s for Abo Smesim and Abo Jiry inlets respectively.

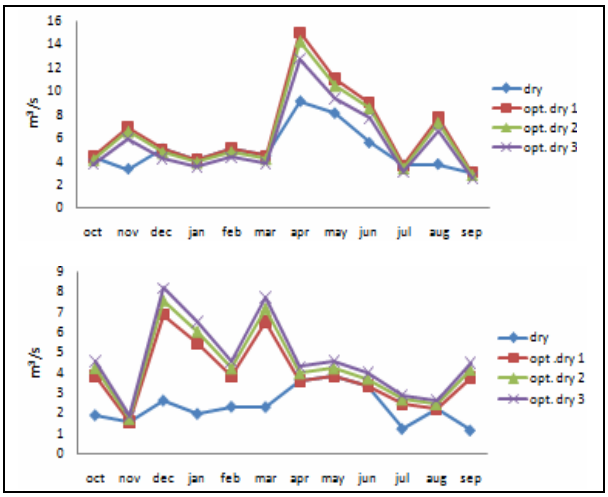

Figure 13: Optimum dry flow for different schemes.

7. Conclusion

Comparison of water quality parameters of the marsh for the present period, reflooded period, and that before drying indicate no significant changes in water quality and all are within the acceptable limits were TDS 784 mg/l, pH 8.05, E.C 1330 µS/cm, DO 5.95 mg/l, Turbidity 30.3 NTU, NO_3 1.55 mg/l, and PO_4 85 µg/l.

Evapotranspiration in the marsh is the main reason of water loss, about 22.33% of total inflow. The present annual storage with the marsh is 46.42% from inlet inflow, which remains inside the marsh and contribute to enhance the ecological restoration in the marsh. The HEC-EFM software application indicates three optimum operations scenarios along the water year 24, 30.3 and 33.6 m^3/s. Implementation of these scenarios to produce and illustrate graphically inundation area ranging 52-72 km^2, water depth grid in the range 0-3.45 m, and a velocity distribution of a range 0-0.85 m/s, for each scenario.

The changing in schematic penalty factor has no significant effect on the optimum flow value.

Increase the inflow into the lower zone of the marsh from Abo Jiry control structure to minimize the deviation of water quality within this part.

References

- Hydrologic Engineering Center, (2009). "HEC-EFM Ecosystem Functions Model, User's Manual", U.S. Army Corps of Engineers, Davis, CA, November.
- IMET and IF, Italian Ministry for the Environment and Territory and Iraq Foundation, (2005). "New Eden, Water & Energy Project" Technical Book 1. Abo-Ziriq Marshland Restoration Project.
- MOE, Ministry of Environment. (2008). "Environment Present Condition". Annual report.

  Munro, D.C., and Touron, H. (1997). "The estimation of marshlands degradation in southern Iraq using multi temporal land sat TM images". Int. J. Remote sensing. 18 (7): 1597-1606.
- Nicholson E, Clark P and Eds. (2002). "The Iraqi Marshlands: A Human and Environmental Study". London: Politico's. Northwestern coastal of the Arabian Gulf. Mar. Poll. Bull., 16:118-120.
- Ochsenschlager, E. L. (2004). "Iraq's marsh Arabs in the Garden of Eden". 307(5713):1305-1307.
- UNEP, United Nations Environment Program (2002). "The Mesopotamian Marshlands: Demise of an Ecosystem" Division of Early Warning and Assessment Nairobi, Kenya. ISBN: 92-807-2069-4.

دراسة بعض الخواص الميكانيكية لمادة بوليمرية مقواة برايش و مسحوق النحاس

الدكتور المهندس علي حسين عتيوي
أستاذ مساعد
قسم هندسة المواد
الجامعة التكنولوجية

المهندس ليث وضاح اسماعيل
مدرس
قسم هندسة المواد
الجامعة التكنولوجية

المهندسة أسيل محمود عبد الله
مدرس مساعد
قسم هندسة المواد
الجامعة التكنولوجية

الخلاصة

في هذا البحث تم استخدم رايش ومسحوق النحاس لتقوية مادة البولي استر لانتاج مادة متراكبـة. تـم إجراء الفحوصات الميكانيكية مثل مقاومة الانحناء واختبار الصدمة للمادة البوليمرية المقواة برايش ومسحوق النحاس، وقد وجد ان أقصى مقاومة انحناء للمادة البوليمرية المقواة بالنحاس (المـسحوق والـرايش) هـي (85.13 Mpa)و (50.08 Mpa) على التوالي، بينما أعلى طاقة ممتصة في فحص الصدمة للمادة البوليمرية المقواة بالنحاس (المسحوق والرايش) هي (0.85 J) و (0.4 J) على التوالي.

Study of Some Mechanical Properties for a Polymer Material Reinforcement with Chip or Powder Copper

Abstract

In this paper, chip and powder copper are used as reinforcing phase in polyester matrix to form composites. Mechanical properties such as flexural strength and impact test of polymer reinforcement copper (powder and chip) were done, the maximum flexural strength for the polymer reinforcement with copper (powder and chip) are (85.13 Mpa) and (50.08 Mpa) respectively was obtained, while the maximum observation energy of the impact test for the polymer reinforcement with copper (powder and chip) are (0.85 J) and (0.4 J) respectively.

الكلمات الرئيسية:- بولي أستر، رايش النحاس، مسحوق النحاس، مقاومة الانحناء، اختبار الصدمة.

الدكتور المهندس علي حسين عتيوي
المهندس ليث وضاح اسماعيل
المهندسة أسيل محمود عبد الله

المقدمة:-

تتألف المواد المتراكبة ذات الاساس البوليمري المقواة بالجسيمات من مدى واسع من مواد التقوية [Brian S., 2004]. تعتبر الهشاشية من المشاكل المهمة التي تعاني منها البوليمرات المتصلدة بالحرارة (Thermosetting) مثل البولي استر غير المشبع (polyester) ، مما يحدد أستعمالها في التطبيقات الهندسية عندما تكون متانة الفشل (Fracture toughness) لها قليلة وخاصة في درجات الحرارة المنخفضة. من جهة أخرى تمتلك هذه المواد البوليمرية خواص معينة مرغوبة جداً مثل الكثافة المنخفضة والمقاومة الجيدة للتآكل. المواد البوليمرية يمكن زيادة مقاومتها ضد التشقق بإضافة جسيمات من مواد معينة والتي تسمى بالحشوات (Fillers) وان طبيعة هذه الجسيمات مثل حجمها وتركيزها ذات اهمية بالغة على مقدار المتانة التي يكتسبها البوليمر[**أ.د. قحطان خلف، 2009**].

ان المادة البوليمرية الناتجة من التقوية بالجسيمات تدعى المادة المتراكبة المقواة بالجسيمات. تحدث التقوية في هذه المواد عندما تعمل الجسيمات كعوائق تشويه المادة الاساس اثناء التحميل وتكون هذه الجسيمات عادة في عدة اشكال منها الكروية أو القشرية أو الابرية أو الخيطية. حيث تعمل هذه الجسيمات على تحسين الخواص الميكانيكية لمادة الاساس [W.D Callister, 2003].

يمكن تقسيم الحشوات بالنسبة لفعاليتها الى الاقسام الآتية [M.S Bhatnagar, 2004]:

أ- حشوات فعالة (Active fillers): وهي الحشوات التي تلعب دوراً كبيراً في تقوية المواد المرنة والمطاط وان اضافة هذه الحشوات الفعالة تحت درجة الانتقال الزجاجي تقلل الهشاشية.

ب- الحشوات غير الفعالة (Inactive fillers): تستعمل هذه الحشوات لتقليل كلفة المادة ولتحسين المنتجات البوليمرية من حيث الشكل والحجم. وتعمل هذه الحشوات على زيادة معقولة في الحجم وبذلك فان نسبة الحشوة للمادة تكون مهمة جداً وتكون هذه الحشوات عضوية مثل (النايلون والرايون) او غير عضوية مثل (الزجاج والكاربون).

الدراسات السابقة وهدف البحث

قام الباحث [N.M. Sofian, 2001] وزملائه بدراسة مادة متراكبة ذات اساس بوليمري مستخدماً المساحيق التالية

(نحاس Cu، زنك Zn، حديد Fe، البرونز Sn) كحشوات للمادة الاساس بولي أثيلـين (Polyethylene) بنسبة كسر حجمي (0-24%)، وقد توصل البـاحثون عمليـاً ان الحشوات ذات كـسر حجمـي (0-16%) التي تم توزيعها بشكل متجانس في مـادة الاساس وبشكل أفضل من القيم الاخـرى للكسر الحجمي. كما وجـد ان الموصـلية الحرارية قد زادت وبشكل كبيـر للمـادة المتراكبة التي تم فيها التوزيع المتجـانس للحشوات. قام الباحث **[Surgasarathi Bose, 2004]** وزميلـه بدراسـة تـاثير الحجم على الخواص الميكانيكيـة لمـادة بوليمرية مقواة بمـسحوق المايكـا حيـث استخدما نايلون (مادة بوليمريـة) مقـواة بمسحوق المايكا بحجوم حبيبيـة مختلفـة ووجد ان متانة الصدمة والانحناء تـزداد عند تقليل الحجم الحبيبي. كما قام الباحـث **[Munir Tasdemir, 2008]** وزميلـه بدراسة الخواص الميكانيكية لمادة متراكبة ذات اساس بـوليمري مقـواة بمـسحوق الحديد، حيث اسـتخدوا مـواد بوليمريـة مختلفة (بولي بروبلين، بولي اثيلين، بولي ستايرين) وتم تقويتها بمـسحوق الحديـد بكسر حجمي (15،10،5) %. ووجدوا ان البولي اثيلين في اختبار الصلادة أعطـى نتائج افضل من البولي بروبلين والبـولي ستايرين عند التقوية بمسحوق الحديد. بينما اختبار الصدمة للبولي اثيلين أعطى نتـائج غير جيدة وأقل من البولي بروبلين والبولي ستايرين.

يهدف البحث الحالي الى الاسـتفادة من رايش النحاس الذي يعتبر من مخلفات عملية الخراطة كمادة تقوية للبولي اسـتر لانتاج مادة متراكبة ذات اساس بـوليمري مقواة برايش النحاس بكسور وزنية مختلفة (0.5%،0.8%،1% and 1.5%) ودراسة بعـض الخـواص الميكانيكيـة للمـادة البوليمرية المقواة مثل مقاومـة الانحنـاء والصدمة ومقارنة النتائج للبـولي اسـتر المقوى بمسحوق النحاس لـنفس الكـسور الوزنية. وفي بحثنا هذا محاولة للمـساهمة في الاستفادة من المخلفات الصناعية خدمةً للأقتصاد الوطني والمحافظة على البيئة.

الجزء العملي:-

- المواد المستعملة

المواد المستعملة فـي تحـضير النمـاذج المصنعة تقسم كالآتي:

1) مادة الاساس

تم أستعمال البولي استر غير المشبع (Polyester) كمادة اسـاس وهـو مـادة بوليمرية من نوع البـوليمرات المتـصلدة بالحرارة (Thermosetting) الـسعودي المنشأ على هيئة سائل لـزج شـفاف ذو لزوجة (1000 بنتي بواز) عنـد درجـة حـرارة ($25\ C^0$) ووزن نـوعي (1.15) يتحول الى الحالة الـصلبة بعـد اضـافة

المصلد اليه الذي يكون ايضاً سائل لـزج شفاف.

2) مادة التقوية

تم أستعمال النحاس النقـي (Cu) وبعـدة اشكال:

* رايش النحـاس المنـتج مـن عمليـة الخراطة ويكون على نوعين رايش نـاعم بحجم حبيبـي حـوالي (300 μm) كمـا موضح في الشكل (1).

* مسحوق النحاس النقي (Cu) ذو الحجم الحبيبي (53-55 μm) كما موضـح فـي الشكل (2).

تم حساب الحجم الحبيبـي للنحـاس (المسحوق والـرايش) بأسـتعمال عمليـة الغربلة بواسطة جهاز الغربلة الكهربائي.

- القوالب المستعملة

لقد تـم تـصنيع قالـب ذو قاعـدة وجوانب من الخشب المـصقول وتكـون الجوانـب متحركـة ومرتبطـة بالقاعـدة بواسطة المثبتات. وهذه الجوانب تكـون متغيرة على وفق ابعـاد العينـة المـراد تصنيعها. حيث ابعاد القالب المستخدم فـي البحث هي (220 x 200 mm).

- تحضير العينات

لقد تم أسـتعمال الطريقـة اليدويـة (Hand-lay-out) في تحضير النمـاذج حيث نبدأ بعملية المزج. علماً أن التقويـة بكسور وزنية مختلفة هـي (1.5% and 1.2%,1%,0.8%,0.5%) وتمزج مـادة الأساس مع المصلد عند درجـة حـرارة الغرفة. ونخلط المـزيج بـشكل مـستمر وببطىء ويستمر المـزج لمـدة (8-10) دقائق الى ان يتجانس الخليط ثم يتم صـب المزيج السائل على شكل سيل من احـدى جوانب القالب بحيث يسيل بصورة مستمرة ومنتظمة ثم يوضع القالـب علـى هـزاز كهربائي ونبدأ عملية هـز القالـب لفتـرة زمنية (1-2 min) للتخلص من الفقاعـات الهوائية.

بعد اجراء العمليـات الـسابقة تـم الحصول على نمـاذج المـواد المتراكبـة (Composite) بهيئة ألـواح بعـدها تـم إجراء عملية التقطيع لغرض تهيئة النماذج حسب المواصفات القياسـية التـي تفـي بمتطلبات الفحوصات الميكانيكية والـشكل (3) يوضح العينـة بعـد أجـراء عمليـة التقطيع.

- الفحوصات

من الفحوصات التي اجريت على النماذج المحضرة :

فحص الصدمة:

لقد تم استعمال جهاز شاربي لفحص الصدمة (Charpy Impact test) حيـث تم أستعمال النماذج بأبعاد قياسـية (80 x 10 x 4 mm) وبدون حـز علـى وفـق النظام العالمي(ISO-179).

فحص الانحناء:

لقد تم تحضير عينات الانحناء بابعاد قياسية (191 x 13 x 4.8 mm) وبنسبة طول الى السمك (span to Depth Ratio) مقدارها 1:32 على وفق المواصفات الامريكية (ASTM D-790).

المناقشة:-

- أختبار فحص الصدمة (Impact Test)

نلاحظ من الجداول (1) ان طاقة الصدمة الممتصة اللازمة لحدوث الكسر للبولي استر بدون تقوية قليلة والتي تبلغ (0.18 J) مقارنة مع جميع النماذج المقواة بالنحاس على اختلاف اشكاله (المسحوق او الرايش) وعلى اختلاف نسب الكسور الوزنية ويعزى سبب ذلك الى ان مادة البولي استر هي مادة هشة مما يحدد أستعمالها في التطبيقات الهندسية **[أ.د. قحطان خلف، 2009]**. ان الفشل يحدث في المادة البوليمرية غير المقواة الخاضعة لفحص الصدمة بتحطيم الارتباطات او القوى فيها وذلك بنمو الشقوق الاولية المحدثة بفعل اجهادات الصدمة وان الشقوق المتولدة تنمو وتتكاثر بشكل كبير وسريع باتجاه السطوح البينية الفاصلة بين السلاسل البوليمرية لان القوى بين هذه السلاسل المتمثلة بقوى فاندرفالز (Vandervalls) تتطلب طاقة قليلة للتغلب عليها. اما الشقوق الممتدة بالاتجاه العمودي على اتجاه السلاسل البوليمرية فأنها تعمل على تحطيم تلك السلاسل خلال عملية نمو الكسر (Propagation)، ومن الجدير بالذكر ان هذا الامر يتطلب طاقة للتغلب على تلك القوى المسؤولة عن ربط الوحدات التركيبية **[J. S. Wu, 1989]**، والتصنيع الجيد للمادة البوليمرية يحافظ على المادة ويمنع الكسر في الظروف الاعتيادية **[Prof. Ger Storbl, 2007]**.

ان الشكل (4) يوضح تأثير تغير الكسر الوزني لمسحوق النحاس المضاف الى البولي استر على الطاقة اللازمة لحدوث الكسر بالصدمة ويلاحظ من المخطط ان هذه الطاقة تزداد مع زيادة الكسر الوزني وذلك نتيجة عمل هذه الدقائق كحواجز امام الشقوق النامية خلال المادة المتراكبة أي تعمل على اعاقة نمو الشق وهذا سيؤدي الى تغيير شكل واتجاه الشق مما يؤدي الى تحوله الى مجموعة شقوق ثانوية، كما ان هذا التغير في شكل الشق واتجاهه يؤدي الى زيادة المساحة السطحية للكسر والطاقة المصروفة. ان سلوك انشاء الشق في المتراكبات يختلف عن مثيلاتها في المواد غير المقواة، ففي المواد المتراكبة ذات الاساس البوليمري يعتمد انتشار الشق على

مناطق متعددة منها المادة الاساس ومنطقة السطح البيني ومـادة التقويـة **[R. M. Jones, 1975]**. ان تخليق العيب ونمـو الشق في المادة المتراكبة المـستعملة فـي البحث حدث في مـادة الاسـاس او عنـد السطح البيني، او عند مادة التقويـة لانـه عادة يكون تخليق ونمو الشق فـي ثلاثـة مواقع هي (مادة الاسـاس او فـي مـادة التقوية او عنـد الـسطح البينـي)، فيمـا لانستبعد وجود فجـوات عنـد أو حـول مناطق التقوية مما يـؤدي الـى مـصدر لتخليق ونمو الشق، وان الكسر الذي حصل في العينات هو كسر هش لانه حدث فجـأة دون ان نتمكن من تمييز أي تـشوه لـدن وهذا هو سلوك الكسر الهش، وهو الكـسر الذي يحدث فجاة دون ان يسبقه أي تـشوه لدن **[انـا. اتـاكر، 1984]**، وقـد عرفـت خصائص الكسر الهش بدقة فـي المـواد الصلبة من قبل العالم (Griffth) وطورت بعدها من قبل العالم (Irwin) الذي فـسر آلية الكسر في المـواد الهندسـية **[S. R. Allen, 1989]**.

وفي نفس الشكل (4) نلاحظ زيـادة في قيمة الطاقة الممتصة بالـصدمة مـع زيادة الكسر الوزني لرايش النحـاس ثـم تنخفض قيمة هذه الطاقـة فـي النمـوذج المقوى برايش النحاس (Chip) ذو الكسر الوزني (1.5%) ويعزى سبب ذلك الى ما يلي، اما التقوية قد تجاوزت الكسر الوزني الحرج اذ ان المادة المتراكبة عندما تتجاوز فيها المادة المـضافة تتغيـر الخـصائص الميكانيكية لها أو بسبب الزوايـا الحـادة للرايش المضاف التي تعمل علـى زيـادة الاجهادات الموضعية (Stress Raisers) وهي المناطق التي يسهل فيها خلق ونمـو الـشقوق **[William D., 2007]** أو السببان المذكوران أعلاه معاً.

ومن الجدول (1) الذي يستعرض قيم الطاقة الممتصة اللازمة للكسر بالـصدمة مع الكسر الوزني لمسحوق رايش النحاس نلاحظ انخفاض قيمـة الطاقـة الممتـصة اللازمة لحدوث الكسر أقل للمادة المتراكبة المقواة برايش النحـاس (Chip) مقارنـةً بتلك المقواة بمسحوق النحاس لنفس الكسر الوزني ولجميع الكسور الـوزني، وهـذا يعود الى النهايات الحادة للرايش (Chip) وهي مناطق تتمركـز فيهـا الاجهـادات ومناطق نمو للشق وتكون مـصدر آخـر لنمو الشقوق ولهذا تحتـاج طاقـة قليلـة لحدوث الكسر حيث ان النهايات الحادة هي مناطق تتمركز فيها الاجهادات ومنـاطق نمـو الـشق **[William D., 2007]**، وللحصول على تقوية عالية يجب اعتمـاد دقائق صغيرة وبمـدى ضـيق وبتوزيـع متجانس داخل مادة الاساس وبكسر وزني مناسب **[William D., 2007]**.

- أختبار مقاومـة الانحنـاء (Flexural Strength)

يوضح الـشكل (5) العلاقـة بـين مقاومة الانحناء والكـسر الـوزني لمـادة التقوية في المادة المتراكبة ذات الاسـاس بولي أستر المقواة بمسحوق النحاس، حيث يلاحظ زيادة المقاومة مع زيـادة الكـسر الوزني ويعزى سبب ذلـك الـى حـدوث التقوية، وتحمـل مـادة التقويـة معظـم الاجهادات المسلطة وتعمل على توزيعهـا في المادة الاساس وبالتـالي تحـول دون تمركز الاجهادات في منطقة معينة، ممـا أدى الى الحاجة الى اجهاد أكبر لحـدوث الفشل عند زيادة الكسر الوزني للمسحوق. كما نتوقع وجود ترابط مـابين مـسحوق النحاس ومادة الاسـاس (البـولي أسـتر) والذي يؤدي الى نشوء سطح بينـي جيـد بحيث ان حصول الكسر يحتاج الى اجهاد أكبر لحدوثـه، وان التقويـة أو تحـسين الخواص الميكانيكية يعتمد علـى الـربط الجيد للسطح البيني ما بين مادة الاسـاس والتقوية **[William D., 2007]**.

في نفـس الـشكل (5) نلاحـظ أن مقاومة الانحناء للمادة المتراكبـة المقـواة برايش النحاس قد قلت عن المادة المتراكبة المقواة بمسحوق النحاس لنفس قيم الكـسر الوزني، فمثلاً عند الكسر الوزني (1.5%) لمسحوق النحاس بلغت مقاومـة الانحنـاء (85.13 Mpa) بينما للمادة المقواة برايش النحاس بلغت (50.08 Mpa) لنفس الكسر الوزني ويعزى سبب ذلك الـى صـعوبة السيطرة على حجم وشكل ومقدار الشقوق للمادة المقواة بالرايش، قد يحتوي الـرايش على شقوق او حزوز حول حافتيه والتـي تكون مراكز الضعف عن التقوية.

يحدث الفشل فـي العينـات بـسبب الاجهادات المسلطة وهـي اجهـاد الـشد والانضغاط والتي تحدث في مواقع مختلفة وبنفس الوقت لان العينـات فـي اختبـار الانحناء الثلاثي النقاط تتعـرض بـصورة عامة الى أجهاد شد على احد جانبي العينة واجهاد انضغاط علـى الجانـب المقابـل **[أ.د. جعفر الحيدري، 2003]**.

الاستنتاجات:-

أ- الطاقة اللازمة لحدوث الكـسر تـزداد بزيادة الكسر الوزني لمسحوق النحاس في البولي استر، بينما للبولي اسـتر المقـوى برايش النحاس تنخفض الطاقـة اللازمـة لحدوث الكسر بعد زيادة الكـسر الـوزني أعلى من 1%.

ب- ان مقاومة الانحناء والطاقة اللازمـة لحدوث الكسر لمادة البولي استر المقـوى بمسحوق النحاس تعطي نتائج أفضل مـن البولي أستر المقوى برايش النحاس لـنفس الكسور الوزنية.

ج- ان مقاومة الانحناء لمادة البولي أستر المقوى برايش النحاس أو بمسحوق النحاس تزداد بزيادة الكسر الوزني.

المراجع :-

- Brian S. Mitchell, "An Introduction to Materials Engineering and Science for Chemical and Materials Engineers", John Willey & Sons, 2004.
- J. S. Wu, K. Friedrich and M. Grossot, "Impact Behavior of Short Fiber/Liquid Crystal Polymer Composites", Composite, Vol.20, No.3, PP. 223-233, 1989.
- M.S Bhatnagar "A Textbook of Polymers, Chemistry and Technology of Polymers – Processing and Aapplication", By Dr. Published by S. Chand & Company LTD, New Delhi, 2004.
- Munir Tasdemir and H. Ozkan Gulsoy, "Mechanical Properties of Polymer Filled with Iron Powder", International Journal of Polymeric Materials, Vol.57, Issu 3, PP. 258-265, 2008.
- N.M. Sofian, M. Rusu, R. Naegu and E. Neagu, "Metal powder-Filled Polyethylene Composites. V. Thermal Properties", Journal of Thermoplastic Composite Materials, Vol 14, No1, PP. 20-30, 2001.
- Prof. Ger Storbl, "The Physics of Polymer", Springer – Verlag Berlin Heidelberg, 2007.
- R. M. Jones, "Mechanics of Composite Materials", 1st Edition, chap.1, New York (1975).
- S. R. Allen and E. J. Roche, "Deformation Behavior of Kevlar, aramid Fiber", Polymer, Vol.30, No.6, PP. 996-1003, 1989.
- Surgasarathi Bose and P.A. Mahan war, "Effect of Particle Size of Filler on Properties of Nylon", Journal of Minerals and Materials Characterization and Engineering, Vol.3, No.1, PP. 23-31, Printed in the USA, 2004.
- W.D Callister, JR." Materials Science and Engineering An Introduction", 6th ed., John Wiely and Sons, Inc., New York, 2003.
- William D. Callister, Jr, "Materials Science and Engineering an Introduction", Joh Wiley & Sons, Inc, 2007.
- أ.د. جعفر الحيدري، "أختبارات المواد الهندسية"، دار المعتز للنشر والتوزيع، 2003.
- أ.د.قحطان خلف الخزرجي، "مبادىء هندسة المواد اللامعدنية"، دار دجلة للنشر، الطبعة الاولى، 2009.
- انا. اتاكر ، ترجمة د. أكرم عزيز محمد "الكيمياء الفيزيائية للبوليمر"، جامعة الموصل، الموصل، 1984. مطابع جامعة.

جدول (1) العلاقة بين نسبة الكسر الوزني والطاقة الممتصة اللازمة لحدوث الكسر بالصدمة

الكسر الوزني %	الطاقة الممتصة اللازمة لحدوث الكسر بالصدمة J	
	بولي أستر مقوى بمسحوق النحاس	بولي أستر مقوى برايش النحاس
0.5	0.45	0.25
0.8	0.52	0.32
1	0.65	0.4
1.2	0.75	0.37
1.5	0.85	0.3

الشكل (1) رايش النحاس المنتج من عملية الخراطة

الشكل (2) مسحوق النحاس المستخدم في التقوية

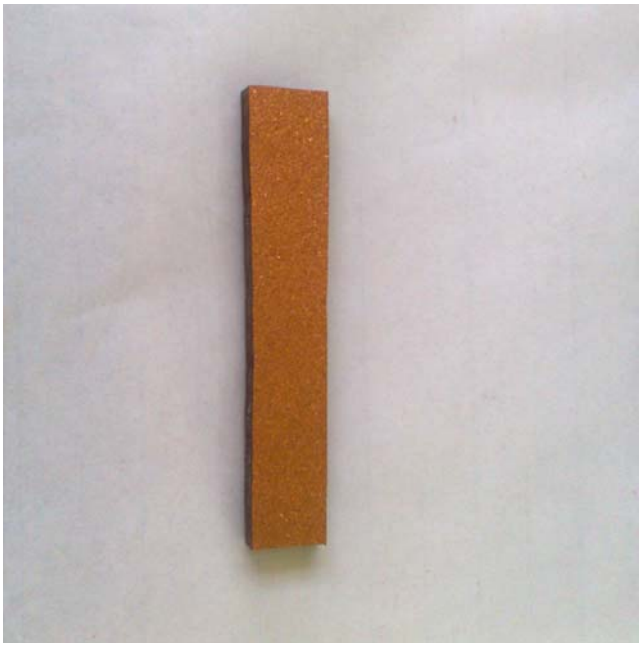

الشكل (3) عينة المادة المتراكبة الناتجة بعد عملية التقطيع المقواة بمسحوق النحاس

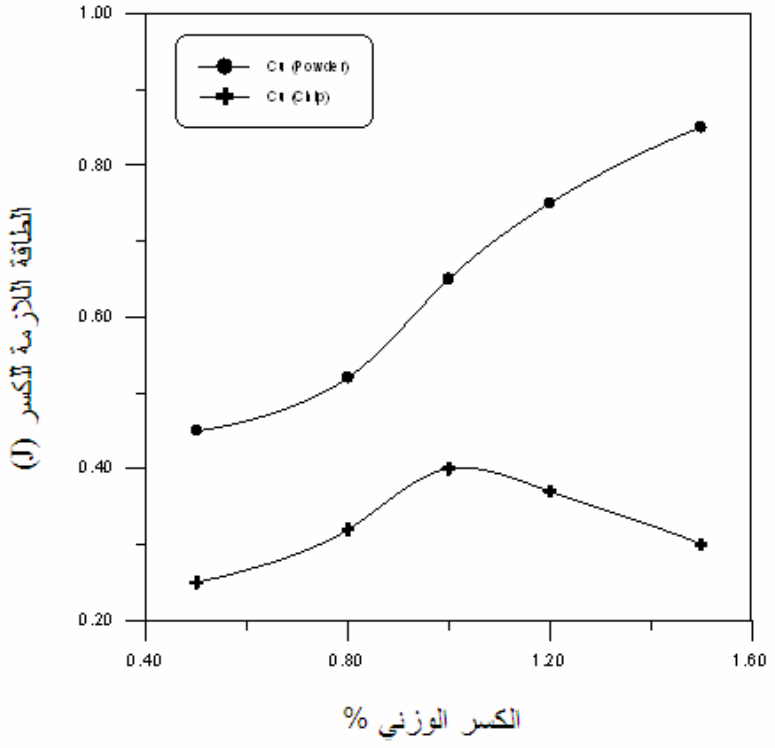

الشكل (4) العلاقة بين الكسر الوزني والطاقة الممتصة اللازمة للكسر للبولي أستر المقوى بالنحاس

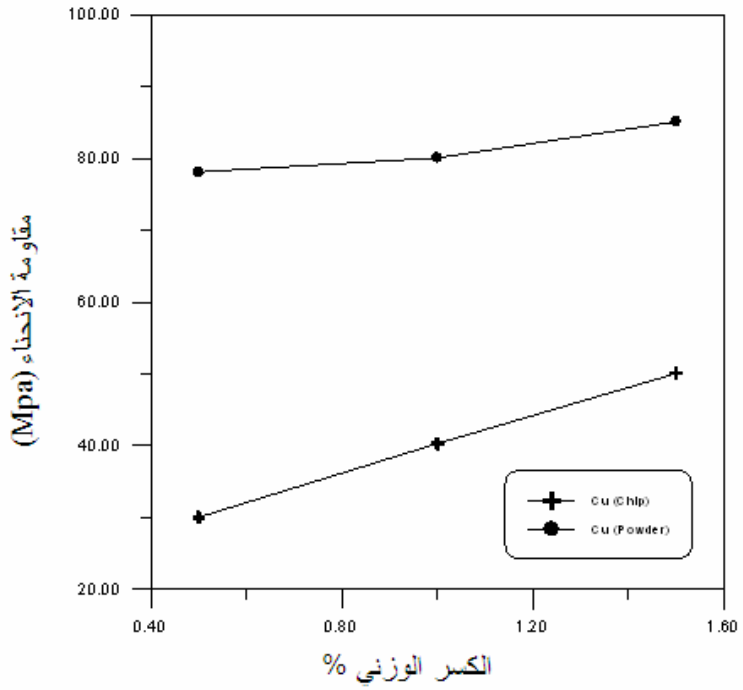

الشكل (5) العلاقة بين الكسر الوزني ومقاومة الانحناء للبولي أستر المقوى بالنحاس